

Comparative Evaluation of Dual-Voltage Automotive Alternators

by

Jamie Carol Byrum

B.S., North Carolina State University (1998)

Submitted to the Department of Electrical Engineering and Computer Science

in Partial Fulfillment of the Requirements for the Degree of

Master of Science in Electrical Engineering and Computer Science

at the Massachusetts Institute of Technology

September 2000

© 2000 Massachusetts Institute of Technology. All rights reserved.

Signature of Author _____

Department of Electrical Engineering and Computer Science

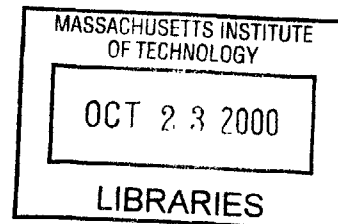
August 31, 2000

Certified by _____

Thomas A. Keim
Principal Research Engineer
Thesis Supervisor

Accepted by _____

Arthur C. Smith
Chairman, Department Committee on Graduate Theses



BARKER

Comparative Evaluation of Dual-Voltage Automotive Alternators

by

Jamie Carol Byrum

Submitted to the Department of Electrical Engineering and Computer Science
In Partial Fulfillment of the Requirements for the Degree of
Master of Science in Electrical Engineering

Abstract

The introduction of 42V / 14V dual-voltage automotive electrical systems in future automobiles necessitates dual-voltage power generation solutions capable of supplying power to both buses simultaneously. A dc / dc converter based system provides such a solution, but the cost, weight, and size of the converter hinder its attractiveness as a viable long term option. By contrast, dual-voltage alternators provide a potentially lighter, smaller, and less costly option for dual-voltage power generation, assuming they can be efficiently constructed with acceptable voltage ripple and control characteristics. This thesis examines two such options, the dual-rectifier alternator and dual-stator alternator, in terms of their electrical performance characteristics and the cost they add to today's automotive electrical system. Numerical simulation tools are used to evaluate one primary performance constraint, voltage ripple, and to size filtering solutions to attenuate ripple to acceptable margins. Implementation issues such as the application of new switched mode rectification techniques, dual-stator alternator controllability as a function of stator – stator turns ratio, dual-voltage power output capabilities, and the appropriateness of aluminum electrolytic capacitors for automotive applications are also discussed. These analyses are used to discuss the cost and weight characteristics of dual-voltage alternators meeting the minimum performance characteristics discussed.

Thesis Supervisor: Thomas A. Keim
Title: Principal Research Engineer

To Grandma.

I miss you.

Acknowledgments

Life has taught me that the successful completion of any serious, difficult undertaking is always based as much upon the strength, encouragement, and moral support derived from others as it is upon the specific resources that enable the work itself. This work is no exception to this precept, and is in many ways the largest illustration of it that I have experienced thus far. Here, I am granted the special privilege to acknowledge both those people who have provided the technical and logistical expertise to make this work possible, as well as those who have provided me the personal strength to see this work through to its end.

Atop this list is Dr. Thomas Keim, whose insight, guidance, and candor brought this work to fruition. During my week-to-week toils and struggles with Saber simulation, academics, and often life itself, Dr. Keim knew how to show enough patience and understanding to keep me sane but still get the job done. More importantly, he encouraged me to believe in the strength of my work during those times when my confidence seemed to waver the most. Dr. Keim always remembered that life did exist beyond the comparative evaluation of dual-voltage automotive alternators, and thereby helped me to remember the bigger picture when all I could see were alternator stators and C core inductors. For these insights, I am deeply grateful to him.

Also deserving of thanks is Prof. John Kassakian, under whose auspices my colleagues and I were granted the wonderful opportunity to interact with the automotive industry at its very core. I also wish to thank the various LEES and Consortium staff members who both technically and personally provided me the expertise and information to make life in the lab both productive and enjoyable: Dave Perreault, for his amazing technical talent and caring demeanor; Vivian Mizuno, for being a big sister, a mother, and your best college buddy all rolled into one; Karin Janson-Strasswimmer and Kiyomi Boyd, for being *nice* experts (a true rarity) on all things logistical at MIT; and Gary DesGroseilliers, for helping us all interact with Consortium company members. I owe a particular debt of gratitude to Anita Chow, one of the brightest and most committed women I know, for all her toils and efforts in formatting this document, in pursuing various technical details, and in being a great friend all at the same time. Beyond the Institute, I gratefully acknowledge the technical support provided by my Research Unit #5 subcommittee, Cornell-Dubilier Electronics, National-Arnold Magnetics, and ON Semiconductor in obtaining information on current industry practice and component pricing data.

However, those who contributed most to the completion of this work probably do not know, or care to know, the first thing about dual-voltage alternators. They are the people who shared with me the late night coffees and dinners in the North End, who taught me Chinese, and who introduced me to opera. They are the people who listened to my heartache and encouraged me. They are the people who kept me strong. First on this list is the now Dr. Vahe Caliskan, who happens to know both about good comedy (well, let's not get carried away) *and* about dual-

Acknowledgments

voltage alternators. Vahe contributed to and advised this work on a daily basis, and was seldom too busy to chat about the definition of mutual inductance or the way deep-dish pizza is made in Chicago. Vahe's alternator models provided the foundation of this work, and his daily expertise provided me the means to carry out the work. More importantly, though, his selflessness and wit made life in the lab more tolerable and even, dare I say, enjoyable. Tim Neugebauer endured a year in the life of Fred for me, and was always willing to help me polish up my Cantonese. Thanks to Tim, Chinese sportscasting is now an exciting career opportunity for me should engineering ever grow tiresome. James Hockenberry always provided a forum for refreshing socially-informed conversation around the lab, and Ernst Scholtz shared his love of South African music with me. I also wish to thank Chef Alfred Q. Chow (the Q's for quick), Ian "the hottie" Lorilla, Amy Ng, Florence Zhu, Xiaozhen Zhang, and the other 10-082 LEES students for making work just a little less burdensome and a windowless basement just a little bit brighter.

Yet, the group to whom I attribute the most credit for completion of this work is the MIT Protestant Student Community and Chaplain John Wuestneck. For it is this group that truly provided me the strength to push onward within an Institute that likes to do things "a little differently". John Wuestneck reached out to me as a new graduate student in a way that no one else did, and he gave me a forum in which to explore my faith and take sanctuary from problem sets and research and a world that most days just didn't make sense. I am proud to call him my friend and my brother in Christ. John McKay, Shelby Savage, and Annika Hill all opened their hearts to me and stood by me through both heartbreak and celebration. John, Shelby, and Annika live and breathe Jesus Christ in all they do, and they are in very large part the reason this thesis is complete. I love each of you dearly. Fellow Wolfpacker, fellow North Carolinian, and fellow former roommate James Taylor has been a true friend through both the fire and the rain, and he always helped me to keep Carolina in my mind. Thanks to my other dear friends in PSC - Paulo, Lora, Katie, Sarah, Jason, Vicki, Susanna, Garrett, Beth, and Mark - for your fellowship, companionship, and Christlike love. You are the force that has sustained me during this work.

Lastly, I owe the ultimate debt of gratitude to two people in Bertie County, North Carolina, who reared me with a Godly hand and loved me even when I was at my most unlovable. To my mother, I am thankful for constant prayers for my safety, well being, and success. When the rest of the world seems to have turned a deaf ear, my mother's unfailing presence has always lifted me from life's valleys and has reminded me that I am indeed not alone in this world. To my father I attribute complete credit (and sometimes blame) for introducing me to the engineer inside me at the age of 10. Were it not for the wire pulls and receptacle installations that my father and I performed together in days gone by, I dare say that this work would not be bearing my name today. Thank you both for loving me enough to rear and educate me in such a way that I can be a giver to society, and not merely a taker from it. I know that this work is not of my own hand, but is the blessing of my Heavenly Father who molds me, enables me, and uses me for His honor and glory. I know that by myself I am nothing, but that I can do all things through Christ who strengthens me.

This work is dedicated in loving memory of my grandmother, Teresa Cannon Mullen Byrum, whose love and generosity I miss each and every day.

Contents

Chapter 1: Introduction.....	23
1.1 Motivations for a Higher Voltage Electrical System	24
1.1.1 Increasing Demand for Electrical Power	24
1.1.2 Potential for Greater Fuel Economy	25
1.2 Implementing 42V with Dual-Voltage Electrical Systems	26
1.2.1 Proposed Dual-Voltage Power Supply Architectures.....	26
1.2.2 Advantages of Dual-Voltage Electrical Systems.....	28
1.3 An Alternative to the dc/dc Converter	29
1.4 Thesis Objectives	30
1.5 Organization of Thesis	31
Chapter 2: Dual-Voltage Alternator Topologies	33
2.1 Functional Description of Dual-Rectifier Alternator Topology.....	33
2.1.1 Component-Level Description.....	33
2.1.2 14V Bus and 42V Bus Control Strategies	35
2.2 Functional Description of Dual-Stator Alternator Topology	36
2.2.1 Component-Level Description.....	36
2.2.2 14V Bus and 42V Bus Control Strategies	37
2.2.3 Dual-Stator Architecture Design Variations.....	38

Contents

2.3	Advantages of Dual-Voltage Alternators.....	39
2.4	Challenges for Dual-Voltage Alternators.....	41
2.4.1	Independent Controllability of 14 and 42V Buses.....	41
2.4.2	Voltage Ripple Created by Thyristor Switching.....	41
2.5	Analysis of Voltage Ripple within this Research.....	42
2.6	Summary	44
Chapter 3: The Search for a Ripple Specification		45
3.1	Voltage Ripple in Prevailing Literature	45
3.2	Relevance of Voltage Ripple Measuring Point	47
3.3	Empirical Ripple Measurements	49
3.4	Industry Feedback and the Development of a 14V Ripple Specification	52
3.5	Development of a 42V Ripple Specification.....	54
3.6	Summary	55
Chapter 4: Ripple Modeling with Dual-Voltage Alternators.....		57
4.1	Software-Based System Modeling	57
4.1.1	Motivations for a Simulation-Based Analysis.....	57
4.1.2	Alternator Modeling in Saber	58
4.1.3	Lead-Acid Battery Modeling for Each Bus	61
4.1.4	Electrical Distribution and Utilization Subsystem Modeling	62
4.2	Simulation Parameters.....	63

4.2.1	Alternator Shaft Speed.....	63
4.2.2	Bus Loading.....	63
4.2.3	Battery Disconnection.....	64
4.3	Unfiltered Voltage and Current Ripple with the Dual-Rectifier Alternator.....	65
4.3.1	Unfiltered Dual-Rectifier Alternator Ripple Waveforms with Battery Connected	65
4.3.2	Observations About Ripple with the Battery Connected.....	70
4.3.3	Unfiltered Dual-Rectifier Alternator Ripple Waveforms with Battery Disconnected.....	70
4.3.4	Observations about Ripple with the Battery Disconnected	75
4.4	Unfiltered Voltage and Current Ripple with the Dual-Stator Alternator.....	75
4.4.1	Unfiltered Dual-Stator Alternator Ripple Waveforms with Battery Connected	75
4.4.2	Observations About Ripple with the Battery Connected.....	80
4.4.3	Unfiltered Dual-Stator Alternator Ripple Waveforms with Battery Disconnected.....	80
4.4.4	Observations about Ripple with the Battery Disconnected	85
4.5	Summary	85
Chapter 5: Ripple Filtering for Dual-Voltage Alternators.....		87
5.1	Passive Filter Design.....	87
5.1.1	Design Considerations.....	87
5.1.2	Survey of Dual-Rectifier Filter Topologies	88
5.1.3	Dual-Rectifier Filter Design Algorithm.....	90

Contents

5.1.4	Design Validation of the Dual-Rectifier Ripple Filter in Saber	92
5.1.5	Ripple Capacitor Selection for the Dual-Stator Architecture	93
5.1.6	Final Dual-Rectifier and Dual-Stator Filter Designs	94
5.2	Filtered Voltage Ripple Results	95
5.2.1	Filtered Dual-Rectifier Alternator Voltage Ripple Waveforms	95
5.2.2	Observations about Filtered Voltage Ripple with the Dual-Rectifier Alternator	100
5.2.3	Filtered Dual-Stator Alternator Voltage Ripple Waveforms	100
5.2.4	Observations about Filtered Voltage Ripple with the Dual-Stator Alternator	105
5.3	Component Design Process.....	105
5.3.1	Inductor and Capacitor Current-Carrying Requirements.....	106
5.3.2	Summary of Filter Current Measurements	108
5.3.3	Capacitor Selection Process.....	115
5.3.4	Inductor Design Process	117
5.4	Summary	120
Chapter 6: Dual-Voltage Alternator Implementation Issues.....		121
6.1	Switched-Mode Rectification Techniques	121
6.2	Controllability of the Dual-Stator Alternator	124
6.2.1	Issues with a 3:1 Stator – Stator Turns Ratio.....	124
6.2.2	Decreasing the Stator – Stator Turns Ratio	125
6.2.3	Tradeoffs between Capacity and Controllability	132

6.3	Suitability of Electrolytic Capacitors for Automotive Applications.....	135
6.4	Summary	138
Chapter 7: Cost and Weight Analyses of Dual-Voltage Alternators.....		139
7.1	Alternator Machine Cost and Weight.....	140
7.1.1	Dual-Rectifier Machine Sizing	140
7.1.2	Dual-Stator Machine Structure	143
7.2	Power Electronics Cost	147
7.3	Passive Filter Cost and Weight	150
7.4	Summary	154
Chapter 8: Conclusions and Further Research.....		155
8.1	Thesis Conclusions.....	155
8.1.1	Unfiltered Voltage Ripple Characteristics.....	156
8.1.2	Filtering Solutions Producing Acceptable Attenuation	156
8.1.3	Implementation Issues Affecting Dual-Voltage Alternator Viability....	157
8.1.4	Power Output Capacity Issues Arising with Dual-Voltage Alternators	157
8.1.5	Cost and Weight Issues Involved with Dual-Voltage Alternator Implementation	158
8.2	Further Research	159

Contents

Appendix A: Saber Automotive Electrical Models	161
A.1 Saber MAST Code for Single-Stator Alternator	161
A.2 Saber MAST Code for Dual-Stator Alternator	164
A.3 Saber MAST Code for Voltage Regulator	169
A.4 Saber MAST Code for Firing Angle Regulator	171
Appendix B: MATLAB Filter Component Estimation Algorithm.....	175

List of Figures

Figure 1.1: Historical and projected trends in automotive electrical system loading.....	25
Figure 1.2: Proposed dual-voltage automotive power supply architectures: (a) 42 V alternator with dc/dc converter; (b) 42 V alternator with dual rectifier; (c) 42 V / 14 V dual-stator alternator	27
Figure 2.1: Component-level diagram of the dual-rectifier alternator topology.	34
Figure 2.2: Component-level diagram of the dual-stator alternator topology	37
Figure 2.3: Illustration of ripple present in each bus's rectifier output current and in the current delivered to each bus's load for the unfiltered dual-rectifier alternator pictured in Figure 2.1.	43
Figure 3.1: Graphical illustration of J1113-2 showing the peak-to-peak voltage magnitudes that mandate certain regions of operation for different classes of loads.....	47
Figure 3.2: Ripple analysis models for a typical automotive electrical system: (a) simple automotive system model including the alternator, battery, and load; (b) ac signal model detailing how ripple is generated and attenuated throughout the system.....	48
Figure 3.3: Ripple measurements taken at alternator output terminals for a 1990 Subaru Legacy Wagon with a Hitachi LR170-732C 14V alternator.....	50
Figure 3.4: Ripple measurements taken at headlamp terminals for a 1990 Subaru Legacy Wagon.	51
Figure 3.5: Summary of maximum peak-to-peak transient and steady-state ripple measurements at the alternator and headlight terminals, as illustrated in Figures 3.3 and 3.4.	52
Figure 3.6: 14V alternator voltage ripple specification for voltage ripple observed at the rectifier output terminals of dual-voltage alternators.....	54
Figure 4.1: Battery model used in simulated automotive electrical system.	61

List of Figures

Figure 4.2: Automotive electrical system simulation model employed in this research to examine alternator voltage ripple.....	63
Figure 4.3: Unfiltered 14V bus ripple waveforms for the dual-rectifier architecture operating at 2000 rpm alternator shaft speed, with the battery <i>connected</i> : (a) voltage waveforms; (b) current waveforms.....	66
Figure 4.4: Unfiltered 42V bus ripple waveforms for the dual-rectifier architecture operating at 2000 rpm alternator shaft speed, with the battery <i>connected</i> : (a) voltage waveforms; (b) current waveforms.....	67
Figure 4.5: Unfiltered 14V bus ripple waveforms for the dual-rectifier architecture operating at 10000 rpm alternator shaft speed, with the battery <i>connected</i> : (a) voltage waveforms; (b) current waveforms.....	68
Figure 4.6: Unfiltered 42V bus ripple waveforms for the dual-rectifier architecture operating at 10000 rpm alternator shaft speed, with the battery <i>connected</i> : (a) voltage waveforms; (b) current waveforms.....	69
Figure 4.7: Unfiltered 14V bus ripple waveforms for the dual-rectifier architecture operating at 2000 rpm alternator shaft speed, with the battery <i>disconnected</i> : (a) voltage waveforms; (b) current waveforms.....	71
Figure 4.8: Unfiltered 42V bus ripple waveforms for the dual-rectifier architecture operating at 2000 rpm alternator shaft speed, with the battery <i>disconnected</i> : (a) voltage waveforms; (b) current waveforms.....	72
Figure 4.9: Unfiltered 14V bus ripple waveforms for the dual-rectifier architecture operating at 10000 rpm alternator shaft speed, with the battery <i>disconnected</i> : (a) voltage waveforms; (b) current waveforms.....	73
Figure 4.10: Unfiltered 42V bus ripple waveforms for the dual-rectifier architecture operating at 10000 rpm alternator shaft speed, with the battery <i>disconnected</i> : (a) voltage waveforms; (b) current waveforms.....	74
Figure 4.11: Unfiltered 14V bus ripple waveforms for the dual-stator architecture operating at 2000 rpm alternator shaft speed, with the battery <i>connected</i> : (a) voltage waveforms; (b) current waveforms.....	76
Figure 4.12: Unfiltered 42V bus ripple waveforms for the dual-stator architecture operating at 2000 rpm alternator shaft speed, with the battery <i>connected</i> : (a) voltage waveforms; (b) current waveforms.....	77

Figure 4.13: Unfiltered 14V bus ripple waveforms for the dual-stator architecture operating at 10000 rpm alternator shaft speed, with the battery <i>connected</i> : (a) voltage waveforms; (b) current waveforms.	78
Figure 4.14: Unfiltered 42V bus ripple waveforms for the dual-stator architecture operating at 10000 rpm alternator shaft speed, with the battery <i>connected</i> : (a) voltage waveforms; (b) current waveforms.	79
Figure 4.15: Unfiltered 14V bus ripple waveforms for the dual-stator architecture operating at 2000 rpm alternator shaft speed, with the battery <i>disconnected</i> : (a) voltage waveforms; (b) current waveforms.	81
Figure 4.16: Unfiltered 42V bus ripple waveforms for the dual-stator architecture operating at 2000 rpm alternator shaft speed, with the battery <i>disconnected</i> : (a) voltage waveforms; (b) current waveforms.....	82
Figure 4.17: Unfiltered 14V bus ripple waveforms for the dual-stator architecture operating at 10000 rpm alternator shaft speed, with the battery <i>disconnected</i> : (a) voltage waveforms; (b) current waveforms.	83
Figure 4.18: Unfiltered 42V bus ripple waveforms for the dual-stator architecture operating at 10000 rpm alternator shaft speed, with the battery <i>disconnected</i> : (a) voltage waveforms; (b) current waveforms.	84
Figure 5.1: Final voltage ripple filter designs for the dual-rectifier architecture: (a) 14V filter; (b) 42V filter.....	94
Figure 5.2: Final voltage ripple filter designs for the dual-stator architecture: (a) 14V filter; (b) 42V filter.....	95
Figure 5.3: Filtered ripple waveforms for the dual-rectifier architecture operating at 2000 rpm alternator shaft speed, with the battery <i>connected</i> : (a) 14V bus voltage waveforms; (b) 42V bus voltage waveforms.	96
Figure 5.4: Filtered ripple waveforms for the dual-rectifier architecture operating at 10000 rpm alternator shaft speed, with the battery <i>connected</i> : (a) 14V bus voltage waveforms; (b) 42V bus voltage waveforms.	97
Figure 5.5: Filtered ripple waveforms for the dual-rectifier architecture operating at 2000 rpm alternator shaft speed, with the battery <i>disconnected</i> : (a) 14V bus voltage waveforms; (b) 42V bus voltage waveforms.	98

List of Figures

Figure 5.6: Filtered ripple waveforms for the dual-rectifier architecture operating at 10000 rpm alternator shaft speed, with the battery *disconnected*: (a) 14V bus voltage waveforms; (b) 42V bus voltage waveforms. 99

Figure 5.7: Filtered ripple waveforms for the dual-stator architecture operating at 2000 rpm alternator shaft speed, with the battery *connected*: (a) 14V bus voltage waveforms; (b) 42V bus voltage waveforms. 101

Figure 5.8: Filtered ripple waveforms for the dual-stator architecture operating at 10000 rpm alternator shaft speed, with the battery *connected*: (a) 14V bus voltage waveforms; (b) 42V bus voltage waveforms. 102

Figure 5.9: Filtered ripple waveforms for the dual-stator architecture operating at 2000 rpm alternator shaft speed, with the battery *disconnected*: (a) 14V bus voltage waveforms; (b) 42V bus voltage waveforms. 103

Figure 5.10: Filtered ripple waveforms for the dual-stator architecture operating at 10000 rpm alternator shaft speed, with the battery *disconnected*: (a) 14V bus voltage waveforms; (b) 42V bus voltage waveforms..... 104

Figure 5.11: Filter current waveforms for the L_1 and L_2 inductors and the shunt capacitors for the dual-rectifier architecture operating at 10000 rpm alternator shaft speed, with the battery *connected*: (a) 14V filter currents; (b) 42V filter currents. 109

Figure 5.12: Filter current waveforms for the L_1 and L_2 inductors and the shunt capacitors for the dual-rectifier architecture operating at 10000 rpm alternator shaft speed, with the battery *disconnected*: (a) 14V filter currents; (b) 42V filter currents. 110

Figure 5.13: 14V filter current waveforms for the L_1 and L_2 inductors and the shunt capacitors for the dual-rectifier architecture operating at 10000 rpm alternator shaft speed, *with the full load on the 14V bus*: (a) battery connected; (b) battery disconnected. 111

Figure 5.14: 42V filter current waveforms for the L_1 and L_2 inductors and the shunt capacitors for the dual-rectifier architecture operating at 10000 rpm alternator shaft speed, *with the full load on the 42V bus*: (a) battery connected; (b) battery disconnected.. 112

Figure 5.15: Filter current waveforms illustrating ripple current through the shunt capacitors connected across the rectifier output terminals of the dual-stator alternator operating at 10000 rpm alternator shaft speed, with the battery *connected*: (a) 14V capacitor ripple current (per capacitor); (b) 42V capacitor ripple current. 113

Figure 5.16: Filter current waveforms illustrating ripple current through the shunt capacitors connected across the rectifier output terminals of the dual-stator alternator operating at 10000 rpm alternator shaft speed, with the battery <i>disconnected</i> : (a) 14V capacitor ripple current (per capacitor); (b) 42V capacitor ripple current.....	114
Figure 6.1: Lundell alternator output power capability versus output voltage, parameterized across alternator shaft speed.	122
Figure 6.2: Boost semi-bridge implementation of the switched-mode rectifier.	122
Figure 6.3: Switched-mode rectifier (SMR) applied to the dual-rectifier alternator.	124
Figure 6.4: Controllability waveforms illustrating the dual-stator alternator output voltage, control handle, and rectifier output current for each bus, with a 3:1 stator-stator turns ratio: (a) 42V bus; (b) 14V bus.	126
Figure 6.5: Averaged equivalent circuit model of the synchronous generator connected to a full-bridge diode rectifier and driving a constant-voltage load.	127
Figure 6.6: Controllability waveforms illustrating the dual-stator alternator output voltage, control handle, and rectifier output current for each bus, with a 2.5:1 stator – stator turns ratio: (a) 42V bus; (b) 14V bus.	131
Figure 6.7: Lundell alternator output power capability versus output voltage for a rewind 42V alternator.....	133
Figure 6.8: Output power capability for two different winding implementations of the dual-stator alternator's 42V stator output at 1800 rpm alternator shaft speed.....	134
Figure 6.9: Operating lifetime (left axis) and percent of operating lifetime used per hour of operation (right axis) versus internal operating temperature for the Cornell Dubilier 301 series 25V capacitors used in the dual-rectifier and dual-stator alternator 14V bus ripple filters.	137
Figure 7.1: Cross-sectional diagram of the stator teeth and slots in a typical 14V single-stator alternator.....	145
Figure 7.2: Cross-sectional diagram illustrating estimated changes in slot depth and machine diameter for a 42V / 14V dual-stator alternator.....	146
Figure 7.3: Scale drawing of the dual-rectifier voltage ripple filter: (a) 14V filter; (b) 42V filter.....	152

List of Figures

Figure 7.4: Scale drawing of the dual-stator voltage ripple filtering capacitors:
(a) 14V filtering capacitors, (b) 42V filtering capacitors..... 153

List of Tables

Table 3.1: Summary of voltage ripple specifications for the 14V and 42V buses of dual-voltage alternators.....	56
Table 4.1: Per-phase resistance and inductance parameters for the 42V single-stator alternator simulation model.	59
Table 4.2: Derived self and mutual inductance parameters for the 42V single-stator alternator simulation model.	59
Table 4.3: Per-phase resistance and inductance parameters for the 42V / 14V dual-stator alternator simulation model.	60
Table 4.4: Derived self and mutual inductance parameters for the 42V / 14V dual-stator alternator simulation model.	60
Table 4.5: Distribution of delivered power for simulations conducted at 2000 rpm and 10000 rpm alternator shaft speeds.	64
Table 5.1: Single-stage passive filter topologies examined as potential dual-voltage alternator filtering solutions.....	89
Table 5.2: Summary of peak-to-peak voltage ripple magnitudes for ripple observed at the dual-rectifier alternator output terminals.	100
Table 5.3: Summary of peak-to-peak voltage ripple magnitudes for ripple observed at the dual-stator alternator output terminals.....	105
Table 5.4: 14V bus loading scenario producing worst-case current-carrying requirements for the 14V L_2 inductor at 10000 rpm.....	107
Table 5.5: 42V bus loading scenario producing worst-case current-carrying requirements for the 42V L_2 inductor at 10000 rpm.....	107
Table 5.6: Dual-rectifier alternator filter current measurements used to size inductors and capacitors for the 14V and 42V voltage ripple filters.....	115
Table 5.7: Dual-stator alternator RMS capacitor current measurements used to size filter capacitors for the 14V and 42V buses..	115

List of Tables

Table 5.8: Filter capacitors chosen for use in the 14V and 42V ripple filters for the dual-rectifier alternator..	117
Table 5.9: Filter capacitors chosen for use in the 14V and 42V ripple filters for the dual-stator alternator.	117
Table 5.10: Inductor core material parameter values for the selected silicon steel C core and MPP toroidal power core materials.	118
Table 5.11: Energy storage and area product calculations for the inductors used in the 14V and 42V ripple filters for the dual-rectifier alternator.	119
Table 5.12: Inductor cores chosen for use in the 14V and 42V ripple filters for the dual-rectifier alternator.	120
Table 7.1: Measured dimensions of a single-stator machine and extrapolated dimensions of a dual-stator machine.	147
Table 7.2: Weight and cost of the single-stator and dual-stator steel stacks and copper windings.	147
Table 7.3: Electrical characteristics and pricing data for the ON Semiconductor MCR265-4 and International Rectifier 50RIA10 SCR thyristors.	149
Table 7.4: Price boundaries for the additional power electronics components required to implement the dual-rectifier and dual-stator alternators, based on high-volume price quotes for the IR 50RIA10 thyristor.	150
Table 7.5: Estimated weight and cost of passive filtering components required to implement the dual-rectifier 14V and 42V ripple filters.	151
Table 7.6: Weight and cost of passive filtering components required to implement the dual-stator 14V and 42V ripple filters	151
Table 7.7: Total volume, weight, and cost per filter for the 14V and 42V dual-rectifier and dual-stator voltage ripple filters.	153

Introduction

In contemplating the challenges and possibilities facing the automotive electrical systems of future production vehicles, Mercedes Benz approached MIT in 1994 with a proposition: synergize the global automotive industry around a new higher voltage electrical system for passenger vehicles. The motivation to study a higher voltage electrical system stemmed from the observation that electrical and electronic features envisioned for future automobiles place a far greater power burden on the automotive electrical system than the current 14V system is able to efficiently supply. Thus began the mission of the original MIT Working Group, a group of 7 automotive OEMs and suppliers seeking to establish a new system voltage and to begin evaluating issues, both logistical and technical, surrounding the installation of a new system voltage in the automobile. The MIT Working Group, which over time has grown into the 47-member¹ MIT / Industry Consortium on Advanced Automotive Electrical / Electronic Components and Systems, put forth a proposal to implement a 42V automotive electrical system to meet the power and efficiency demands of future automotive electrical loads. This proposal has since won international acceptance, and a worldwide effort is underway to implement 42V automotive electrical systems in future vehicles. [1]

An issue of primary interest to this design and implementation effort involves the architectural makeup of these new higher voltage systems. Due to the costs and challenges presented by converting the entire electrical system from a completely 14V system to a completely 42V system, the automotive industry generally agrees that a dual-voltage 42V / 14V system is the most technically feasible and cost effective way to introduce 42V into the automobile. This move, however, introduces the new challenge of generating both 42V and 14V within the vehicle simultaneously. Several options exist for automotive dual-voltage power generation, each with its own set of performance, weight, and cost characteristics. The option most examined heretofore is the dc / dc converter based architecture, in which a 42V alternator generates power for the 42V bus and a dc / dc buck converter generates power for the 14V bus. By contrast, a class of alternators called *dual-voltage alternators* provides for dual-voltage power generation within the alternator unit itself, without the need to supplement the alternator with an external power converter. Though dual-voltage alternators have been examined far less than the dc / dc converter architecture for 42V / 14V automotive applications, they present great potential for dual-voltage power generation at a fraction of the cost and size of the dc / dc converter based architecture. This thesis will examine this potential by examining some of the electrical performance, weight, and cost characteristics that dual-voltage alternators present as candidates for automotive dual-voltage power generation.

¹ August 2000 membership

This chapter will introduce the analysis of dual-voltage alternators by first motivating the need for a higher voltage automotive electrical system, and then by discussing the need for dual-voltage power generation within 42V automotive electrical systems. It will then discuss the three dual-voltage power generation architectures being considered by the automotive industry, emphasizing the ways in which the two dual-voltage alternator architectures potentially provide attractive alternatives to the dc / dc converter architecture. Finally, the technical objectives of this research will be discussed, and the organization of the thesis will be previewed.

1.1 Motivations for a Higher Voltage Electrical System

The pursuit of a higher voltage automotive electrical system has been motivated by two main considerations. The first involves the ever-increasing demand for electrical power by electrical loads within the vehicle, while the second involves the desire to attain higher fuel economy by reducing the mechanical load driven by the engine. [2]

1.1.1 Increasing Demand for Electrical Power

As more performance, convenience, and safety features have been added to the automobile over the last two decades, the demand for electrical power has grown nearly beyond the limits of what can be efficiently produced by the current 14V system. Electrical loading within the average automobile has increased by approximately 4% per year in recent years, causing the total electrical load to double within the last twenty years and to quadruple since the shift from 6V to 12V in the mid 1950s. [3] The historical and projected trends in electrical loading for a high-end vehicle are illustrated in Figure 1.1.

The growth in power demand during recent years has been accelerated by the growth in convenience features (e.g., CD / stereo systems, power windows, power seat adjusters), safety features (anti-lock braking systems, interior diagnostic indicators) and body electronics (active suspension systems). Also, paralleling the total load growth in the automobile has been the growth in the number of high power loads, which demand larger amounts of current per load from the 14V bus. These loads necessitate larger wire sizes within the electrical distribution system, adding extra weight and cost to the vehicle.

Miller et. al. [4] assert that the absolute maximum power capacity for the present 14V system is 3 kW. However, this operating point is far from efficient for the present system due to the added costs of operating high power loads on the 14V bus as it exists today. The present 14V automotive electrical system is capable of supplying approximately 1.6 kW of power to automotive loads, and this system can be resized to handle up to 3 kW of loading. However, such an expansion also necessitates that the system be capable of carrying over 200 A of current to loads throughout the system. Such high current levels require much larger wiring, switching, and fusing systems whose costs grow at a rate disproportionate to the added power capacity.

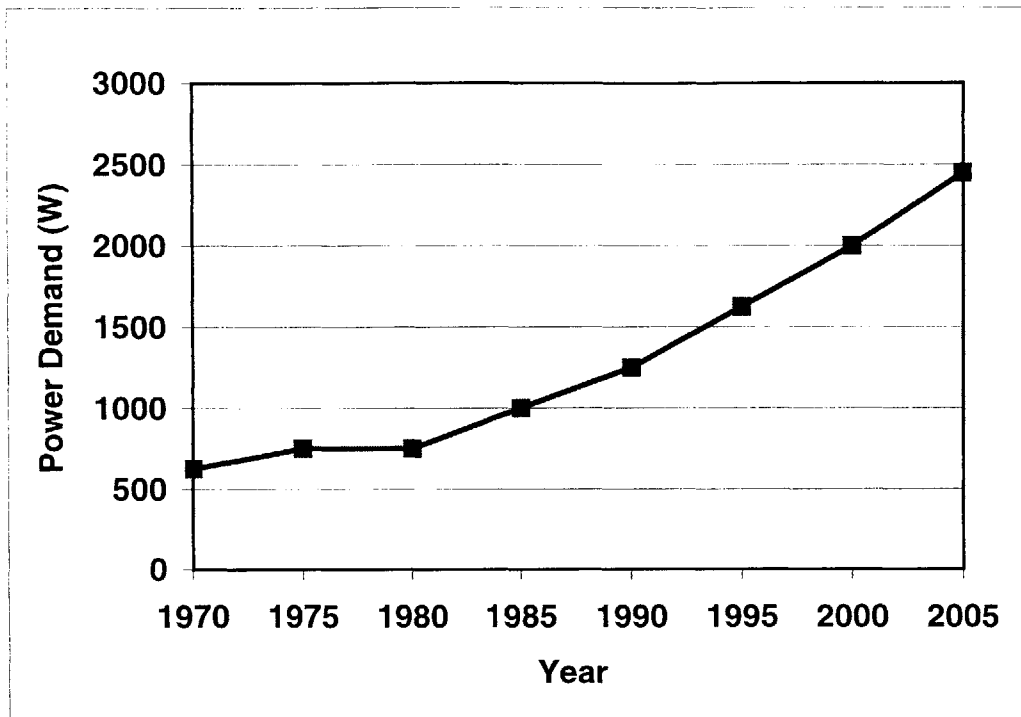


Figure 1.1: Historical and projected trends in automotive electrical system loading (adapted from [5]).

Thus, as power levels continue to increase in the automobile, the economic feasibility of the present 14V system continues to decrease.

Increasing the automotive electrical bus voltage from 14V to 42V alleviates the issues brought about by a continually growing power demand because it allows a given amount of power to be delivered to the electrical system with one-third the amount of current required in the 14V system. This serves to reduce the size of the wiring harness for a given power level, since the amount of current delivered to the loads is reduced for a given power level. The 3 kW barrier that exists with the present 14V system can thus be lifted, since the high current levels which produce this barrier are reduced by a factor of three. This facilitates the ability of the system to supply the automobile's ever-increasing power demand, as well as the ability of the system to supply future high power loads (such as electric active suspension) that cannot be supplied by the present system.

1.1.2 Potential for Greater Fuel Economy

The move to a higher voltage electrical system is also motivated by the industry's mandate to improve automotive fuel efficiency in as many ways as possible. This occurs in part by improving the efficiency with which electricity is distributed throughout the vehicle, and by

converting present mechanically powered loads into electrically powered loads when it is advantageous to do so.

A 42V system improves electrical efficiency by reducing the amount of current necessary to power a given electrical load, thereby reducing the ohmic losses present in the distribution system. Reduced electrical losses in the vehicle decrease the amount of electricity that must be generated to supply a given load, so the amount of fuel needed to power a given electrical load decreases. As stated earlier, reduced current levels also allow for a reduction in wire size, which implies a reduction in the weight of the electrical system for a given power level. These reductions in power losses and in weight both directly translate into improvements in automotive fuel efficiency.

The move to 42V also enables some loads that are at present mechanically powered by the engine, such as the air conditioning compressor and engine valves, to be powered electrically. Electromechanical engine valves are of particular interest because of the opportunities they provide for improved fuel economy and engine performance. Engine valves in today's vehicles are controlled via the crankshaft, so valve characteristics such as profile, lift, and timing cannot be independently controlled on a per-valve basis. By contrast, electromechanical engine valves allow each of these characteristics to be independently controlled for each valve, such that fuel economy, torque, and emissions can be optimized across a range of operating conditions for the engine. [6]

1.2 Implementing 42V with Dual-Voltage Electrical Systems

The introduction of 42V to the automotive electrical system increases the electrical efficiency of the system and enables the addition of future higher power loads providing increased comfort, safety, and fuel efficiency. However, the transition to a 42V electrical system comes at the cost of redesigning those loads that are well suited to 42V operation, and accommodating those loads that are not well suited. These costs can be mitigated by a solution which allows for the inclusion of both 42V and 14V loads, and which also allows loads to migrate from the 14V bus to the 42V bus over time. Dual-voltage electrical systems provide such a solution by allowing loads of both voltages to remain a part of the electrical system, while providing a way for loads to migrate between the buses over time regardless of the time at which 42V is introduced into the vehicle.

1.2.1 Proposed Dual-Voltage Power Supply Architectures

A **dual-voltage electrical system** is a system that generates and distributes both 42V and 14V simultaneously within the vehicle, thereby allowing both 42V and 14V loads to be powered simultaneously. This system is based around a **dual-voltage power supply** that provides power to both buses. Three dual-voltage power supply architectures under consideration by the automotive industry are pictured in Figure 1.2.

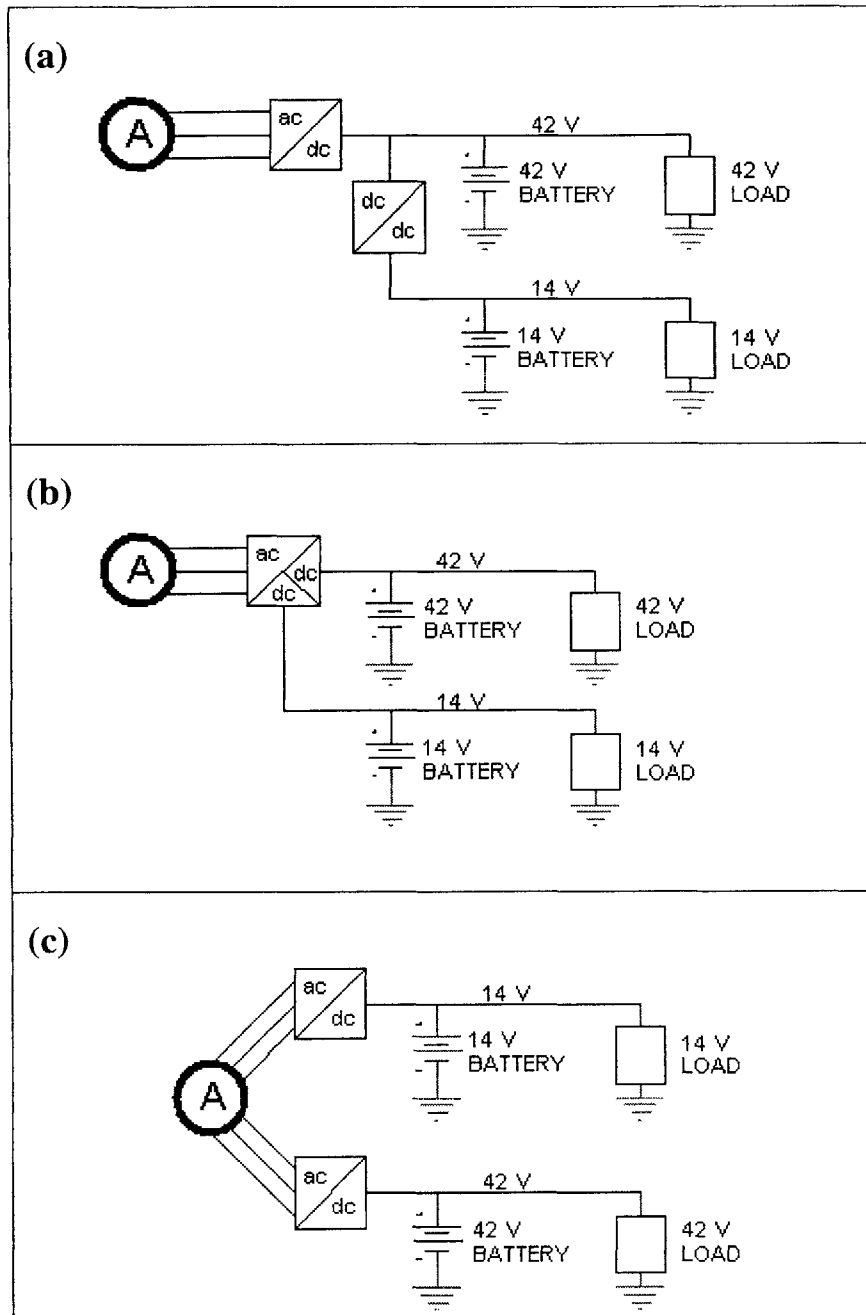


Figure 1.2: Proposed dual-voltage automotive power supply architectures: (a) 42V alternator with dc / dc converter; (b) 42V alternator with dual rectifier; (c) 42V / 14V dual-stator alternator.

The *dc / dc converter* architecture (Figure 1.2(a)) is the least intrusive to the alternator, since the converter is simply connected to the dc rectifier output of a 42V alternator. In this configuration, the converter functions as a buck converter to step the 42V generated by the alternator down to 14V for the low voltage bus. Like the *dc / dc converter*, the *dual-rectifier alternator* architecture (Figure 1.2(b)) utilizes a 42V alternator and a standard full-bridge diode rectifier to generate 42V dc. However, this architecture uses a phase-controlled half-bridge rectifier to generate 14V dc for the low voltage bus. The *dual-wound alternator* architecture (Figure 1.2(c)) differs from the dual-rectifier architecture in that the alternator itself contains two sets of stator windings. In the implementation presented here, the high voltage winding is connected to a standard full-bridge diode rectifier and is regulated via standard field current control, while the low voltage winding is connected to a full-bridge thyristor rectifier and is regulated via phase angle control of the thyristors. Thus, each of these three dual-voltage architectures uses different rectification and/or control techniques to meet the goals for dual-voltage power generation in future automobiles.

1.2.2 Advantages of Dual-Voltage Electrical Systems

Dual-voltage automotive electrical systems are advantageous because they (1) allow loads which do not benefit from 42V operation to remain on the 14V bus, and (2) enable a period of transition during which loads can migrate from 14V operation to 42V operation, eliminating the need for all loads to transition to 42V immediately after 42V power generation is introduced in the vehicle. While 42V facilitates the implementation of certain high-power loads in the vehicle, there are some pre-existing loads which do not stand to benefit from operating at an increased voltage. Some loads, such as filament-based incandescent lights, experience decreased lifetimes as voltage increases. Electronic control units (ECUs), used for applications such as engine control, traction control, and climate control, also prefer to operate at lower voltages. This is because ECUs depend on linear regulators to convert the 14V bus voltage to the 5V or lower used by each ECU's internal circuitry. The efficiency of such regulators decreases as the input voltage increases, so an increased bus voltage increases the power consumption of the ECU. [7] Therefore, the need exists to allow certain high power loads to realize advantages of higher-voltage operation, while simultaneously allowing other low power loads to operate at their present 14V level.

A dual-voltage system also provides automakers a transition period during which appropriate 14V loads can be reengineered for 42V operation, making the introduction of the higher voltage within the automobile logistically more manageable. If the present 14V system were completely replaced with a 42V system during the course of one model year, all loads would either be forced to migrate to 42V in concert with the generation system, or to provide individual point-of-load buck converters to convert 42V down to the operating voltage for each individual load. Such an immediate transition would prove very difficult for the many suppliers who provide electrical and electronic parts to the industry, as these suppliers would have very little time to retool components to be compatible with the higher voltage. A 42V / 14V dual-voltage system allows this transition to occur much more smoothly, as both voltages would be available in the vehicle and components could gradually be retooled to operate at the higher voltage. This eases the design burden on automakers and suppliers by providing the industry an opportunity to gain

manufacturing and field experience with 42V over time, as 42V components and systems become more numerous within the vehicle.

1.3 An Alternative to the dc / dc Converter

Heretofore, the majority of dual-voltage power supply development for automotive applications has focused around the dc / dc converter. This is perhaps because the dc / dc converter provides a modular, familiar power conversion solution that can be attached to the rectified output of a standard high voltage Lundell alternator that has been rewound and regulated to 42V. Dc / dc converters already exist at various ratings for a range of power conversion applications, so the power converter industry is quite familiar with its electrical characteristics and production costs. Dc / dc converters are also non-intrusive to the alternator and can be thus be designed independent of the alternator's electrical characteristics and physical housing. Furthermore, dc / dc converters have been designed to provide bi-directional power conversion, allowing energy to be transferred from the 14V battery to the 42V battery for emergency starting in the event that the 42V battery has become discharged.

However, the automotive dc / dc converter exhibits two significant shortcomings that warrant the study of dual-voltage alternator solutions: cost and weight. The dc / dc converter is a potentially costly addition to the vehicle because it requires relatively high cost active and passive components and large input and output filters. [8] This cost is partially attributable to stringent EMI ripple specifications which govern the converter and necessitate large filters to attenuate EMI down to acceptable limits. The converter also contains a number of high-current FETs that significantly drive the total cost of the module.² Thus, the cost and weight characteristics of an appropriately sized dc / dc converter potentially limit its viability as a dual-voltage power generation solution.

Given this weight and cost of the dc / dc converter, the motivation exists to examine the potentially cheaper alternatives presented by the dual-rectifier and dual-stator alternators. Dual-voltage alternators present an attractive alternative because they integrate dual-voltage functionality into the alternator itself, eliminating the need to supplement the generation system with a separate power converter. They generally require fewer and simpler components and thus have the potential to be significantly lighter and less costly than the dc / dc converter. However, dual-voltage alternators have been studied far less than the dc / dc converter architecture for this dual-voltage automotive power application, so much less is known about the ability of dual-voltage alternators to generate power for automotive electrical systems in a cost effective manner and with as little added weight as possible. This is because few, if any, such dual-voltage alternators have been produced and tested within an automobile. Therefore, this thesis will set out to examine these two dual-voltage alternators to determine each architecture's baseline electrical performance characteristics, and to quantify the relative costs and weights required to achieve certain minimum performance levels comparable to the dc / dc converter.

² A brief inventory of the bill of materials for one automotive dc / dc converter design is given in Section 2.3.

1.4 Thesis Objectives

The goal of this thesis is to discuss the viability of the dual-rectifier and dual-stator alternators for dual-voltage automotive power generation applications by evaluating cost and weight characteristics of dual-voltage alternators meeting minimum performance specifications. In pursuing this goal, this thesis seeks to accomplish five main objectives:

1. *Analyze and quantify unfiltered voltage ripple produced by dual-voltage alternators.*

Heretofore, much discussion has taken place in industry concerning the potential for large ripple magnitudes produced by dual-voltage alternators. However, little work has been done to quantify this ripple to either validate or eliminate these concerns. This thesis uses numerical simulation of dual-voltage alternator models to quantify voltage ripple at the rectifier output terminals for both the dual-rectifier and dual-stator alternators.

2. *Design filtering solutions to attenuate this ripple down to predetermined limits of acceptability.*

The viability of dual-voltage alternators can only be meaningfully evaluated when these alternators meet an acceptable set of minimum performance specifications. This thesis will establish this set of voltage ripple specifications for the 14V and 42V buses. Ripple filtering solutions will then be designed to attenuate voltage ripple on both buses down to these limits of acceptability.

3. *Discuss implementation issues that effect the viability of dual-voltage alternators, such as the application of switched-mode rectification (SMR) techniques, dual-stator controllability as a function of turns ratio, and the appropriateness of aluminum electrolytic capacitors for automotive applications.*

Several implementation issues, both relating to and separate from the attenuation of voltage ripple, influence the viability of dual-voltage alternators. These issues include the potential benefits of employing switched-mode rectification (SMR) techniques with dual-voltage alternators, the effect of smaller turns ratios on the controllability of the dual-stator alternator, and the appropriateness of electrolytic capacitors for automotive voltage ripple filtering applications. These issues will each be briefly surveyed in terms of the effect that each has on the employability of dual-voltage alternator schemes within the automotive electrical system.

4. *Explore how machine design and winding strategy affect the power output characteristics of the dual-rectifier and dual-stator alternators.*

The dual-rectifier alternator relies strictly upon power electronics to generate power at two different voltages from a 42V single-stator synchronous machine. By contrast, the dual-stator alternator uses two distinct sets of stator winding outputs to supply power at two different voltages. This thesis will show that the dual-rectifier alternator is advantageous only when the level of 14V loading is small relative to the level of 42V loading, since the dual-rectifier's 42V single stator machine loses up to two-thirds of its power output capacity as the automobile's 14V load set becomes predominant. This thesis will also uncover the dual-stator alternator design tradeoff that occurs as adjustments in the number of 42V stator turns are used to trade 42V power output capacity with a lightly loaded 14V bus for 14V bus controllability with a lightly loaded 42V bus.

5. *Analyze relevant cost and weight issues for dual-rectifier and dual-stator alternators meeting minimum performance voltage ripple specifications.*

The ultimate test of the viability of dual-voltage alternators is the cost and weight that each alternator adds to the automotive electrical system. The automotive industry is extremely cost and weight conscious, so successful dual-voltage power generation solutions must minimize the impact that the additional dual-voltage functionality has on weight and cost of the power generation subsystem. This thesis will therefore examine the effect that the implementation of dual-voltage functionality has on the machine cost, power electronics cost, and filtering cost of the alternator. In doing so, this thesis will evaluate the cost and weight impacts that ripple-compliant dual-voltage alternators have on the automotive electrical system.

1.5 Organization of Thesis

This thesis consists of eight chapters which develop the analysis of voltage ripple with dual-voltage alternators and discuss costs and implementation issues relevant to the viability of dual-voltage alternators. *Chapter 2* provides functional descriptions for the two dual-voltage alternator topologies under consideration and motivates the need for an analysis of voltage ripple filtering solutions. The development of the ripple specifications employed in this thesis is described in *Chapter 3*. *Chapter 4* explores the inherent, unfiltered voltage ripple that occurs with both the dual-rectifier and dual-stator alternators, and *Chapter 5* develops filtering solutions to attenuate voltage ripple down to acceptable magnitudes. Meanwhile, *Chapter 6* discusses implementation issues in addition to voltage ripple that affect the viability of dual-voltage alternators as effective dual-voltage power supply solutions, such as the relationship between power capacity and controllability with the dual-stator alternator. This work culminates in *Chapter 7*, which analyzes cost and weight issues involved with dual-voltage alternators having given levels of output power capacity and meeting minimum ripple performance specifications. Lastly, *Chapter 8* summarizes the findings of the thesis and presents suggestions for future work.

Dual-Voltage Alternator Topologies

Heretofore, the automotive industry has focused its development of dual-voltage automotive power supply systems almost exclusively around the dc / dc converter architecture. However, the high cost and extra weight that the dc / dc converter adds to the automotive electrical system makes this option less than ideal. Thus, the motivation exists to explore the viability of alternatives to the dc / dc converter for dual-voltage generation in future automotive electrical systems. Dual-voltage alternators provide such an alternative to the dc / dc converter by enabling dual-voltage generation within the alternator unit itself, without the need to augment the electrical system with an additional separate converter module.

The two dual-voltage alternator topologies to be analyzed within this research are the dual-rectifier alternator and the dual-stator alternator. The dual-rectifier alternator achieves dual-voltage generation with the addition of a thyristor-controlled half-bridge rectifier connected to the three-phase stator winding. The dual-stator alternator generates both 42V and 14V with the addition of a second three-phase stator winding connected to a separate thyristor-controlled full-bridge rectifier. Each of these topologies presents its own set of strengths and weaknesses with regard to cost, controllability, and quality of the voltages produced for the automotive electrical system.

2.1 Functional Description of Dual-Rectifier Alternator Topology

2.1.1 Component-Level Description

A component-level diagram of the dual-rectifier alternator topology is provided in Figure 2.1. This architecture was earlier proposed by Patterson as a potential solution for dual-voltage 32V / 14V automotive electrical systems. [2.1] In the present application, the topology is based around a typical three-phase Lundell alternator that is wound and regulated for 42V. Connected to the three-phase stator outputs is a normal six-diode full-bridge rectifier to produce 42V dc. However, this topology also includes a second rectifier to produce 14V dc. This second rectifier is a half-bridge rectifier consisting of three thyristors connected anode-to-anode with the top three diodes in the 42V full-bridge. By employing phase angle control of the three thyristors, the half-bridge rectifier can be regulated to produce 14V dc for the low voltage bus.

The electrical operation of this topology may be described as follows: For a given cycle of ac stator phase current, current begins flowing either to the 42V load via the appropriate diode in the top of the 42V bridge, or to the 14V load via the appropriate thyristor in the half-bridge controlled rectifier. The thyristor and diode both share a common anode connected to one of the three alternator output phases. Since the thyristor's cathode is connected to the 14V bus voltage

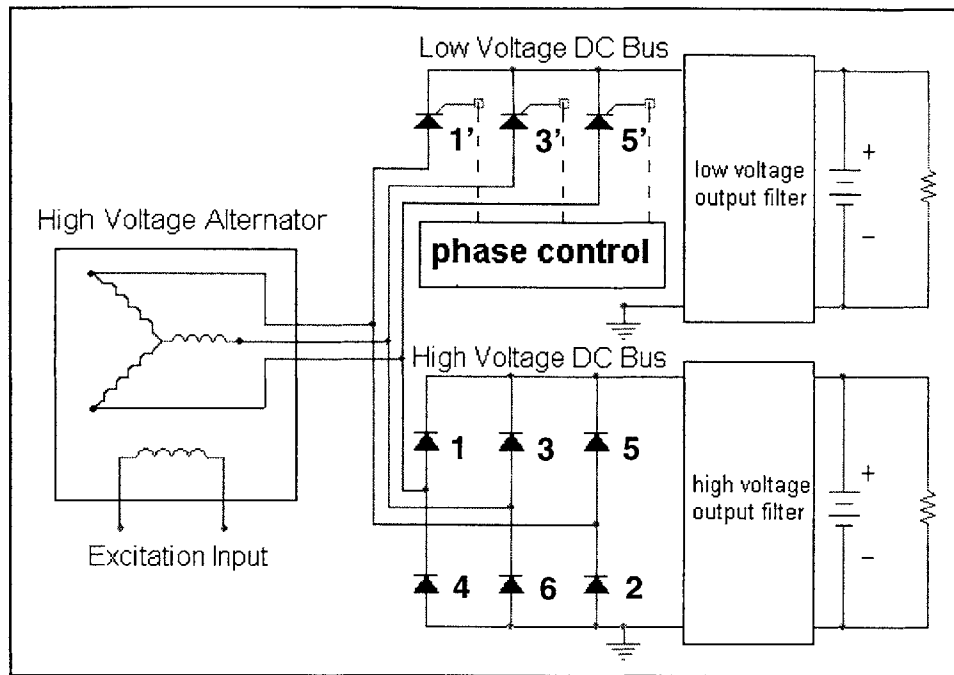


Figure 2.1: Component-level diagram of the dual-rectifier alternator topology.

while the diode's cathode is connected to the 42V bus voltage, the rising phase voltage causes the thyristor to become forward biased slightly before the diode. However, the phase current cannot pass through the thyristor until it is activated via a firing pulse sent to the gate of the thyristor. Thus, current typically begins flowing to the 42V load via the appropriate diode as soon as the phase current becomes positive and the diode is no longer reverse biased. For instance, assuming no firing pulse is sent to the thyristor before the diode becomes forward biased, the current through phase a will flow to the 42V bus via diode 1 as soon as that current increases above zero. Until a firing pulse is sent to the corresponding thyristor 1' in the half-bridge, thyristor 1' will remain off and all of the stator ac current will flow through the diode. Once a firing pulse is sent to thyristor 1', the thyristor will turn on and act similarly to a short, with a small on-state voltage. As a result, the potential observed at the anode of thyristor 1' will be pulled down to the 14V bus voltage. Since the anode of thyristor 1' and diode 1 share the same node, the potential at the anode of diode 1 will also be pulled down to the 14V bus voltage. This shuts off the diode by back-biasing it, since the diode's anode is held at the 14V bus voltage and the diode's cathode is held at the 42V bus voltage. Thus, the stator ac current that was previously flowing through diode 1 is very quickly switched over to thyristor 1', such that the current through thyristor 1' increases very quickly from zero to full stator ac current. This process occurs three times per electrical cycle, once for each of the three phases.

2.1.2 14V Bus and 42V Bus Control Strategies

By controlling the amount of time that current is allowed to flow through each thyristor relative to the total time that the given phase's ac stator current is positive, it is possible to regulate the average voltage of the thyristor-rectified 14V bus. This relative time period of conduction is regulated by the phase angle α , which is defined as the delay angle between the point each thyristor is initially forward biased and the point the thyristor is activated. As the phase angle α is decreased, the amount of time during which current flows through each thyristor increases. This serves to provide more current to the resistively loaded 14V bus, which in turn increases the average voltage of the 14V bus. As α increases, the amount of time during which current flows through each thyristor to the 14V load decreases, which in turn decreases the average voltage of the 14V bus. Using thyristor phase angle control, the alternator has a mechanism through which to regulate the low voltage bus based on the amount of current that is supplied to that bus.

While phase angle control is used to regulate the voltage of the 14V bus, traditional field current control is used to regulate the 42V bus. Under this control strategy, the amount of current that flows through the rotor field of the alternator is strictly regulated, since this current is responsible for producing magnetic flux that links each of the stator's three windings individually as the rotor spins through a complete revolution. The magnetic rotor flux ϕ bears a proportional relationship to field current prior to saturation as follows: [2.2]

$$\phi = KI_f \quad (2.1)$$

Thus, increasing the level of field excitation current through the rotor serves to increase the magnetic flux generated by the rotor winding. As this increased amount of flux links the three stator windings individually during rotation, the stator windings each undergo a larger *change* in flux, which directly translates into a larger internal voltage (or back EMF) being generated within each of the stator's three-phase windings. The magnitude of this internal voltage also directly varies with the number of turns N_s in each stator winding linked by the rotor flux. Therefore the internal voltage E generated within each phase bears a proportional relationship with the magnetic flux generated by the rotor field winding, the number of turns in each stator winding, and the speed ω with which the rotor spins, as follows:

$$E = N_s \phi \omega \quad (2.2)$$

Given the proportionality between field current and rotor flux in the machine's unsaturated region, each stator winding's internal voltage is related to field current I_f by

$$E = KN_s \omega I_f \quad (2.3)$$

Therefore, field excitation current controls the phase voltage generated within the stator phase windings, which in turn controls the dc value of the 42V rectifier voltage.

It should be noted that the phase angle control of the 14V bus acts subordinately to the field current control of the 42V bus. Consider, for example, the case when the 14V bus is heavily loaded, and the thyristor phase angle is reduced to $\alpha = 0^\circ$. In this case, each thyristor turns on as soon as the ac stator current for the corresponding phase becomes positive, causing each thyristor to act like a diode. This causes the thyristors to back-bias the diodes as soon as the phase current becomes positive, thereby prohibiting any current from flowing through the diodes to the 42V bus. At $\alpha = 0^\circ$ the control handle for the 14V bus is at its upper limit, and the current supplied to the 14V bus becomes purely a function of the field excitation current, which is itself purely a function of the regulation of the 42V bus. Since the 42V bus is receiving none of the ac stator current at $\alpha = 0^\circ$, the 42V bus voltage will rely completely upon the battery to supply current to the bus, and the bus voltage will thus begin to sag below 42V. The 42V field current regulator will then attempt to increase the field current in order to increase this sagging 42V bus voltage. If and when the field current increases to a level where the current feeding the 14V bus satisfies the 14V bus regulator, the phase angle α can begin to increase again. In general, however, the 14V firing angle controller adjusts α according to the fraction of time per electrical cycle that the thyristors must conduct the alternator-generated ac stator current (whose magnitude is a function of the 42V field current controller) in order to maintain the 14V bus voltage. In this way, the 14V firing angle controller acts subordinately to the 42V field excitation current controller in regulating the 14V bus voltage.

2.2 Functional Description of Dual-Stator Alternator Topology

2.2.1 Component-Level Description

A component-level diagram for the dual-stator alternator topology is given in Figure 2.2. The most significant difference between this configuration and the dual-rectifier or single 42V configuration is that the dual-stator alternator has two distinct electrical outputs provided by two distinct sets of three-phase stator windings inside the machine. Whereas the power electronics of both buses share the same set of stator windings in the dual-rectifier machine, the dual-stator machine allows each bus to have its own dedicated set of stator windings and its own dedicated full-bridge rectifier. In this particular configuration, one set of stator windings is connected to a six-diode uncontrolled full-bridge rectifier to provide 42V dc, while the other set of stator windings is connected to a six-thyristor controlled full-bridge rectifier to provide 14V dc. Regulation of the 42V bus is provided by standard field excitation current control, while regulation of the 14V bus is provided by phase angle control of the thyristor bridge. The fundamental operation of this thyristor bridge configuration is described in Kassakian, et. al., and an analysis of thyristor rectifier operation for constant voltage (battery) loads is provided in Caliskan. [2.3, 2.4]

During operation, the rotor field is injected with excitation current, which in turn induces ac currents in both sets of three-phase stator windings as the rotor spins. Differences in the magnitudes and phase shifts of the internal voltages induced within two sets of stator windings

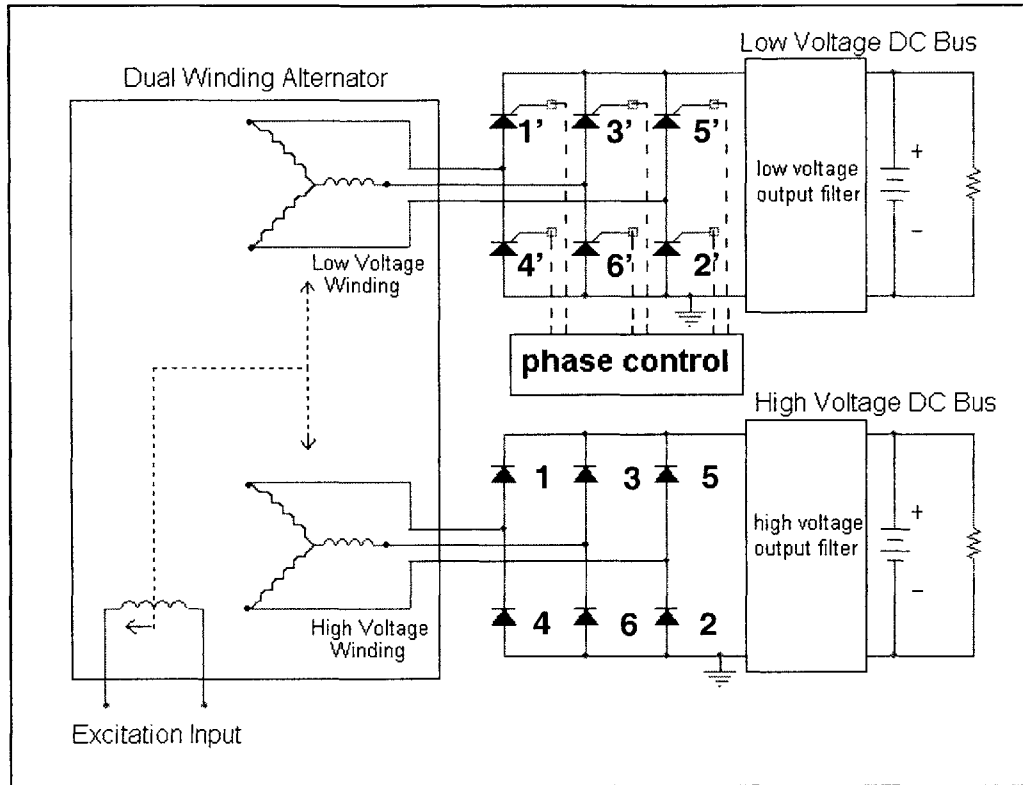


Figure 2.2: Component-level diagram of the dual-stator alternator topology.

depend upon the winding ratio and relative angular displacement with which the stators are wound inside the machine. However, unlike the dual-rectifier topology, current is not switched or shared between the two buses since each bus has a dedicated set of stator windings and a dedicated rectifier. As will be examined later, this gives the dual stator a significant advantage over the dual-rectifier in terms of voltage ripple magnitudes observed at the outputs of the 14V and 42V rectifiers.

2.2.2 14V Bus and 42V Bus Control Strategies

As stated earlier, regulation of the 42V bus is achieved by controlling the field current through the alternator rotor, while regulation of the 14V bus is achieved by controlling the phase angle of the thyristor firing pulses sent to the 14V bridge rectifier. Field current regulation operates as described in Section 2.1.2 for the dual-rectifier topology, with the internal voltages induced within each phase of the two sets of three-phase stator windings bearing a proportional relationship to the level of field current in the rotor. In the case of the dual-stator topology, the field current controls the internal voltages in the stator windings for both buses. Thus, as the 42V voltage regulator increases the field current in response to a sagging voltage on the 42V bus, *both buses* see increased internal voltages within their stator windings. However, the ratio of the magnitudes of these internal voltages is dictated by the turns ratio between the stator windings of

the two buses. In response to this increased field current, the 14V regulator may increase the phase angle for the thyristor bridge in order to mitigate the increased 14V internal voltage and maintain the 14V bus voltage at its previous level. If the 14V rectifier did not have this capability, then the voltages of both buses would rise and fall according to the command of the 42V regulator alone. Thus, once again the phase angle control of the 14V bus acts subordinately to the field current control of the 42V bus, since the 14V regulator sets the thyristor phase angle based upon the 14V internal voltage dictated by the 42V regulator at any given time.

2.2.3 Dual-Stator Architecture Design Variations

It should be noted that the implementation described above is not necessarily the only way to configure the power electronics and control design of the dual-stator architecture. For example, the 14V controlled rectifier can also be implemented with diodes instead of thyristors in the lower half of the bridge while maintaining the same level of controllability. Another possible modification involves moving the controlled rectifier to the 42V stator outputs and the diode rectifier to the 14V stator outputs. In this case, field current control is used to regulate the 14V bus voltage and phase angle control is used to regulate the 42V bus voltage. This configuration gives primary control responsibility of the two stator's internal voltages to the 14V bus, since the 14V field current regulator adjusts the level of field excitation current based on the voltage level of the 14V bus. Implementing this configuration involves winding the dual-stator alternator rotor similarly to the 14V alternator's rotor, since the 14V bus voltage is connected across the rotor winding in order to supply field current. It also involves winding the two stators with a turns ratio greater than the 3:1 stator – stator turns ratio typically assumed (see Chapter 4). This is important in the case of a lightly loaded 14V bus and a heavily loaded 42V bus. If the 14V bus of this dual-stator alternator design is lightly loaded, field current is regulated to a relatively low level due to the low demand for 14V bus current. However, this low level of 14V field excitation current also produces a low level of 42V internal voltage, prohibiting the 42V bus from receiving enough current to supply a significant load. This situation is resolved by increasing the stator – stator turns ratio above 3:1, such that enough 42V internal voltage is produced to source the desired amount of current to the 42V bus with even a low level of field excitation current.

This dual-stator alternator configuration proves worthwhile only within automotive electrical systems that have the majority of the total automotive load connected to the 14V bus, since the 14V field current regulator maintains primary control authority over the alternator. Fluctuations in 14V bus voltage affect both the 14V and 42V buses in this configuration. Thus, it is advantageous for the majority of the load to exist on the 14V bus such the architecture's primary control handle can directly regulate the bus voltage connected to the majority of the system's loads. This configuration is also advantageous when the 14V load predominates because diodes are used to supply the higher 14V current demand. Assuming that thyristor costs dominate diode costs, it is advantageous to use diodes instead of thyristors for higher current applications due to the relationship between device rating and device cost.

However, given these variations, this thesis chooses to consider the dual-stator implementation illustrated in Figure 2.2 which uses field current regulation to maintain the 42V bus voltage and phase angle regulation to maintain the 14V bus voltage. This is in part because 42V bus loads will definitely dominate the total alternator power demand in future vehicles, making this implementation advantageous for reasons converse to those described above. The Figure 2.2 configuration is also analyzed here to maintain consistency with historical conceptions and previous analyses of the dual-stator alternator.

2.3 Advantages of Dual-Voltage Alternators

One goal of this thesis is to delineate the advantages of the dual-rectifier and dual-stator alternator topologies relative to the dc / dc converter and to each other. As a class of dual-voltage power supply architectures, dual-voltage alternators present two potential advantages over the dc / dc converter.

- The number, size, and weight of the additional components required to implement a dual-voltage alternator are all less than for a dc / dc converter, so extra weight and cost added to the vehicle are reduced.
- They may integrate the complete dual-voltage generation system into the alternator housing, eliminating the need to install a separate power conversion module.

Dual-voltage alternators have the potential to provide a smaller, lighter, and cheaper dual-voltage power supply solution than is possible with dc / dc converters currently under evaluation. This is because dc / dc converters by definition mandate the addition of a separate power conversion module to the vehicle. Yet, the ability of dual-voltage alternators to provide size and cost advantages rests on the designer's ability to formulate *reasonably sized* filtering solutions that attenuate thyristor-generated voltage ripple down to acceptable limits. For example, changes in machine geometry and the addition of a second rectifier do not impede the ability of each architecture to be integrated into the alternator housing as a single unit. However, such integration will occur only if filtering stages can be designed which lend themselves to integration within a single alternator unit and minimize the size and weight added to the architecture. If such filtering stages can be designed, the ability to package the complete dual-voltage alternator solution within a single housing gives dual-voltage alternators a significant advantage over the 42V alternator with dc / dc converter topology. This saves both time and space during the assembly of the vehicle, both of which translate into reduced assembly costs.

Dual-voltage alternators also exhibit a potential cost savings over the dc / dc converter topology because a fewer number of active components are needed to implement the dual-voltage functionality. For example, a four-cell dc / dc buck converter was designed at the MIT Laboratory for Electromagnetic and Electronic Systems for the purposes of this automotive application. The bill of materials for this converter included the following (see [1.8]):

- 4 power MOSFETs (one per cell)
- 4 power diodes (one per cell)
- 4 converter inductors (one per cell)
- 4 input capacitors (one per cell)
- 4 output capacitors (one per cell)
- LC input filter stage
- LC output filter stage
- heatsinking for FETs and diodes
- control circuitry

This contrasts with the following *additional* components (relative to a conventional alternator) for the dual-rectifier topology

- 3 thyristors
- 2 LC output filtering stages (one per rectifier)
- thyristor phase angle control circuitry

and the following additional components for the dual-stator topology

- windings for second stator
- 6 thyristors
- 2 LC output filtering stages (one per rectifier)
- thyristor phase angle control circuitry

As illustrated above, both the dual-rectifier and dual-stator alternators can be manufactured with significantly fewer components than the dc / dc converter. Again, though, the dual-rectifier and dual-stator alternators will prove advantageous only if the cost savings realized in active switching components are not completely counteracted by the extra cost burden of ripple filtering components. If filtering stages can be designed which only minimally increase the total size and weight of the architecture, then a cost savings over the dc / dc converter can also be realized because of the less stringent packaging requirements of dual-voltage alternators. This is because the dc / dc converter module mandates its own packaging to withstand the harsh vibration and temperature characteristics of the under-hood environment, while each dual-voltage alternator architecture is potentially integrable within the machine housing itself. Hence, dual-voltage alternators show promise for minimizing the extra cost and weight burden that dual-voltage power generation adds to the vehicle by requiring fewer additional components and by providing a possible means to eliminate the packaging and mounting of an extra power module.

2.4 Challenges for Dual-Voltage Alternators

While dual-voltage alternators provide an advantage over the dc / dc converter topology in terms of size, weight, and cost, they also face two main performance challenges: (1) independent controllability of both voltage buses under a variety of dynamic loading conditions, and (2) low frequency voltage ripple created by thyristor switching within the controlled rectifiers.

2.4.1 Independent Controllability of 14V and 42V Buses

Discussions within the MIT Consortium have revealed that various automotive engineers are skeptical about the ability of dual-voltage alternators, specifically dual-stator alternators, to independently and dependably regulate both the 14V and 42V buses under the range of loading scenarios that would be present within a complete dual-voltage automotive electrical system. Consider a loading condition in which the dual-stator alternator is generating power for a very lightly loaded 42V bus and a very heavily loaded 14V bus. Since the current demanded by the 42V bus is relatively low, the alternator voltage regulator will reduce the rotor field current until the internal voltage of the 42V stator windings is capable of driving just enough current to maintain the desired bus voltage level. At the same time, this reduces the internal voltage of the 14V stator windings. The 14V bus's controlled rectifier attempts to compensate for the reduced internal voltage by reducing the phase angle α . However, the phase angle regulator may not be able to completely compensate for this reduced internal voltage, even at a phase angle of $\alpha = 0^\circ$. The net effect is that the 14V phase angle regulator saturates at its maximum control value ($\alpha = 0^\circ$) and is unable to provide the demanded current to the 14V bus.

This problem is mitigated by appropriately choosing the turns ratio between the two sets of stator windings. Heretofore, the implicit assumption has existed that the turns ratio of the stator windings should be 3:1, given that the ratio of bus voltages is 3:1. This assumption perpetuates the control problem by limiting the 14V winding internal voltage to 1/3 of the 42V winding internal voltage. Thus, when the stator's 42V internal voltage is at a minimum level relative to the 42V bus voltage, the 14V internal voltage will *also* be at a minimum level relative to the 14V bus voltage. This greatly reduces available control authority in the case described above, when the 42V bus is very lightly loaded relative to the 14V bus. If a smaller turns ratio (like 2.5:1) is selected, the above scenario becomes a less difficult problem. This is because the 14V internal voltage would be greater with a turns ratio of 2.5:1 than with a turns ratio of 3:1, for a given 42V internal voltage value. This greater internal voltage would restore some control authority to the 14V bus when the 42V bus is lightly loaded, thus reducing the control problem.

2.4.2 Voltage Ripple Created by Thyristor Switching

A second problem inherent to dual-voltage alternators involves voltage ripple created by thyristor switching within each topology's 14V controlled rectifier. This is particularly a problem with the dual-rectifier alternator, where the anode of each of the three extra thyristors is connected to the anode of the corresponding diode in upper half of the full diode bridge (see

Figure 2.1). When a firing pulse is given and a thyristor is activated during a given cycle of ac stator phase current, the thyristor acts similarly to a short and the shared anode node is pulled down to the 14V bus voltage seen at the cathode of the thyristor. Since a voltage much higher than 14V is seen at the cathode of the corresponding high-voltage diode, the diode becomes back-biased and therefore deactivates. This causes the 42V current that was flowing through the diode before the thyristor was activated to be transferred to the 14V bus via the thyristor, as illustrated in Figure 2.3. This abrupt transfer of current from the 42V bus to the 14V bus produces both high-frequency reverse recovery voltage transients and a significant fundamental voltage ripple harmonic as current is switched between the two buses.

By contrast, the ripple problem tends to be inherently less severe with the dual-stator alternator. Here, two separate rectifiers are connected to two separate sets of stator windings. Thus, there is no opportunity for current to be stolen from one rectifier to another as with the dual-rectifier alternator. However, the use of a thyristor bridge rectifier for the 14V bus does create the potential for some low-frequency voltage ripple as each of these thyristors cut on and off once per electrical cycle. Chapter 4 will analyze this unfiltered voltage ripple at the rectifier outputs for both the dual-rectifier and dual-stator alternators.

2.5 Analysis of Voltage Ripple within this Research

As previously discussed, the automotive industry considers voltage ripple to be one of the primary challenges that dual-voltage alternators must overcome in order to be viable power generation options for dual-voltage automotive electrical systems. In order to examine and design solutions for this issue, a specification must first be identified which provides limits of acceptability for ripple within the electrical system. Such a specification should ideally strike a balance between the immunity of system loads to ripple transients, and the amount of filtering required within the system to meet these immunity levels. Once a specification is in place, analyses will be performed to determine the magnitudes of unfiltered ripple that would exist in systems powered by dual-rectifier or dual-stator alternators. These analyses of unfiltered ripple will be examined in light of the agreed-upon ripple specifications to determine the degree to which voltage ripple falls outside the margins of acceptability. Filtering solutions will then be designed to attenuate the observed ripple down to the specified magnitudes. The goal of these filtering designs will be to provide a proof-of-concept as to whether filtering solutions can be designed to provide acceptable ripple characteristics for dual-voltage alternator systems. Once these solutions are designed, initial size, weight, and cost estimates will be developed such that the efficacy of the two dual-voltage alternators can be compared relative to each other and to the dc / dc converter.

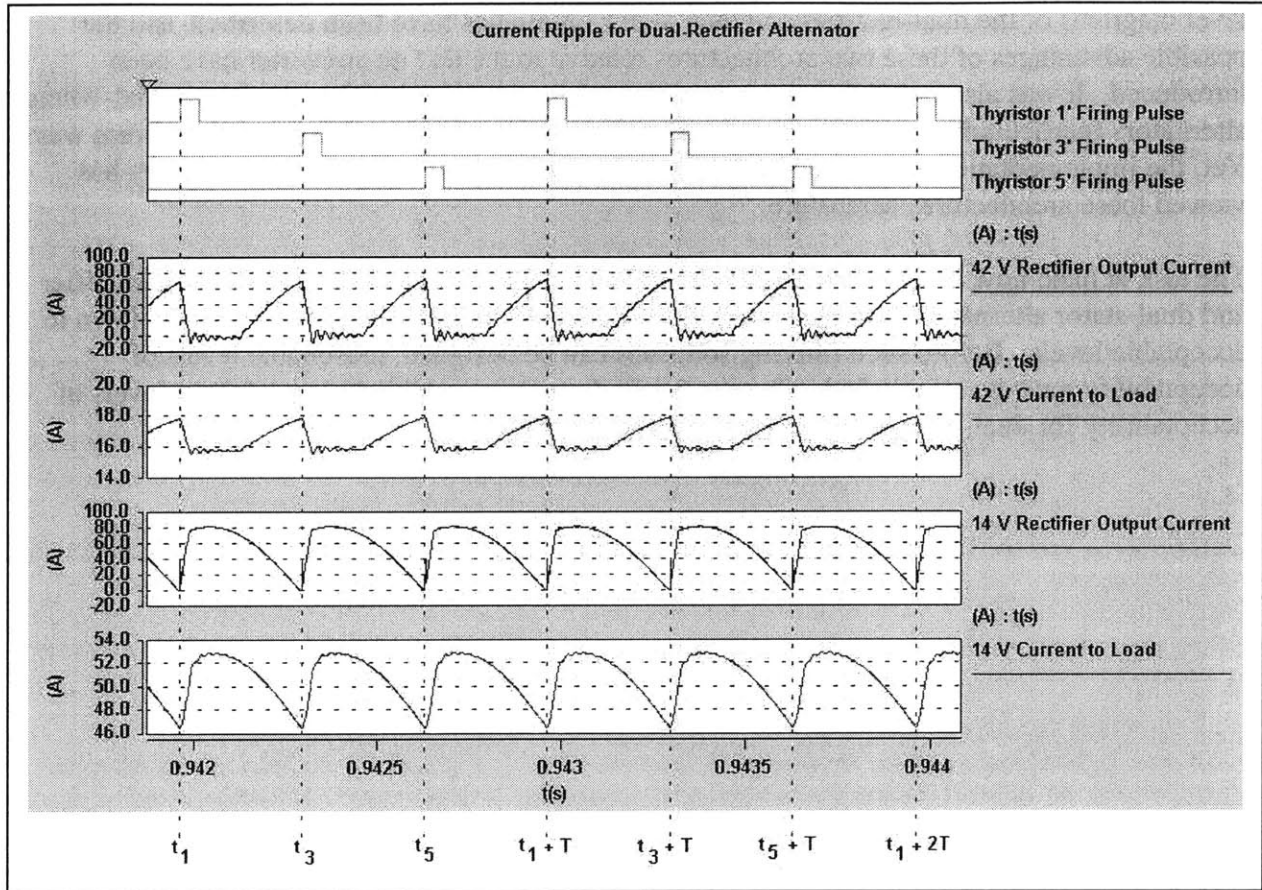


Figure 2.3: Illustration of ripple present in each bus's rectifier output current and in the current delivered to each bus's load for the unfiltered dual-rectifier alternator pictured in Figure 2.1. (Note: The current delivered to each load set is equal to the current supplied by the rectifier minus the current sunk by the battery.) Just prior to time t_1 , current is passing through diode 1 to the 42V bus, as is seen from the increasing 42V bus current. At time t_1 , thyristor 1' is activated by its firing pulse, and current is commutated from diode 1 on the 42V bus to thyristor 1' on the 14V bus. This is noted by observing the sharp fall in 42V bus current and the corresponding sharp rise in 14V bus current. The same repeats at t_3 when current commutates from diode 3 to thyristor 3', and at t_5 when current commutates from

2.6 Summary

The purpose of this chapter was to discuss the functionality, strengths, and challenges of the dual-voltage alternator topologies under consideration by the automotive industry. Component-level diagrams of the dual-rectifier and dual-stator topologies have been described, and the possible advantages of these two architectures relative to the dc / dc converter have been introduced. It was also noted that the power electronics contained within these two dual-voltage alternators (particularly the dual-stator alternator) can be implemented in several different ways. Yet, the implementations presented here reflect the primary ways in which the industry has viewed these architectures heretofore.

The task at hand now involves analyzing the voltage ripple characteristics of the dual-rectifier and dual-stator alternators, and evaluating filtering solutions that attenuate this ripple down to acceptable levels. Before such filtering solutions can be designed, reasonable levels of acceptability must be established. Chapter 3 will discuss the establishment of these levels of acceptability for dual-voltage automotive electrical systems.

The Search for a Ripple Specification

This thesis has identified the issue of voltage ripple resulting from thyristor phase angle regulation as a primary factor affecting the efficacy of the dual-rectifier and dual-stator alternators for automotive dual-voltage power generation. One goal of this work is to quantify the severity of this voltage ripple and to size passive filtering solutions that will attenuate the ripple to an acceptable level. The first step in this process is to identify the maximum voltage ripple magnitudes that the designer is willing to tolerate within the automotive electrical system.

The search for these maximum levels of acceptability for peak-to-peak voltage ripple occurred on three different levels for the purposes of this research. First, the prevailing Society of Automotive Engineers (SAE) literature was examined to find a specification for voltage ripple within the frequency range of the electrical frequency of the machine. Laboratory measurements were also performed to observe the voltage ripple magnitudes present at different measurement points within a typical automobile. Various automotive OEMs and component suppliers were then polled to determine the ripple magnitude limits used by industry to evaluate alternators currently in production.

3.1 Voltage Ripple in Prevailing Literature

In seeking to establish a benchmark against which to evaluate the voltage ripple inherent with the dual-rectifier and dual-stator alternators, input was first sought from the prevailing industry literature. The SAE J1113 standard defines a methodology for testing the electromagnetic emissions and immunity characteristics of automotive electrical components, based on the frequency range of the disturbance. [13] Given a three-phase alternator design with 12 poles (6 pole pairs), the electrical frequency of the machine is determined as follows:

$$\begin{aligned} \text{Alternator Electrical Frequency} &= \frac{\text{shaft rotations}}{\text{minute}} * \frac{1 \text{ minute}}{60 \text{ seconds}} * \frac{6 \text{ pole pairs}}{\text{shaft rotation}} \\ &= \frac{1}{10} * \text{alternator RPM} \end{aligned} \quad (3.1)$$

For the dual-rectifier alternator, the dominant ripple event occurs each time a 14V thyristor is fired. Since each thyristor is fired once per cycle of ac stator phase current, three firings occur per electrical cycle. Thus, the fundamental ripple frequency for the dual-rectifier alternator is equal to three times the electrical frequency of the machine.

$$\begin{aligned} \text{Dual - Rectifier Ripple Frequency} &= 3 * \text{Alternator Electrical Frequency} \\ &= \frac{3}{10} * \text{alternator RPM} \end{aligned} \quad (3.2)$$

By contrast, the dual-stator alternator has two distinct three-phase outputs connected to two distinct six-pulse, full-bridge rectifiers. Commutation occurs six times per electrical cycle, producing a fundamental ripple frequency six times the electrical frequency of the machine.

$$\begin{aligned} \text{Dual - Stator Ripple Frequency} &= 6 * \text{Alternator Electrical Frequency} \\ &= \frac{6}{10} * \text{alternator RPM} \end{aligned} \quad (3.3)$$

Given an alternator shaft speed range of 2000 rpm (idle) to 10000 rpm (high speed), the voltage ripple frequencies for these alternators lie between 600 Hz and 6 kHz. While the majority of subsections of SAE J1113 deal with frequency bands between 10 kHz and 1000 MHz, SAE J1113-2 directly addresses conducted immunity guidelines between 30 Hz and 250 kHz. More specifically, J1113-2 defines a testing procedure to evaluate the immunity of automotive electrical loads to conducted electrical transients between 30 Hz and 250 kHz. [14]

This evaluation procedure addresses ripple based on three load-criticality levels and three regions of load operation. J1113-2 classifies automotive loads affected by ripple into one of three categories:

- Class A – loads that are solely for convenience purposes (radio, interior reading lamp)
- Class B – loads that enhances the driver's ability to operate the vehicle (speedometer)
- Class C – loads that are essential to vehicle operation (braking system)

It also defines three regions of operation:

- Region I – load operates as designed
- Region II – load operation deviates from design, but returns to normal when the disturbance is removed
- Region III – load operation deviates from design, and operator action returns function to normal when the disturbance is removed.

Figure 3.1 illustrates the ripple magnitudes within which different regions of performance are expected from different classes of loads. According to J1113-2, non-critical Class A loads

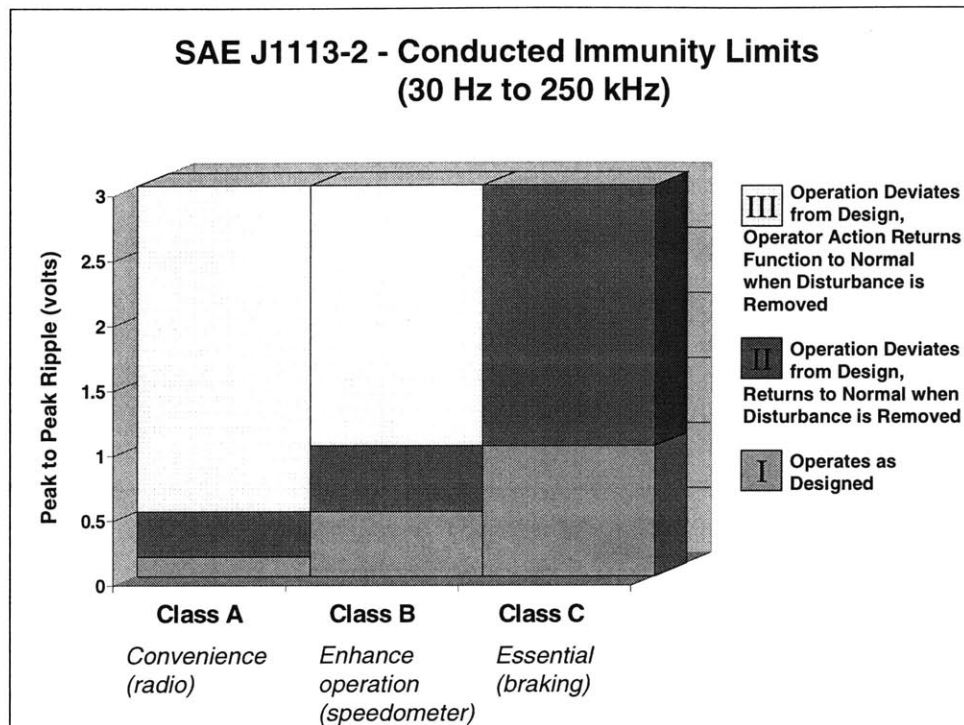


Figure 3.1: Graphical illustration of J1113-2 showing the peak-to-peak voltage magnitudes that mandate certain regions of operation for different classes of loads.

should be able to tolerate up to 0.15 Vpp ripple to maintain designed performance, and up to 0.5 Vpp to maintain operation that returns to normal when the ripple is removed. Anything above 0.5 Vpp and up to 3 Vpp may cause operation to deviate from normal, but operation should be able to return to normal when operator action is taken after the disturbance is removed. Class B loads operate in Region I at up to 0.5 Vpp ripple, Region II at up to 1.0 Vpp ripple, and Region III between 1.0 Vpp and 3.0 Vpp. Likewise, Class C loads operate in Region I at up to 1.0 Vpp ripple and Region II between 1.0 Vpp and 3.0 Vpp ripple. It should be noted that as the criticality of the load increases, the amount of ripple the load can tolerate and still maintain normal operation also increases. Thus, critical loads such as braking systems should be designed to tolerate larger ripple magnitudes than should convenience loads such as car stereos.

3.2 Relevance of Voltage Ripple Measuring Point

J1113-2 specifies the degree to which loads should be able to tolerate ripple *at the load terminals*. However, in order to understand the ripple magnitudes that appear at various loads, the system designer must consider the ripple characteristics of the entire automotive electrical system. Figure 3.2 illustrates this system consisting of the power supply, battery, load, and line inductances that attenuate ripple between the source, battery, and load. Voltage ripple

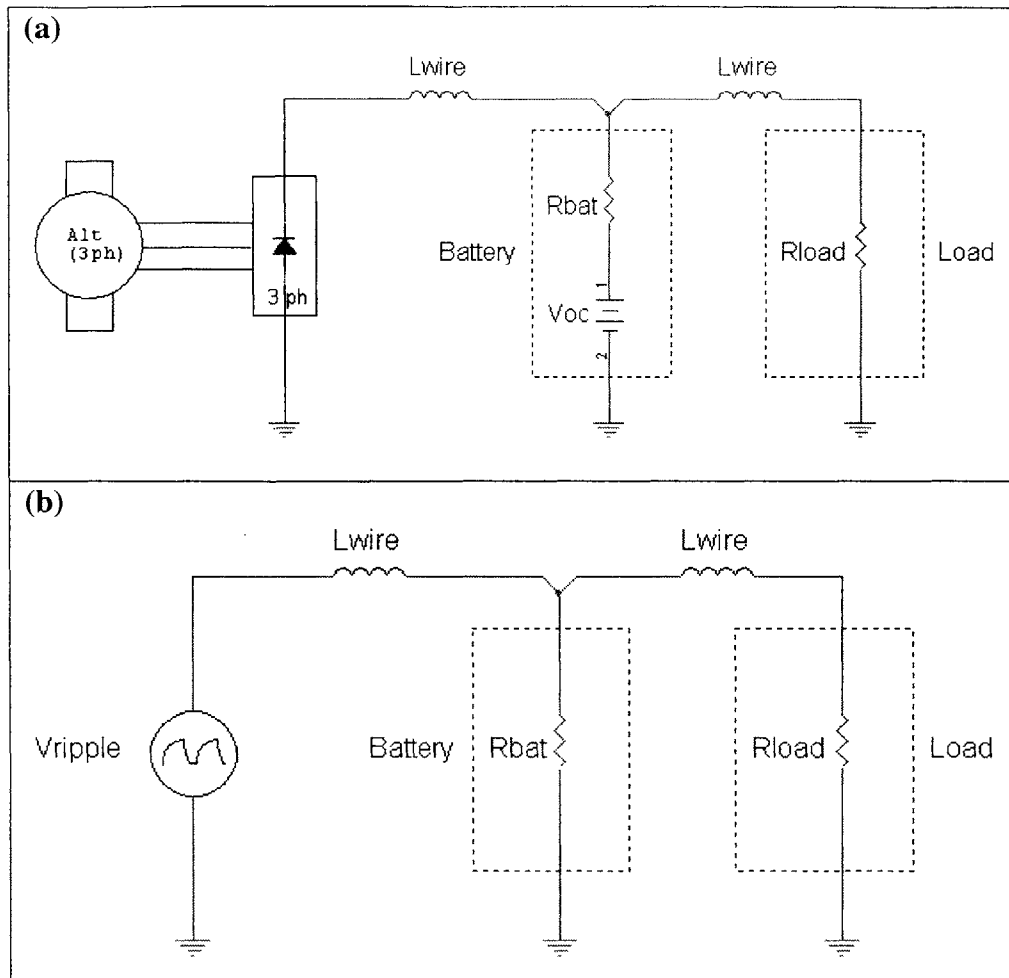


Figure 3.2: Ripple analysis models for a typical automotive electrical system: (a) simple automotive system model including the alternator, battery, and load; (b) ac signal model detailing how ripple is generated and attenuated throughout the system.

disturbances are initially created by the power supply, whether it be an alternator or dc/dc converter. However, this ripple is attenuated by the line inductance of the cable between the power supply and battery, such that the peak-to-peak ripple observed at the battery terminals is significantly smaller than ripple at the power supply terminals. The battery, because of its low internal impedance, also serves to sink a great deal of the ripple current injected into the system by the power supply. Ripple is further attenuated by the line inductances that connect the battery to the various loads in the system. Since the length of cabling that connects the different loads to the battery varies greatly, different loads will observe different degrees of ripple attenuation depending on their placement within the system. Thus, the ripple seen at the terminals of a given load is affected by the ripple produced at the power source, the battery in the system, and the length of wire that connects the given load to the battery.

3.3 Empirical Ripple Measurements

The magnitude of ripple observed at different nodes in the automotive electrical system greatly depends upon the measurement point and upon the length of wire that connects the measurement point to the battery and to the alternator. In addition, Consortium members have suggested that voltage ripple may also depend upon the alternator shaft speed. Thus, before an attempt was made to set a limitation for acceptable ripple that would apply to the entire 14V automotive electrical system, ripple magnitude measurements were taken on a present-day vehicle at various electrical nodes and alternator shaft speeds. The goal of these measurements was to characterize, or at least observe, how ripple is attenuated in an actual present-day automotive electrical system between the alternator and load.

Figures 3.3 and 3.4 illustrate measurements taken on a 1990 Subaru Legacy Wagon with a Hitachi LR170-732C 14V alternator. The measurements illustrate voltage ripple observed at the alternator and headlamp at alternator shaft speeds of 1500 rpm, 4500 rpm, 9000 rpm, and 12000 rpm for a heavily loaded 14V bus. Figure 3.5 summarizes the measurements in terms of maximum peak-to-peak transients and cyclic ripple amplitude as functions of alternator shaft speed. The peak-to-peak transients primarily represent high frequency reverse recovery transients that occur during the diode switching events within the rectifier. By contrast, the cyclic ripple represents the humped waveforms that occur as a natural result of current commutation from diode to diode during the rectification process.

Several relevant observations may be noted from these waveforms. First, voltage ripple appears to bear a positive dependence upon alternator shaft speed for the measurements taken. Voltage ripple magnitudes also appear to increase more steeply as a function of alternator shaft speed at the alternator than at the load. Furthermore, the maximum reverse recovery transients and steady state ripple both have greater magnitudes at the alternator than at the load, across the relevant range of alternator shaft speeds. This behavior is expected, given the large amounts of ripple current sunk by the battery and the large degree of attenuation that occurs across the line inductances between the alternator and load. Greater attenuation at higher shaft speeds is also expected, since the inductive line impedance increases with ripple frequency. However, the most significant observation is that voltage ripple magnitudes at the headlamp greatly exceed the J1113-2 150 mV specification for Region I performance for Class A loads across the entire range of alternator shaft speeds observed. The headlamp ripple measurements also exceed the less stringent 500 mV specification for the more important Class B loads. These observations suggest that the electrical components in automobiles on the road today may routinely be called upon to operate with ripple voltages far in excess of J1113-2, calling into question the degree to which J1113-2 is actually considered during the design of present-day automotive electrical systems.

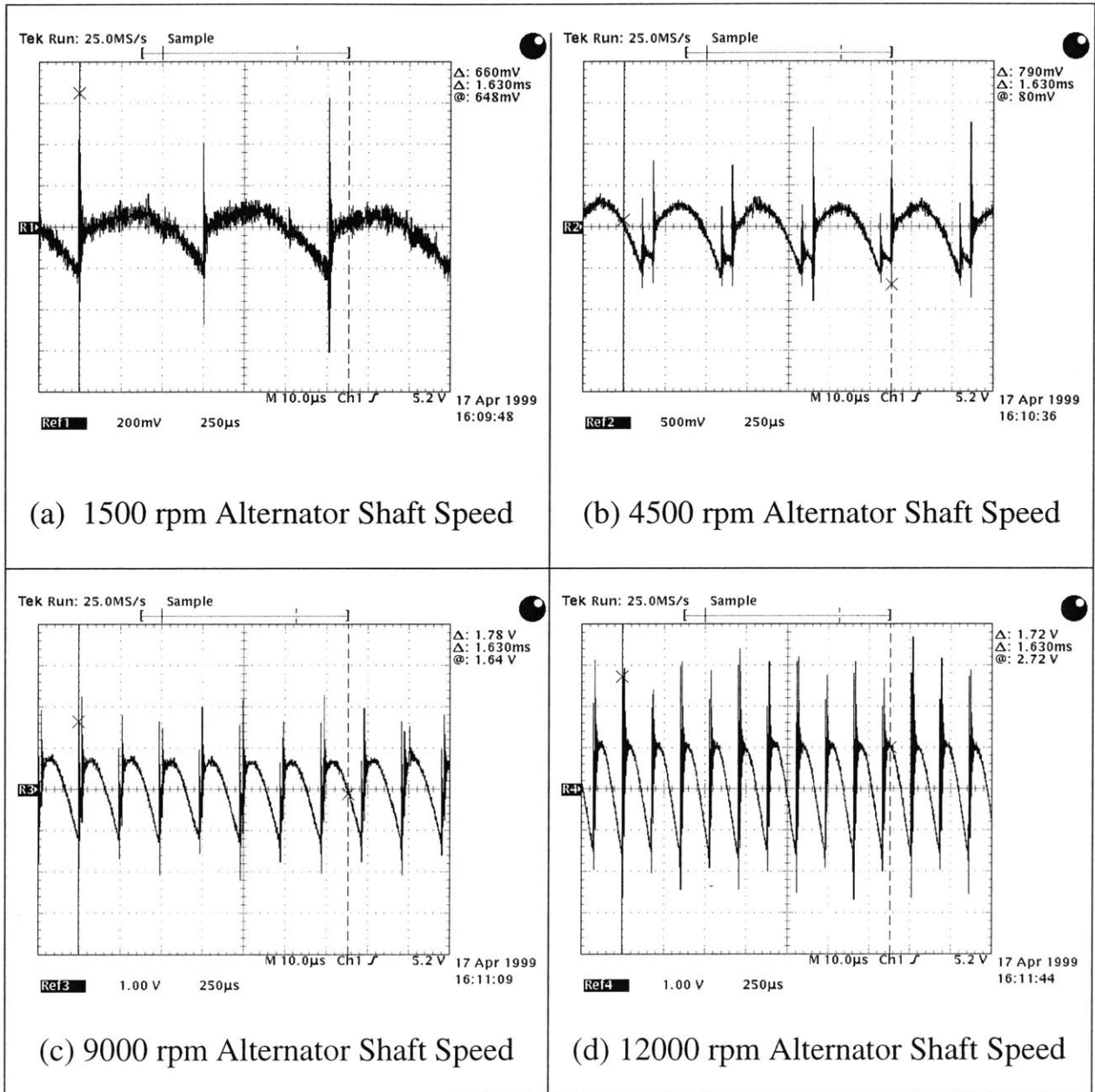


Figure 3.3: Ripple measurements taken at **alternator output terminals** for a 1990 Subaru Legacy Wagon with a Hitachi LR170-732C 14V alternator.

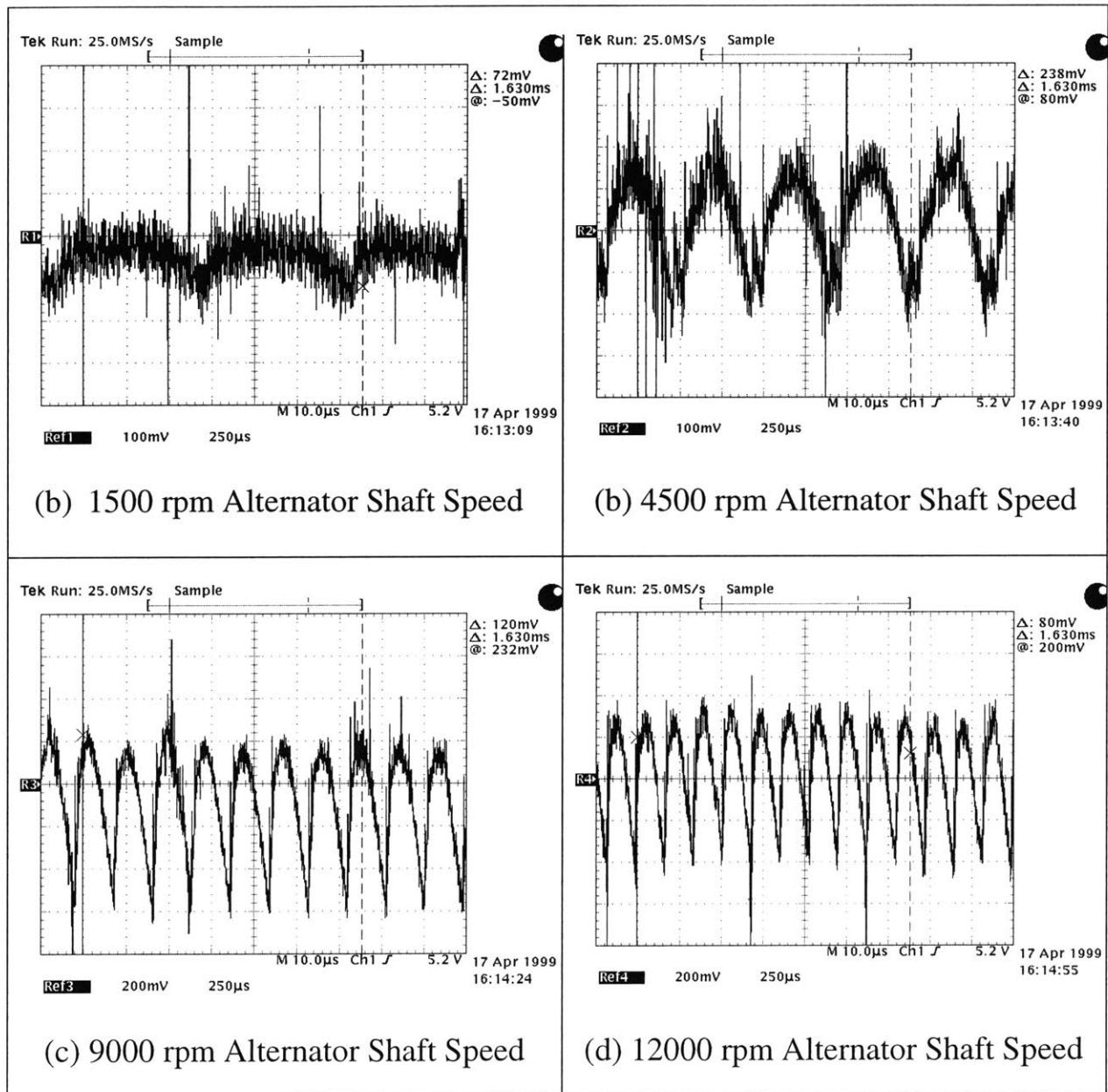


Figure 3.4: Ripple measurements taken at **headlamp terminals** for a 1990 Subaru Legacy Wagon.

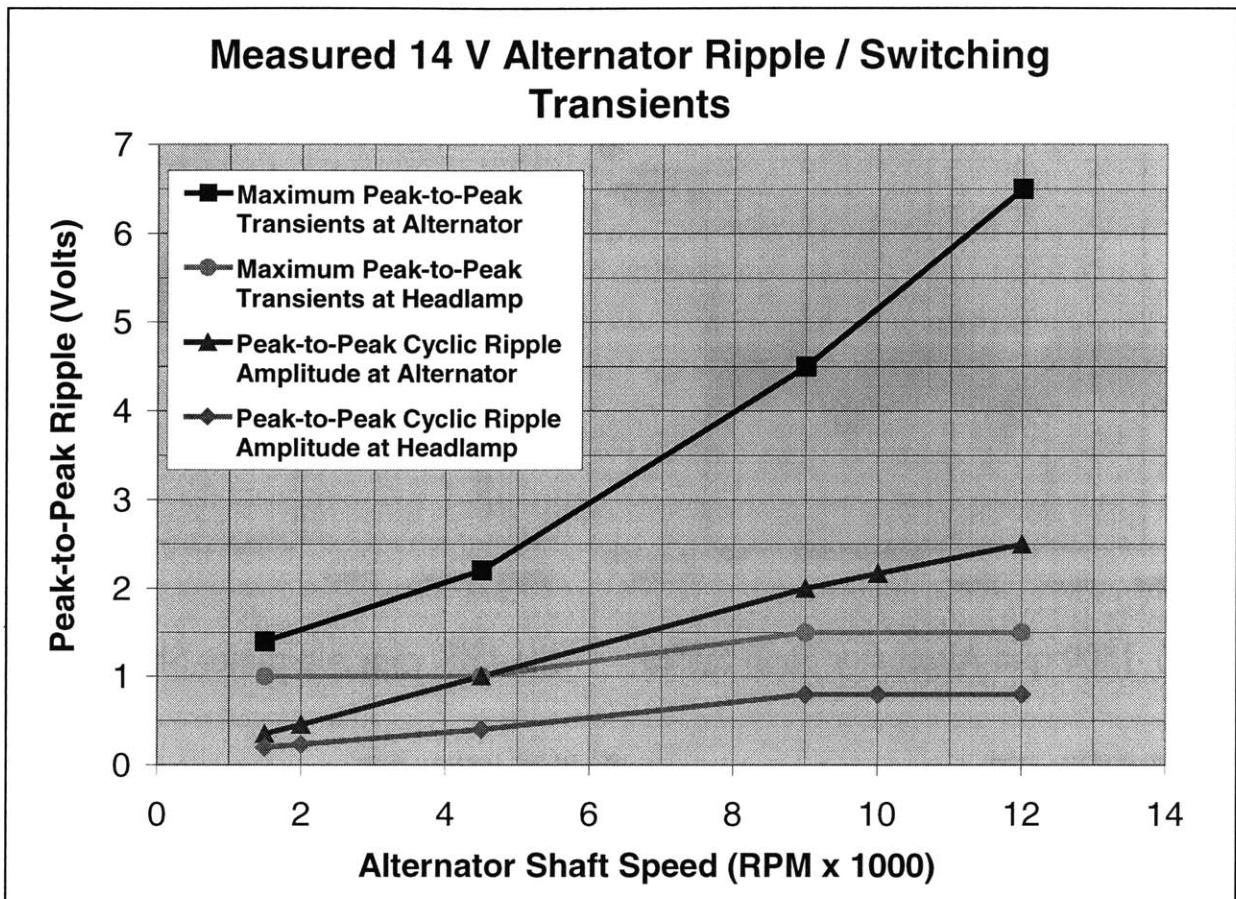


Figure 3.5: Summary of maximum peak-to-peak transient and steady-state ripple measurements at the alternator and headlamp terminals, as illustrated in Figures 3.3 and 3.4. The chart illustrates that ripple was observed to increase with increasing alternator shaft speed. Ripple at the alternator was also observed to increase with a steeper slope as a function of shaft speed than was ripple at the headlamp.

3.4 Industry Feedback and the Development of a 14V Ripple Specification

Investigations of prevailing automotive electrical specifications and measurements of voltage ripple on a present-day automobile provided differing suggestions for a 14V voltage ripple specification for the dual-voltage alternators under consideration. Thus, in an effort to reconcile J1113-2 with the observed measurements and to bring clarity to the search for an appropriate specification, Consortium members were polled as to how the industry currently treats ripple in present-day automobiles within the frequency range of interest.

The industry feedback dealt with both the measuring point at which ripple is evaluated in the system, and the ripple magnitudes that are allowed. The measurements in Figures 3.3 and 3.4

clearly illustrate that ripple magnitudes vary widely at different measurement points in the system. Thus, the need arises to choose a standardized measurement point and a worst-case ripple allowance at this point, such that the rest of the automotive electrical system continues to function normally under this worst-case disturbance. In an effort to standardize the location of observed ripple, industry feedback suggested that voltage ripple is presently evaluated at the rectifier output terminals for an alternator functioning within a complete automotive electrical system. By contrast, the system engineer is ultimately concerned with the performance of different electrical loads when subjected to voltage ripple disturbances at the load's terminals. However, the number of factors that contribute to voltage ripple magnitudes at the load make it very difficult for the engineer to control and regulate the magnitude of ripple that each load observes. Thus, the industry chooses to observe ripple at its source, the rectifier output terminals, and to make reasonable assumptions as to how ripple is attenuated between the alternator output and the loads.

However, Consortium members provided varying answers as to the voltage ripple magnitudes that they allow at the rectifier output terminals. Company A stated that it limits rectifier output ripple as a linearly increasing function of alternator shaft speed. This methodology is consistent with Figure 3.3 and 3.4 laboratory measurements suggesting that ripple does increase with alternator shaft speed. Company B stated that it places a ceiling on rectifier output ripple, regardless of alternator shaft speed. Thus, to bring consensus to these two methods for limiting alternator voltage ripple, a new specification was formed to limit the allowable voltage ripple on the 14V bus of the dual-rectifier and dual-stator alternators. This specification, illustrated in Figure 3.6, states that ripple at the 14V rectifier output terminals shall be limited to 1 V_{pp} at 2000 rpm, linearly increasing to a maximum of 5 V_{pp} at 10000 rpm. Ripple at shaft speeds above 10000 rpm shall be limited to the maximum 5 V_{pp}. This specification is more restrictive than the specifications reported by Consortium members, but not excessively so.

The purpose of this specification is to define levels of acceptability for voltage ripple at the 14V power supply output terminals created by thyristor and diode switching. Since no other established specification deals with voltage ripple within the frequency range of 600 Hz to 6 kHz, it was necessary to create a specification that drew upon voltage ripple measurements on present-day automobiles, and upon industry feedback as to how ripple within this frequency range is currently treated. This specification is intended to serve as a benchmark only for the purposes of this research, and does not seek to imply a larger industry standard. It does, however, quantify the amount of voltage ripple that shall be considered acceptable with the dual-rectifier and dual-stator alternators in this thesis. This quantification becomes extremely useful as filters are designed to attenuate this ripple to acceptable levels

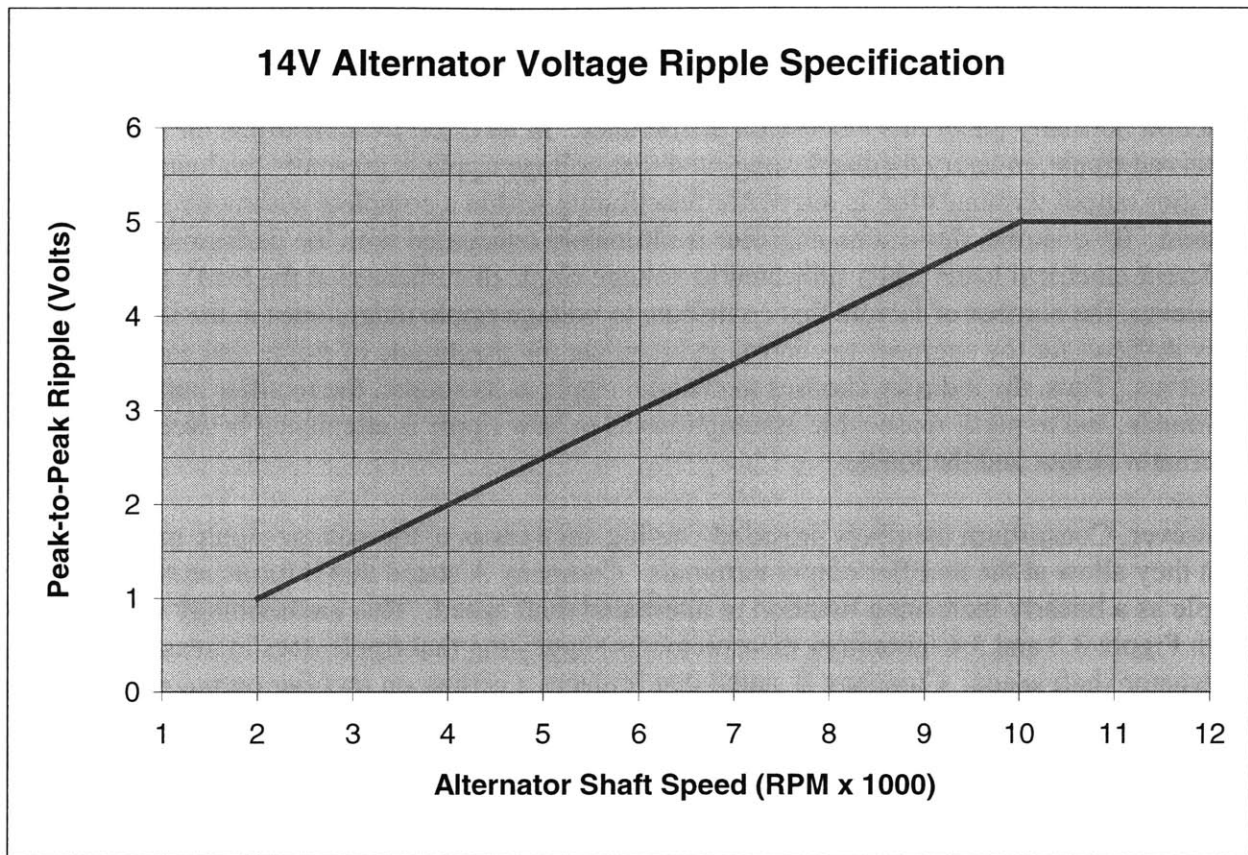


Figure 3.6: 14V alternator voltage ripple specification for voltage ripple observed at the rectifier output terminals of dual-voltage alternators. This specification is intended to apply only to the scope of this dual-voltage alternator evaluation, and does not seek to imply a larger industry standard.

3.5 Development of a 42V Ripple Specification

An inherent challenge with the development of a new 42V automotive electrical system paradigm is the development of new specifications to define acceptable electrical characteristics for the 42V bus. The initial formation of these specifications has been undertaken by the *Work Group "Standardisation" (WGS)*, a partnership led by SICAN GmbH and consisting of 19 German automakers and components suppliers¹. One of the primary objectives of the WGS is to establish and document permitted voltage levels and test procedures for loads on the 42V electrical system. [15]

¹ January 2000 membership

The January 2000 working draft of the WGS specification (WGS / WD 01/2000-2) specifies the maximum operating voltage $U_{\text{eff-op,max}}$ and the effective value of the maximum operating voltage $U_{\text{op,max}}$ for the 42V system. [16] $U_{\text{eff-op,max}}$ represents the average maximum value of the operating voltage, while $U_{\text{op,max}}$ represents the effective value *plus ripple*. The specification defines these values as follows:

$$\text{Effective Value of Maximum Operating Voltage} = U_{\text{eff-op,max}} = 48\text{V}$$

$$\text{Maximum Operating Voltage} = U_{\text{op,max}} = 50\text{ V (including ripple)}$$

These specifications imply that 2 V of ripple is allowed above the maximum operating voltage, and that 4 V peak-to-peak is allowed in general. In defining the test procedure for the maximum operating voltage, the specification mandates a test signal with 4 Vpp of voltage ripple within the frequency range of 50 Hz to 20 kHz. Thus, the WGS specification in general allows for a maximum voltage ripple magnitude of 4 Vpp.

The specification is non-specific as to the location within the automotive electrical system where 4 Vpp of ripple is allowed, stating only that the voltage should be measured "at the electric/electronic equipment terminals". Since the accompanying test procedure allows for a signal with 4 Vpp ripple to be applied directly to the device under test (DUT), it is implied that loads on the 42V bus should be designed to tolerate 4 Vpp at the load terminals. Since the specification is non-specific as to the allowable voltage at the power supply output terminals, this thesis will limit observed voltage ripple at the power supply output terminals to 4 Vpp.

3.6 Summary

When the issue of voltage ripple created by diode and thyristor switching was first considered, it was assumed that a clear and accepted specification for ripple of this range of frequencies already existed. However, examination of relevant specifications and conversations with the automotive industry revealed no such consensus for the 14V bus. Thus, the first task of this research became the establishment of a reasonable ripple specification for the 14V bus based on empirical measurements and present-day accepted practice. Meanwhile, voltage ripple on the 42V bus is currently being considered by the WGS (Forum Bordnetz) in its quest to construct a specification for the electrical characteristics of the 42V bus. Based on this research and on the work of the WGS, this chapter presents specifications for the 14V and 42V buses that will be used to measure unfiltered voltage ripple at the power supply outputs. These specifications will then be used to design passive filtering solutions to attenuate voltage ripple to the specified limits.

Bus	Applicable Ripple Limitation
14V	1 Vpp at 2000 rpm alternator shaft speed, linearly increasing to 5 Vpp at 10000 rpm alternator shaft speed
42V	4 Vpp

Table 3.1: Summary of voltage ripple specifications for the 14V and 42V buses of dual-voltage alternators.

Ripple Modeling with Dual-Voltage Alternators

One of the most significant challenges facing dual-voltage alternators is the issue of voltage ripple produced at the rectifier output terminals for each bus. Chapter 3 analyzed and quantified acceptable voltage ripple limits for both the 42V and 14V buses. This chapter will serve to analyze the magnitudes of voltage ripple produced by the dual-rectifier and dual-stator alternators in light of these limits of acceptability. This analysis is necessary to determine the degree of filtering required to attain acceptable voltage ripple characteristics from the two dual-voltage alternator topologies under consideration.

4.1 Software-Based System Modeling

Since only prototype versions of dual-rectifier and dual-stator alternators exist presently, this analysis of unfiltered voltage ripple with dual-voltage alternators relies on system modeling and simulation using Saber simulation software¹. Concurrent research within the MIT Consortium has developed models of the dual-rectifier alternator, the dual-stator alternator, and the resistively loaded automotive electrical system. This research employs these models to analyze the voltage ripple characteristics of dual-voltage alternators connected to a complete automotive electrical system.

4.1.1 Motivations for a Simulation-Based Analysis

The electrical transient characteristics of dual-voltage automotive electrical systems are difficult to analyze for two reasons. First, such systems are highly diverse and complex. Automotive electrical systems typically contain a battery and a large number of loads distributed around the vehicle with different lengths and sizes of wire. Transient events are difficult to analyze because they can result from any number of events occurring on the bus, all of which vary with bus loading, battery state of charge, and alternator shaft speed. Wire lengths and the resulting inductances also become relevant, since the wire is responsible for attenuating voltage ripple between the generation system and load. These complexities tend to make an equation-based analytical investigation of electrical transients very difficult.

It is also difficult to observe the electrical characteristics of dual-voltage electrical systems in the field because such systems do not exist in today's automobiles. Dual-voltage alternators have not been produced in large volumes, so the observation of their electrical characteristics would necessarily rely upon the construction of representative prototypes of these topologies.

¹ Saber is a product of Avant! Systems (formerly Analogy, Inc.), 9205 S.W. Gemini Drive, Beaverton, OR 97008.

Furthermore, accurate analysis of dual-voltage alternator voltage ripple would rely upon observing a dual-voltage alternator functioning within an actual automobile, since voltage ripple magnitudes are dictated in large part by how the alternator interacts with the rest of the automotive electrical system. Thus, the motivation exists to find alternative analysis methods for dual-voltage alternators that rely neither on the derivation of mathematical models nor on the availability of an actual dual-voltage alternator from which to take measurements. The chosen solution for this analysis problem is software-based system modeling and electrical simulation.

4.1.2. Alternator Modeling in Saber

The simulations performed for this thesis research are based on mathematical models of a three-phase claw-pole (Lundell) alternator defined using Saber's MAST modeling language. These models were developed during the course of a MIT Consortium research program investigating the transient characteristics of dual-voltage automotive electrical architectures. [17] The models define operation for a single-stator² and a dual-stator synchronous machine, based upon parameters for the leakage inductances, magnetizing inductances, saliency inductances (dual-stator machine only), and winding resistances for both the stator and rotor windings. The models use these parameters to consider both the self inductance of each individual winding and the mutual inductances that occur between each two-winding combination in the machine. The self inductance of each winding in each alternator is defined as the sum of the leakage and magnetizing inductances for the winding of interest. For the dual-rectifier alternator, mutual inductances are calculated based on the magnetizing inductances for each combination of two windings from the set of rotor, stator phase a , stator phase b , and stator phase c windings. For the dual-stator alternator, mutual inductances are calculated for each combination of two windings from the set of rotor, stator 1 phase a , stator 1 phase b , stator 1 phase c , stator 2 phase a , stator 2 phase b , and stator 2 phase c windings. The models use flux linkage equations that contain matrices of these inductances to derive terminal voltage and current characteristics for each machine based on alternator shaft speed and field current excitation. These winding resistances and inductances, along with their derived self and mutual inductance parameters, are listed in Tables 4.1 – 4.4. The MAST code that uses these parameters to create mathematical models of the single-stator and dual-stator machines is provided in Appendix A.

Typical values for these parameters were derived from measurements performed within the Consortium for a typical single-stator 14V, 60A / 120A claw-pole alternator. The present 14V alternator is capable of delivering up to 60 A (840 W) at engine idle speed and 120 A (1680 W) at high speed. However, the analyses performed for this research require a single-stator 42V machine for the dual-rectifier topology and a dual-stator 42V / 14V machine for the dual-stator topology. In order to realize models for these machines, these analyses modify the 14V values of the above resistance and inductance parameters based on the desire to create 42V dual-rectifier and dual-stator alternator models with at least the same total output power capability as the present 14V alternator. A first-pass conversion of the present 14V alternator into a 42V single-stator alternator involves rewinding the machine with three times the original number of

² Recall that the dual-rectifier alternator topology is based upon a 42V single-stator alternator.

Parameter	Description
R_s	stator winding resistance
L_{ls}	stator leakage inductance
L_{ms}	stator magnetizing inductance
R_r	rotor winding resistance
L_{lr}	rotor leakage inductance
L_{mr}	rotor magnetizing inductance

Table 4.1: Per-phase resistance and inductance parameters for the 42V single-stator alternator simulation model. Stator inductance and resistance parameters are assumed equal for each phase.

Parameter	Description	Expression
L_s	stator self inductance	$L_{ls} + L_{ms}$
L_r	rotor self inductance	$L_{lr} + L_{mr}$
L_{ss}	stator – stator mutual inductance	$L_{ms}\cos(\theta)$
M	peak stator – rotor mutual inductance	$\sqrt{L_{mr}L_{ms}}$

Table 4.2: Derived self and mutual inductance parameters for the 42V single-stator alternator simulation model. Stator self inductances are assumed equal for each phase. Also, stator – stator mutual inductances are assumed equal for each stator phase – stator phase combination, and peak stator – rotor mutual inductances are assumed equal for each stator phase – rotor combination. (Note: θ defines the electrical phase angle between stator windings, equal to $2\pi/3$.)

Parameter	Description
R_{s1}	14V stator winding resistance
R_{s2}	42V stator winding resistance
L_{ls1}	14V stator leakage inductance
L_{ls2}	42V stator leakage inductance
L_{ms1}	14V stator magnetizing inductance
L_{ms2}	42V stator magnetizing inductance
L_{g1}	14V stator saliency inductance magnitude
L_{g2}	42V stator saliency inductance magnitude
R_r	rotor winding resistance
L_{lr}	rotor leakage inductance
L_{mr}	rotor magnetizing inductance

Table 4.3: Per-phase resistance and inductance parameters for the 42V / 14V dual-stator alternator simulation model. Stator inductance and resistance parameters are assumed equal for each phase of the stator of interest.

Parameter	Description
L_{s1}	14V stator self inductance
L_{s2}	42V stator self inductance
L_r	rotor self inductance
L_{ms11}	14V stator – 14V stator mutual inductance
L_{ms22}	42V stator – 42V stator mutual inductance
L_{ms12}	14V stator – 42V stator mutual inductance
L_{g12}	14V stator – 42V stator saliency inductance
M_1	peak stator – rotor mutual inductance
M_2	peak stator – rotor mutual inductance

Table 4.4: Derived self and mutual inductance parameters for the 42V / 14V dual-stator alternator simulation model. Stator self inductances are assumed equal for each phase of the stator of interest. Also, all stator – stator mutual inductances that combine a phase of stator x with a phase of stator y are assumed equal, and all peak stator – rotor mutual inductances that combine a phase of stator z with the rotor are assumed equal.

turns per stator winding, since the desired output voltage has increased by a factor of three. A first-pass design of the dual-stator 42V / 14V alternator involves winding the 42V stator with three times the number of turns as the 14V stator (i.e., $N = 3:1$ turns ratio). Initial designs of both alternators also involve rewinding the rotor with three times the number of turns present within the 14V alternator rotor. The degree to which these first pass designs are capable of generating a total power output of 840 W at idle speed and 1680 W at high speed is analyzed in the discussion of dual-stator turns ratios in Chapter 6 and in the discussion of single and dual-stator machine costs in Chapter 7.

4.1.3 Lead-Acid Battery Modeling for Each Bus

The automotive battery model employed within the simulated automotive electrical system consists simply of a dc source voltage V_{oc} connected to an internal series resistance (see Figure 4.1). The dc source voltage represents the open-circuit (i.e., non-loaded) voltage present at the battery terminals, and can generally be described as a linear function of the battery's state of charge (SOC). [18] This dc source voltage is modeled as an integrator function such that V_{oc} decreases as excess current is drawn from the battery and increases as excess current is delivered to the battery. The integrator function attempts to maintain 5 A of current delivered to each battery, to approximate a reasonable amount of current being delivered to a fully charged battery under normal operating conditions in the vehicle.

The series resistance in the battery model accounts for the voltage increase (decrease) that occurs across the battery terminals when current is charging (discharging) the battery. However, battery impedance is typically difficult to quantify for automotive lead-acid batteries, since this impedance varies greatly with state of charge, temperature, and with the specific battery being observed. Thus, reasonable impedances were chosen for the simulation model to approximate the terminal voltage increase or decrease that occurs as current is delivered to or drawn from a typical automotive battery. Since the internal resistance of the battery increases linearly with the number of cells, the series resistance chosen for the 42V battery model is three times the series resistance chosen for the 14V battery model. A value of $R_{int} = 25 \text{ m}\Omega$ was chosen for the 14V battery model, and $R_{int} = 75 \text{ m}\Omega$ was chosen for the 42V battery model.

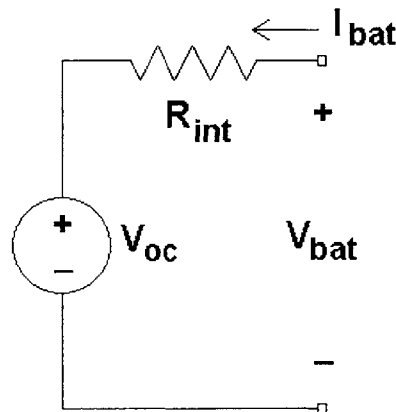


Figure 4.1: Battery model used in simulated automotive electrical system.

4.1.4 Electrical Distribution and Utilization Subsystem Modeling

The voltage ripple characteristics of the dual-rectifier and dual-stator alternators are relevant only when such characteristics are observed within the context of the complete automotive electrical system. System variations such as the presence or absence of a battery, the degree of ripple attenuation that occurs over the wire inductances, and the loading attached to each bus affect the manner in which ripple is attenuated between the alternator output terminals and the load terminals. Thus, it is desirable to model and study the dual-rectifier and dual-stator alternators with each one connected to and generating power for the overall automotive electrical system. The automotive electrical system model to be used for each bus for the purposes of this research is illustrated in Figure 4.2.

The distribution subsystem, which includes all cabling and switching devices that connect the alternator and battery to the various electrical loads, is modeled with an ideal wire and a series line inductance between the alternator and battery and between the battery and load for both the 42V and 14V buses. The length of this wire is given in the per-bus simulation model in Figure 4.2, which draws upon a typical industry test procedure for the evaluation of alternator voltage ripple. The maximum self inductance of each wire is calculated as follows: [19]

$$L_0' = \frac{\mu_0}{2\pi} \cdot \ln\left(\frac{4h}{d}\right) \quad (4.1)$$

where:

L_0' = inductance per unit length (H/m)

μ_0 = permeability = $4\pi \cdot 10^{-7}$ H/m

h = height above ground plane = 0.5 m

d = wire diameter

Given the model provides for 2 m of wire with a cross sectional area of 25 mm² connecting both the positive and negative terminals of the alternator to the battery, each of these two leads is modeled with a series inductance of 2.34 μ H. The 1.5 m of 50 mm² wire connecting both the positive and negative terminals of the battery to the load is modeled with a series inductance of 1.65 μ H.

This simulation model represents the various electrical loads connected to each bus with a single lumped resistive load for each bus. Most automotive loads (headlamps, convenience accessories, linear regulators for low voltage electronics) appear resistive to the system bus, such that a resistive loading model allows voltage ripple to be reasonably approximated in the overall simulation model. A resistive loading model also allows the desired amount of current drawn from the alternator for a given simulation scenario to be set very easily.

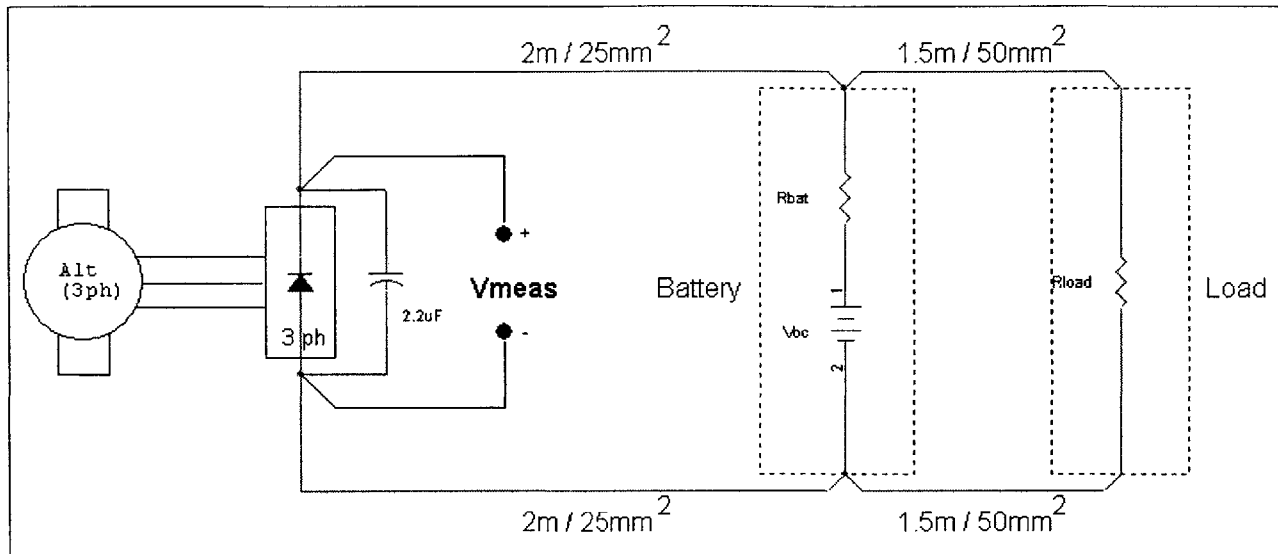


Figure 4.2: Automotive electrical system simulation model employed in this research to examine alternator voltage ripple. Note that this model represents a single-voltage electrical system, and that the distribution system and load will be replicated for both the 14V and 42V buses in the dual-voltage system simulation.

4.2 Simulation Parameters

4.2.1 Alternator Shaft Speed

Chapter 3 presented an alternator voltage ripple specification in which the maximum allowable ripple magnitude increases as a function of alternator shaft speed. This speed dependency reflects the assertion by some automotive industry members that their own voltage ripple limits increase with alternator shaft speed. Thus, unfiltered voltage ripple for dual-voltage alternators should be examined across a representative range of alternator shaft speeds to determine the degree to which dual-voltage alternators either adhere to or violate this specification. Since the 14V specification in Chapter 3 presents a linearly increasing maximum ripple magnitude between alternator shaft speeds of 2000 rpm (approximately idle) and 10000 rpm (high engine speed), the following simulations will examine both 14V and 42V voltage ripple at the rectifier output terminals at 2000 rpm and 10000 rpm.

4.2.2 Bus Loading

Early on, this research sought to examine voltage ripple for varying amounts of power demanded by the 14V and 42V buses. Voltage ripple measurements like those presented in Chapter 2 were made for a variety of loading conditions. Simulations were also performed for a number of scenarios mixing no loading, medium loading, and full loading conditions for both buses. However, a weak correlation at best was seen between bus loading and maximum peak-to-peak

ripple magnitudes for both the measurements and simulations. The measurements and simulations did seem to indicate that voltage ripple somewhat increases with bus loading, but the initial correlation was not strong enough to warrant a complete examination of voltage ripple as a function of bus loading.

Given these observations, this thesis quantifies ripple for the case in which the alternator is supplying the same level of output power as a fully loaded present-day 14V alternator, with power equally split between the 14V and 42V bus loads. As discussed in Section 4.1.2, the dual-rectifier and dual-stator machine models were configured such that these models have at a minimum the same output power capability as the present 14V alternator, i.e. 840 W at idle and 1680 W at high speed. Idle speed is typically assumed to be 1800 rpm and high speed is assumed to be 6000 rpm. By contrast, this thesis will examine voltage ripple at 2000 rpm and 10000 rpm alternator shaft speeds. Thus, for the sake of simplicity, each alternator's maximum power output at 2000 rpm is assumed to be 840 W. Similarly, the alternator's maximum current output capability typically saturates beyond approximately 120 A, so 1680 W is assumed to be the maximum power output at 10000 rpm.

Table 4.5 details the manner in which alternator output power is distributed for the 2000 rpm and 10000 rpm simulation scenarios. Each of the battery models is designed to sink 5 A of current under a fully charged, periodic steady state bus condition, while the remaining output power is split equally between the 14V and 42V buses. According to Table 4.5, the resistive loads in the simulation are sized such that 280 W is delivered to each load at 2000 rpm and 700 W is delivered to each load at 10000 rpm, in addition to the power delivered to each battery.

	2000 rpm		10000 rpm	
	Power Delivered	Current	Power Delivered	Current
14V Load	280 W	20 A	700 W	50 A
42V Load	280 W	6.67 A	700 W	16.67 A
14V Battery	70 W	5 A	70 W	5 A
42V Battery	210 W	5 A	210 W	5 A
Total Power Delivered	840 W		1680 W	

Table 4.5: Distribution of delivered power for simulations conducted at 2000 rpm and 10000 rpm alternator shaft speeds. In each case, the alternator is supplying its assumed maximum output power capability and excess power not delivered to the batteries is split equally between the 14V and 42V bus loads.

4.2.3 Battery Disconnection

The automotive lead-acid battery acts as a significant ripple filter for the bus by sinking large amounts of ripple current that would otherwise flow to the system loads. This is due to the low impedance of the battery relative to the impedance of system loads at ripple frequencies. However, if the battery were to become disconnected from the bus during normal operation, the

system would lose this ripple filtering capability, and a much larger degree of ripple current would flow to the loads. Such a condition is conceivable, as one of the battery leads could become disconnected during normal vehicle operation. Consortium members have suggested that they wish to design dual-voltage electrical systems for this fault condition, to prevent valuable system loads from being damaged by excessive voltage ripple due to a disconnected battery. Thus, this research will examine unfiltered voltage ripple for cases in which the 14V and 42V batteries are both connected to and disconnected from their respective buses, in order to evaluate the degree to which voltage ripple worsens when a battery is disconnected from either bus. The no-battery condition will be simulated by progressively disconnecting the two batteries from their respective buses after the alternator field current has risen to a level where power is being supplied to both buses. Ripple filters will then be sized for the worst case no-battery condition, such that filtered alternator voltage ripple remains at acceptable levels even if a battery becomes disconnected from either bus.

4.3 Unfiltered Voltage and Current Ripple with the Dual-Rectifier Alternator

The following waveforms detail unfiltered ripple results derived from Saber simulations of the dual-rectifier alternator. The waveforms illustrate voltage ripple observed at the alternator rectifier, battery, and load terminals for both the 14V and 42V buses. Waveforms are also provided to illustrate current ripple for current leaving the rectifier terminals, current entering the battery terminals, and current entering the load terminals. Each of these sets of voltage and current waveforms are provided for both the connected and disconnected battery scenarios at both 2000 rpm and 10000 rpm alternator shaft speeds. In all cases, the waveforms illustrate voltage and current ripple after the waveforms have reached periodic steady state, at which time the electrical behavior of the waveforms changes very little on a cycle-to-cycle basis.

4.3.1 Unfiltered Dual-Rectifier Alternator Ripple Waveforms with Battery Connected

Figures 4.3 – 4.6 illustrate unfiltered voltage and current ripple observed with the dual-rectifier alternator at both 2000 rpm and 10000 rpm with the battery connected.

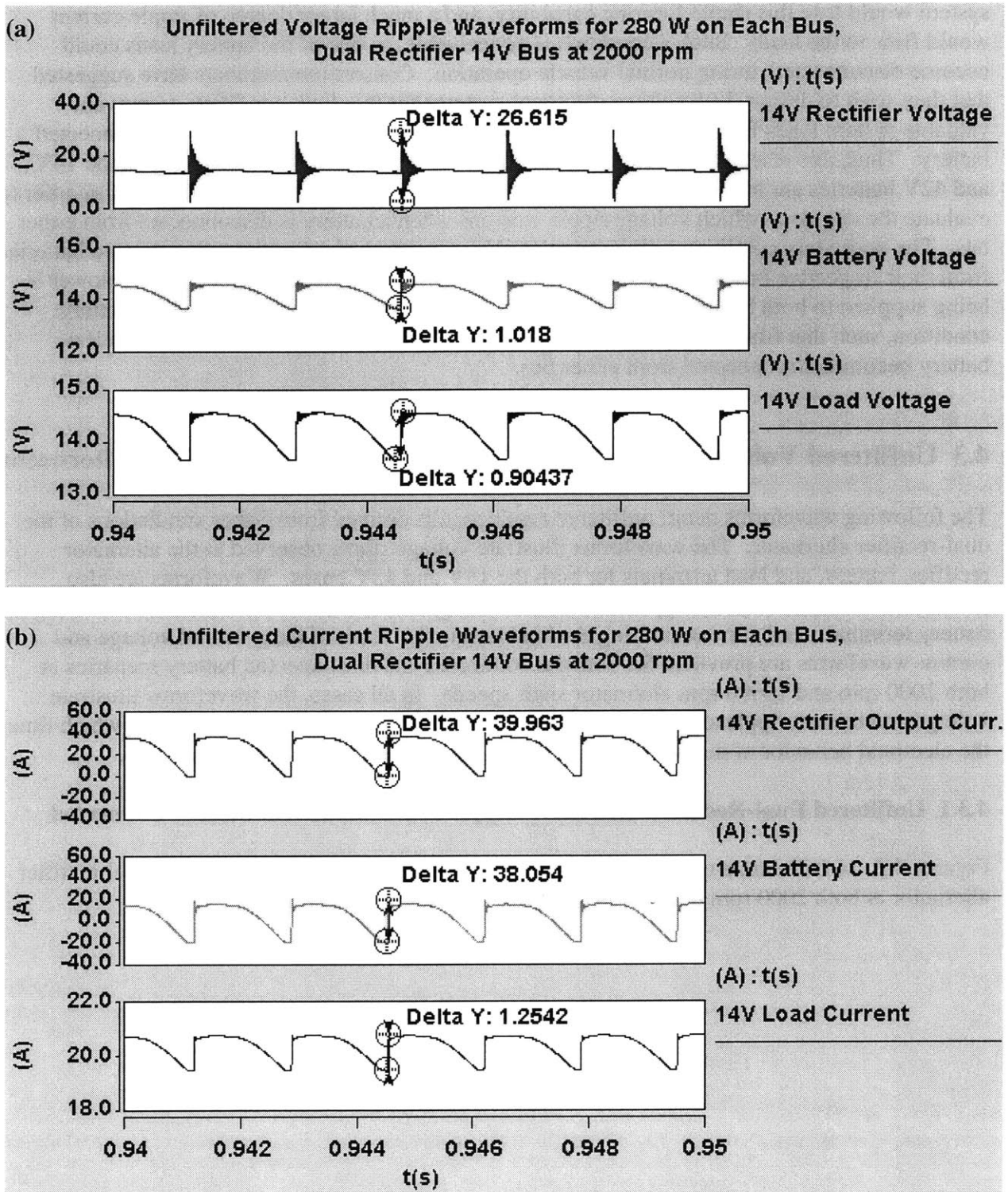


Figure 4.3: Unfiltered 14V bus ripple waveforms for the dual-rectifier architecture operating at 2000 rpm alternator shaft speed, with the battery *connected*: (a) voltage waveforms; (b) current waveforms.

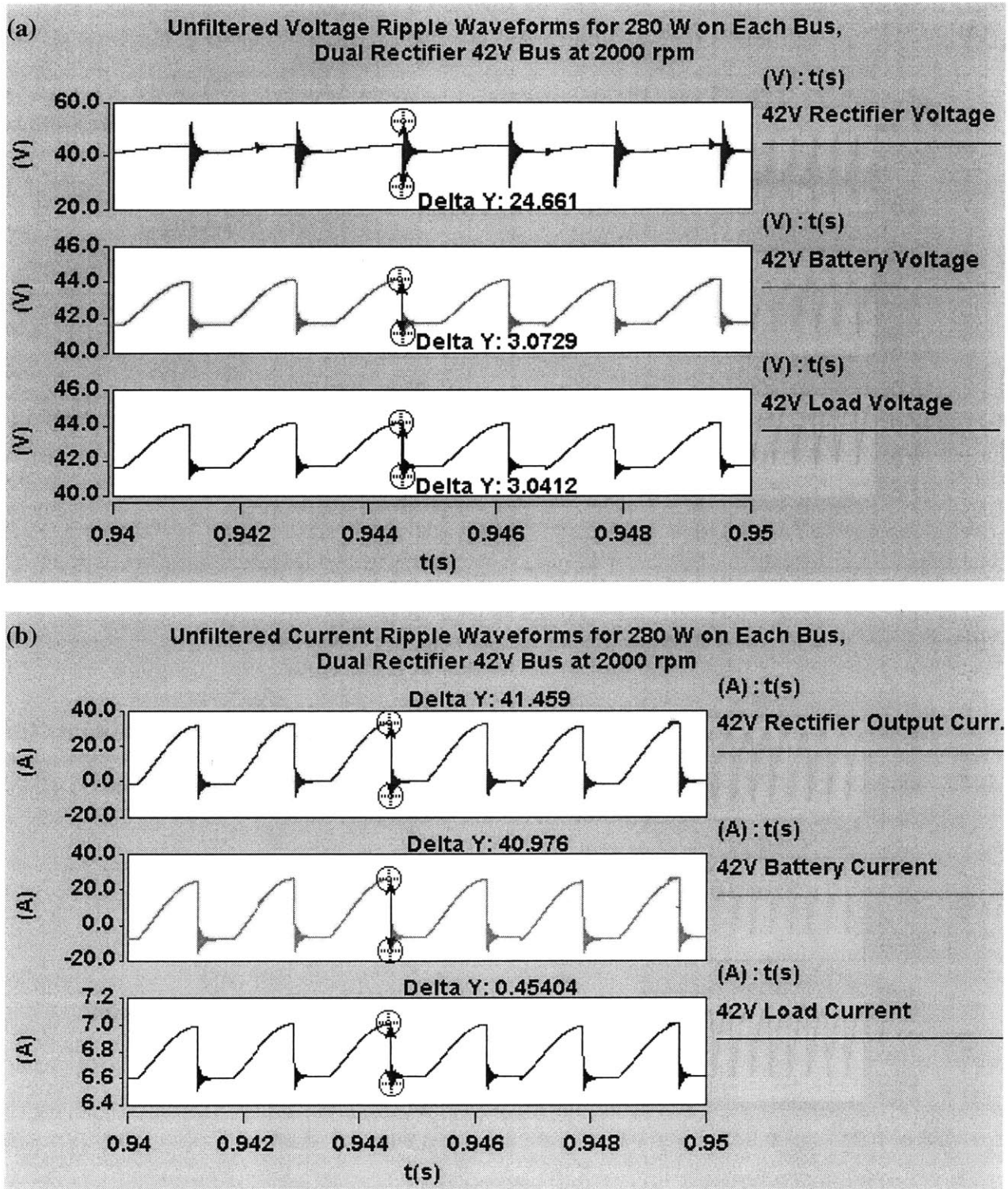


Figure 4.4: Unfiltered 42V bus ripple waveforms for the dual-rectifier architecture operating at 2000 rpm alternator shaft speed, with the battery *connected*: (a) voltage waveforms; (b) current waveforms.

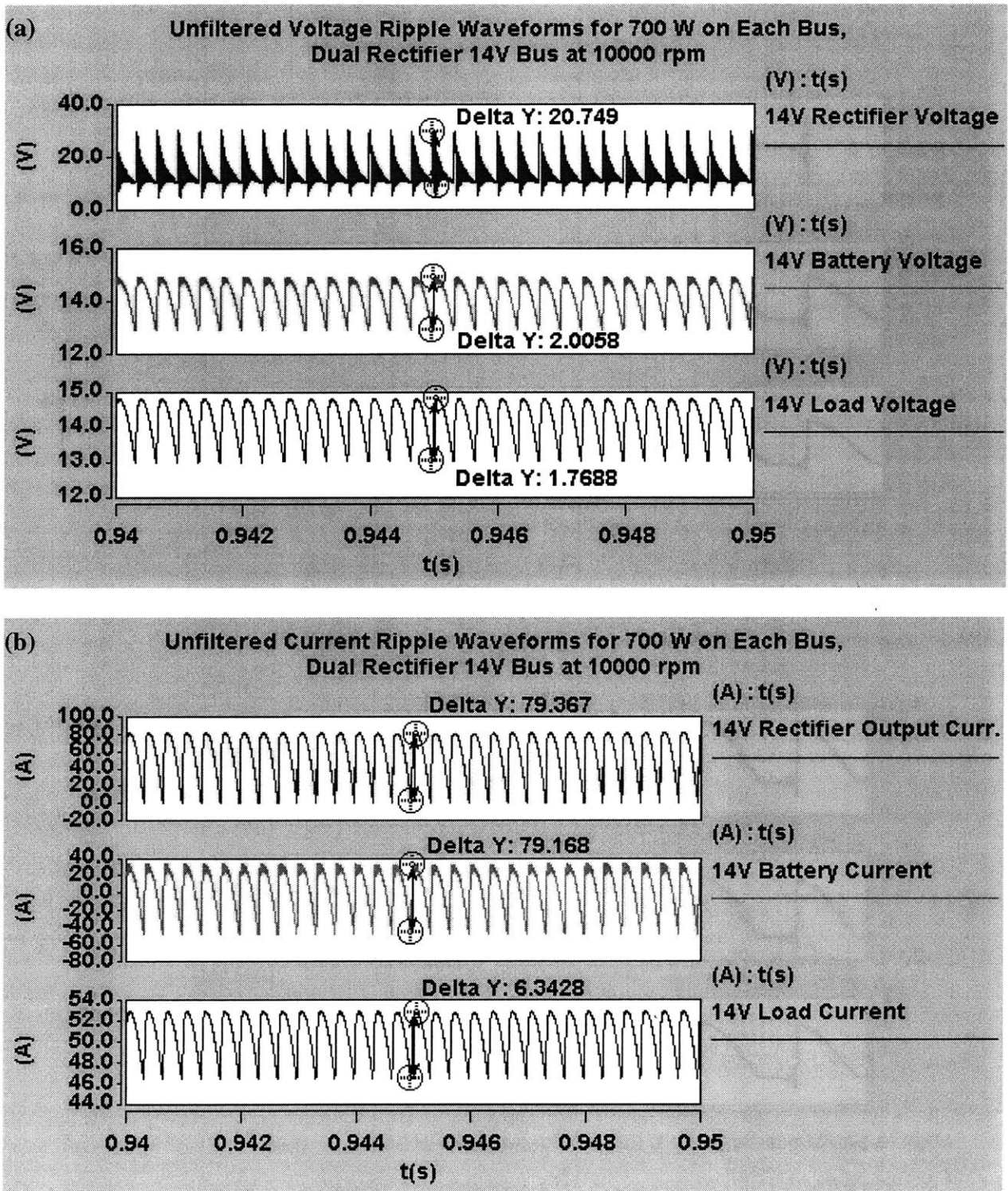


Figure 4.5: Unfiltered 14V bus ripple waveforms for the dual-rectifier architecture operating at 10000 rpm alternator shaft speed, with the battery *connected*: (a) voltage waveforms; (b) current waveforms.

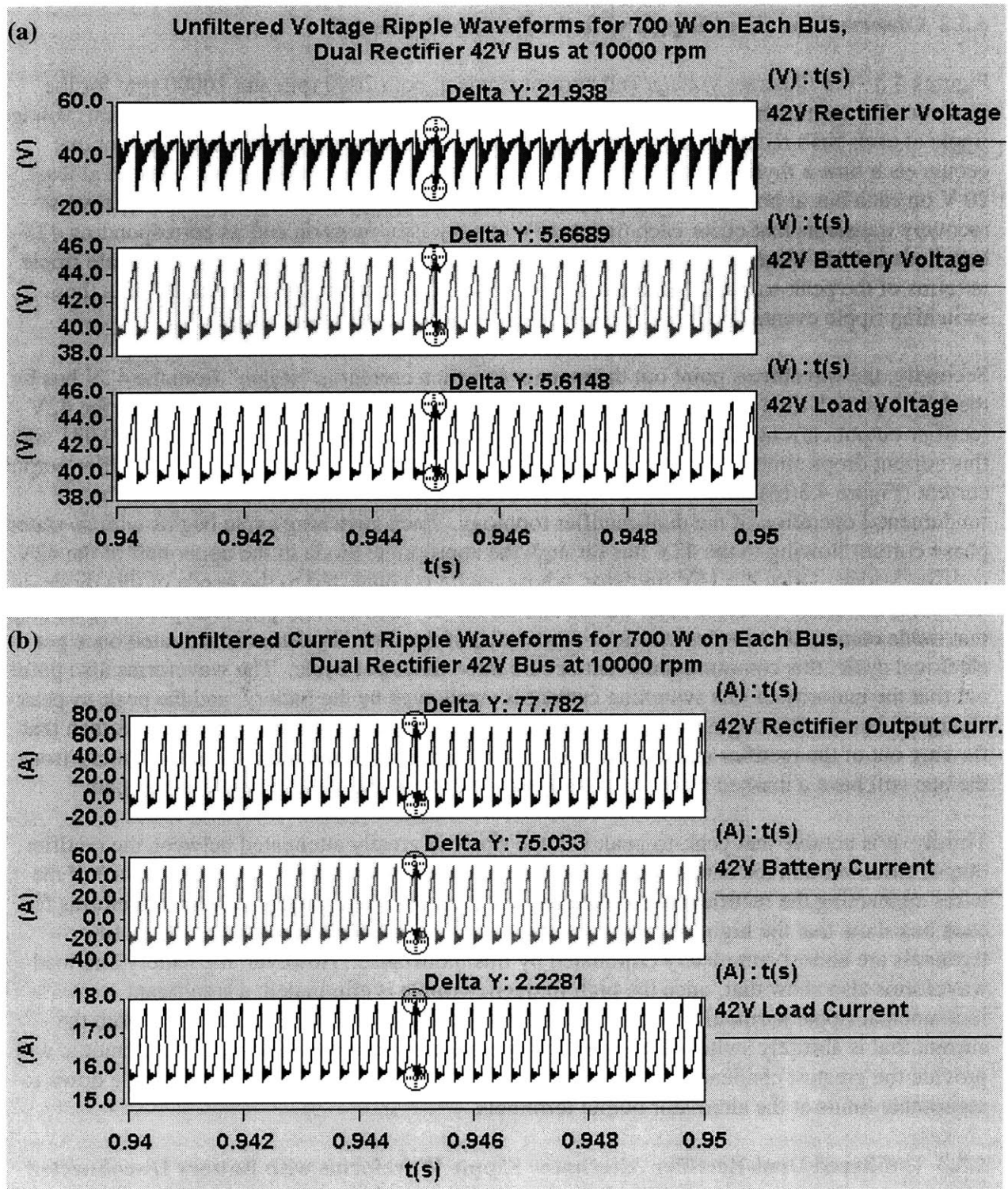


Figure 4.6: Unfiltered 42V bus ripple waveforms for the dual-rectifier architecture operating at 10000 rpm alternator shaft speed, with the battery *connected*: (a) voltage waveforms; (b) current waveforms.

4.3.2 Observations about Ripple with the Battery Connected

Figures 4.3 - 4.6 illustrate voltage and current ripple at both 2000 rpm and 10000 rpm for the dual-rectifier architecture. These waveforms highlight three relevant observations. First, voltage ripple at each bus's rectifier output terminals is dominated by a high frequency transient that occurs each time a thyristor is switched on. This transient has a peak-to-peak swing of at least 20 V on each bus at both 2000 rpm and 10000 rpm. These ripple events represent the reverse-recovery transients that occur each time a 14V bus thyristor turns on and its corresponding 42V bus diode is back-biased off. Since the specifications employed in this research evaluate ripple in terms of the peak-to-peak transients that occur at the alternator output terminals, it is these switching ripple events that must be reduced to the limits specified in Chapter 3.

Secondly, the waveforms point out the manner in which current is "stolen" from the 42V bus by the 14V bus each time a thyristor is activated. For example, Figure 4.4(b) shows how the 42V rectifier output current ramps up from 0 A to 35 A at the beginning of a cycle. At $t = 0.941$ sec, this current drops almost instantaneously back to 0 A. At the same time, the 14V rectifier output current (Figure 4.3(b)) jumps very quickly from 0 A to 35 A. These events illustrate the fundamental operation of the dual-rectifier topology. Each switching cycle begins with ac stator phase current flowing to the 42V bus through the appropriate diode in the upper half of the 42V rectifier bridge. Once the 14V thyristor, whose anode is connected to the anode of this diode, is activated, the diode becomes back-biased and all the ac stator current previously flowing through that diode commutates to the thyristor. Since each of the three thyristors is activated once per electrical cycle, this commutation event occurs three times per cycle. The waveforms also point out that the majority of this switching current is swallowed by the battery, and the peak-to-peak change in current flowing into the load terminals is at least an order of magnitude less than that flowing out of the rectifier output terminals. This suggests that the removal of the battery from the bus will have a marked effect on the amount of current and voltage ripple at the load.

Thirdly, it is notable that peak-to-peak voltage ripple is greatly attenuated between the rectifier output terminals and the battery terminals. This attenuation is caused by the inductance of the wires connecting the rectifiers to the batteries for each bus. The battery voltage waveforms for each bus show that the high frequency reverse-recovery transients observed at the rectifier terminals are almost completely eliminated by this inductance. However, the battery and load waveforms also show that, once the high frequency ripple is eliminated, a significant fundamental ripple harmonic remains. This fundamental harmonic results directly from the current that is abruptly switched between the two buses as described above. This harmonic will provide the greatest challenge for a ripple filter that tries to reduce peak-to-peak ripple down to acceptable limits at the alternator output terminals.

4.3.3 Unfiltered Dual-Rectifier Alternator Ripple Waveforms with Battery Disconnected

The waveforms shown in Figures 4.7 - 4.10 illustrate unfiltered voltage and current ripple for the same scenarios depicted in Figures 4.3 - 4.6, but with the 14V and 42V batteries disconnected from their respective buses.

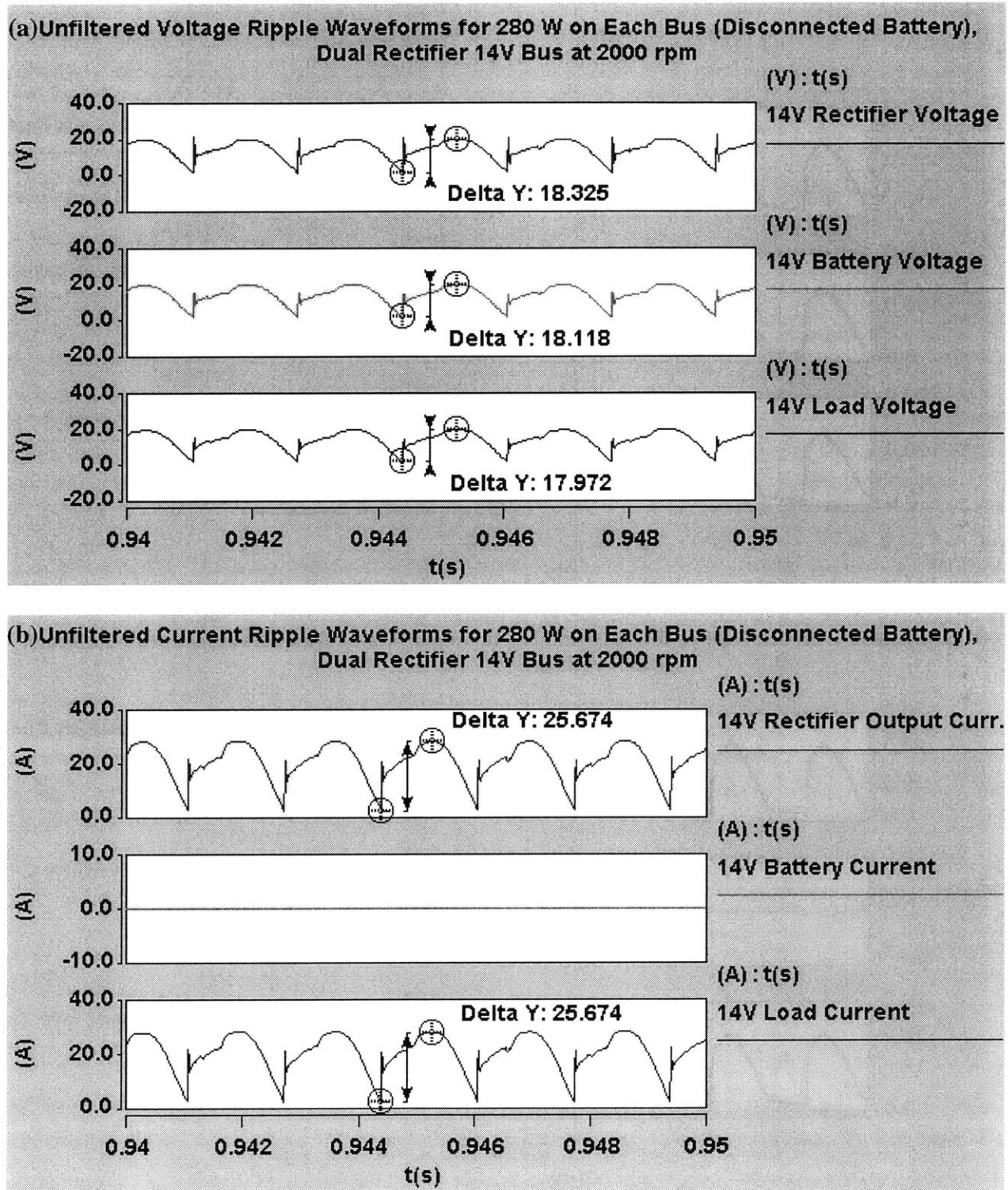


Figure 4.7: Unfiltered 14V bus ripple waveforms for the dual-rectifier architecture operating at 2000 rpm alternator shaft speed, with the battery *disconnected*: (a) voltage waveforms; (b) current waveforms.

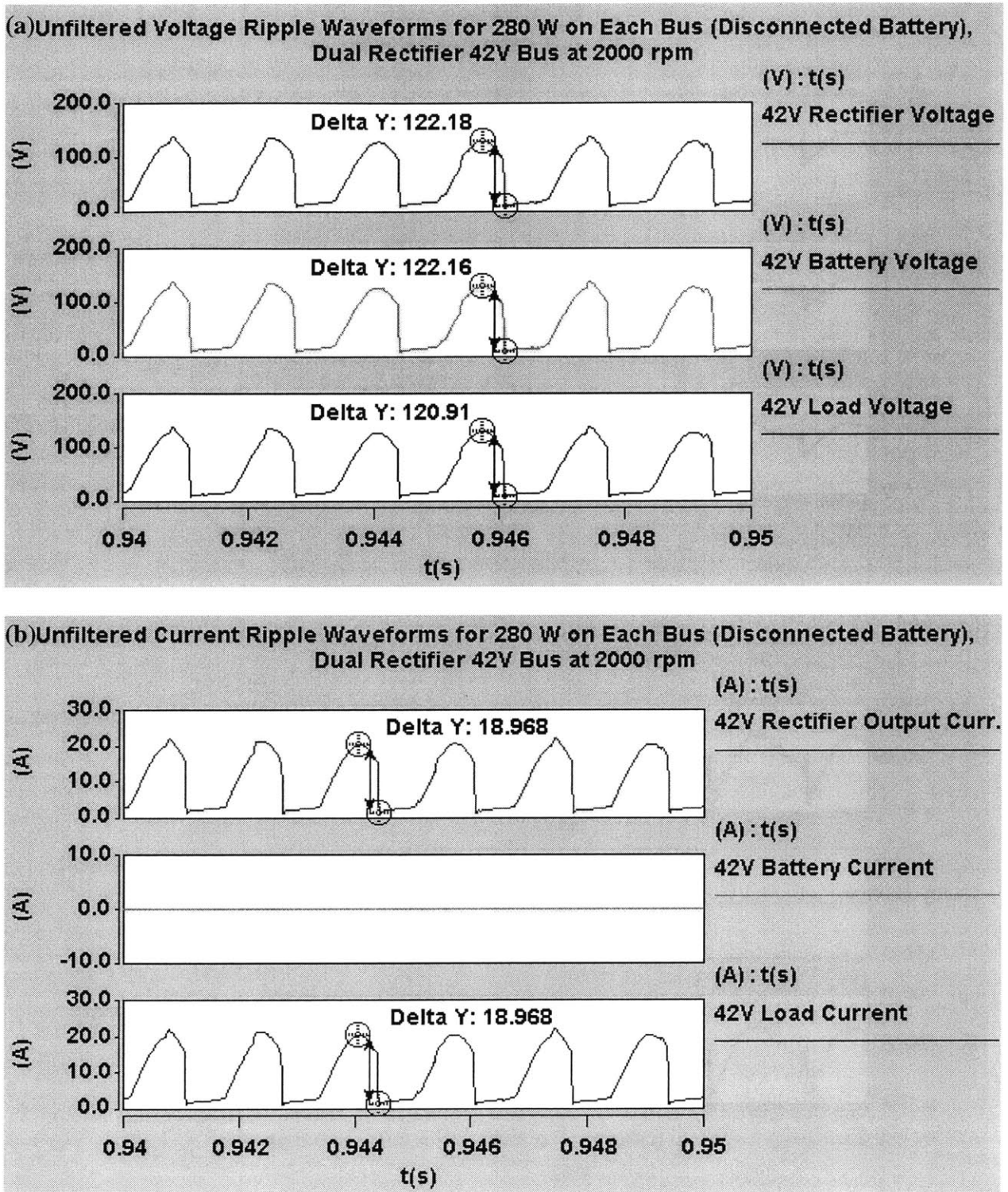


Figure 4.8: Unfiltered 42V bus ripple waveforms for the dual-rectifier architecture operating at 2000 rpm alternator shaft speed, with the battery *disconnected*: (a) voltage waveforms; (b) current waveforms.

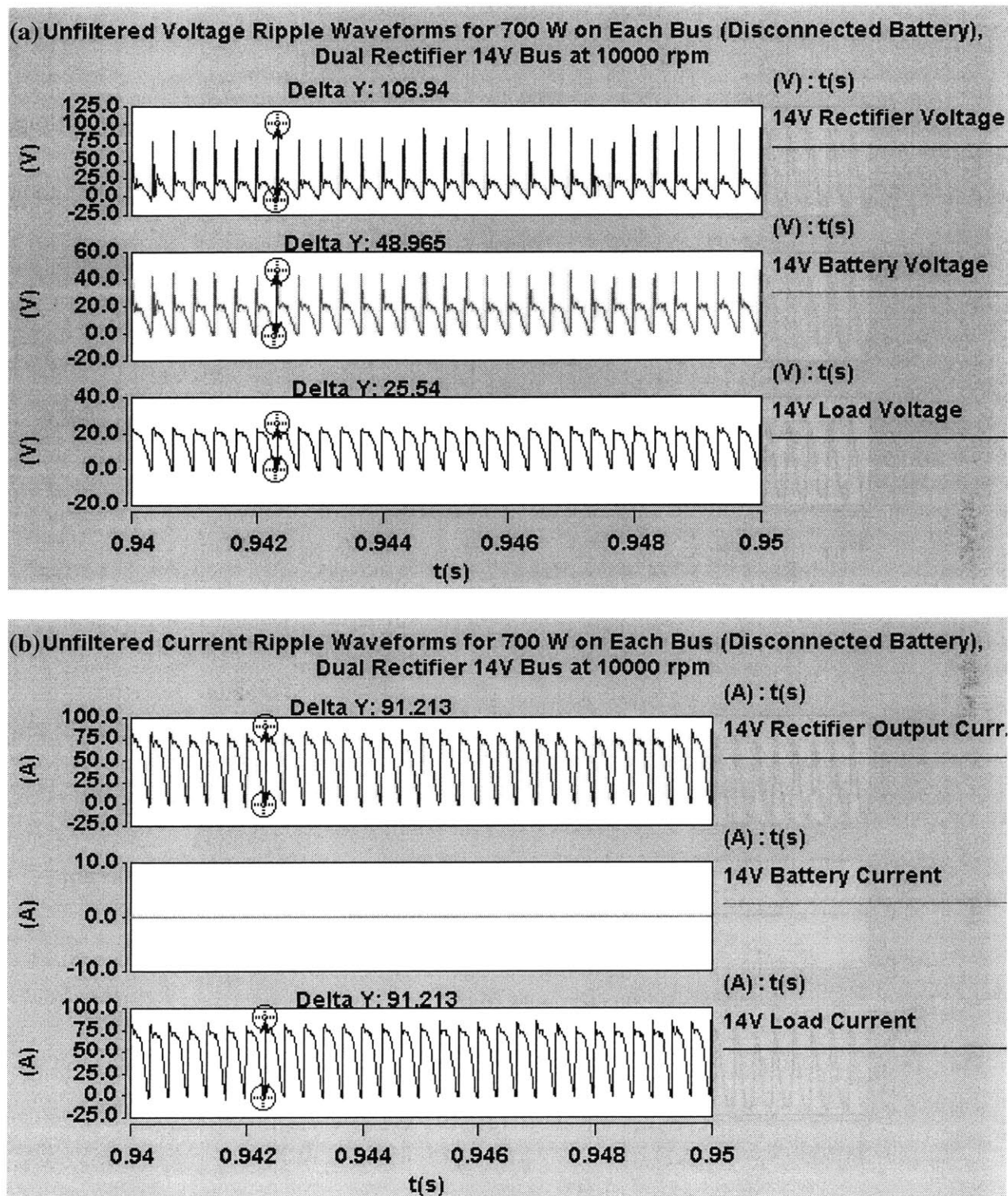


Figure 4.9: Unfiltered 14V bus ripple waveforms for the dual-rectifier architecture operating at 10000 rpm alternator shaft speed, with the battery *disconnected*: (a) voltage waveforms; (b) current waveforms.

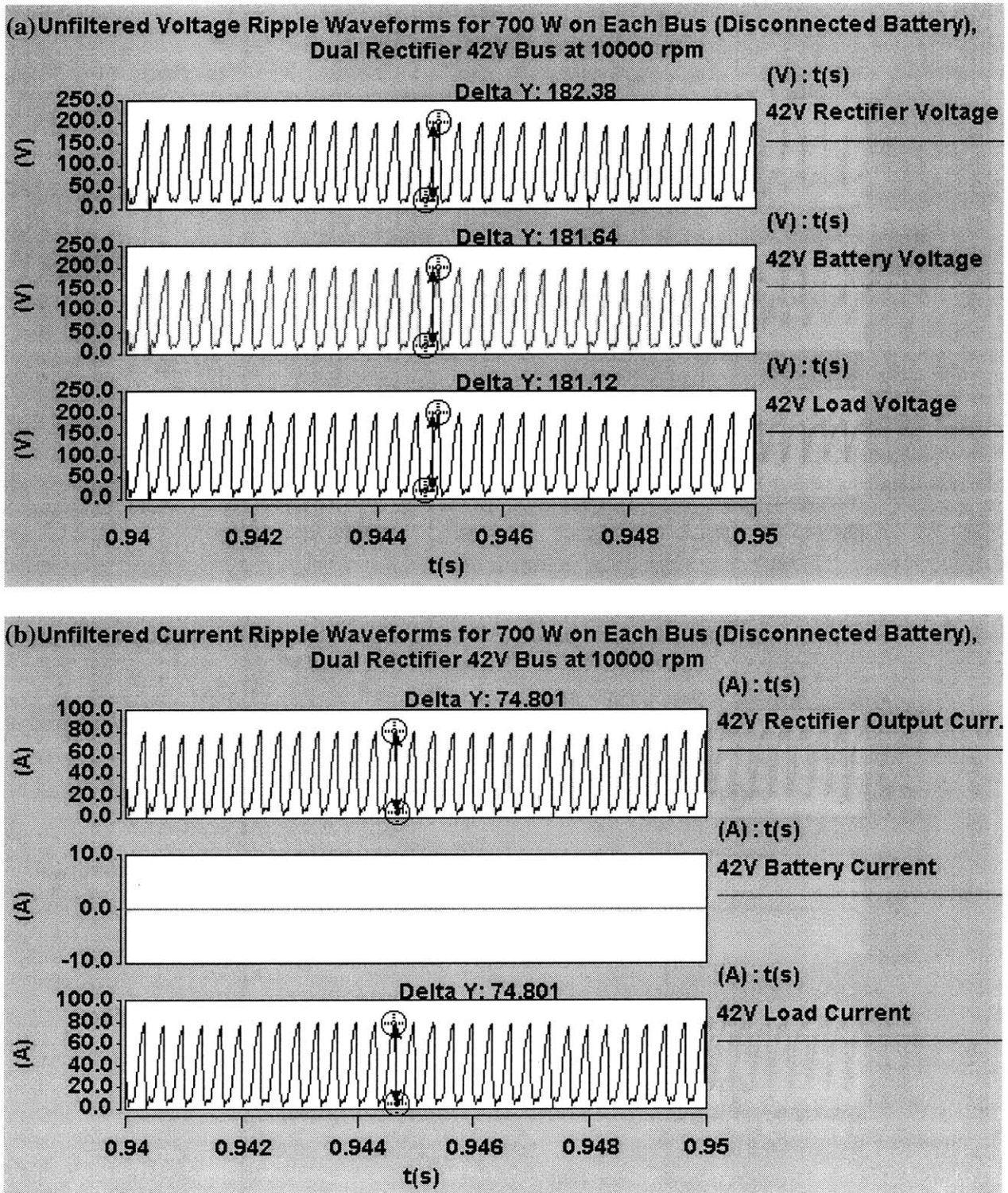


Figure 4.10: Unfiltered 42V bus ripple waveforms for the dual-rectifier architecture operating at 10000 rpm alternator shaft speed, with the battery *disconnected*: (a) voltage waveforms; (b) current waveforms.

4.3.4 Observations about Ripple with the Battery Disconnected

Figures 4.7 - 4.10 illustrate voltage and current ripple for the dual-rectifier architecture with each battery disconnected from its bus. As expected, the ripple amplitudes observed at the load for each bus increase dramatically, since the battery is no longer present to sink ripple harmonics in the rectifier output current. In the cases with the batteries connected, a large degree of voltage ripple attenuation occurred between the rectifier output and the load as ripple current was sunk by each battery. However, a much smaller degree of attenuation occurs between the battery and the load with each battery disconnected. The requirement to meet ripple specifications with the battery disconnected has a large effect on the ripple filter design, because the battery and wire inductance can no longer be depended upon to attenuate ripple between the rectifier and load.

The fundamental harmonic also seems to play a much larger role in the total harmonic content of voltage ripple observed at the rectifier output. For both the 2000 rpm and 10000 rpm cases for both buses, a large fundamental ripple harmonic is observed relative to any high frequency ripple that occurs during the switching event. This is particularly the case with the 42V bus waveforms where the fundamental harmonic overwhelmingly dominates voltage ripple, and very little high frequency content is observed. The fundamental ripple harmonic becomes more significant here because the battery is no longer present to clamp the bus voltage to a relatively constant level. As currents are switched back and forth between the two rectifiers, the battery is no longer available to absorb the ripple current. Therefore, more ripple current flows to the load, causing larger fluctuations of bus voltage at the fundamental ripple frequency. This amplifies the filtering problem, as the filter in this case will be required to attenuate a much larger fundamental harmonic compared to cases with the battery connected. The frequency of this fundamental harmonic is also on the order of the electrical frequency of the machine and can be as low as 600 Hz. Ripple of such a large magnitude and at such a low frequency has the potential to make the filter design for this machine quite challenging within certain size and cost constraints.

4.4 Unfiltered Voltage and Current Ripple with the Dual-Stator Alternator

The following waveforms detail unfiltered ripple results derived from Saber simulations of the dual-stator alternator. Like the dual-rectifier case, these waveforms illustrate voltage ripple observed at the alternator rectifier, battery, and load terminals for both the 14V and 42V buses. Waveforms are also provided to illustrate current ripple for current leaving the rectifier terminals, current entering the battery terminals, and current entering the load terminals. Again, these waveforms illustrate voltage and current ripple after the waveforms have reached periodic steady state, for both the connected and disconnected battery scenarios at 2000 rpm and 10000 rpm alternator shaft speeds.

4.4.1 Unfiltered Dual-Stator Alternator Ripple Waveforms with Battery Connected

Figures 4.11 – 4.14 illustrate unfiltered voltage and current ripple observed with the dual-stator alternator at both 2000 rpm and 10000 rpm with the battery connected.

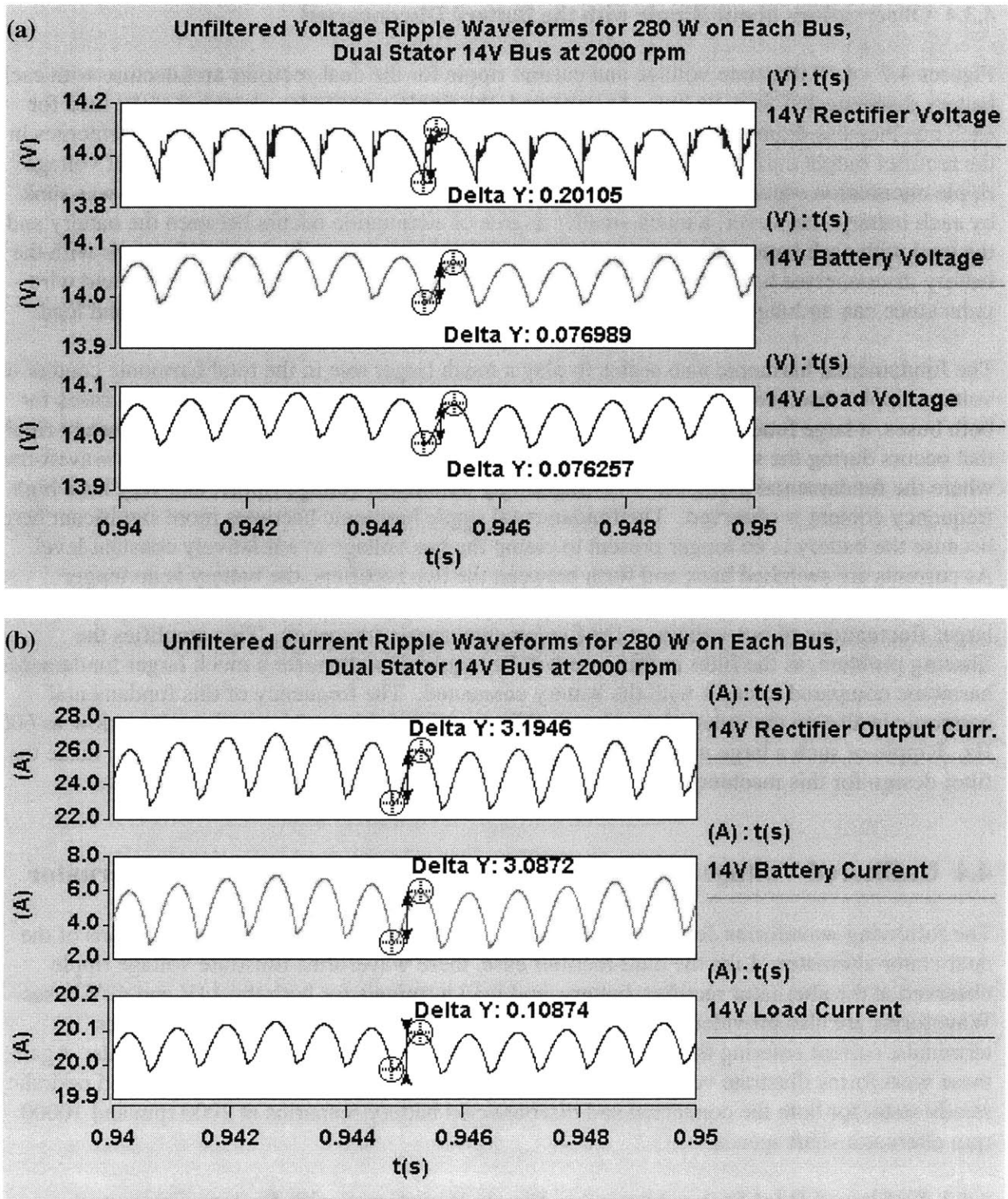


Figure 4.11: Unfiltered 14V bus ripple waveforms for the dual-stator architecture operating at 2000 rpm alternator shaft speed, with the battery *connected*: (a) voltage waveforms; (b) current waveforms.

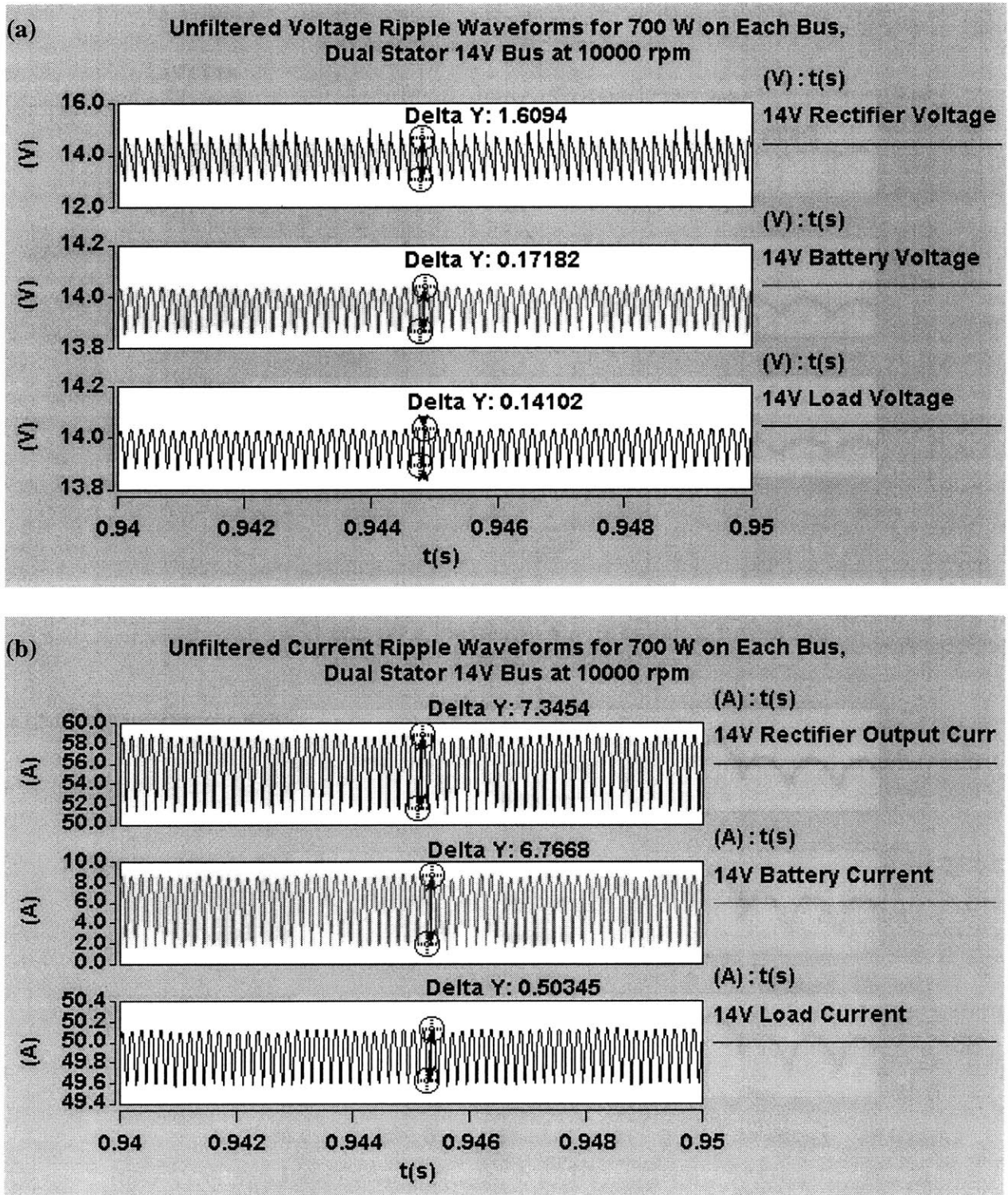


Figure 4.13: Unfiltered 14V bus ripple waveforms for the dual-stator architecture operating at 10000 rpm alternator shaft speed, with the battery *connected*: (a) voltage waveforms; (b) current waveforms.

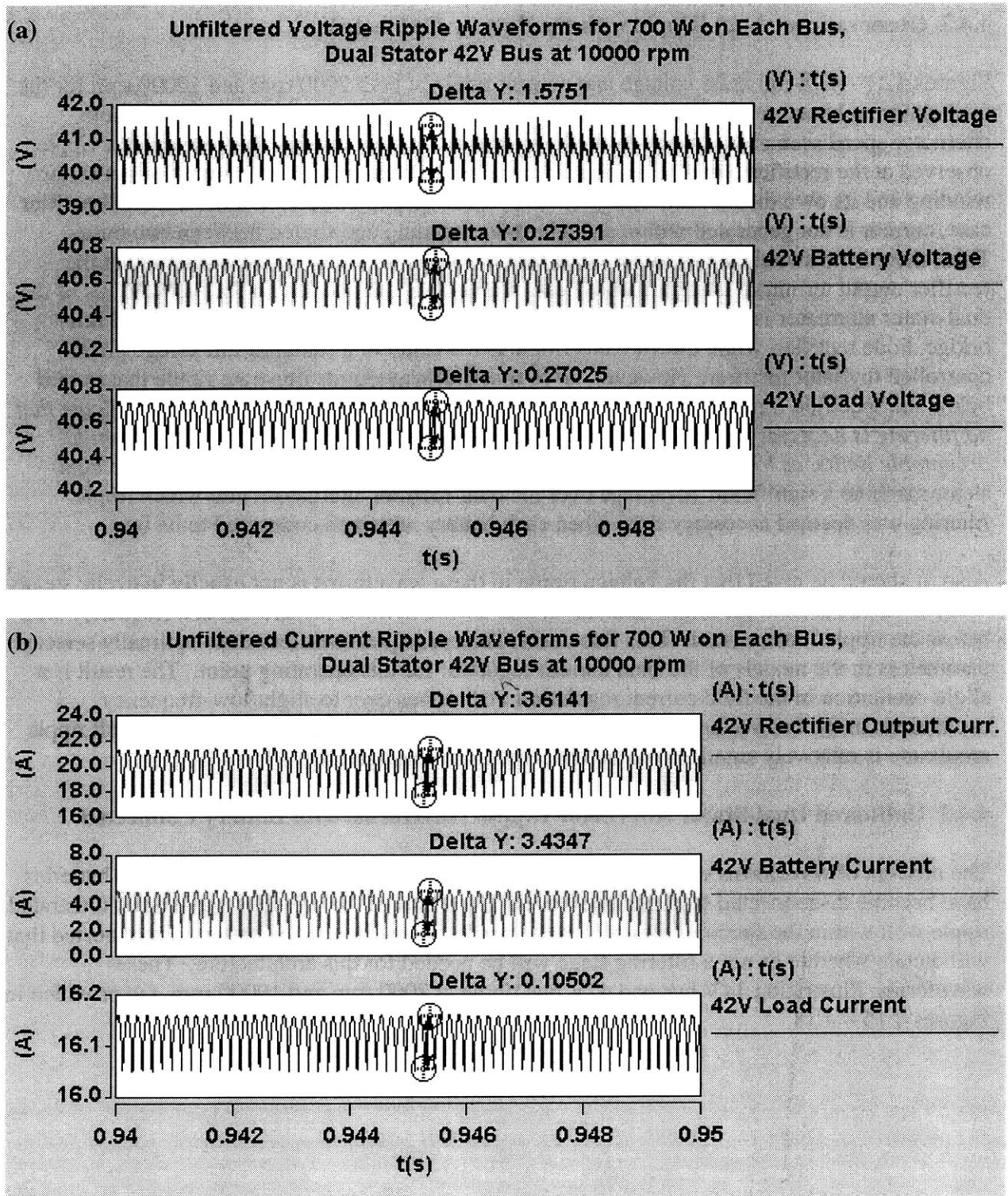


Figure 4.14: Unfiltered 42V bus ripple waveforms for the dual-stator architecture operating at 10000 rpm alternator shaft speed, with the battery *connected*: (a) voltage waveforms; (b) current waveforms.

4.4.2 Observations about Ripple with the Battery Connected

Figures 4.11 - 4.14 illustrate voltage and current ripple at both 2000 rpm and 10000 rpm for the dual-stator architecture. According to these waveforms, the ripple on both buses for both alternator speed scenarios is well within the specifications used within this research for ripple observed at the rectifier output terminals. This is because each bus has its own distinct stator winding and its own distinct full-bridge rectifier within the alternator. Unlike the dual-rectifier case, current is not generated within a single stator winding and shared between two buses. Thus, there is no switched current between the two buses, so voltage ripple observed at the rectifier output terminals is significantly less. The ripple that does occur for the 42V bus of the dual-stator alternator is the ordinary six-pulse voltage ripple that results from a typical full-bridge diode rectifier, while the 14V bus ripple is the result of a standard full-bridge phase-controlled thyristor rectifier. However, all four sets of waveforms illustrate ripple that is well below the specified limits. *Given this, the simulations performed for this research indicate that no filtering is necessary to attenuate voltage ripple with the dual-stator alternator down to acceptable limits, as long as each battery remains connected to its bus.* This gives the dual-stator machine a significant advantage over the dual-rectifier alternator, with which ripple filtering was deemed necessary even when each battery remained connected to its bus.

Also, it should be noted that the voltage ripple in these waveforms is not exactly in cyclic steady state, as can be seen in the slight fluctuation that occurs in these waveforms at a frequency well below the ripple fundamental. This fluctuation is a consequence of less-than-optimally selected parameters in the models of the field current regulator for this operating point. The result is a slight oscillation in the field current regulation that carries over to slight low-frequency oscillations in the bus voltage. The magnitude of the impact of this effect on the overall ripple amplitude is relatively small, as can be observed from the figures.

4.4.3 Unfiltered Dual-Stator Alternator Ripple Waveforms with Battery Connected

The next set of waveforms explores unfiltered voltage and current ripple after the two batteries have become disconnected from the two buses. Even though the previous waveforms illustrated ripple well within the specified limits, it is the ripple observed with the battery disconnected that will dictate whether or not a filtering stage will be needed for this architecture. These waveforms, illustrating 14V bus and 42V bus ripple at 2000 rpm and 10000 rpm, are provided in Figures 4.15 – 4.18.

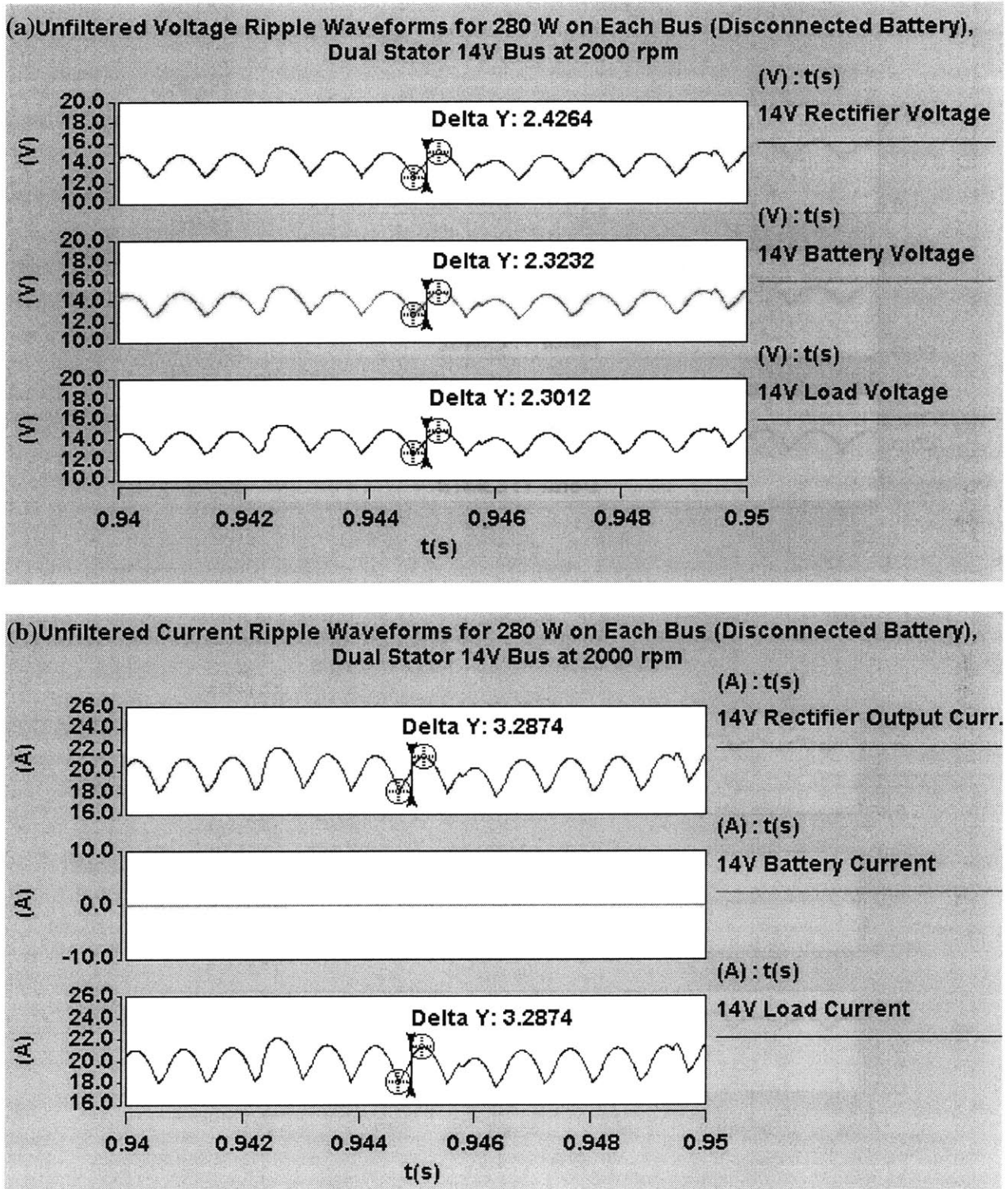


Figure 4.15: Unfiltered 14V bus ripple waveforms for the dual-stator architecture operating at 2000 rpm alternator shaft speed, with the battery *disconnected*: (a) voltage waveforms; (b) current waveforms.

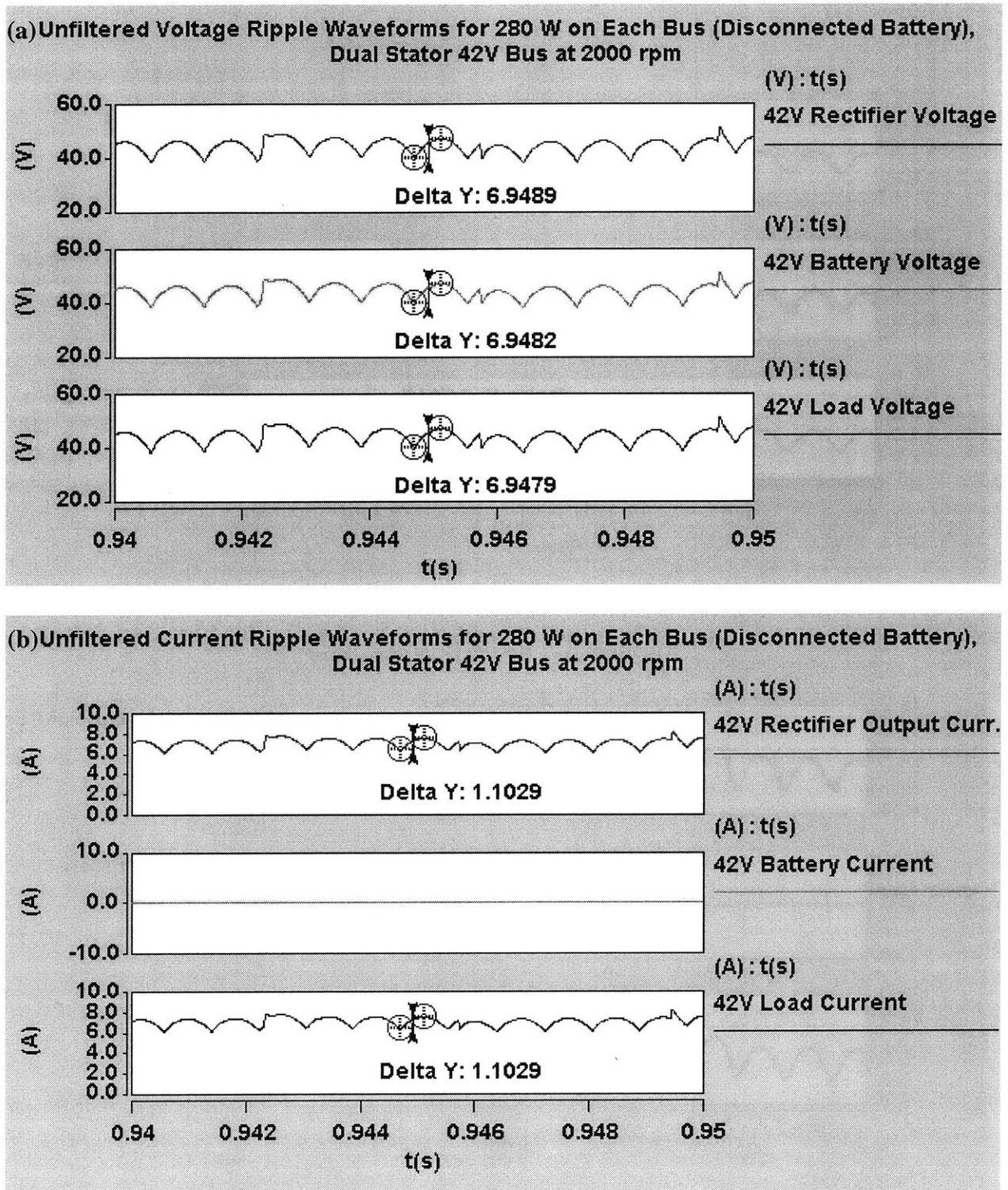


Figure 4.16: Unfiltered 42V bus ripple waveforms for the dual-stator architecture operating at 2000 rpm alternator shaft speed, with the battery *disconnected*: (a) voltage waveforms; (b) current waveforms.

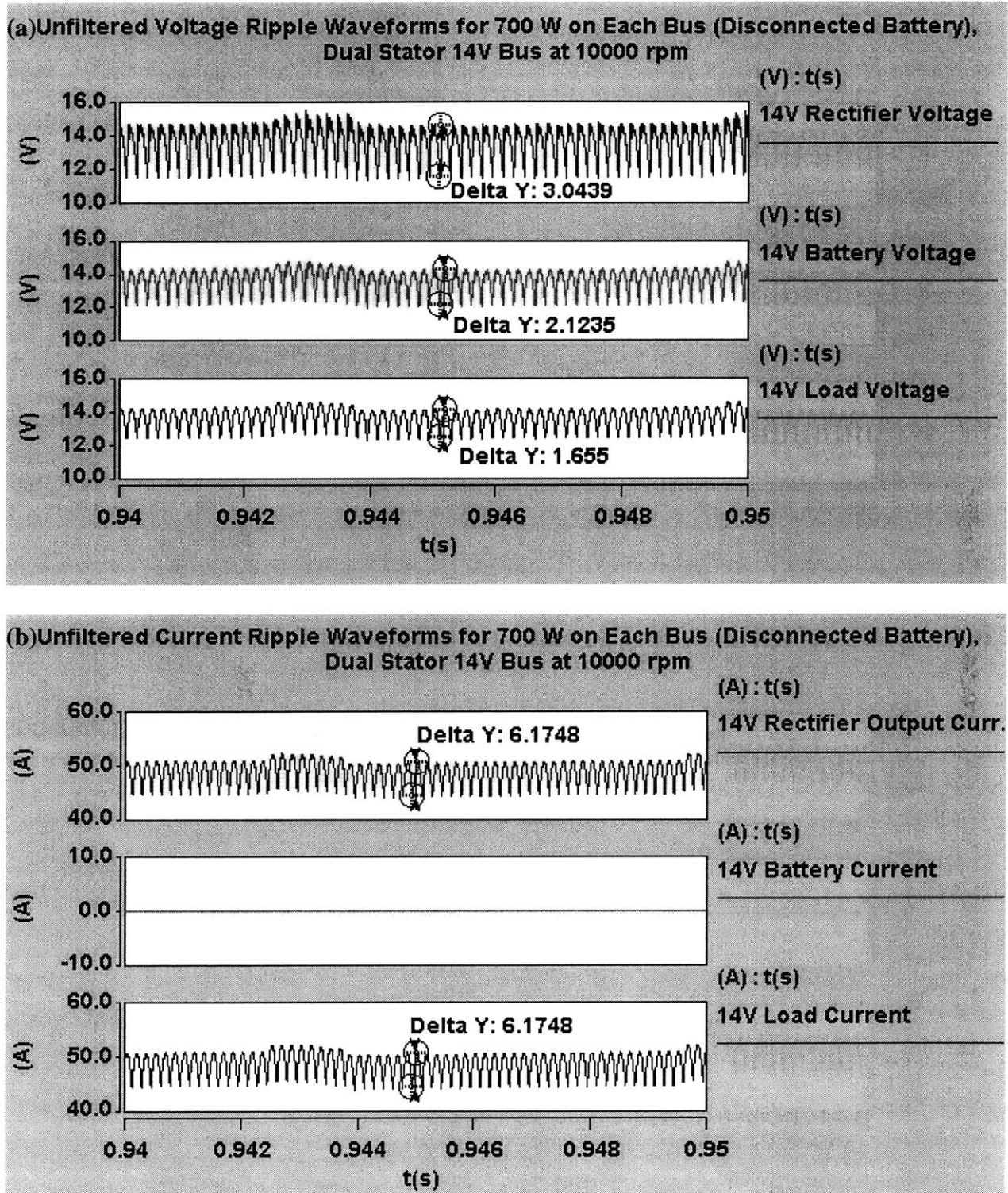


Figure 4.17: Unfiltered 14V bus ripple waveforms for the dual-stator architecture operating at 10000 rpm alternator shaft speed, with the battery *disconnected*: (a) voltage waveforms; (b) current waveforms.

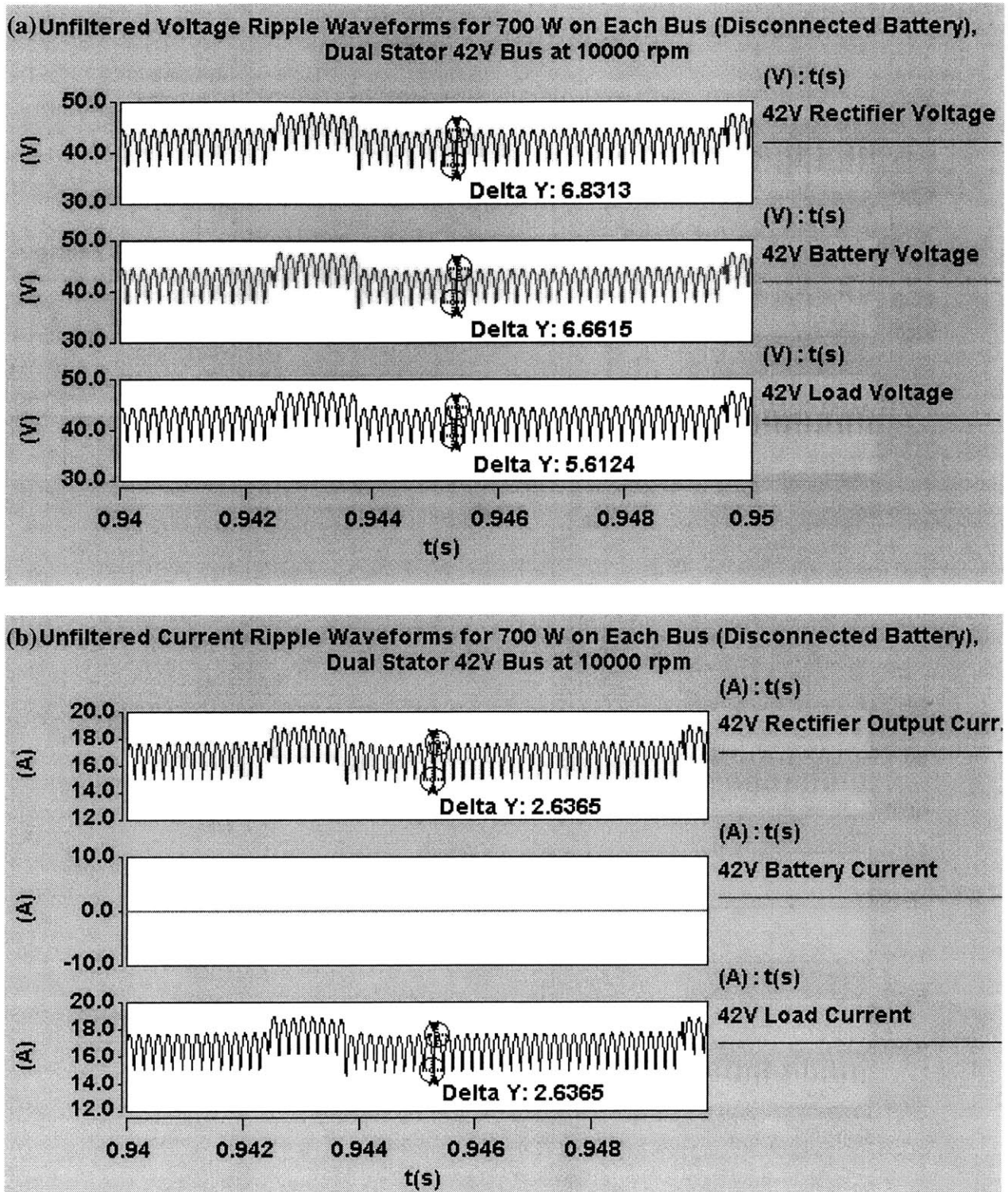


Figure 4.18: Unfiltered 42V bus ripple waveforms for the dual-stator architecture operating at 10000 rpm alternator shaft speed, with the battery *disconnected*: (a) voltage waveforms; (b) current waveforms.

4.4.4 Observations about Ripple with the Battery Disconnected

Figures 4.15 - 4.18 illustrate voltage and current ripple for the same scenarios depicted in Figures 4.11- 4.14, except that the batteries for each bus are disconnected. These figures illustrate that, unlike the cases with the battery connected, peak-to-peak voltage ripple on each bus is greater than the applicable limits of acceptability. Figure 4.15 shows 2.4 V_{pp} of voltage ripple on the 14V bus at 2000 rpm, which is well above the specified limit of 1 V_{pp}. Figures 4.16 and 4.18 illustrate ripple magnitudes at the 42V rectifier of 6.9 V_{pp} at 2000 rpm and 6.8 V_{pp} at 10000 rpm, both of which are well in excess of the allowed 4 V_{pp} for the 42V bus. Once again, a much smaller degree of attenuation occurs between the rectifier terminals and the load terminals, since ripple current resulting from the rectification process is no longer sunk by the now-disconnected battery. The observed peak-to-peak ripple also appears to occur at the fundamental ripple frequency (1200 Hz at 2000 rpm, 6000 Hz at 10000 rpm), indicating the presence of a large low-frequency fundamental voltage ripple harmonic. Thus, a filtering stage connected to the rectifier output terminals for each bus will be necessary to attenuate voltage ripple down to 4 V_{pp} on the 42V bus, and to 1 V_{pp} (2000 rpm) and 5 V_{pp} (10000 rpm) on the 14V bus.

4.5 Summary

This chapter sought to (1) describe the simulation models used to examine voltage ripple for dual-voltage alternators, and (2) present unfiltered voltage and current ripple results obtained from these simulation models. Models for a dual-stator and a single-stator (used in the dual-rectifier architecture) claw-pole alternator were briefly described in terms of the inductances and resistances that make up each model. The conventions used to model the battery and the distribution and utilization subsystems were also detailed. After previewing the simulation models, this chapter described the alternator shaft speed, bus loading, and battery connect / disconnect scenarios under which voltage ripple would be examined. Voltage and current ripple waveforms were then presented for the 14V and 42V buses at 2000 rpm and 10000 rpm alternator shaft speeds with the batteries both connected and disconnected, for both the dual-rectifier and dual-stator alternators. These waveforms clearly indicated that a voltage ripple filtering stage is needed for the dual-rectifier alternator, whether the batteries are connected or disconnected from their respective buses. The dual-stator alternator exhibited acceptable peak-to-peak voltage ripple with the batteries connected, but ripple grew beyond the limits of acceptability when the batteries were disconnected from their respective buses. Given that the automotive industry wishes to prevent damage to system loads in the event that the batteries become disconnected, a filtering stage was deemed necessary for the dual-stator architecture as well. Thus, the primary achievement of this chapter was to illustrate the necessity of voltage ripple filters for both dual-voltage architectures, given the voltage ripple acceptability limits presented in Chapter 3. The next chapter will focus upon the design of ripple filtering stages for the 14V and 42V buses for both dual-voltage architectures, such that filter size and cost can be compared for the two architectures with both meeting the given minimum performance specifications for voltage ripple.

Ripple Filtering for Dual-Voltage Alternators

Chapter 4 illustrated the degree to which voltage ripple exceeds the specified limits for both buses when the batteries become disconnected. This chapter focuses upon designing filters to attenuate this voltage ripple down to acceptable margins for this failure condition. While various active and passive filter topologies are possible, this research explores only single stage passive filters for purposes of reduced cost and simplicity. The goal of this ripple examination is to establish a proof of concept as to whether reasonable passive filters can be designed to attenuate voltage ripple for dual-voltage alternators. This is because passive filters do not require extra semiconductor components and thus have the potential to be the most cost-effective filtering solution, if they can be designed to be of reasonable sizes and weights.

The following analysis will first identify a filter topology and determine the necessary inductances, capacitances, and resistances to achieve the desired ripple attenuation at the output terminals of each rectifier. It will then size the passive components based on the desired voltage rating and current through each component. Ultimately, the sizing of these components will help determine the relative weights and costs of the dual-rectifier and dual-stator architectures and will aid in comparing the desirability of these two architectures.

5.1 Passive Filter Design

As described above, this thesis performs a first order examination of passive filtering topologies to determine their efficacy in filtering voltage ripple for dual-voltage alternators. Passive filters provide the simplest potential filtering solution, because they can be implemented without the inclusion of costly semiconductor devices and control hardware. However, passive filters are desirable only to the degree that they can achieve the desired attenuation performance while adding minimal weight and cost to the system. This work attempts to quantify the weight and cost that passive filtering stages add to the automotive electrical system in order to evaluate the appropriateness of passive filters for this application.

5.1.1 Design Considerations

The filter design process was approached with the goal of using the simplest filter topology with the smallest number of components that can be used to sufficiently attenuate voltage ripple for each dual-voltage alternator architecture. Chapter 4 illustrated that peak-to-peak voltage ripple with the dual-rectifier alternator is very large in instances with the battery either connected to or disconnected from each bus. It also illustrated that dual-rectifier alternator voltage ripple is often dominated by reverse-recovery transients that occur each time a device in the rectifier bridge switches on. These high frequency transients are most effectively attenuated by a filter with at

least a second-order rolloff which, when compared to a first-order filter, allows for a higher corner frequency (and thus a smaller filter size) for the same level of attenuation. However, higher order filters require more intricate designs with greater numbers of components. Thus, a second-order filter with a minimum number of components is appropriate for the dual-rectifier alternator to produce a significant degree of rolloff while minimizing the component count and complexity of the filter.

However, Chapter 4 also pointed out that voltage ripple with the dual-stator alternator is significant only when the battery becomes disconnected from either bus. In this case peak-to-peak voltage ripple is not dominated by reverse-recovery transients, and the degree to which peak-to-peak ripple violates the specifications is much smaller than with the dual-rectifier alternator. Thus, this chapter will show that the simple addition of capacitance to each bus of the dual-stator alternator is able to attenuate peak-to-peak ripple down to the specified limits with the battery disconnected.

5.1.2 Survey of Dual-Rectifier Filter Topologies

This research examined several different passive filter topologies for the dual-rectifier alternator based on the number and placement of the passive components and on the attenuation characteristic that is achievable with each filter. Phelps and Tate discuss nine different passive filter topologies, six single-stage filters and three dual-stage filters, for input filter applications. [20] Each filter topology has a unique damping characteristic, a different number of poles and zeros, and a different level of complexity.

In the interest of choosing a simple filter topology with a low parts count, only the single-stage filters were examined for this application (see Figure 5.1). Filter (b) exhibits only a -20 dB per decade roll-off at high frequencies due to the presence of a zero in the transfer function, so this filter was immediately eliminated as a potential solution. Filter (a) exhibits a low parts count and low dc losses, but it contains no resistance (ignoring the component parasitics) and thus provides no damping for the filter. To remedy this, filter (c) provides a damping resistor in series with the inductor, and filter (d) provides a damping resistor in parallel with the load capacitor. However, the damping resistor for filter (c) is placed directly in the dc current path, so dc losses could become very large. The load damping filter (filter (d)) provides a possible solution, assuming the load resistance is sufficiently small. If the load resistance is significantly smaller than the damping resistance, then the total parallel resistance remains dominated by the load resistance and dc current is delivered primarily to this load resistance. If, however, the damping resistance is set sufficiently low, the damping resistance will begin to dominate the load resistance. The damping ratio ζ is inversely proportional to the damping resistance, so smaller resistances are used to achieve higher levels of damping. Thus, a tradeoff exists between the level of damping and the degree to which the damping resistance dominates the load resistance, making this filter potentially unattractive.

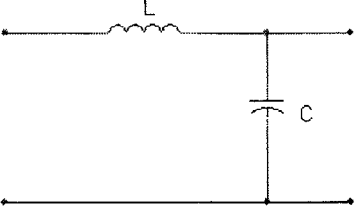
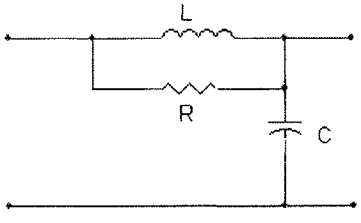
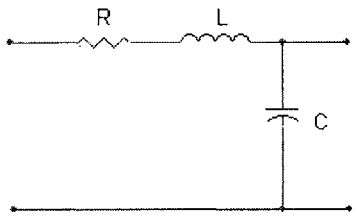
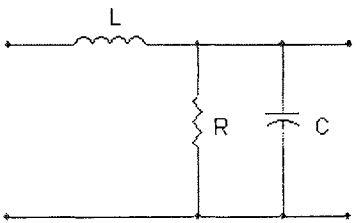
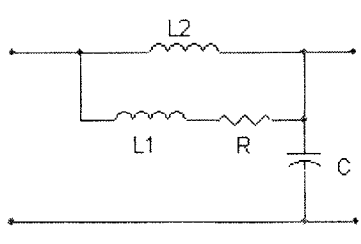
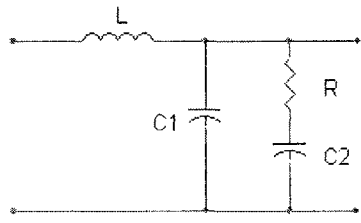
(a)	Topology	Gain Expression
	$\frac{1}{s^2 LC + 1}$	
	$\frac{s \frac{L}{R} + 1}{s^2 LC + s \frac{L}{R} + 1}$	
	$\frac{1}{s^2 LC + sRC + 1}$	
	$\frac{1}{s^2 LC + s \frac{L}{R} + 1}$	
	$\frac{s \frac{L_1 + L_2}{R} + 1}{s^3 \frac{L_1 L_2}{R} C + s^2 L_2 C + s \frac{L_1 + L_2}{R} + 1} \approx \frac{1}{s^2 L_1 C + sRC + 1}$	
	$\frac{sRC_2 + 1}{s^3 LRC_1 C_2 + s^2 L(C_1 + C_2) + sRC_2 + 1} \approx \frac{1}{s^2 LC_1 + s \frac{L}{R} + 1}$	

Table 5.1: Single-stage passive filter topologies examined as potential dual-voltage alternator filtering solutions (as discussed in [20]).

The two modified single-stage filters (filters (e) and (f)) provide more efficient damping methods and are thus more viable options for this application. Both maintain -40 dB / decade attenuation at high frequencies even with the presence of a zero in the transfer function. Filter (e) is similar to filter (c) in that it provides damping with a series damping resistor. However, the larger inductor L_2 carries the bulk of the dc current and ensures that the damping resistor remains out of the dc current path, minimizing dc losses. As L_2 is sized sufficiently larger than L_1 , the zero in the transfer function cancels with a pole and the transfer function becomes nearly second-order. Similarly, filter (f) is comparable to filter (d), except that capacitor C_2 prevents the damping resistor from competing with the load resistance for dc current. Thus filters (e) and (f) resolve the difficulties encountered with filters (b) and (d), while providing sufficient damping capabilities and maintaining two-pole rolloff at high frequencies. Phelps and Tate state that filter (e) has a lower output impedance than filter (f) for equal component volumes and equal damping, giving filter (e) an advantage over filter (f). Thus, this research will examine the application of the filter (e) topology to ripple filter designs for the dual-rectifier and dual-stator architectures.

5.1.3 Dual-Rectifier Filter Design Algorithm

Once the filter topology was chosen, an iterative process was performed for the dual-rectifier architecture to select the inductance, capacitance, and resistance values for each architecture's ripple filter. The first step was to retrieve a sample of the numerical voltage values representing unfiltered ripple for the disconnected battery simulations performed in Saber. The 14V ripple samples were taken from the 2000 rpm disconnected battery simulations for each architecture, since this case has the most demanding attenuation requirement (1 Vpp) and thus represents the worst case filtering scenario. By contrast, the 42V ripple samples were taken from the 10000 rpm disconnected battery simulations. The 42V bus's ripple attenuation requirement (4 Vpp) is independent of alternator shaft speed, so the worst case filtering scenario occurs at 10000 rpm where unfiltered ripple is greatest.

The ripple voltage values for each architecture were then fed into a MATLAB script which iteratively selected real, integer pole values for a two-pole filter. (See Appendix B.) For each iteration, MATLAB created a numerical filter based on the two pole values for that iteration. The filter was then applied to the unfiltered ripple sample using a MATLAB numerical filtering function, and the now-filtered ripple output sample was saved. The peak-to-peak ripple present in this ripple sample was measured, and the pole pair was marked acceptable if the peak-to-peak ripple was below the limits for the applicable bus. If the filtered peak-to-peak ripple remained above the acceptable limit, the pole pair was marked unacceptable. A new, lower pole pair was then chosen, and the iteration repeated.

Each time a particular pole pair iteration was identified as acceptable, an initial set of component values was chosen based on the values of the two poles. Recall the filter (e) simplified gain expression from Table 5.1, which occurs for a sufficiently large value of L_2 :

$$H(s)_{simplified} = \frac{1}{s^2 L_1 C + sRC + 1} \quad (5.1)$$

The poles for this transfer function are found to be:

$$poles = \frac{-RC \pm \sqrt{R^2 C^2 - 4L_1 C}}{2L_1 C} \quad (5.2)$$

If a value of the damping resistor is chosen, values for the inductance and capacitance can be calculated based upon the chosen pole values for the given iteration. The average value of the two poles can be expressed as follows:

$$pole_{avg} = -\frac{RC}{2L_1 C} = -\frac{R}{2L_1} \quad (5.3)$$

Thus, the damping leg inductance L_1 is calculated to be:

$$L_1 = -\left(\frac{R}{2 \cdot pole_{avg}} \right) \quad (5.4)$$

The difference between the lower pole and the average of the pole values is equivalent to the radical portion of the expression in Equation (5.2) as follows:

$$\begin{aligned} pole_{lower} - pole_{avg} &= -\frac{\sqrt{R^2 C^2 - 4L_1 C}}{2L_1 C} \\ &= -\sqrt{\frac{R^2}{4L_1^2} - \frac{1}{L_1 C}} \end{aligned} \quad (5.5)$$

Using Equation (5.5), an expression relating capacitance to L_1 , the lower pole, and the average of the two poles can be derived.

$$\begin{aligned} (pole_{lower} - pole_{avg})^2 &= \frac{R^2}{4L_1^2} - \frac{1}{L_1 C} \\ &= (pole_{avg})^2 - \frac{1}{L_1 C} \end{aligned} \quad (5.6)$$

$$\begin{aligned}\frac{1}{L_1 C} &= (pole_{avg})^2 - (pole_{lower} - pole_{avg})^2 \\ &= -(pole_{lower})^2 + 2 pole_{lower} pole_{avg}\end{aligned}\quad (5.7)$$

$$C = \frac{1}{L_1 pole_{lower} (2 pole_{avg} - pole_{lower})}\quad (5.8)$$

Thus, the algorithm selected component values by specifying a damping resistance ($R = 100 \text{ m}\Omega$ in this application) and then used Equations (5.4) and (5.8) to select the inductance L_1 and the capacitance C . However, these equations were derived using the simplified second-order version of the transfer function, which assumes that L_2 is sufficiently large to produce a pole – zero cancellation in the original transfer function. The algorithm determines an acceptable value for L_2 by performing a series of sub-iterations to gradually increase L_2 until an acceptable value is found. For each chosen L_2 (and using the values for R , C , and L_1 decided previously), the filter (e) transfer function is used to filter the unfiltered ripple sample. If the peak-to-peak ripple in the filtered output sample is below the specified limits, an acceptable L_2 value has been chosen. If not, L_2 is doubled and the iteration repeats until an acceptable value for L_2 has been found.

The output of the completed MATLAB algorithm was a table of pole pair values and their corresponding inductance, capacitance, and damping resistance values describing different filter designs that produced the required attenuation characteristics. From this table, one pole pair / component value set was selected for actual implementation. Many component value sets included either very large inductors and very small capacitors, or very large capacitors and very small inductors. Thus, this selection looked for a component set in which both the capacitors and inductors were as reasonably sized as possible.

5.1.4 Design Validation of the Dual-Rectifier Ripple Filter in Saber

The final result of this design process was a set of pole pair values and their corresponding inductance, capacitance, and resistance values used to describe dual-rectifier filter designs that attenuated the input ripple sample down to the specified limits. However, these component values were intended only to provide a starting point for determining the eventual component values that will be applied to the final filter designs. This is because the MATLAB algorithm makes two simplifications that affect the accuracy of the component values deemed acceptable.

- Only ideal components are used, so loss parameters such as equivalent series resistance (ESR) are ignored.
- It is assumed that the filter does not significantly load the rectifier, such that the unfiltered voltage ripple at the rectifier output terminals does not change as filters are applied to the rectifier output terminals.

In order to achieve a final set of component values, the values provided by the MATLAB script were tested within the appropriate Saber simulation models for each alternator architecture. The Saber filter models included approximate ESR values for the inductors and capacitors such that the filter's attenuation characteristics could be more accurately evaluated with non-ideal components. While each inductor could be designed to have a given ESR value, the capacitor ESR values were chosen based on the specifications of off-the-shelf capacitors. Once a capacitor with a given ESR value was chosen and tested via simulation, ripple current through the capacitor was observed to see whether the ripple current fell within the rating of the chosen capacitor. When ripple current was observed to be above the rating for the chosen capacitor, other capacitors with higher ripple current ratings were sought. This was met with limited success in simulation, since capacitors with higher ripple current ratings also typically had lower ESR values, which served to *increase* the amount of ripple current observed through the capacitor in simulation (see section 5.3.9). A second solution involved connecting capacitors in parallel to split the ripple current among the parallel paths. This method was met with greater success, as off-the-shelf capacitors were located which were able to handle the amount of ripple current shunted through each parallel-connected capacitor. In the end, the overall goal of this validation process was to use Saber simulations to fine-tune the MATLAB algorithm's filter design results, in order to produce both acceptable attenuation characteristics and acceptable ripple current magnitudes through the filter shunt capacitors.

5.1.5 Ripple Capacitor Selection for the Dual-Stator Architecture

Since only capacitors were needed to filter dual-stator voltage ripple down to the specified limits, the filter design process for the dual-stator alternator was much simpler than for the dual-rectifier alternator. Like the dual-rectifier filter design process, capacitors for the dual-stator alternator were sized primarily based upon the amount of ripple current that needed to be sunk through the capacitors. An iterative trial-and-error process using specifications for commercially available capacitors was performed in Saber to determine the appropriate filter capacitance for each bus. For the dual-stator 42V bus, single capacitors could not be found which produced the appropriate level of attenuation and had a sufficient ripple current rating, so parallel-connected capacitors were used to balance the need for attenuation with the ripple current capabilities of the selected capacitor. Additional resistance was also inserted in series with the capacitors for each bus in order to reduce the amount of ripple current sunk by the capacitor, and thereby bring the RMS ripple current sunk by the capacitor in line with each capacitor's ripple current rating. Ultimately capacitor solutions were located which possessed enough capacitance to sufficiently attenuate voltage ripple, and also exhibited enough ripple current capability to sink the amount of RMS ripple current required for the desired level of attenuation.

¹ The technical issues affecting the selection of specific aluminum electrolytic capacitors for each filter are discussed in more detail in section 5.3.9.

5.1.6 Final Dual-Rectifier and Dual-Stator Filter Designs

The final ripple filter designs for the 14V and 42V buses of the dual-rectifier architecture are provided in Figure 5.1, and corresponding filter designs for the dual-stator architecture are provided in Figure 5.2. Note that the large inductor L_2 in each dual-rectifier filter design carries the majority of dc current being delivered to each bus, while the small inductor L_1 in the damping leg carries the majority of ripple current. Each filter also contains multiple parallel shunt capacitors, such that the ripple current sunk to ground per capacitor is reduced to levels consistent with ripple current ratings of the off-the-shelf capacitors being considered. Section 5.3 details the dc and ripple currents that pass through each filter component for each architecture, along with the impact that these currents have on the design and selection of the capacitors and inductors.

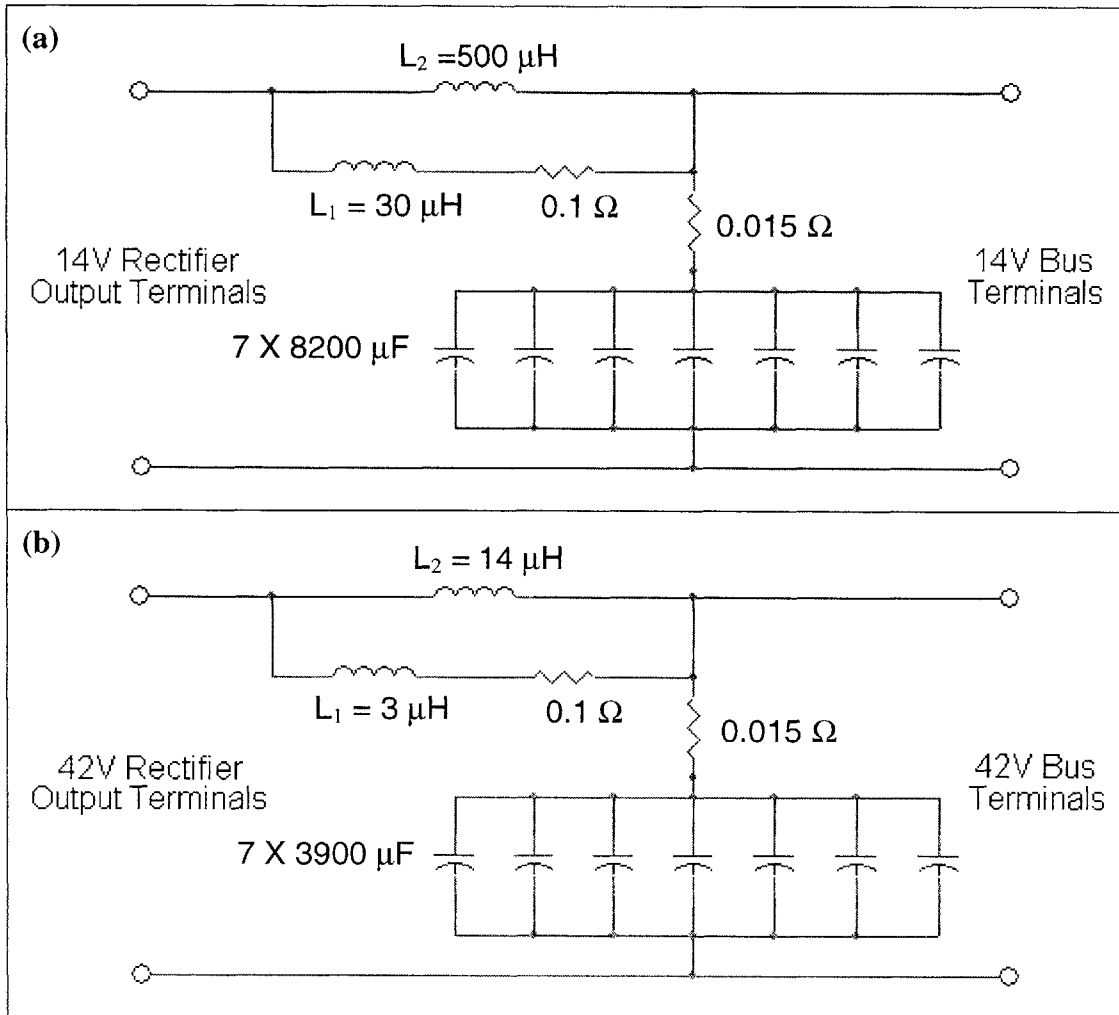


Figure 5.1: Final voltage ripple filter designs for the dual-rectifier architecture: (a) 14V filter; (b) 42V filter.

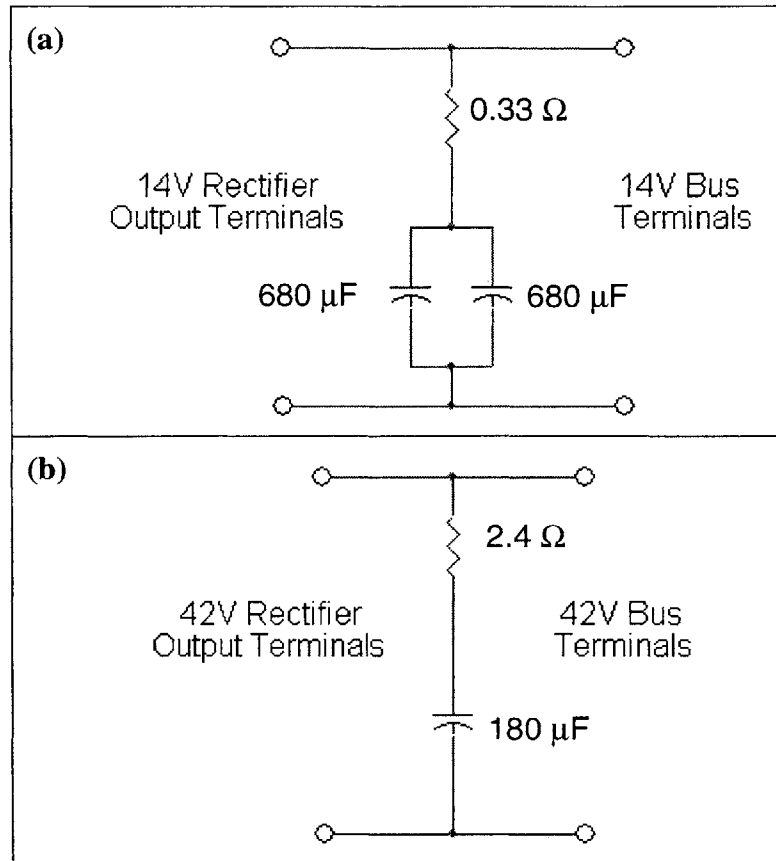


Figure 5.2: Final voltage ripple filter designs for the dual-stator architecture: (a) 14V filter; (b) 42V filter.

5.2 Filtered Voltage Ripple Results

The following waveforms illustrate the voltage ripple attenuation achieved using the filters in Figures 5.1 and 5.2 with the dual-rectifier and dual-stator alternators. Recall that each filter is connected directly to the rectifier output terminals of the appropriate bus, as illustrated in Figures 2.1 and 2.2. These waveforms portray voltage ripple observed at the filter output terminals at the point where the filter is connected to the rest of the bus. Waveforms are provided for both the 2000 rpm and 10000 rpm simulation cases to illustrate compliance with specifications at both idle and high alternator shaft speeds. Waveforms are also provided for both the connected battery and disconnected battery simulation scenarios to illustrate compliance with specifications under the worst-case disconnected battery condition.

5.2.1 Filtered Dual-Rectifier Alternator Voltage Ripple Waveforms

Figures 5.3 – 5.6 illustrate filtered voltage ripple observed with the dual-rectifier alternator at both 2000 rpm and 10000 rpm with the batteries both connected and disconnected.

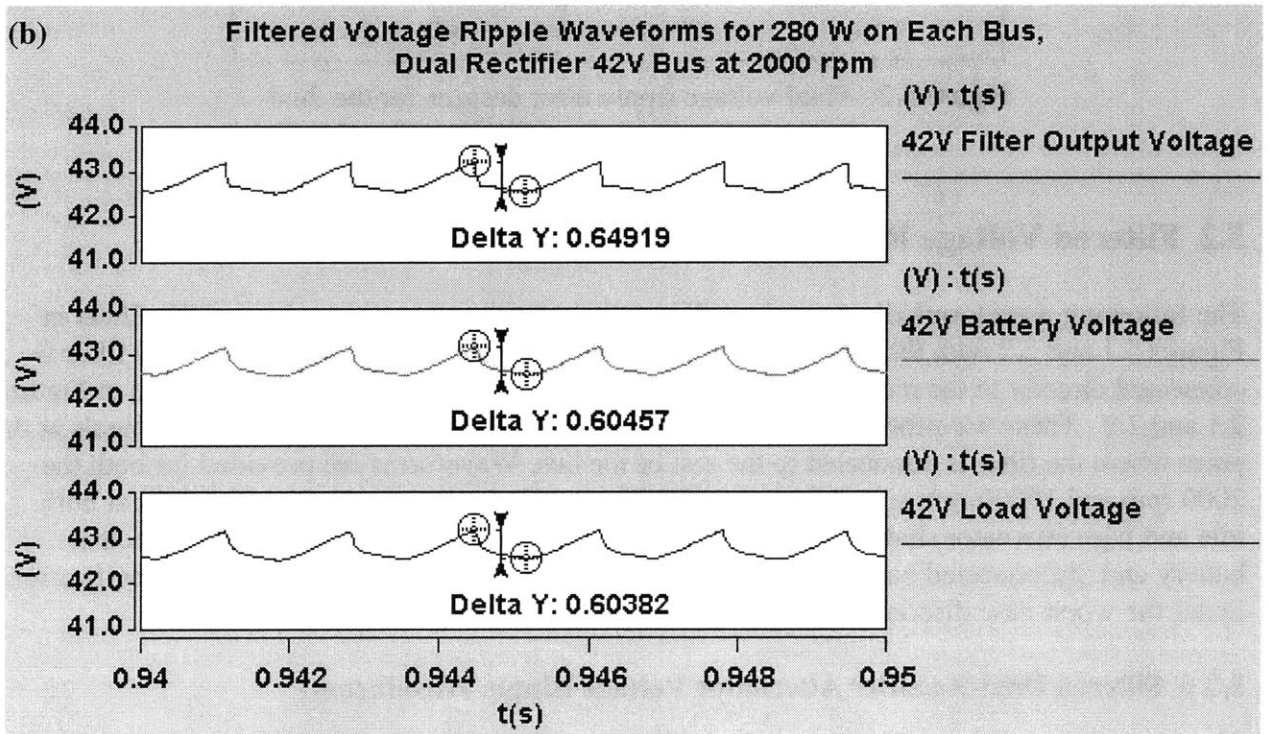
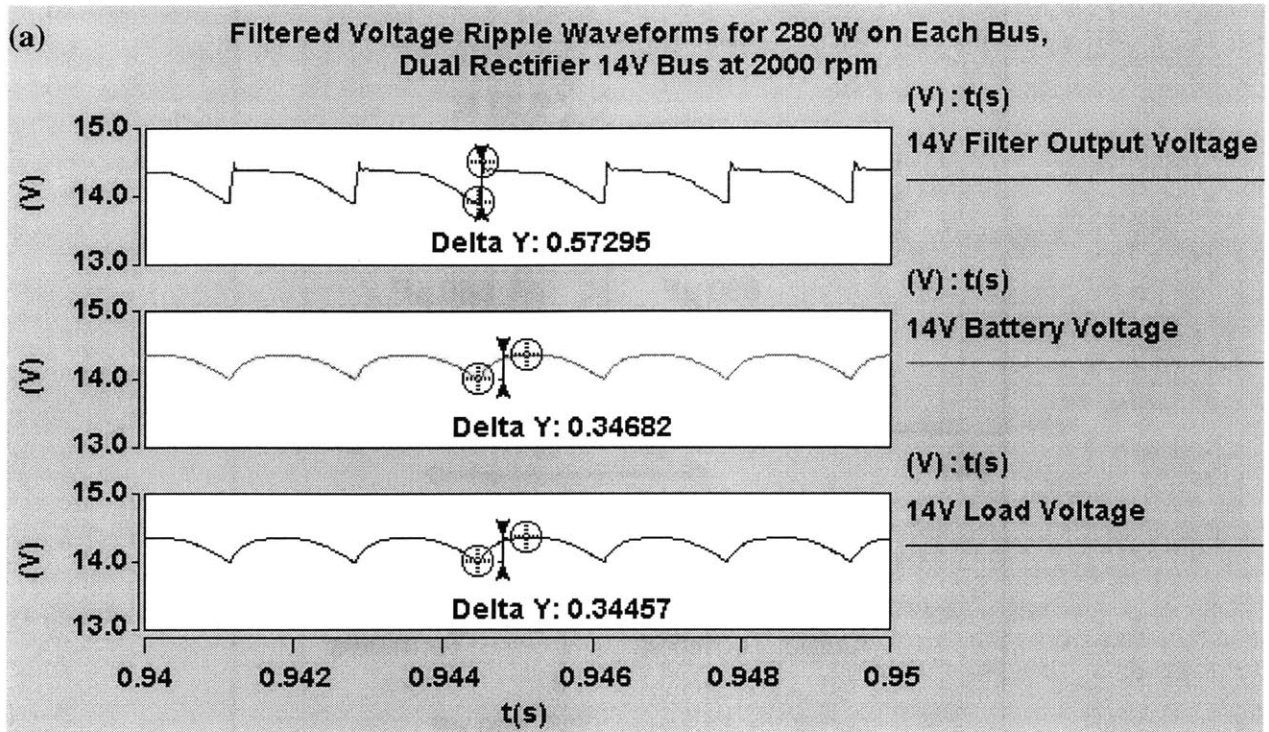


Figure 5.3: Filtered ripple waveforms for the dual-rectifier architecture operating at 2000 rpm alternator shaft speed, with the battery *connected*: (a) 14V bus voltage waveforms; (b) 42V bus voltage waveforms.

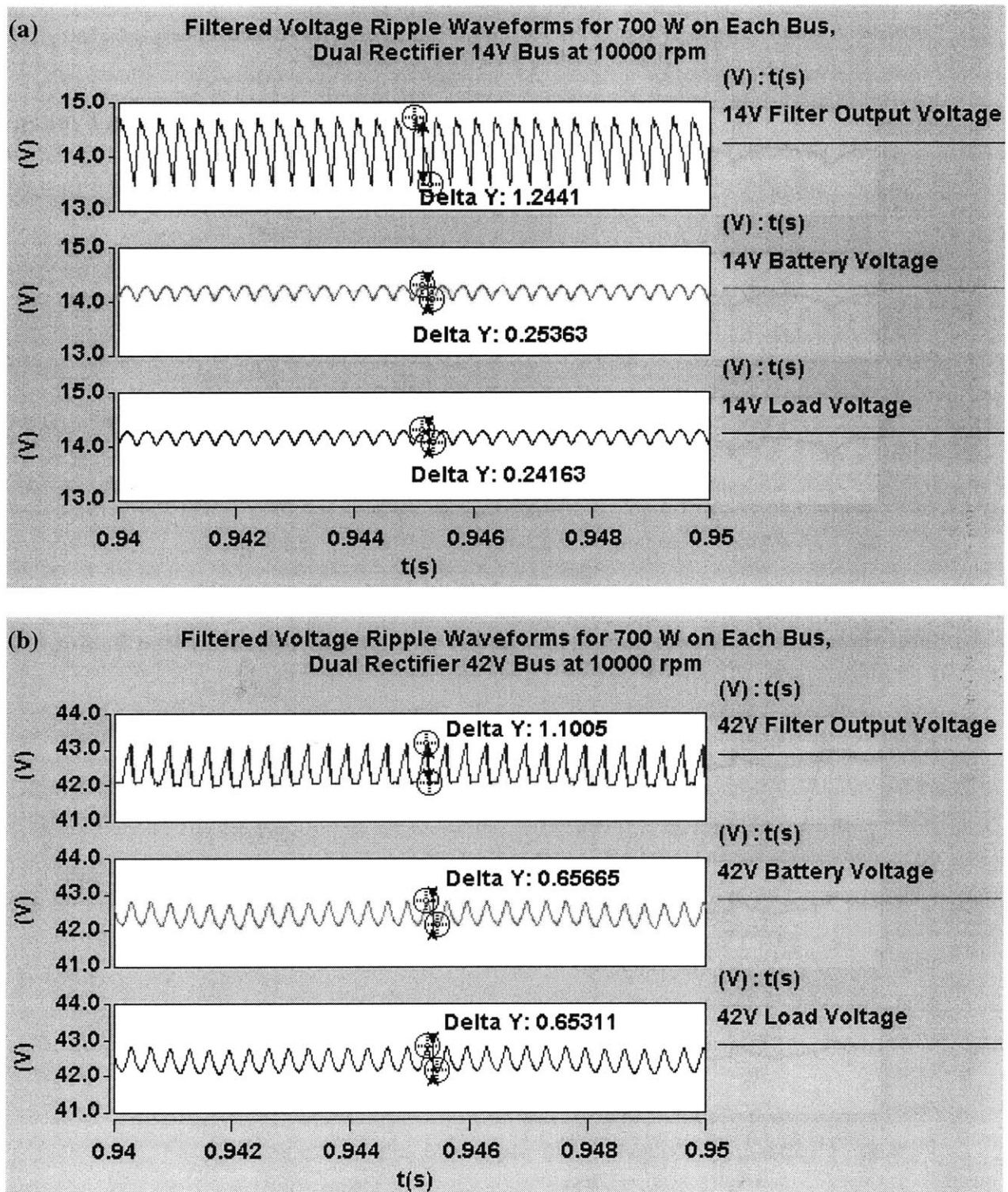


Figure 5.4: Filtered ripple waveforms for the dual-rectifier architecture operating at 10000 rpm alternator shaft speed, with the battery *connected*: (a) 14V bus voltage waveforms; (b) 42V bus voltage waveforms.

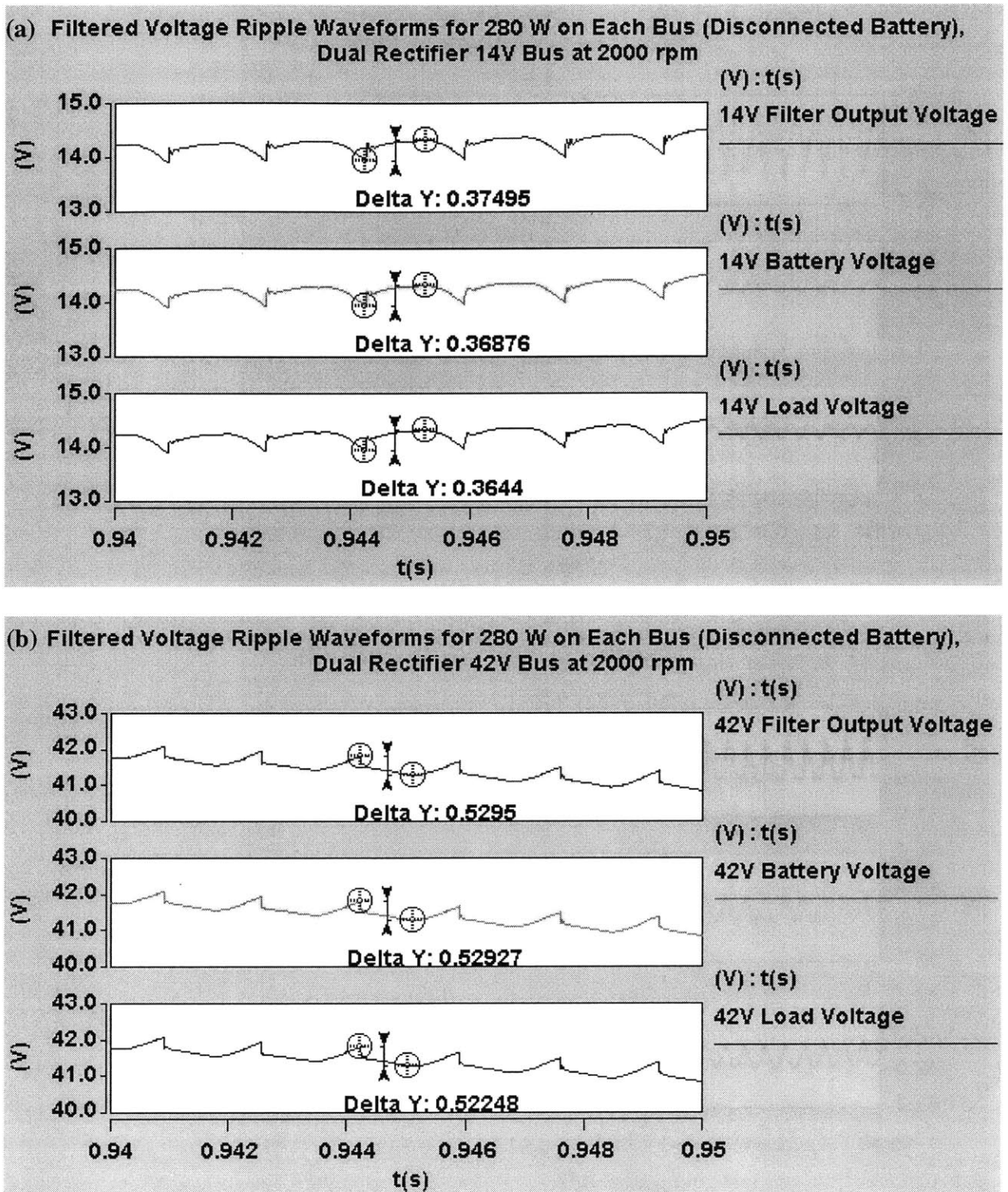


Figure 5.5: Filtered ripple waveforms for the dual-rectifier architecture operating at 2000 rpm alternator shaft speed, with the battery *disconnected*: (a) 14V bus voltage waveforms; (b) 42V bus voltage waveforms.

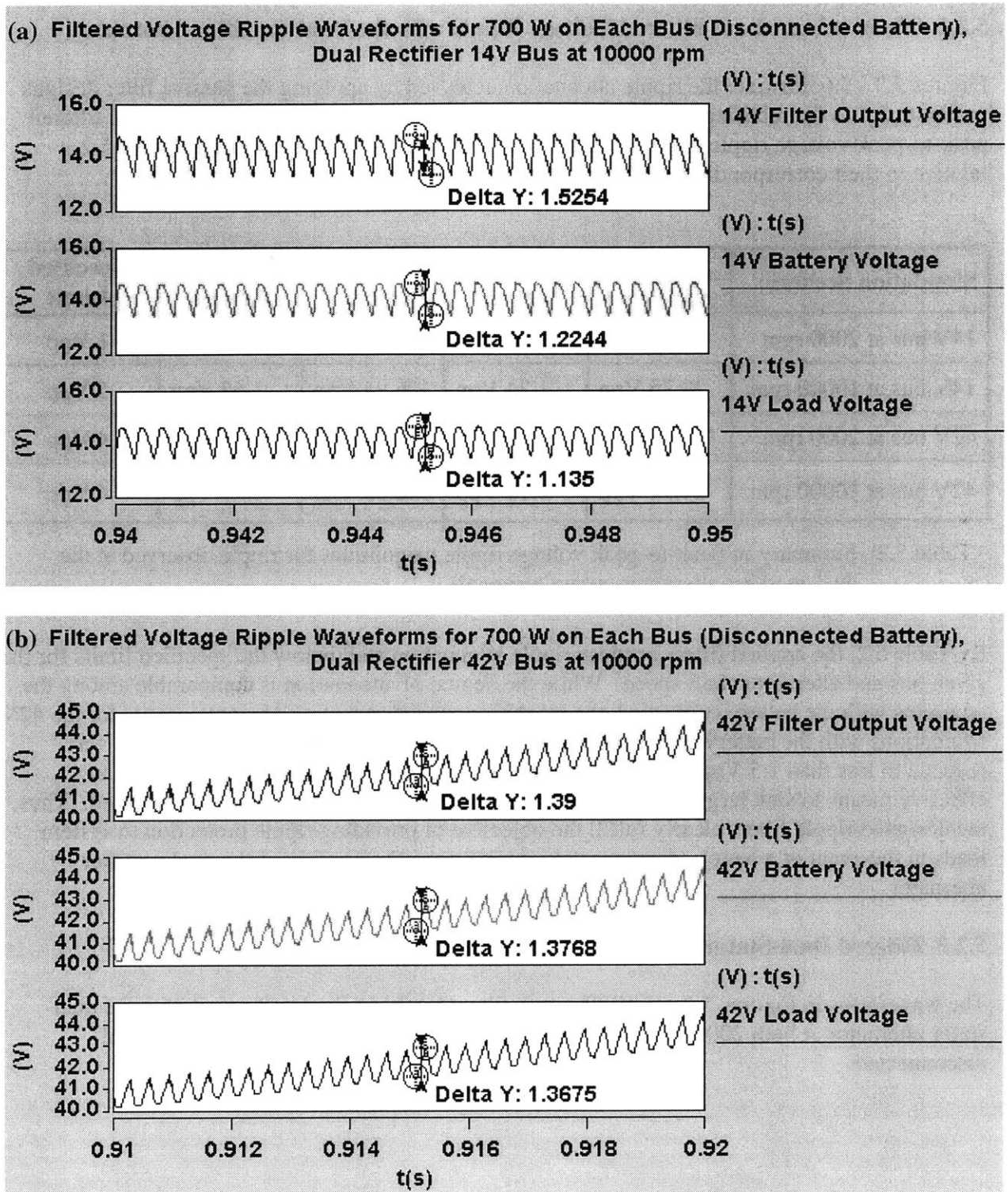


Figure 5.6: Filtered ripple waveforms for the dual-rectifier architecture operating at 10000 rpm alternator shaft speed, with the battery *disconnected*: (a) 14V bus voltage waveforms; (b) 42V bus voltage waveforms.

5.2.2 Observations about Filtered Voltage Ripple with the Dual-Rectifier Alternator

Figures 5.3 - 5.6 illustrate the ripple attenuation achieved by applying the passive filter designs in Figure 5.1 to the rectifier outputs of the dual-rectifier alternator. The magnitudes of filtered peak-to-peak voltage ripple observed from these waveforms are summarized in Table 5.2, relative to their corresponding unfiltered voltage ripple magnitudes from Chapter 4.

Simulation Scenario	Battery Connected		Battery Disconnected		Specified Limit
	<i>Unfiltered</i>	<i>Filtered</i>	<i>Unfiltered</i>	<i>Filtered</i>	
14V bus at 2000 rpm	26.62 Vpp	0.57 Vpp	18.33 Vpp	0.37 Vpp	1 Vpp
14V bus at 10000 rpm	20.75 Vpp	1.24 Vpp	106.94 Vpp	1.53 Vpp	5 Vpp
42V bus at 2000 rpm	24.66 Vpp	0.65 Vpp	122.18 Vpp	0.53 Vpp	4 Vpp
42V bus at 10000 rpm	21.94 Vpp	1.10 Vpp	182.38 Vpp	1.39 Vpp	4 Vpp

Table 5.2: Summary of peak-to-peak voltage ripple magnitudes for ripple observed at the dual-rectifier alternator output terminals.

By Table 5.2, the applied filters produce ripple attenuation well below the specified limits for the given bus and alternator shaft speed. While the degree of attenuation is comparable among the scenarios with the battery connected, the most pronounced reduction of ripple occurs for the 42V simulations with the battery disconnected, where over 100 Vpp of ripple in both cases was reduced to less than 1.5 Vpp. This is because the filter takes over the battery's role as an effective means to sink large ripple current magnitudes while the battery is disconnected. Thus, the designed ripple filters clearly fulfill the objective of providing ripple protection to system loads in the event of a battery disconnection during normal operation of the dual-rectifier alternator.

5.2.3 Filtered Dual-Stator Alternator Voltage Ripple Waveforms

The waveforms in Figures 5.7 – 5.10 illustrate filtered voltage ripple observed with the dual-stator alternator at both 2000 rpm and 10000 rpm with the batteries both connected and disconnected.

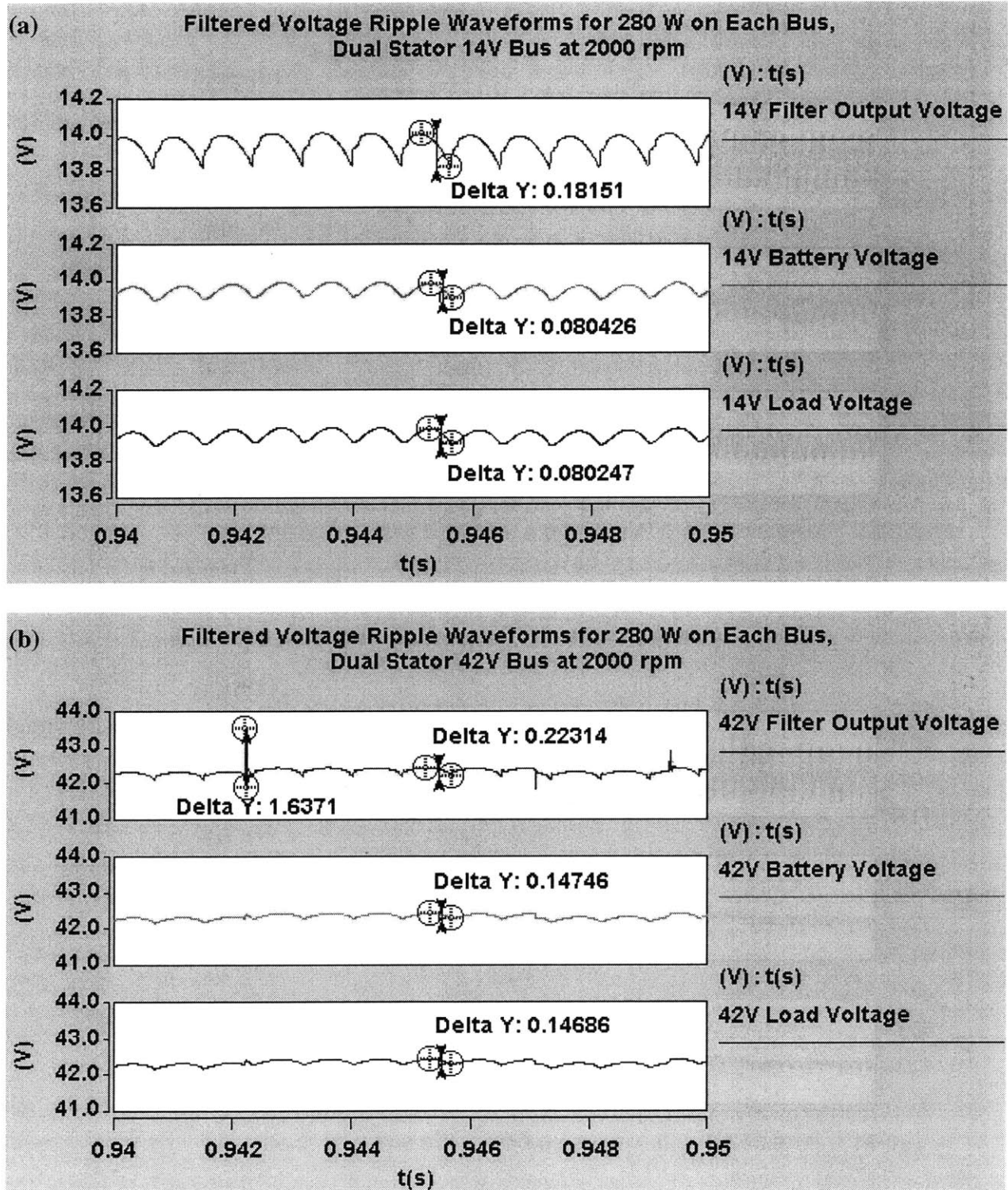


Figure 5.7: Filtered ripple waveforms for the dual-stator architecture operating at 2000 rpm alternator shaft speed, with the battery *connected*: (a) 14V bus voltage waveforms; (b) 42V bus voltage waveforms.

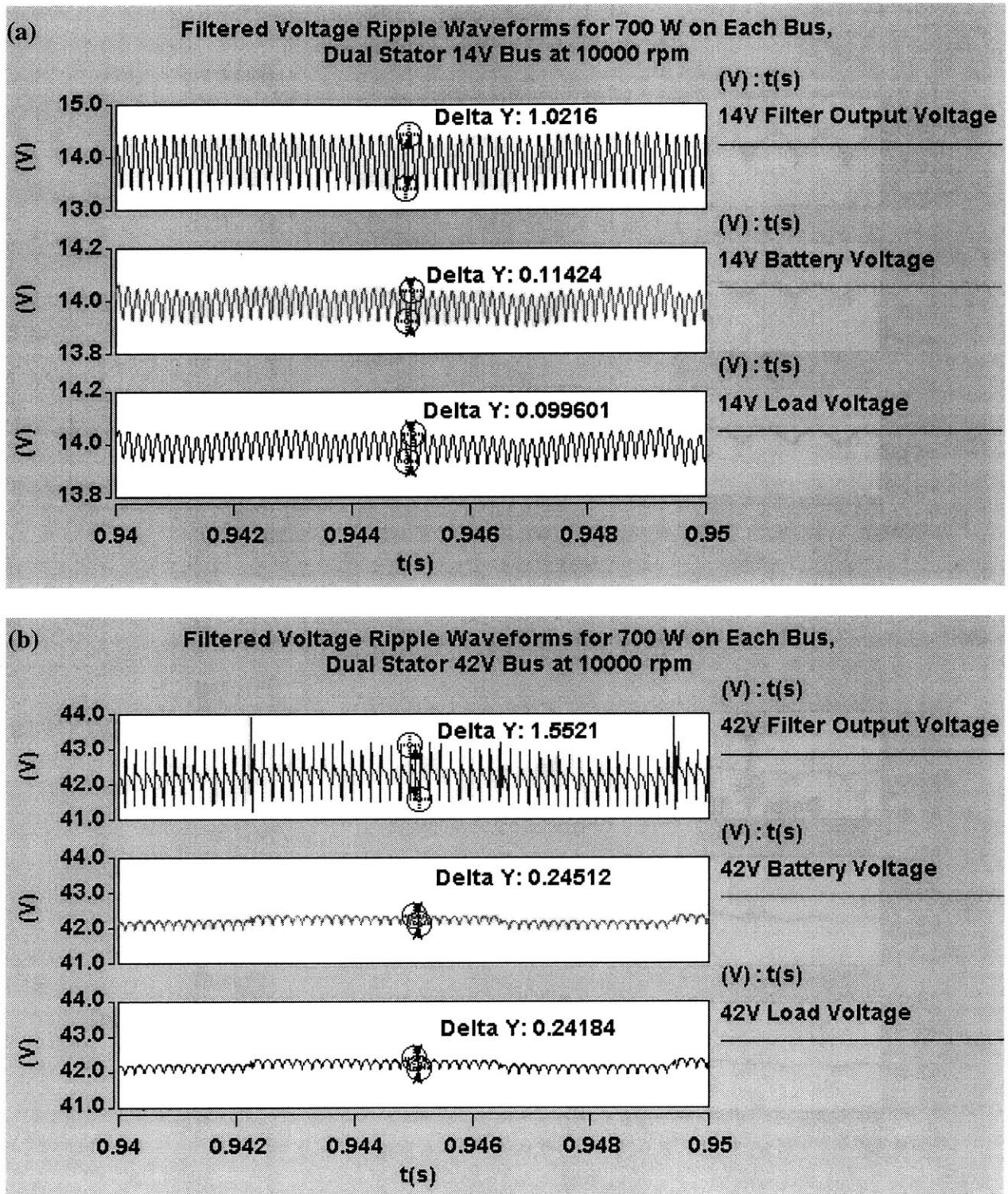


Figure 5.8: Filtered ripple waveforms for the dual-stator architecture operating at 10000 rpm alternator shaft speed, with the battery *connected*: (a) 14V bus voltage waveforms; (b) 42V bus voltage waveforms.

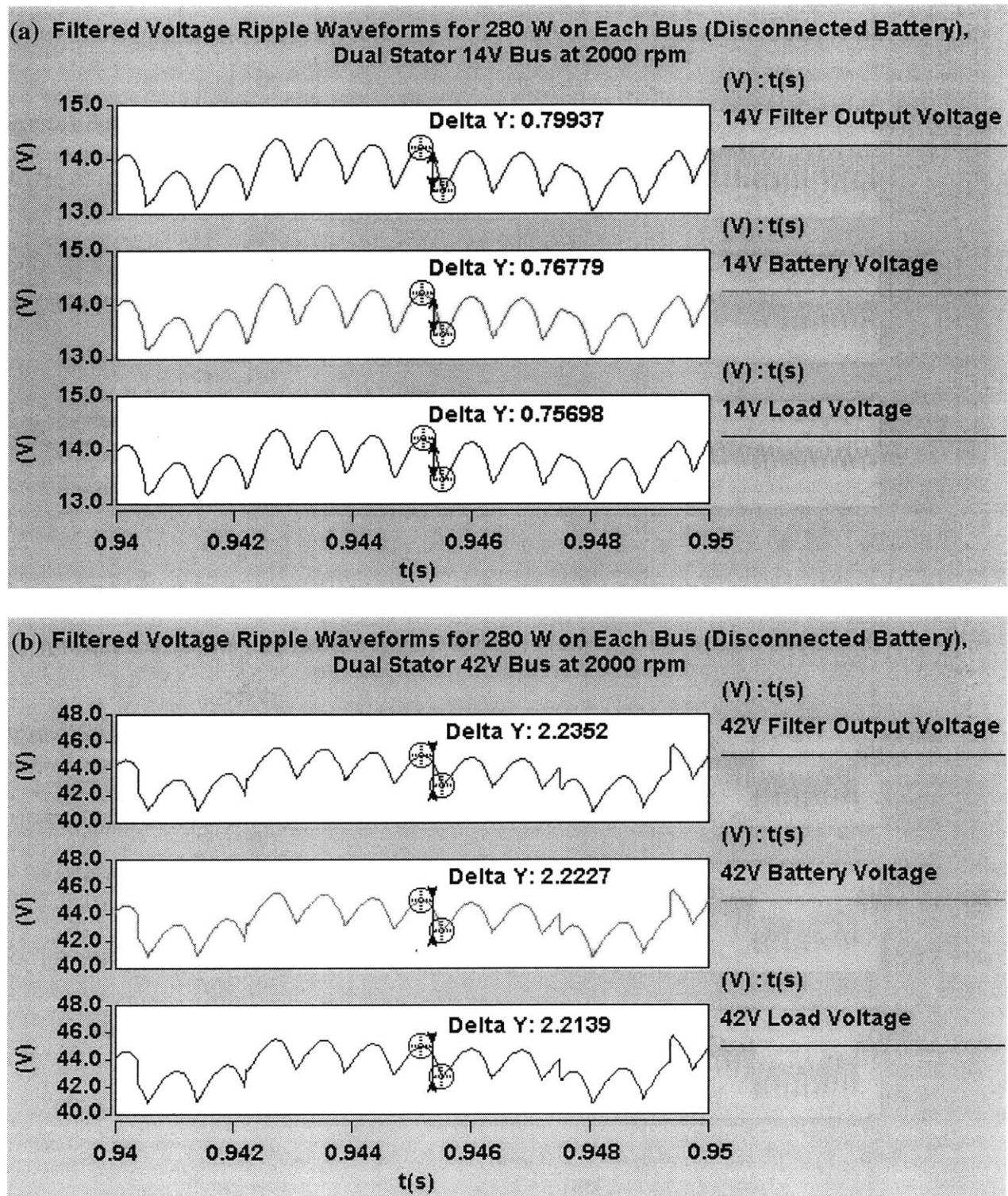


Figure 5.9: Filtered ripple waveforms for the dual-stator architecture operating at 2000 rpm alternator shaft speed, with the battery *disconnected*: (a) 14V bus voltage waveforms; (b) 42V bus voltage waveforms.

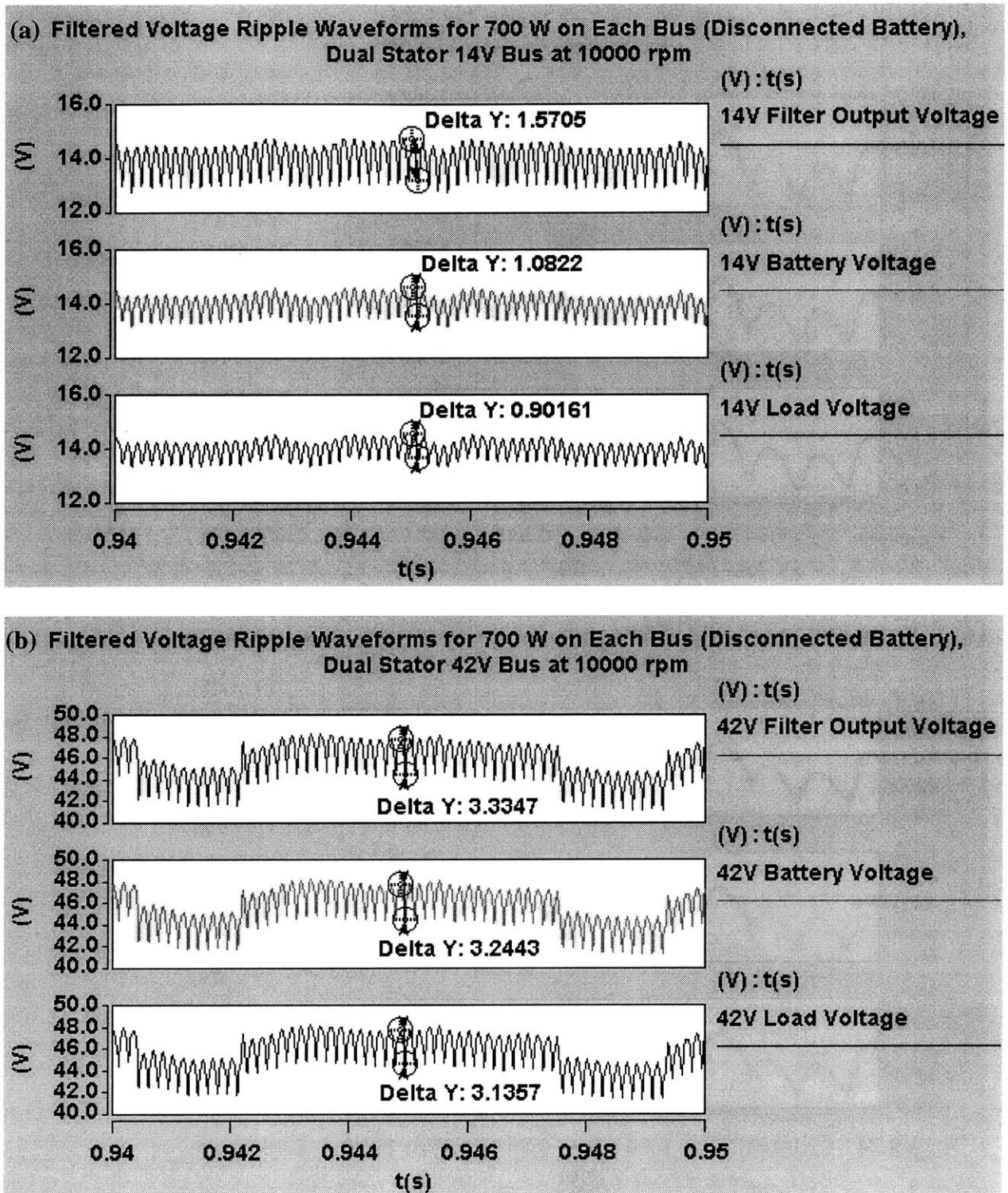


Figure 5.10: Filtered ripple waveforms for the dual-stator architecture operating at 10000 rpm alternator shaft speed, with the battery *disconnected*: (a) 14V bus voltage waveforms; (b) 42V bus voltage waveforms.

5.2.4 Observations about Filtered Voltage Ripple with the Dual-Stator Alternator

Figures 5.7 - 5.10 illustrate the degree of voltage ripple attenuation achieved by installing filter capacitors across the 14V and 42V rectifier output terminals of the dual-stator alternator. The waveforms depict filtered voltage ripple observed across each bus's filter capacitor, battery, and load at 2000 rpm and 10000 rpm, in situations with the battery both connected and disconnected. The magnitudes of peak-to-peak voltage ripple observed from these waveforms are summarized in Table 5.3, along with the magnitudes of unfiltered voltage ripple observed in Chapter 4 under the same set of simulation scenarios.

Simulation Scenario	Battery Connected		Battery Disconnected		Specified Limit
	<i>Unfiltered</i>	<i>Filtered</i>	<i>Unfiltered</i>	<i>Filtered</i>	
14V bus at 2000 rpm	0.20 Vpp	0.18 Vpp	2.43 Vpp	0.80 Vpp	1 Vpp
14V bus at 10000 rpm	1.61 Vpp	1.02 Vpp	3.04 Vpp	1.57 Vpp	5 Vpp
42V bus at 2000 rpm	0.23 Vpp	0.22 Vpp	6.95 Vpp	2.24 Vpp	4 Vpp
42V bus at 10000 rpm	1.58 Vpp	1.55 Vpp	6.83 Vpp	3.33 Vpp	4 Vpp

Table 5.3: Summary of peak-to-peak voltage ripple magnitudes for ripple observed at the dual-stator alternator output terminals.

It is noted from these waveforms that the added filter capacitors provide very little attenuation when the battery remains connected to each bus. However, when either battery is disconnected, the filter capacitors serve to sink ripple current previously sunk by the battery and thereby attenuate voltage ripple along the bus. Chapter 4 concluded that voltage ripple is significant only when either battery becomes disconnected, and the results presented in Table 5.3 conclude that the addition of shunt capacitance serves to attenuate this ripple down to acceptable levels for both buses at both 2000 rpm and 10000 rpm. Thus, the addition of moderate amounts of capacitance to the rectifier output terminals of each bus clearly serves to protect system loads from excessive voltage ripple in the event of battery disconnection from either bus.

5.3 Component Design Process

The size and cost of the passive filter designs developed for the dual-rectifier and dual-stator alternators can only be evaluated by sizing the inductors and capacitors required to implement these filters. This sizing process occurs by designing inductors and selecting capacitors which meet the electrical performance requirements observed during the design of the filter topology. The inductor design process involves evaluating the current-carrying and energy storage requirements of each inductor, and using these requirements to select a core type, core geometry,

and winding strategy. The capacitor selection process, which occurred concurrent with the filter design, involves selecting commercially available capacitors of the proper capacitance and voltage rating that are capable of handling the degree of ripple current observed in the system simulations. Designing the specific components required to implement each filter enables a more quantitative evaluation of the practicality of each filter, in terms of the weight and cost that each filter adds to the automobile. This in turn enables a more quantitative and meaningful comparison of the desirability of dual-rectifier and dual-stator alternators, since filtering solutions will have been designed that allow both architectures to meet the minimum performance requirements established herein for voltage ripple.

5.3.1 Inductor and Capacitor Current-Carrying Requirements

The inductor energy storage requirements and capacitor ripple current requirements for each filter are most effectively determined by evaluating simulation waveforms for current being passed through each inductor and capacitor in each filter. Inductor energy storage is based upon the peak current passed through each inductor, while each capacitor's ripple current performance is based upon the level of RMS current passed through the capacitor as a function of ripple frequency and ambient temperature. If an inductor is inadequately sized using material with an insufficient saturation flux density, magnetic saturation of the material will occur and the inductance rating will become compromised. Likewise, if a capacitor is inadequately sized using a component whose ripple rating is insufficient, overheating (based on excessive power dissipation) and reduced component lifetime will occur. Thus, peak inductor current and RMS capacitor current values are needed to adequately size these components to handle the required amount of current at the given ripple frequency and operating temperature.

The peak current-carrying requirement for each inductor is determined based on a worst-case assessment of the alternator speed and loading scenario that maximizes the level of current being passed through the inductor. The current-carrying requirement for each bus's large L_2 inductor is dominated by the dc current delivered by the rectifier, so the worst-case current requirement for this inductor occurs when dc load current for the bus of interest is at a maximum level. Dc load current is maximized for a given bus when the alternator is running at high speed and is supplying full rated current to the bus of interest, minus the current supplied to the battery of the opposite bus. This thesis has presumed that the alternator has a maximum power output capability of 1680 W at high speed (10000 rpm), and that a charged battery sinks approximately 5 A of dc current in steady state. Thus, the worst-case current-carrying scenario for the L_2 inductor occurs when the bus of interest is demanding the maximum 1680 W output power level, minus the power supplied to the battery of the opposite bus. This worst-case loading scenario for the 14V bus is detailed in Table 5.4, and the worst-case loading scenario for the 42V bus is detailed in Table 5.5.

Bus	Load		Battery		Total Rectifier Output	
	current	power delivered	current	power delivered	current	power delivered
14V Bus	100 A	1400 W	5 A	70 W	105 A	1470 W
42V Bus	0 A	0 W	5 A	210 W	5 A	280 W
Total Power Delivered						1680 W

Table 5.4: 14V bus loading scenario producing worst-case current-carrying requirements for the 14V L_2 inductor at 10000 rpm. Worst-case loading occurs when the given bus is supporting the maximum total output power capability of the alternator (minus power supplied to the batteries), while the other bus remains unloaded.

Bus	Load		Battery		Total Rectifier Output	
	current	power delivered	current	power delivered	current	power delivered
14V Bus	0 A	0 W	5 A	70 W	5 A	70 W
42V Bus	33.33 A	1400 W	5 A	210 W	38.33 A	1610 W
Total Power Delivered						1680 W

Table 5.5: 42V bus loading scenario producing worst-case current-carrying requirements for the 42V L_2 inductor at 10000 rpm. Worst-case loading occurs when the given bus is supporting the maximum total output power capability of the alternator (minus power supplied to the batteries), while the other bus remains unloaded.

Note that while each filter's L_2 inductor carries the majority of dc rectifier current supplied to each bus, some of the dc current is carried by the smaller L_1 inductor. Thus, the current-carrying requirements for each filter's L_2 inductor will be slightly smaller than the total rectifier current values listed in Tables 5.4 and 5.5. The exact proportion of total dc current carried by the L_2 inductor is observed from simulation waveforms of the above loading scenarios.

By contrast, the current-carrying requirement for the smaller L_1 inductor is dominated by rectifier-generated ripple current. According to the ripple current waveforms from Chapter 4, peak-to-peak ripple current is significantly greater at high speed than at idle, since a larger amount of current is being switched between the dual-rectifier alternator's two rectifiers. Thus, a worst-case analysis of the current-carrying requirements of the dual-rectifier alternator's two L_1 filter inductors clearly occurs at high speed. In light of this, simulations were performed at 10000 rpm with each bus bearing the alternator's rated load individually and with the rated load split between the two buses, such that worst-case ripple current through the L_1 inductor could be detected from these two loading scenarios.

Overall, simulations were performed for the dual-rectifier alternator with the 14V bus supporting the entire 1400 W system load (1680 W alternator output power – 280 W supplied to batteries) and with the 42V bus supporting the entire system 1400 W system load, with the batteries both connected and disconnected. Simulations were also performed with the 1400 W system load split evenly between the two buses. In some cases the peak current through a given inductor was greater with the battery connected, and in some cases the current was greater with the battery disconnected for the given period of simulation being observed.² Thus, the maximum peak current observed across these simulations for each inductor was used to size each inductor.

Maximum RMS ripple current was also observed for each capacitor in each filter, for both the dual-rectifier and dual-stator architectures. By contrast with the inductor design process, capacitor selection was based as much upon the ripple current ratings of available capacitors as it was upon achieving a desired capacitance. The process began by selecting an initial capacitance using the MATLAB estimation algorithm described in Section 5.1.3. Capacitor RMS ripple current was observed in simulation and, based on the degree to which ripple current fell within or exceeded the ripple current rating of the chosen capacitor, different capacitor solutions (chosen from commercially available capacitors) were tested in simulation. In most cases, the amount of ripple current was much larger than could be sunk by a single capacitor of reasonable size and capacitance. Thus, parallel capacitors were used in order to divide the ripple current sunk to ground, such that reasonably low ripple current magnitudes could be achieved per capacitor. In order to verify that the magnitude of RMS ripple current per capacitor fell below the rated value for the chosen capacitor type, simulations were observed at 10000 rpm with the maximum output power split equally between the two buses. These simulations were observed with the batteries both connected and disconnected, to verify acceptable ripple current magnitudes across the range of possible alternator loading scenarios. These ripple current results are illustrated in Figures 5.11 – 5.16.

5.3.2 Summary of Filter Current Measurements

Table 5.6 summarizes the maximum filter current measurements for peak inductor current and capacitor RMS ripple current for the dual-rectifier alternator, as observed from the Saber simulation waveforms in Figures 5.11 – 5.14. Table 5.7 summarizes maximum capacitor RMS ripple current measurements for the dual-stator alternator as observed from waveforms in Figures 5.15 – 5.16. These values are used to size the inductors and capacitors used to implement the voltage ripple filters illustrated in Figures 5.1 and 5.2 for the dual-rectifier and dual-stator alternators.

² Simulation revealed that field-current regulation of the 42V bus with the battery disconnected became difficult with the chosen regulator model, as slight oscillations of the average 42V bus voltage occurred as soon as the battery was removed.

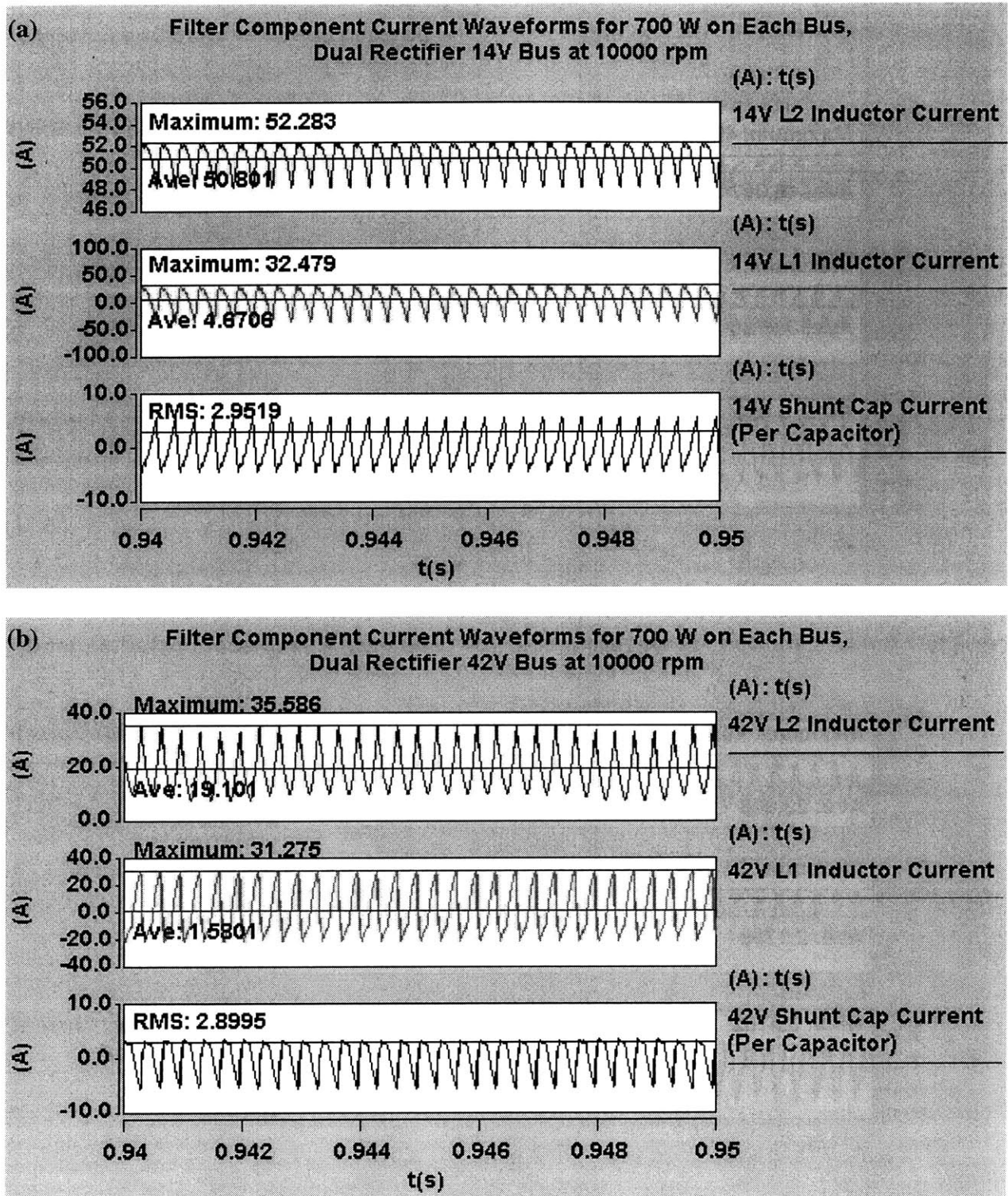


Figure 5.11: Filter current waveforms for the L_1 and L_2 inductors and the shunt capacitors for the dual-rectifier architecture operating at 10000 rpm alternator shaft speed, with the battery *connected*: (a) 14V filter currents; (b) 42V filter currents.

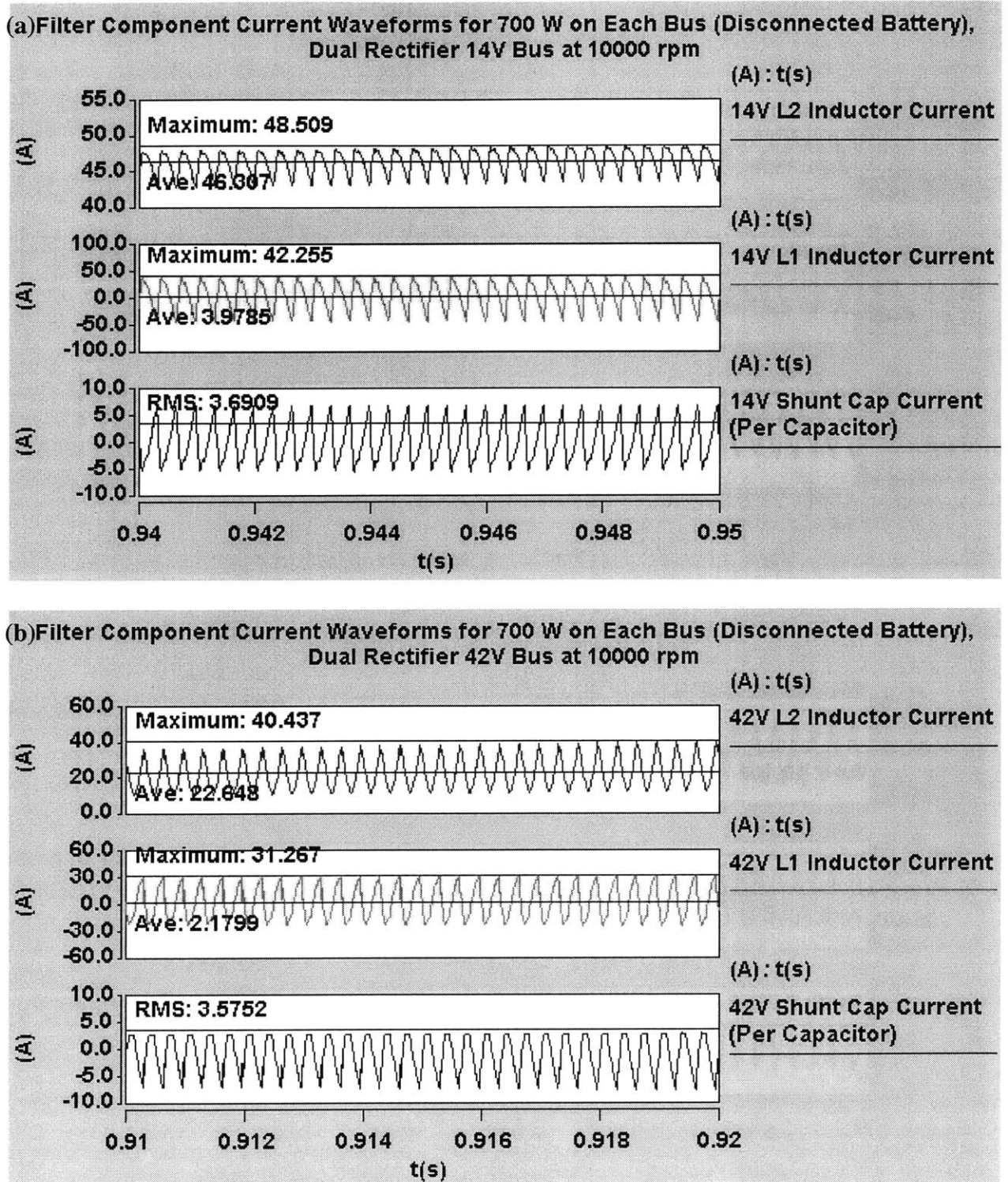


Figure 5.12: Filter current waveforms for the L_1 and L_2 inductors and the shunt capacitors for the dual-rectifier architecture operating at 10000 rpm alternator shaft speed, with the battery *disconnected*: (a) 14V filter currents; (b) 42V filter currents.

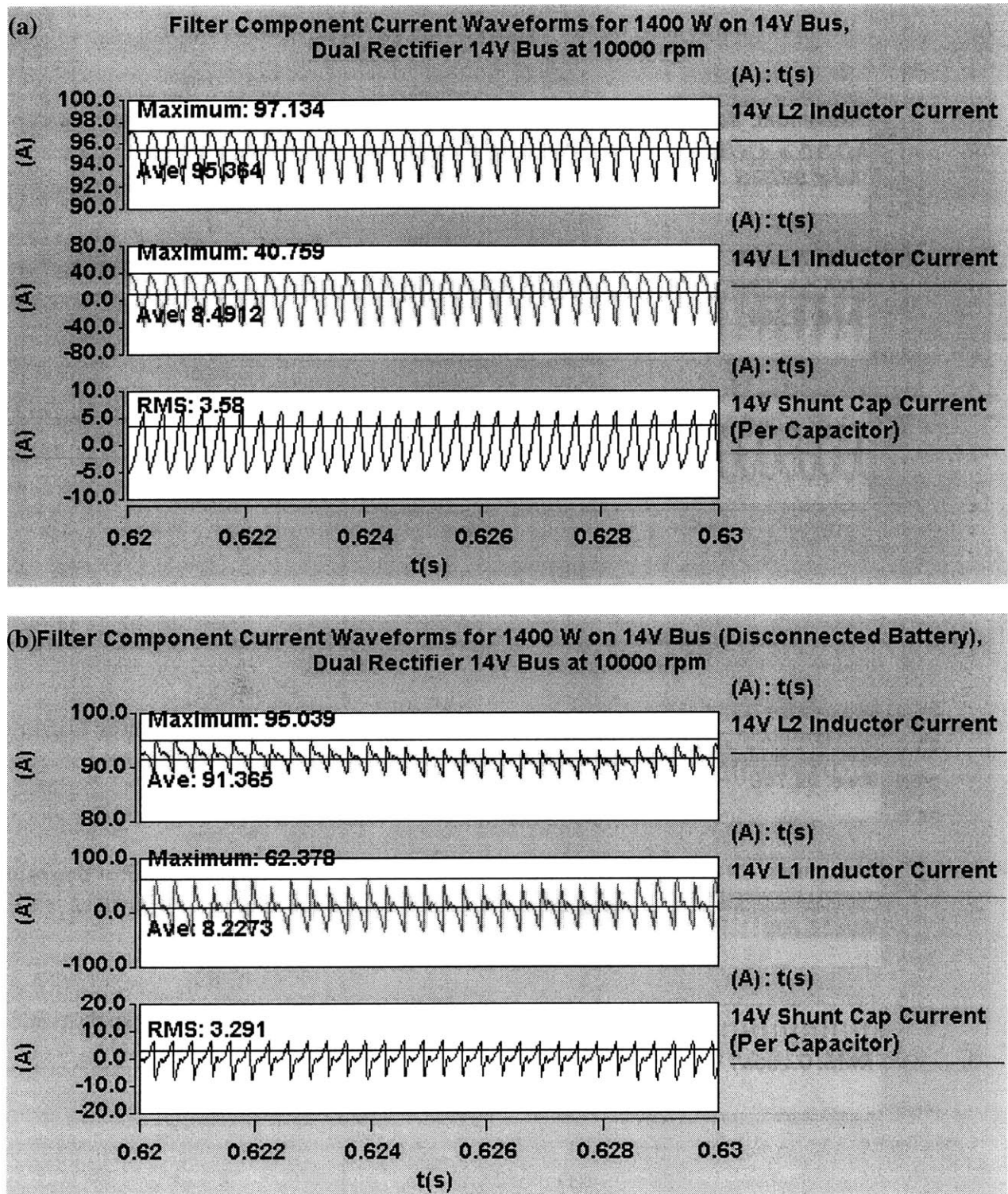


Figure 5.13: 14V filter current waveforms for the L_1 and L_2 inductors and the shunt capacitors for the dual-rectifier architecture operating at 10000 rpm alternator shaft speed, with the full load on the 14V bus: (a) battery connected; (b) battery disconnected.

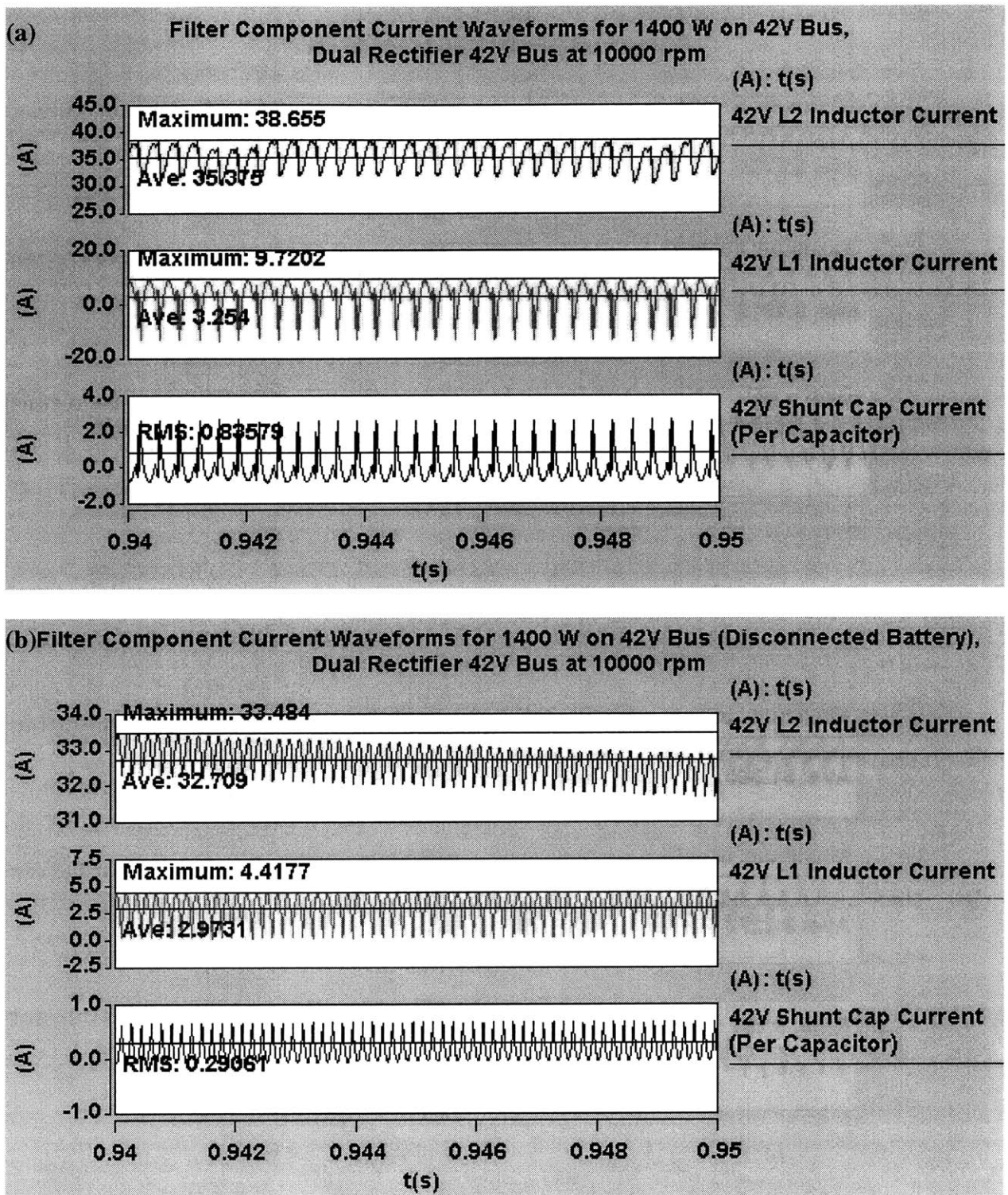


Figure 5.14: 42V filter current waveforms for the L_1 and L_2 inductors and the shunt capacitors for the dual-rectifier architecture operating at 10000 rpm alternator shaft speed, with the full load on the 42V bus: (a) battery connected; (b) battery disconnected.

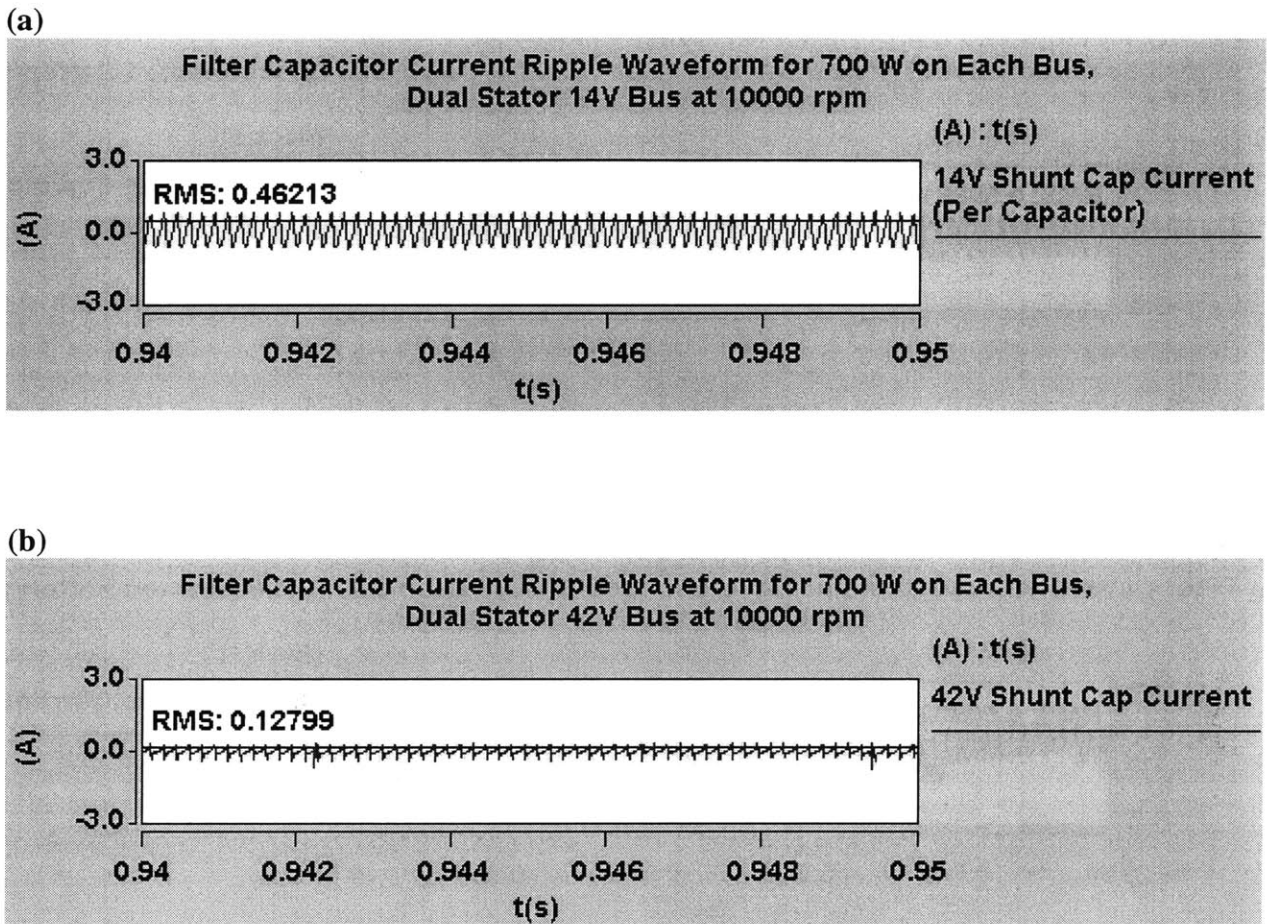


Figure 5.15: Filter current waveforms illustrating ripple current through the shunt capacitors connected across the rectifier output terminals of the dual-stator alternator operating at 10000 rpm alternator shaft speed, with the battery *connected*: (a) 14V capacitor ripple current (per capacitor); (b) 42V capacitor ripple current.

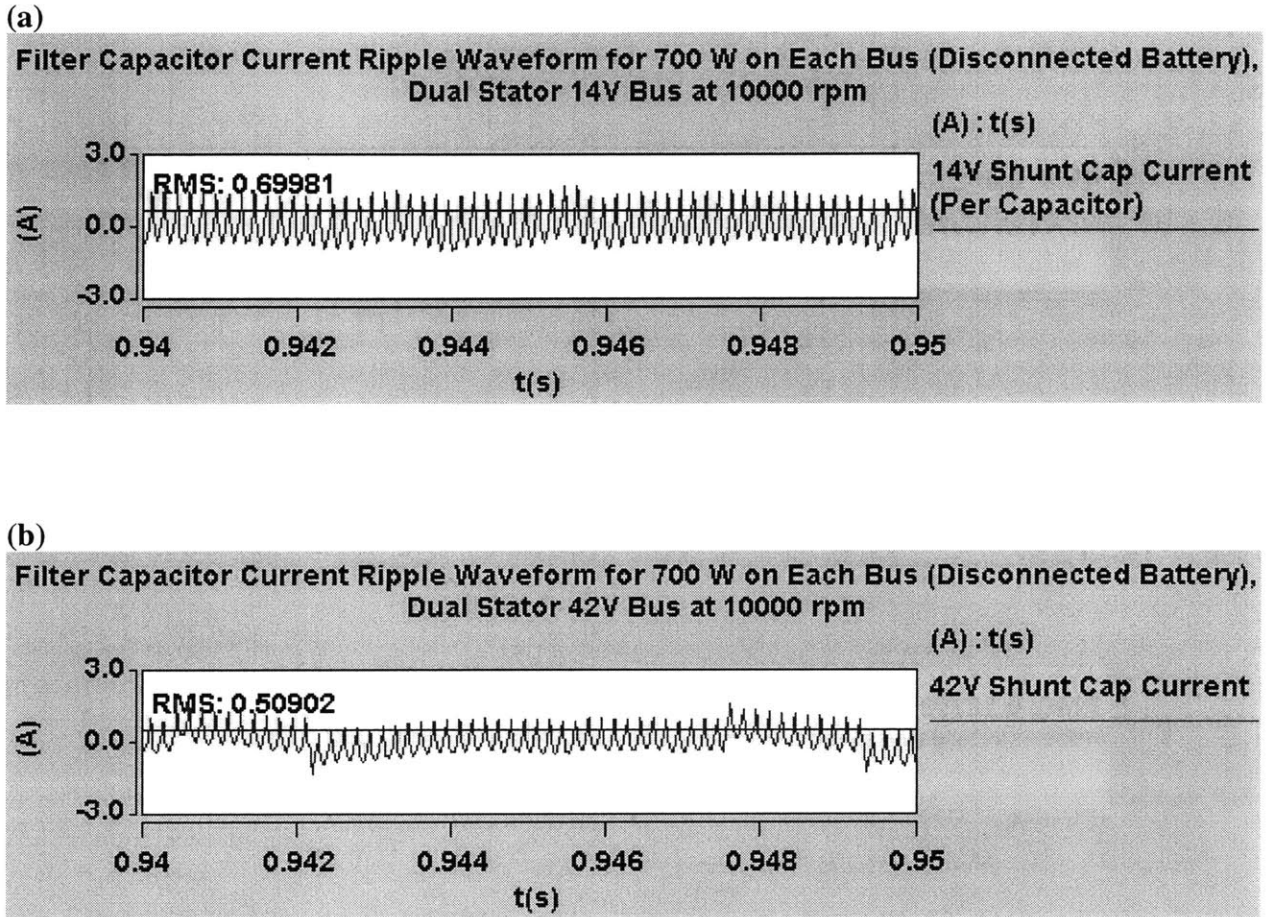


Figure 5.16: Filter current waveforms illustrating ripple current through the shunt capacitors connected across the rectifier output terminals of the dual-stator alternator operating at 10000 rpm alternator shaft speed, with the battery *disconnected*:
(a) 14V capacitor ripple current (per capacitor); (b) 42V capacitor ripple current.

Component	Value	Current Value	Simulation Scenario
14V Inductor L_1	30 μH	$I_{\text{pk}} = 62.38 \text{ A}$	1400 W on 14V bus, battery disconnected
14V Inductor L_2	500 μH	$I_{\text{pk}} = 97.13 \text{ A}$	1400 W on 14V bus, battery connected
14V Capacitor C_x	8200 μF	$I_{\text{RMS}} = 3.69 \text{ A}$ ($f_{\text{ripple}} = 3000 \text{ Hz}$)	700 W on each bus, battery disconnected
42V Inductor L_1	3 μH	$I_{\text{pk}} = 31.28 \text{ A}$	700 W on each bus, battery connected
42V Inductor L_2	14 μH	$I_{\text{pk}} = 40.44 \text{ A}$	700 W on each bus, battery disconnected
42V Capacitor C_x	3900 μF	$I_{\text{RMS}} = 3.58 \text{ A}$ ($f_{\text{ripple}} = 3000 \text{ Hz}$)	700 W on each bus, battery disconnected

Table 5.6: Dual-rectifier alternator filter current measurements used to size inductors and capacitors for the 14V and 42V voltage ripple filters.

Component	Value	Current Value	Simulation Scenario
14V Capacitor C_x	680 μF	$I_{\text{RMS}} = 0.70 \text{ A}$ ($f_{\text{ripple}} = 6000 \text{ Hz}$)	700 W on each bus, battery disconnected
42V Capacitor C_x	180 μF	$I_{\text{RMS}} = 0.51 \text{ A}$ ($f_{\text{ripple}} = 6000 \text{ Hz}$)	700 W on each bus, battery disconnected

Table 5.7: Dual-stator alternator RMS capacitor current measurements used to size filter capacitors for the 14V and 42V buses.

5.3.3 Capacitor Selection Process

The initial MATLAB filter analysis suggested that relatively large capacitances ($> 1000 \mu\text{F}$) were needed to attenuate voltage ripple down to acceptable levels, particularly with the dual-rectifier alternator. This need for large amounts of capacitance necessitated the use of aluminum electrolytic capacitors based on their large capacitance and energy storage capabilities per unit volume.³ The specific electrolytic capacitor component chosen for each filter was determined through an iterative simulation-based selection process which tested different commercially available capacitors and varied the capacitance until a solution providing the proper level of attenuation was found. This solution often differed from the MATLAB analysis value (for the dual-rectifier alternator) because the Saber analyses took into account the ESR of the chosen capacitor, something not accounted for in the early MATLAB analysis.

When selecting aluminum electrolytic capacitors for filtering applications, one must evaluate four relevant parameters: capacitance, voltage rating, ripple current rating, and temperature. In this analysis the ripple current rating tended to be the most constraining parameter, since the

³ A detailed discussion of the appropriateness of aluminum electrolytic capacitors for automotive applications is provided in Chapter 6.

desired level of ripple attenuation was produced only when excessive levels of RMS ripple current (relative to the ripple current rating of the chosen capacitor) were sunk by the single filter capacitor for each bus. Ripple current ratings were further constrained by the fact that each filter is required to operate within a maximum under-hood ambient temperature of 105° C. The RMS ripple current allowed at 105° C for the chosen capacitors is less than half the amount allowed at 85° C, so significant capacitor oversizing is required to enable the capacitors to withstand under-hood temperatures. In addition to the influences of capacitance level and temperature derating, the magnitude of allowable ripple current was also strongly influenced by the ESR of the chosen capacitor. This is because the capacitive impedance of aluminum electrolytics at the chosen capacitance and frequency is similar in magnitude to the capacitor's ESR. This caused the level of ripple current observed through each capacitor to be extremely sensitive to changes in ESR caused by the selection and testing of different commercially available capacitors.

The issue of excessive ripple current was mitigated by (1) using parallel-connected capacitors of lower capacitance to divide ripple current among multiple paths, and (2) inserting resistance orders-of-magnitude larger than the capacitor ESR in order to decrease the sensitivity of ripple current to the specific capacitor choice. The dual-rectifier alternator filters required as many as seven parallel-connected capacitors to divide ripple current such that the ripple current per-capacitor was reduced to within the ripple current specifications for the chosen capacitors. By contrast, the dual-stator alternator's 14V filter required two parallel-connected capacitors, while the 42V bus required only one. This is due in part to the fact that the 14V rectifier is phase controlled using thyristors, while the 42V rectifier is a standard six-diode full bridge rectifier. Thyristor-based controlled rectifiers tend to have larger ripple magnitudes than standard diode rectifiers, so it is consistent that the 14V filtering capacitors were required to sink more ripple current than the 42V filtering capacitor.

The addition of extra resistance between the capacitor and bus also helped to reduce ripple current to acceptable levels. The need for extra series resistance became apparent as capacitors were sought that could both produce acceptable levels of attenuation and sink the amount of ripple current produced by that level of attenuation. Capacitors with increasing capacitance ratings tend to have decreasing ESR characteristics and thus increasing ripple current ratings. However, as larger capacitors were applied to the circuit in order to achieve higher ripple current handling capabilities, the amount of ripple current through each capacitor also tended to increase since the total impedance of the capacitor had grown smaller. This increase in ripple current passing through the capacitor (or parallel-connected capacitor bank) always outpaced the gains achieved by choosing larger capacitors with larger ripple current handling capabilities. Thus, the need existed to adjust the total impedance of the capacitor while holding constant the capacitor ripple current rating, i.e. while using the same choice of capacitor. This need was met by adding extra series resistance between the capacitor and bus. The addition of series resistance allowed more direct control of the tradeoff between attenuation and low levels of ripple current since the ripple current rating was now fixed. It also allowed a capacitor solution to be identified which both produced acceptable levels of attenuation and held RMS ripple current below the chosen capacitor's rating. These capacitor selections are listed in Tables 5.8 and 5.9. [21]

Component	Description	Manufacturer / Part Number	Ripple Current Rating
14V Capacitor (7 per filter)	8200 μF aluminum electrolytic (25V, -55° C to +105° C)	Cornell - Dubilier p/n: 301R822U025HS2	3.62 A_{RMS} (360 Hz at 105° C) 3.87 A_{RMS} (1 kHz at 105° C) 3.99 A_{RMS} (5 kHz at 105° C)
42V Capacitor (7 per filter)	3900 μF aluminum electrolytic (63V, -55° C to +105° C)	Cornell - Dubilier p/n: 301R822U025HS2	3.56 A_{RMS} (360 Hz at 105° C) 3.95 A_{RMS} (1 kHz at 105° C) 4.18 A_{RMS} (5 kHz at 105° C)

Table 5.8: Filter capacitors chosen for use in the 14V and 42V ripple filters for the dual-rectifier alternator.

Component	Description	Manufacturer / Part Number	Ripple Current Rating
14V Capacitor (2 per filter)	680 μF aluminum electrolytic (25V, -55° C to +105° C)	Cornell - Dubilier p/n: 301681U025FQ2	0.80 A_{RMS} (1 kHz at 105° C) 0.85 A_{RMS} (5 kHz at 105° C) 0.86 A_{RMS} (10 kHz at 105° C)
42V Capacitor (1 per filter)	180 μF aluminum electrolytic (63V, -55° C to +105° C)	Cornell - Dubilier p/n: 301R181M063EK2	0.60 A_{RMS} (1 kHz at 105° C) 0.66 A_{RMS} (5 kHz at 105° C) 0.68 A_{RMS} (10 kHz at 105° C)

Table 5.9: Filter capacitors chosen for use in the 14V and 42V ripple filters for the dual-stator alternator.

5.3.4 Inductor Design Process

The inductor design process utilized in this research uses McLyman's area product approach to select a core geometry appropriate to the energy storage requirements of the inductor being designed. [22] The area product A_p of a core is defined as the product of the available window area W_a and the effective cross-sectional area A_c of the core, both measured in square centimeters.

$$A_p = W_a A_c \quad (\text{cm}^4) \quad (5.9)$$

McLyman relates the area product of a core to its peak energy storage requirement and saturation flux density as follows.

$$A_p = \left(\frac{2(\text{Energy}) \cdot 10^4}{B_m K_u K_j} \right)^{(x)} \quad (\text{cm}^4) \quad (5.10)$$

where

$$\text{Energy} = \text{peak inductor energy storage} = \frac{1}{2} LI_{pk}^2 \quad (\text{Joules}) \quad (5.11)$$

B_m = saturation flux density (Tesla)

K_u = window utilization factor

K_j = current density constant

x = current density exponent

McLyman uses a value of $K_u = 0.4$ for the window utilization factor, which is defined as the fraction of the inductor's total window area that is occupied by the winding. Meanwhile, the current density parameters K_j and x are empirically obtained for different core types in McLyman based on a least squares curve fit of inductor current density (for a given temperature rise) and area product to the following equation:

$$J = K_j A_p^y \quad (\text{Amps/cm}^2) \quad (5.12)$$

where

$$y = \frac{1-x}{x} \quad (5.13)$$

McLyman's area product approach involves calculating the area product needed by the inductor being designed, and then selecting a commercially available core with an area product close to the calculated value. By (5.10), the area product needed for a particular design depends on the saturation flux density B_m and current density parameters K_j and x , all of which depend upon the choice of core material for the inductor. Given the large inductance and peak current requirements of the L_1 and L_2 inductors in the dual-rectifier alternator's 14V filter and the L_2 inductor in the dual-rectifier alternator's 42V filter, a material with a relatively high saturation flux density is needed to prevent core saturation for large currents. Thus, silicon steel C core material was chosen for this application due to its large saturation flux density and energy storage capability. By contrast, the 42V filter's L_1 inductor has a much smaller inductance and peak current requirement, so a core material with a smaller saturation flux density and smaller energy storage capability is appropriate in order to minimize the core's cost. Therefore, a Molybdenum Permalloy Powder (MPP) toroidal powder core was chosen for this application due to its smaller saturation flux density, lower core loss, and smaller size. The material parameter values discussed above for the silicon steel and MPP core materials are listed in Table 5.10.

Parameter	Silicon steel C core	MPP toroidal powder core
B_m	1.5 T	0.3 T
K_j (for $\Delta T = 25^\circ \text{C}$)	323	403
x	1.16	1.14

Table 5.10: Inductor core material parameter values for the selected silicon steel C core and MPP toroidal power core materials.

These parameters allow for the calculation of area product based on the energy storage requirement for each inductor, as listed in Table 5.11.

Component	Inductance	Energy Storage Requirement $\frac{1}{2}LI_{pk}^2$	Area Product $A_p = \left(\frac{2(\text{Energy}) \cdot 10^4}{B_m K_u K_j} \right)^{(x)}$
14V Inductor L ₁	30 μ H	58.37 mJ	8.03 cm ⁴
14V Inductor L ₂	500 μ H	2358.75 mJ	586.38 cm ⁴
42V Inductor L ₁	3 μ H	1.47 mJ	0.57 cm ⁴
42V Inductor L ₂	14 μ H	11.45 mJ	1.21 cm ⁴

Table 5.11: Energy storage and area product calculations for the inductors used in the 14V and 42V ripple filters for the dual-rectifier alternator.

In [23] McLyman tabulates an extensive listing of commercially available inductor cores of different geometries and materials, ranked according to their area product values. For each of the inductors being designed, the core with the area product value nearest the desired value for the given inductor was chosen from the listing. In the case of the tape wound C cores, the area product chosen from the listing was reduced by the material's stacking factor⁴ (SF = 0.85 for 2 mil silicon steel) in order to calculate the *effective* area product of the core. [24] Thus, each C core was chosen such that its effective area product roughly matched the calculated area product needed for the given inductor design. A summary of the chosen core geometries for each of the four dual-rectifier filter inductors is given in Table 5.11.

Component	Core Type	Manufacturer / Part Number	Area Product
14V Inductor L ₁ (30 μ H)	2 mil silicon steel C core	National Arnold p/n: CL-166-A	CL-166-A
14V Inductor L ₂ (500 μ H)	2 mil silicon steel C core	National Arnold p/n: CL-75	CL-75
42V Inductor L ₁ (3 μ H)	toroidal MPP powder core	Arnold Engineering p/n: A-441051-2	A-441051-2
42V Inductor L ₂ (14 μ H)	2 mil silicon steel C core	National Arnold p/n: CL-69	CL-69

Table 5.12: Inductor cores chosen for use in the 14V and 42V ripple filters for the dual-rectifier alternator.

⁴ Since the lacquer and space between the laminations in a tape wound C core do not contribute to the core's magnetic properties, a stacking factor is used to account for the difference between the cross sectional area of a laminated core and the cross sectional area of a functionally equivalent solid iron core.

5.4 Summary

This chapter served to detail the design process for, and illustrate the results derived from, passive filtering stages designed to attenuate the voltage ripple observed at the rectifier output terminals of the dual-rectifier and dual-stator alternators. The chapter began by detailing the design considerations for each architecture's filter pair and then previewing various passive filtering topologies in order to identify an appropriate filter design. The filter design process was then described. For the dual-rectifier alternator a single-stage filter topology was chosen, and numerical MATLAB analyses of unfiltered ripple were performed to choose initial filter component values. Each filter was modeled and adjusted in Saber until a final filter design was identified which produced proper ripple attenuation within the constraints of reasonable component values and capacitor ripple current ratings. For the dual-stator alternator, the simple addition of capacitance to each bus was used to attenuate voltage ripple down to acceptable limits. Again, Saber simulations were used to size this added capacitance such that acceptable ripple attenuation was achieved within the constraints of the chosen capacitors' ripple current ratings. Once acceptable filters were designed for each architecture, voltage ripple waveforms were observed in order to validate the degree of attenuation achieved at the filter output terminals, battery terminals, and load terminals for each bus.

After describing the filter design process and validating the effectiveness of the chosen designs, this chapter described the process for sizing the actual inductors and capacitors required to implement each filter design. This process first evaluated the worst-case current carrying requirements (peak current through inductors, RMS ripple current through capacitors) of each component, based on an analysis of simulations which maximized the amount of current that each component could be required to carry under normal operation. These simulation results were used to size inductors and select commercially available capacitors used to implement each voltage ripple filter. The challenges of component design, particularly with the selection of appropriate filter capacitors, were discussed, and final component choices were presented.

The results detailed in this chapter emphasize that voltage ripple significantly hinders the feasibility of the dual-rectifier alternator in its present form, but hinders the feasibility of the dual-stator alternator very little. This chapter served to provide a proof of concept that voltage ripple filters could be designed to attenuate voltage ripple down to acceptable limits for both the dual-rectifier and dual-stator alternators. Yet, at the same time this chapter illustrated that the filters required to attenuate dual-rectifier voltage ripple are much more intricate and potentially much larger and more costly than the simple shunt capacitors required to attenuate dual-stator voltage ripple. After a discussion of dual-voltage alternator implementation issues in Chapter 6, Chapter 7 will quantify this disparity by detailing the approximate weights and costs added by each filter to the dual-rectifier and dual-stator alternators. In doing so, Chapter 7 will serve to delineate the effect that the required filter designs have on the ultimate feasibility of both dual-rectifier and dual-stator architectures within dual-voltage automotive electrical systems.

Dual-Voltage Alternator Implementation Issues

This chapter will serve to discuss various technical issues both related to and apart from voltage ripple filtering which surround the implementation and control of dual-voltage alternators within dual-voltage automotive electrical systems. First, newly developed switched-mode rectification (SMR) techniques will be discussed in terms of benefits that can be realized for voltage ripple filtering. The controllability of the dual-stator alternator will also be discussed in terms of stator – stator turns ratios needed to maintain adequate control authority over both buses within the entire range of possible loading scenarios. Furthermore, the appropriateness of aluminum electrolytic capacitors for automotive electrical applications will be surveyed in light of assertions that their lifetimes make them unacceptable for automotive use.

6.1 Switched-Mode Rectification Techniques

One implementation technique of great promise for dual-voltage alternators involves the use of switched-mode rectification (SMR) to realize substantial benefits in regard to output power capability, load dump protection, and ripple filtering. Perreault and Caliskan develop this technique in [25], which draws upon the fact that the output power capability of a standard Lundell alternator varies substantially with output voltage for a given alternator shaft speed. This output power capability for each value of alternator shaft speed is maximized at some load matched output voltage value, which increases as the alternator shaft speed of interest increases. The present Lundell alternator is constructed such that the maximum output power achievable at 1800 rpm (idle speed) is realized for an output voltage of 14V. However, the 14V output voltage limits the output power capability achievable at higher shaft speeds to a level far below the maximum output power realizable with higher output voltages at those speeds (see Figure 6.1).

This technique seeks to correct this inefficiency by "setting" the output voltage seen by the alternator to the optimal load-matched voltage for the speed at which the alternator is operating. This allows the alternator to maximize its power output capability across a large range of alternator shaft speeds, not just 1800 rpm. The result is a substantial increase in output power capability, particularly at higher speeds. For example, the output power achievable at 6000 rpm alternator shaft speed increases from the present 1.5 kW to 4 kW when the optimal load-matched voltage exists at the alternator output. The optimal load-matched output voltage seen by the machine is dynamically set using a switched-mode rectifier configuration (see Figure 6.2). This boost semi-bridge implementation replaces the three diodes in the bottom of the rectifier bridge with three ground-referenced FETs, each containing a parasitic reverse p-n junction to act as the rectifier diode. Each bridge leg combined with the connected phase inductance forms a basic boost converter. By varying the duty ratio of each phase's boost switch set, the *average* output voltage seen by each phase can be varied to match the optimal load-matched voltage for the

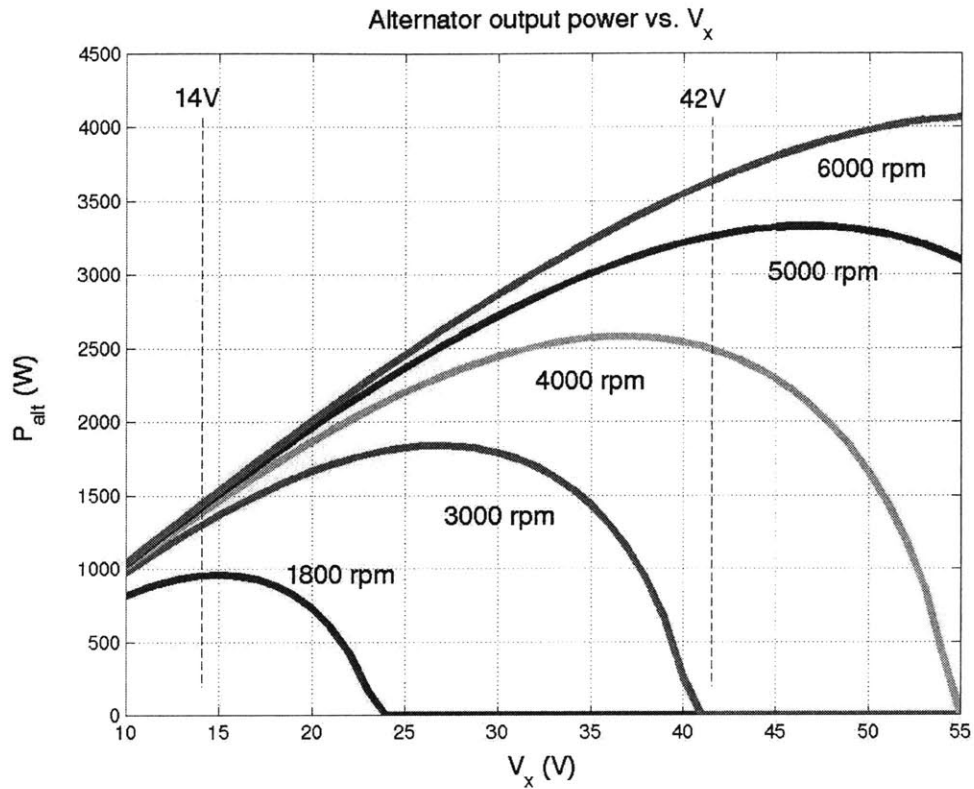


Figure 6.1: Lundell alternator output power capability versus output voltage, parameterized across alternator shaft speed. Note that the maximum output power capability of the alternator for increasing values of alternator shaft speed is achieved at increasing values of output voltage V_x . (used from [25] by permission)

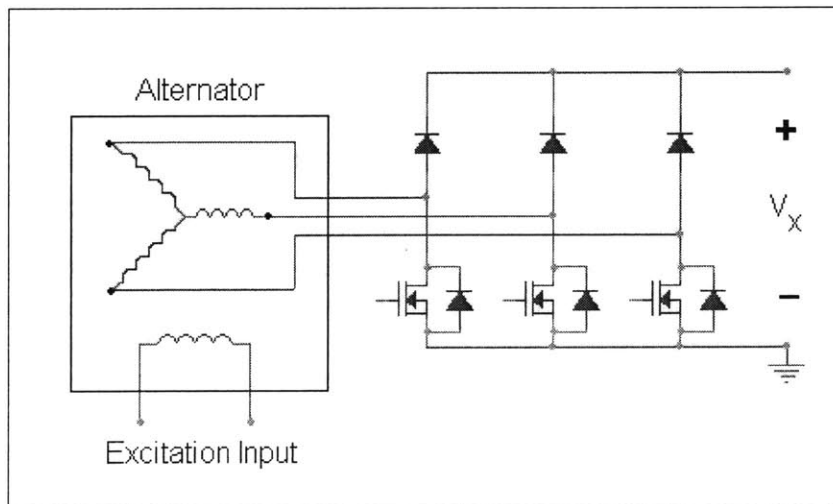


Figure 6.2: Boost semi-bridge implementation of the switched-mode rectifier. (adapted from [25])

given alternator shaft speed. Since the switching frequency of the FETs is much greater than the electrical frequency of the machine, each phase effectively sees this average load-matched output voltage, and maximum power output for the given alternator shaft speed is achieved.

Perreault and Caliskan offer that this technique also presents substantial benefits for the issue of dual-voltage alternator voltage ripple by increasing the fundamental ripple frequency and decreasing the size of necessary ripple attenuation filters. The potential for filter size reduction is most considerable with the dual-rectifier alternator, whose switched current characteristics necessitate very large passive filtering stages to produce acceptable voltage ripple characteristics. An implementation of SMR with the dual-rectifier alternator is illustrated in Figure 6.3.

The fundamental ripple frequency is increased because the FETs are switched much faster than the rate at which the thyristors are fired in the standard non-SMR dual-rectifier configuration. In the standard configuration, the thyristor whose ac stator phase current predominates is fired at a delay angle α after the thyristor becomes forward biased. When the thyristor is activated, it back-biases its corresponding diode in the upper half of the 42V rectifier bridge and steals the current formerly flowing through this diode. In the SMR implementation, the operative thyristor switches once every FET period, rather than once for each rectifier conduction interval. Since this occurs at a frequency several times greater than the frequency at which the thyristors are fired in the standard implementation, the fundamental frequency of ripple is substantially increased. This allows for a significant decrease in filter size, since the corner frequency of the filter can be considerably increased.

Given their ability to improve maximum power output capability and to decrease the size of passive filtering components required to attenuate voltage ripple, load-matched SMR techniques greatly improve the feasibility of dual-voltage alternators as viable dual-voltage power supply solutions. These techniques are particularly promising for the dual-rectifier alternator, whose viability in the present implementation is strained by the component sizes required to attenuate voltage ripple. Continued analysis of dual-voltage alternators should thus explore the degree to which dual-rectifier voltage ripple filters can be made smaller and more practical by applying switched-mode rectification techniques.

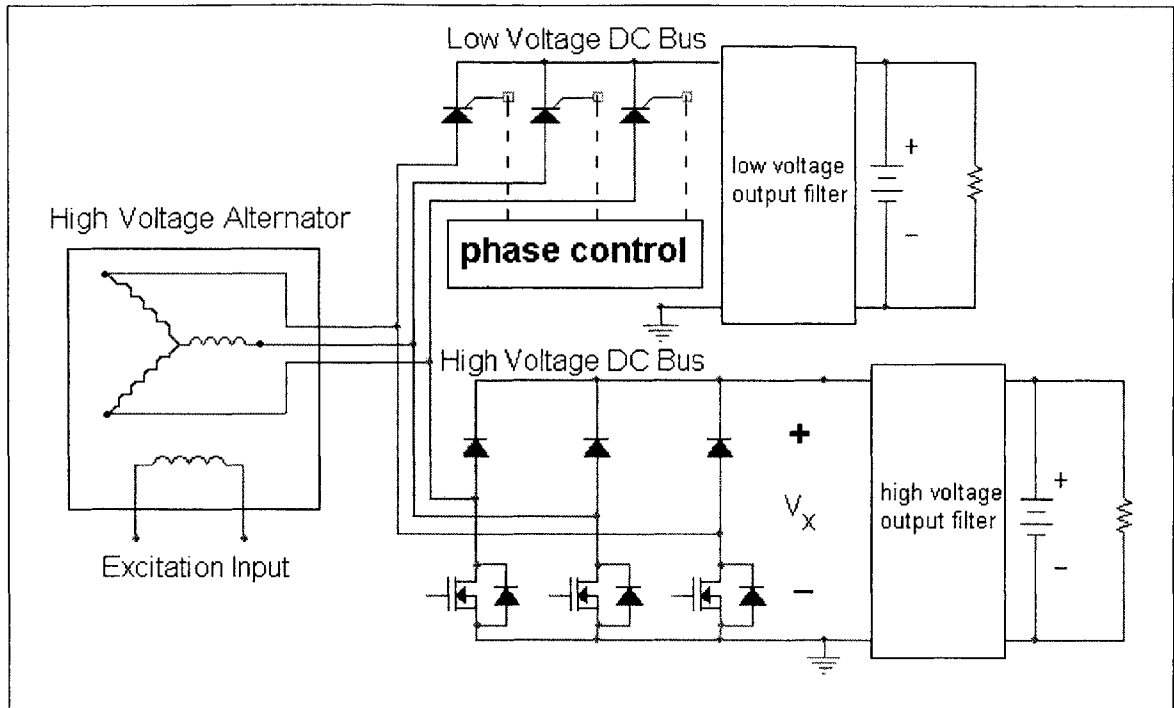


Figure 6.3: Switched-mode rectifier (SMR) applied to the dual-rectifier alternator.
(adapted from [25])

6.2 Controllability of the Dual-Stator Alternator

6.2.1 Issues with a 3:1 Stator – Stator Turns Ratio

An obvious prerequisite for any feasible dual-voltage power supply architecture is the ability of the architecture to successfully regulate both the 14V and 42V buses to their designated voltages. As discussed in Section 2.4.1, this becomes an issue with the dual-stator alternator under the traditional assumption that the two stator sets are wound with a 3:1 turns ratio, i.e. three times as many turns per phase exist within the 42V stator as compared to the 14V stator. This assumption is problematic because the 14V winding's internal voltage is always limited to 1/3 of the 42V winding's internal voltage, since both sets of windings are excited by the same magnetic flux produced by the rotor winding. Thus, when the 42V winding's internal voltage is set by the rotor field current to a minimum level due to light 42V bus loading, the 14V winding's internal voltage will also be set to a minimum level relative to the 14V bus voltage. If the 14V bus is heavily loaded while the 42V bus is lightly loaded, the 14V phase angle regulator saturates at its maximum control angle ($\alpha = 0^\circ$) and is unable to provide the demanded current to the 14V bus while maintaining the desired voltage level.

This problem is illustrated in Figure 6.4. In this simulation, a dual-stator alternator with a 3:1 turns ratio is powering the 42V bus loaded with only the battery and the 14V bus loaded with 560 W plus the battery at 2000 rpm alternator shaft speed. Figure 6.4(a) illustrates the 42V bus voltage, rotor field current, and level of current supplied to the lightly loaded 42V bus. Figure 6.4(b) illustrates the 14V bus voltage, firing angle α used to regulate the 14V bus, and level of current supplied to the heavily loaded 14V bus. This demonstrates the worst-case control condition described above, since the 42V internal voltage is regulated to a minimum level in order to maintain the 42V bus voltage level. As explained above, the 14V internal voltage is also regulated to a minimum level, since the 14V internal voltage is limited to 1/3 of the 42V internal voltage (per the 3:1 turns ratio). However, this level of field current excitation is unable to produce a large enough 14V internal voltage to maintain the bus voltage of the very heavily loaded 14V bus, as is noted from the sagging voltage measured at the 14V rectifier output terminals. Thus, the control angle α is reduced and eventually saturates at $\alpha = 0^\circ$, while the 14V load voltage remains below the desired 14V voltage level.

6.2.2 Decreasing the Stator – Stator Turns Ratio

This problem is mitigated by decreasing the turns ratio that defines the number of per-phase turns on the 42V stator winding relative to the 14V stator winding. Decreasing the turns ratio serves to decrease the ratio between the 42V internal voltage magnitude and the 14V internal voltage magnitude, which serves to *increase* the 14V internal voltage for a given level of 42V internal voltage. The turns ratio should be decreased to such a level that, even when the 42V bus is very lightly loaded, the 14V internal voltage is large enough to supply the demanded level of current to the 14V bus. Initial observation suggests that this may be accomplished by either increasing the number of turns in the 14V winding or decreasing the number of turns in the 42V winding. However, further analysis reveals that the problem is mitigated only when the number of 42V turns is decreased for a fixed number of 14V turns. This is because an increase in the number of 14V turns tends to actually *decrease* the available 14V bus current and thereby decreases the 14V bus voltage even more. A brief analysis is provided below.

Based on Equation (2.3), the internal voltage amplitude of a stator phase varies proportionally with both the number of per-phase stator turns and the rotor field current as follows:

$$E = KN_s \omega I_f \quad (6.1)$$

In the case in which the turns ratio is reduced by increasing the number of 14V stator turns, the same level of field current is required to maintain the 42V internal voltage since the number of 42V stator turns has not changed. However, since the number of 14V stator turns has increased, the 14V internal voltage increases for the same level of field current, per Equation (6.1). The effect of this increase in 14V stator turns can be approximated using an averaged equivalent circuit model of a single-voltage synchronous generator with bridge rectifier driving a constant-voltage load, developed by Caliskan in [17]. This model includes the effective voltage, V_e , and impedance, Z_e , of the alternator reflected to the dc side, as illustrated in Figure 6.5.

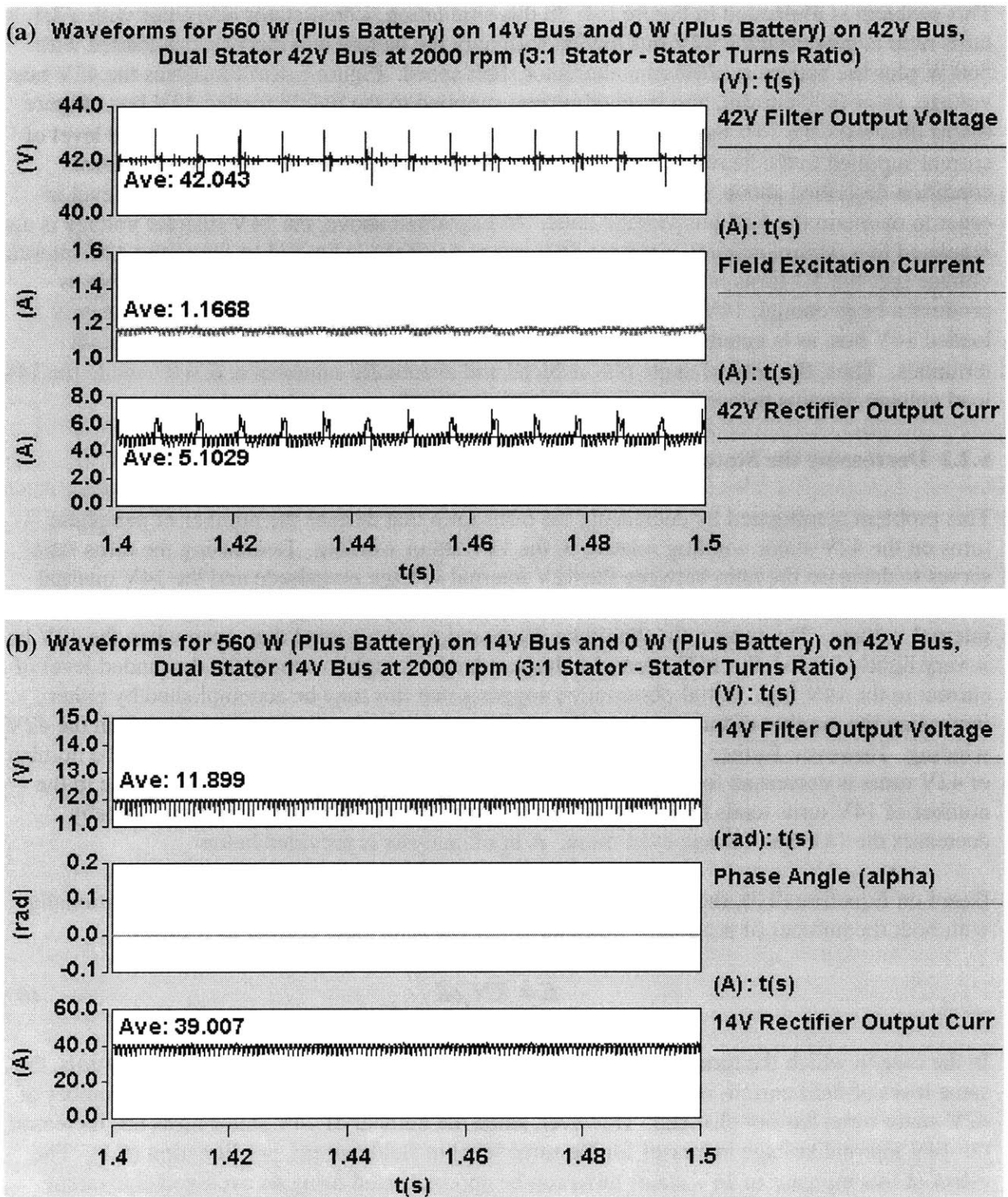


Figure 6.4: Controllability waveforms illustrating the dual-stator alternator output voltage, control handle, and rectifier output current for each bus, with a 3:1 stator-stator turns ratio: (a) 42V bus; (b) 14V bus.

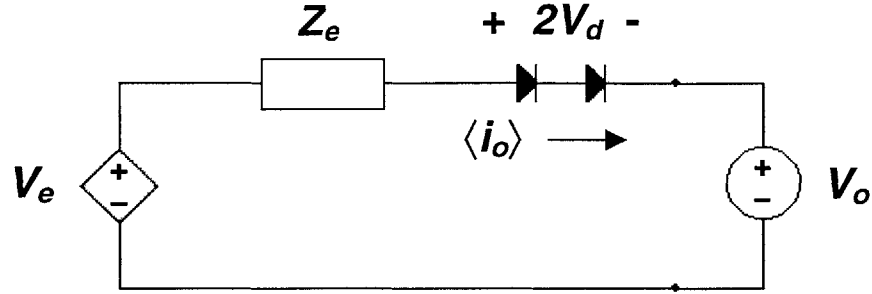


Figure 6.5: Averaged equivalent circuit model of the synchronous generator connected to a full-bridge diode rectifier and driving a constant-voltage load.

According to [17], the equivalent circuit's effective internal voltage and impedance are related to the internal voltage E , per-phase armature impedance L_s , and per-phase armature resistance R_s of the instantaneous alternator model as follows:

$$V_e = \frac{3\sqrt{3}}{\pi} E \cos\left(\varphi - \frac{\pi}{6}\right) \quad (6.2)$$

$$Z_e = \frac{3R_s}{2} + \frac{\sqrt{3}\omega L_s}{2} \quad (6.3)$$

where φ is the phase angle between the internal voltage and phase current in each phase of the instantaneous model. The average current delivered to the load by the averaged equivalent circuit model is:

$$\langle i_o \rangle = \frac{V_e - (2V_d + V_o)}{Z_e} \quad (6.4)$$

Assume that the stator-stator turns ratio is decreased to $3:X$, where $X > 1$, by increasing the number of 14V stator turns by a factor of X . Also assume that a constant slot area is maintained such that as the number of turns increases by a factor X , the cross sectional area of the wire decreases by X . By (6.1) and (6.2), both the 14V internal voltage E and the 14V equivalent circuit's effective voltage V_e scale by the number of 14V stator turns. The armature inductances scale by the square of the number of stator turns, according to the following inductance equation for a coil wrapped around a flux-carrying core with an air gap: [11]

$$L = \frac{\mu_0 A_c N^2}{(\mu_0/\mu_c)\ell_c + g} \quad (6.5)$$

where

- μ_0 = permeability of air gap in free space (H/m)
- A_c = cross sectional area of core (m²)
- N = number of turns
- μ_c = permeability of core material (H/m)
- ℓ_c = mean magnetic path length for flux (m)
- g = length of gap (m)

Given the assumption that a factor of X increase in the number of turns increases the wire length by X and decreases the cross sectional area by X, the armature resistance also scales by the square of the number of stator turns as follows:

$$R_{wire} = \frac{\rho(LX)}{(A_w / X)} = \left(\frac{\rho L}{A_w} \right) X^2 \quad (6.6)$$

where

- ρ = resistivity of copper ($\Omega \cdot m$)
- L = wire length before scaling (m)
- A_w = wire cross sectional area before scaling (m²)

Since the instantaneous model's armature impedance and resistance scale by the square of the number of stator turns, the average impedance also scales by the square of the number of stator turns per Equation (6.3). Thus, the average current supplied to the 14V bus with the number of 14V stator turns increased by X becomes:

$$\begin{aligned} \langle i_o \rangle_{\text{increased 14V turns}} &= \frac{XV_e - (2V_d + V_o)}{X^2 Z_e} \\ &= \frac{1}{X} \cdot \frac{V_e - \frac{2V_d + V_o}{X}}{Z_e} \quad (\text{for } X > 1) \quad (6.7) \end{aligned}$$

The effective voltage V_e in Equations (6.4) and (6.7) dominates the output voltage plus diode drop for this operating point, since a large internal voltage relative to the output voltage is needed in order to deliver full rated current to the 14V bus. Thus, when compared to (6.4), Equation (6.7) shows that increasing the number of 14V turns by X actually serves to *decrease*

the available current output to the 14V bus. This occurs because as the 14V internal voltage increases by the factor X, the armature impedance between the internal voltage and load increases by X^2 such that the current delivered to the load actually decreases.

Note that the single-voltage synchronous generator model in Figure 6.5 and the resulting average current equations above ignore stator - stator coupling effects. These coupling effects impact the output current that can be obtained from the bus of interest by inducing additional voltage within the armature winding, depending on the current flowing through the opposite set of armature windings to the opposite bus. These effects are limited under the loading scenario of interest here, since the amount of current being supplied to the opposite bus (i.e., 42V bus) is small. However, these effects are responsible for the discrepancies between the manner in which field current ideally varies with changes in the number of stator turns, and the manner in which the two vary in the simulation results.

As suggested above, the issue of 14V bus controllability is ultimately solved by decreasing the number of 42V stator turns relative to the 3:1 turns ratio implementation. Decreasing the number of 42V stator turns reduces the 42V internal voltage for a constant level of field current, per Equation (6.1). Thus, in order maintain the previous level of 42V internal voltage for a decreased number of 42V stator turns, the field current must increase by a proportional amount. This increased level of field current is beneficial because it also increases the 14V internal voltage for the same number of per-phase 14V stator turns. However, since the number of 14V turns remains the same compared to the 3:1 case, the 14V armature impedance does not change, and *more* current can be supplied to the 14V load. Sufficient controllability will be restored to the 14V bus when a turns ratio is chosen for which a fully loaded 14V bus can supply the total demanded current and maintain the desired voltage level with a phase angle of $\alpha \geq 0^\circ$, while the 42V bus is unloaded.

To illustrate this, assume that the turns ratio is decreased from 3:1 to Y:1, where $Y < 3$. The number of 42V stator turns divides by a factor of $3 / Y$, causing a $3 / Y$ reduction in the 42V internal voltage for a constant field current. To compensate, field current increases by $3 / Y$ (ideally, ignoring the effects of stator-stator coupling) in order to restore the 42V internal voltage to a sufficient value to maintain the 42V bus voltage. Per Equation (6.1), this causes the 14V internal voltage to also increase by a factor $3 / Y$ as compared to the 3:1 case, since the number of 14V stator turns has not changed. The new level of average 14V output current becomes

$$\begin{aligned} \langle i_o \rangle_{\text{decreased 42V turns}} &= \frac{(3/Y)V_e - (2V_d + V_o)}{Z_e} \\ &= \frac{3}{Y} \cdot \frac{V_e - \frac{2V_d + V_o}{(3/Y)}}{Z_e} \quad (\text{for } Y < 3) \quad (6.8) \end{aligned}$$

Again, since the 14V effective voltage V_e dominates the 14V output voltage plus diode drop for this operating condition, Equation (6.8) illustrates that the current delivered to the 14V load does increase when the number of 42V turns decreases.

This condition is examined in Figure 6.6, which illustrates the 42V and 14V voltage, current, and control characteristics realized by decreasing the stator-stator turns ratio to 2.5:1 for the same loading scenario depicted in Figure 6.4. Note that the smaller number of per-phase 42V stator turns causes the field current level to increase from 1.17 A to 1.30 A in order to maintain the desired voltage on the 42V bus. This increased field current produces a larger 14V internal voltage, since the number of per-phase 14V stator turns has not changed. The larger 14V internal voltage enables the desired 14V bus voltage level to be maintained without saturating the phase angle controller at $\alpha = 0^\circ$. This is noted by observing the phase angle $\alpha = 6.74^\circ$ (0.118 rad) in Figure 6.6 for which the desired voltage level is maintained on the 14V bus.

The exact turns ratio which restores independent controllability to both buses for the dual-stator alternator varies depending on the winding strategy of the machine and the designed power output capabilities of each bus. For the case analyzed here, a 2.5:1 turns ratio was sufficient to restore controllability to the heavily loaded 14V bus at 2000 rpm alternator shaft speed. This analysis therefore illustrates that with winding ratios less than 3:1, the issue of independent controllability of both buses can be mitigated across the range of possible loading scenarios.

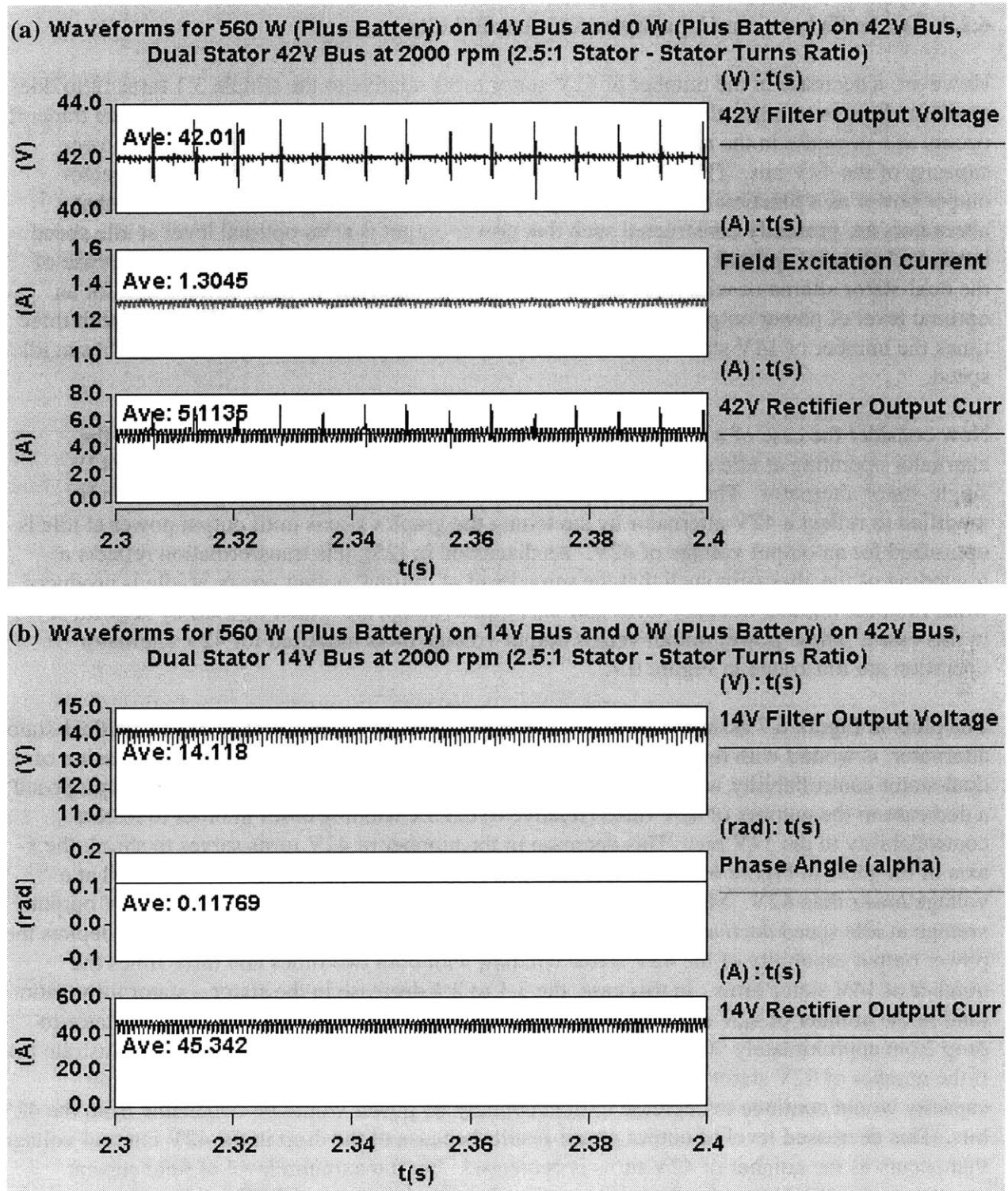


Figure 6.6: Controllability waveforms illustrating the dual-stator alternator output voltage, control handle, and rectifier output current for each bus, with a 2.5:1 stator – stator turns ratio: (a) 42V bus; (b) 14V bus.

6.2.3 Tradeoffs between Capacity and Controllability

However, a decrease in the number of 42V stator turns relative to the simple 3:1 turns ratio does result in changes to other alternator performance characteristics. One such performance tradeoff occurs as a decrease in the number of 42V turns also decreases the maximum output power capacity of the 42V bus. This tradeoff is evaluated by recalling the discussion of alternator output power as a function of output voltage from Section 6.1. This discussion stated that alternators are presently constructed such that power output is at its optimal level at idle speed but is far below its optimal level at higher operating speeds. When extrapolated to the case of the dual-stator alternator with a 3:1 stator – stator turns ratio, the 14V stator is wound for an optimal level of power output to the 14V bus at idle speed. Similarly, the 42V stator with three times the number of 14V stator turns is wound for optimal power delivery to the 42V bus at idle speed.

Now consider the case of a heavily loaded 42V bus and a lightly loaded 14V bus with the alternator operating at idle speed, which for this analysis is equivalent to the case of a 42V single-stator alternator. The power output versus output voltage plots in Figure 6.1 can be modified to reflect a 42V alternator by stretching the graph's x-axis until output power at idle is optimized for an output voltage of 42V. As discussed in [25], this transformation reflects a rewinding of the alternator such that the same level of optimal output power at idle is produced when both the number of stator turns and the output voltage are scaled upward by X (with $X = 3$ in this case). These power output versus output voltage plots modified for 42V alternator operation are illustrated in Figure 6.7.

The plots in Figure 6.7 assume that the 42V alternator, or 42V stator in the case of the dual-stator alternator, is wound with three times the original number of 14V turns. Yet, the discussion of dual-stator controllability with a heavily loaded 14V bus and a lightly loaded 42V bus proposed a decrease in the number of 42V turns (relative to the $3X$ winding case) in order to restore controllability to the 14V bus. This decrease in the number of 42V turns serves to shrink the x-axis of the plots in Figure 6.7, such that the optimal idle-speed power output is realized at a voltage *lower* than 42V. Meanwhile, the maximum power output achievable for a 42V output voltage at idle speed decreases. An example of this is illustrated in Figure 6.8, which depicts the power output capability of the 42V stator winding with both two times and three times the number of 14V stator turns. In this case, the 3:1 to 2:1 decrease in the stator – stator turns ratio (and in the number of 42V stator turns) caused the output power capacity of the 42V stator to drop from approximately 900 W to 600 W for a 42V load voltage. These plots also illustrate that if the number of 42V stator turns were to decrease further, the 42V stator's power output capacity would continue to decrease until eventually *no* power would be obtainable from the 42V bus. This decreased level of output power results because of the drop in the 42V internal voltage that occurs as the number of 42V turns is decreased. For a maximum level of field current excitation, the 42V internal voltage varies directly with the number of 42V stator turns per Equation (6.1). Thus, as the maximum 42V internal voltage decreases due to a drop in the number of 42V stator turns, the maximum amount of current that can be delivered to the 42V load also decreases.

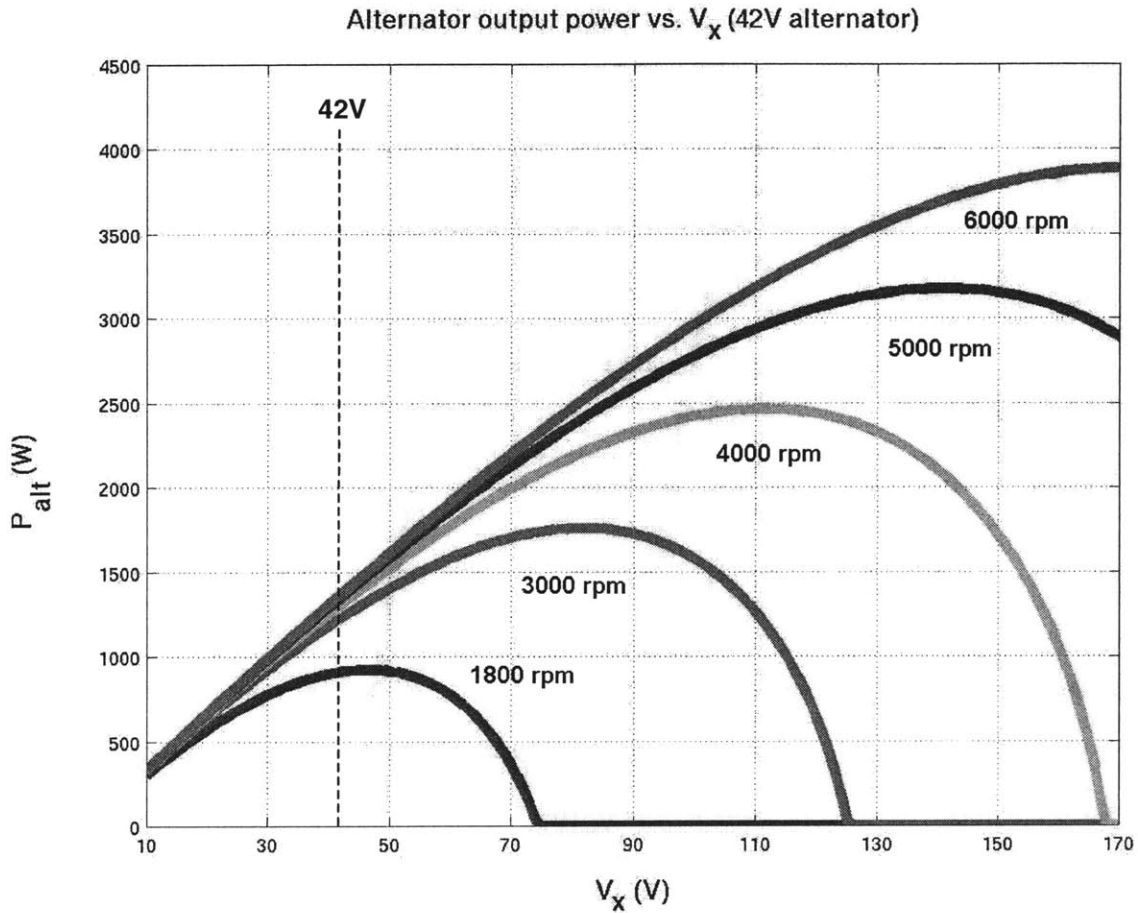


Figure 6.7: Lundell alternator output power capability versus output voltage for a rewind 42V alternator. This plot assumes that the stator and rotor are wound with three times the number of turns of the 14V alternator represented in Figure 6.1. (adapted from [25])

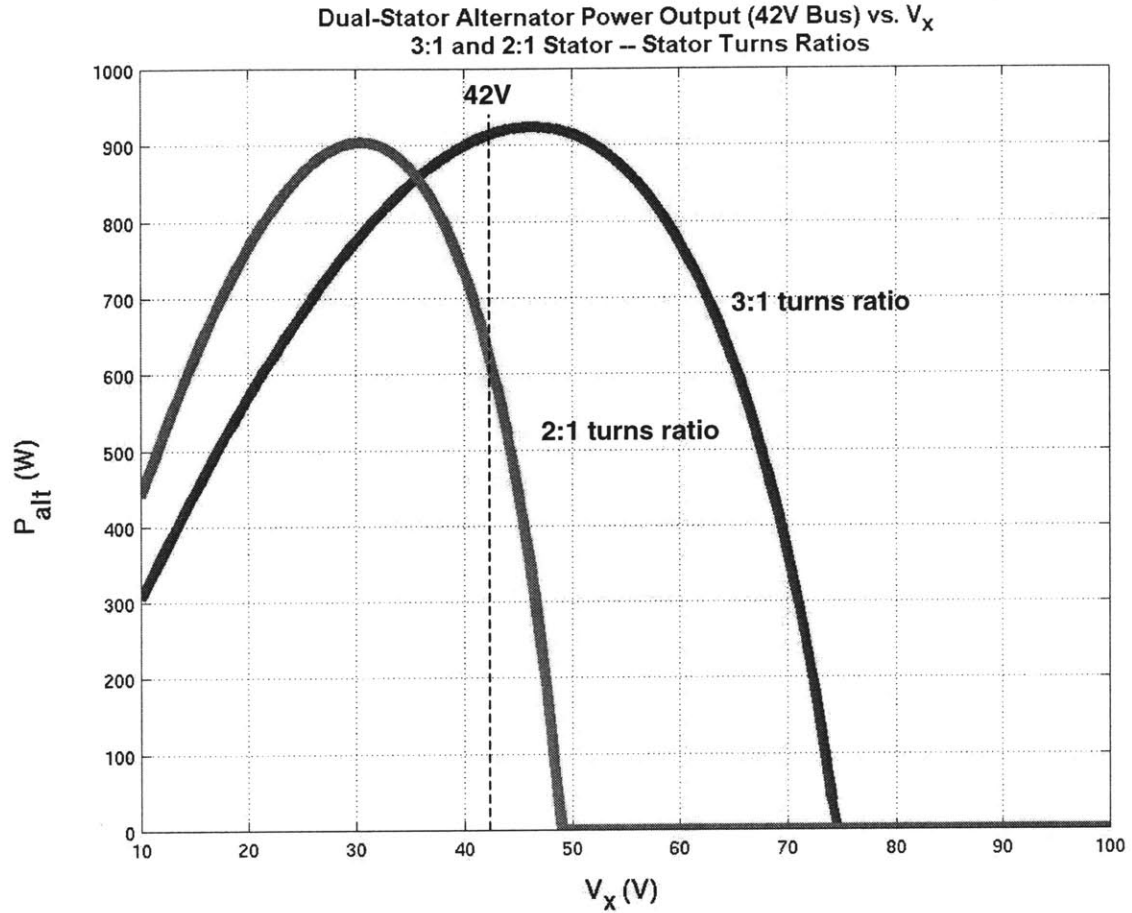


Figure 6.8: Output power capability for two different winding implementations of the dual-stator alternator's 42V stator output at 1800 rpm alternator shaft speed. The 3:1 turns ratio implementation reflects a 42V stator wound with three times the number 14V stator turns, while the 2:1 turns ratio implementation reflects a 42V stator wound with two times the number of 14V stator turns. (adapted from [25])

This discussion highlights the fact that the number of 42V stator turns cannot be decreased indefinitely to mitigate 14V control issues when the 42V bus is lightly loaded. Thus, when determining the actual number of turns that should exist within the 14V and 42V stators of a given dual-stator alternator design, the machine designer must consider all reasonable loading scenarios for both buses of the automobile of interest. The designer must then balance the power demands of the 42V bus at idle speed with the power demands of the 14V bus, such that a winding strategy can be implemented which maximizes the alternator's ability to supply adequate current to both bus voltages across the entire range of operating conditions.

6.3 Suitability of Electrolytic Capacitors for Automotive Applications

Aluminum electrolytic capacitors were employed in the design of dual-voltage alternator ripple filters in Chapter 5 because of the large capacitance and energy storage capabilities they provide per unit volume. Particularly in the case of the dual-rectifier alternator, no other commercially available capacitor type is able to provide the amount of capacitance needed to attenuate voltage ripple down to acceptable levels with a reasonable number of components. However, the use of aluminum electrolytic capacitors under such high temperature and ripple current conditions brings into question whether the typical operating lifetimes of these capacitors are appropriate for automotive applications.

Aluminum electrolytic capacitors already exist in various automotive applications throughout the automobile. For example, the trunk-mounted audio amplifier system in a 1997 Mercury Sable was found to have four 2200 μF (16V, 85° C) aluminum electrolytic can-type capacitors connected in parallel and shunting the 14V bus to ground. Capacitor manufacturers also report inquiries into the use of aluminum electrolytics within antilock braking systems. [26] However, neither of these applications necessarily requires the operation of electrolytics within under-hood operating conditions with an ambient temperature of 105° C.

It is this very high ambient temperature requirement that provides the greatest challenge for aluminum electrolytics within the under-hood environment. According to [27], the operating life of an aluminum electrolytic capacitor doubles for every 10° C decrease in operating temperature, down to about 40° C. Thus, the operating life of the capacitor is shortest when the capacitor operates within an ambient temperature very near its maximum operating temperature rating. Under-hood automobile temperatures can range between -40° C and 100° C [28], so components designed for under-hood operation should be able to operate within this temperature range with acceptable component lifetimes.

Given the operating environment of an aluminum electrolytic capacitor relative to its rated temperature and voltage, the operating life of the capacitor can be estimated as follows (from [21]):

$$L_{op} = M_v L_b 2^{\left[\frac{T_m - T_a}{10}\right]} \quad (6.9)$$

where

$$M_v = 4.3 - 3.3 \frac{V_a}{V_r} \quad (6.10)$$

and

L_{op} = expected operating life (hours)

M_v = voltage derating multiplier

L_b = expected operating life at full rated voltage and temperature (hours)

T_m = maximum internal operating temperature (° C)

T_a = actual internal operating temperature (° C)

V_a = applied voltage (V)

V_r = rated voltage (V)

Using this formula, the expected operating lifetime for the electrolytic capacitors used to filter voltage ripple for the dual-rectifier and dual-stator alternators can be calculated. The Cornell Dubilier 301 series capacitors used in this application exhibit an expected operating life L_b of 6000 hours at rated voltage and temperature. The maximum internal operating temperature T_m , i.e. "hot-spot" temperature at the capacitor core, is 108° C for these capacitors.¹ The 25V rated capacitors used in each architecture's 14V filter typically experience a maximum applied voltage of approximately 14.7 V, per the simulations performed in Chapter 5. Given these parameters, the expected component operating lifetime for the 14V filter capacitors used in this application varies with internal operating temperature as shown in Figure 6.9.

Figure 6.9 illustrates both the manner in which expected capacitor operating lifetime varies with the capacitor's internal core temperature, and the percent of operating lifetime that is spent per hour of operation at the given internal operating temperature. The latter plot is meaningful when capacitor wear is considered as a cumulative process that occurs at a rate based on the internal operating temperature of the capacitor at a given time. Using these plots, the appropriateness of aluminum electrolytic capacitor lifetimes for automotive applications can be evaluated as follows: An automobile that is driven a total of 250,000 miles over its lifetime at an average speed of 25 miles per hour has a total lifetime of 10,000 hours. By Figure 6.9, the 25V aluminum electrolytic capacitors used in this application exhibit a lifetime of 14,000 hours when the capacitor is *continuously* operated at its maximum internal core temperature of 108° C. This

¹ *Internal* operating temperature refers to the temperature at the capacitor core, and takes into account the ambient temperature plus the temperature rise that occurs between the case and core due to ripple current and leakage current.

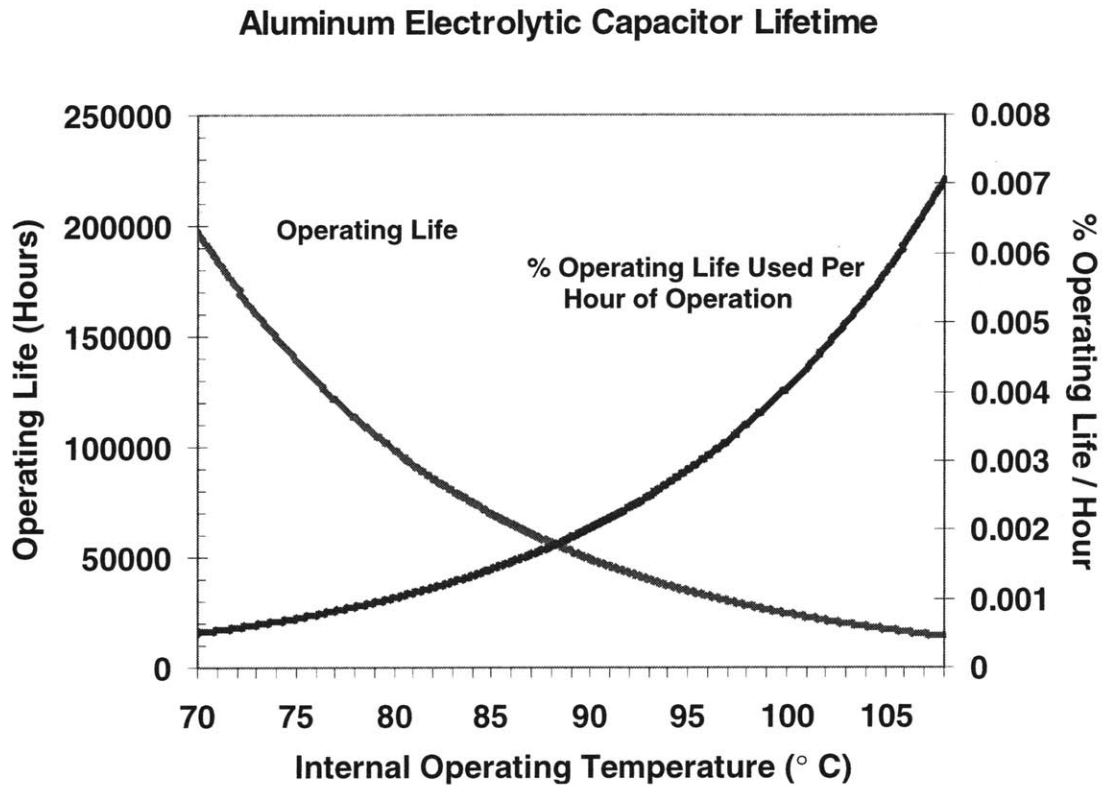


Figure 6.9: Operating lifetime (left axis) and percent of operating lifetime used per hour of operation (right axis) versus internal operating temperature for the Cornell Dubilier 301 series 25V capacitors used in the dual-rectifier and dual-stator alternator 14V bus ripple filters.

core temperature represents worst-case under-hood temperature operation, so the capacitor's lifetime is likely to be longer depending on the under-hood temperature profile for the vehicle over its lifetime.

Two observations are notable about the above analysis. First, a significant tradeoff exists between the ambient temperature in which each aluminum electrolytic capacitor typically operates and the expected operating lifetime of the capacitor. Thus, design decisions made concerning the placement of aluminum electrolytics within the vehicle can greatly affect the ability of the capacitor to survive for the life of the vehicle. Secondly, the above lifetime calculations suggest that aluminum electrolytics cannot be ruled inappropriate for automotive applications based on lifetime concerns alone, if capacitors of the appropriate voltage and temperature ratings are used. Aluminum electrolytic capacitor lifetimes increase with the margin at which the capacitors operate below both the rated temperature and the rated voltage. Thus, commercially available aluminum electrolytics are available which, when appropriately selected to handle the voltage, temperature, and ripple current demands of the application, can survive for the lifetime of the automobile.

6.4 Summary

The purpose of this chapter was to discuss additional implementation issues affecting the efficacy of dual-voltage alternators for dual-voltage automotive power supply applications. First, the use of switched-mode rectification (SMR) techniques to enable load-matched operation for automotive alternators was previewed in terms of the benefits offered for both power output capacity and the filterability of voltage ripple. As well as increasing the maximum power output capability of the alternator, load-matched SMR techniques significantly increase the fundamental frequency of rectifier output voltage ripple. This allows dual-voltage alternator voltage ripple to be filtered with much smaller passive components, since the fundamental ripple component exists at frequencies on the order of the switching frequency of the FETs (100 kHz) as opposed to the electrical frequency of the machine (600 Hz - 6000 Hz). The next issue discussed dealt with the independent controllability of both buses with the dual-stator alternator. Given the implicit assumption of a 3:1 turns ratio between the two stator windings, the alternator is unable to supply sufficient current to the 14V bus when the 14V bus is heavily loaded and the 42V bus is lightly loaded. As shown here, this issue is mitigated by decreasing the turns ratio and thereby increasing the 14V internal voltage to enable more current to be supplied to the 14V bus. However, implementing this decreased turns ratio by decreasing the number of 42V turns serves to limit the output power capacity of the 42V bus, thereby creating a tradeoff between maximum 42V output power capacity and the controllability of the 14V bus for a lightly loaded 42V bus. The appropriateness of aluminum electrolytic capacitors for automotive applications was also discussed, in response to industry feedback that the lifetimes of aluminum electrolytics may be inadequate for use within a vehicle. Aluminum electrolytic capacitors were chosen for use within the dual-voltage alternator ripple filters designed in Chapter 5, since they are the only capacitors capable of reasonably providing the capacitance needed to filter the large ripple magnitudes produced by the dual-rectifier alternator. An analysis of the expected operating lifetimes of aluminum electrolytics revealed that capacitor lifetime is very sensitive to the ambient temperature within which the capacitor operates, but that these capacitors do have lifetimes on the order of the lifetime of an automobile when appropriately rated for voltage and temperature.

Each of the implementation issues considered in this chapter contributes to the viability of dual-rectifier and dual-stator alternators as dual-voltage automotive power supply solutions. The dual-stator alternator is only practical if it is wound with a turns ratio that allows for adequate control authority over both buses over the range of possible loading scenarios. Likewise, aluminum electrolytic capacitors provide feasible filtering solutions only if they exhibit lifetimes appropriate for automotive applications. Finally, the use of switched-mode rectification has the potential to greatly improve the viability of the dual-rectifier alternator by increasing the fundamental frequency of ripple and thereby decreasing the size of passive filtering components. Thus, the successful implementation of dual-voltage alternator solutions within 42V / 14V automotive electrical systems requires the careful consideration of each of these issues.

Cost and Weight Analyses of Dual-Voltage Alternators

Dual-voltage alternators are most meaningfully compared when a set of minimum performance criteria has been established against which each architecture is evaluated. This thesis has focused primarily upon establishing a set of performance specifications for voltage ripple and designing each architecture to meet these specifications. The goal of this chapter is to use these analyses to develop metrics assessing the relative costs and weights mandated by dual-voltage alternators with acceptable voltage ripple characteristics.

This chapter will analyze dual-voltage alternators according to the cost and weight of the machine, the associated power electronics, and the required filter stage to attenuate voltage ripple. Component and materials costs and weights will be examined individually for each of these subunits, to provide insight into how cost and weight is influenced by the machine design, the inclusion of additional power electronics, and the chosen filter design. These costs and weights culminate this work by providing both qualitative and quantitative analyses of the dual-rectifier and dual-stator alternators based on electrical performance, weight, and cost.

Performing accurate cost analyses of dual-voltage alternators is particularly challenging for two reasons. First, dual-voltage alternators have been commercially explored on only a limited basis and have yet to be engineered for and produced in high volume automotive quantities. Because of this, optimized cost-effective production strategies have yet to be developed for dual-voltage alternators. Also high-volume markets have not developed for components such as high-current, low-voltage thyristors, making cost estimates of such parts somewhat speculative. A second reason for the difficulty of dual-voltage alternator cost formulations arises due to the difficulty of obtaining high-volume pricing information for those components and manufacturing processes that do exist presently. Since the automotive industry purchases components and materials in such massive quantities, the industry is often able to dictate component and material prices that are unavailable to other industries. This makes accurate representations of these pricing trends very difficult to obtain from outside the automotive industry. Therefore, the cost analysis presented here seeks not to estimate exact costs for components and materials needed to produce dual-voltage automotive alternators, but to provide cost boundaries based on quotes for similar components and materials presently available.

7.1 Alternator Machine Cost and Weight

The cost and weight of the electric machines required to implement dual-rectifier and dual-stator alternators are best characterized by examining their cost and weight relative to the present single voltage alternator. This examination is performed by assessing changes in the single voltage alternator's machine structure and windings that are necessary to implement the machine portion of the dual-rectifier and dual-stator alternators.

7.1.1 Dual-Rectifier Machine Sizing

As described in Chapter 2, the dual-rectifier alternator is based around a 42V single voltage Lundell alternator. Thus, the machine cost and weight of the dual-rectifier alternator are equal to those of an appropriately rated 42V single voltage alternator. This research has investigated the use of such a 42V alternator based upon the power capability of the present 60A / 120A 14V Lundell alternator. As mentioned in Chapter 4, the simplest method by which to convert this machine to a 42V single voltage alternator involves rewinding the rotor and stator with three times the number of turns in the 14V alternator using wire having one-third the cross-sectional area. The 3X increase in the number of turns allows three times the internal voltage to be generated within the stator windings without increasing field current beyond reasonable levels or magnetically saturating the machine. For a given power rating, the amount of current demanded by the load decreases by a factor of three as the voltage across the load increases by a factor of three. This 3X decrease in the maximum demanded current allows wire size to be reduced by a factor of three while maintaining the same current density and thus the same thermal characteristics. The 3X increase in the number of turns using wire having one-third the cross-sectional area implies that the total stator slot area occupied by the windings remains the same size and carries the same current density as the baseline 14V alternator.

When designed in this manner, the 42V alternator has the same output power capability as the present 14V alternator when the 42V alternator is powering a 42V load. The same machine dimensions are maintained in this conversion from 14V to 42V, so the reluctance path for flux remains unchanged. The rotor also generates the same magnetomotive force (i.e., ampere-turns). As the rotor is rewound with three times its original number of turns, the rotor impedance increases by the square of the increase, which in this case is nine. However, the 42V bus voltage is now being used to generate field current, as opposed to the 14V bus voltage with the 14V alternator. A 3X increase in the voltage across the field winding taken together with the 9X increase in the field impedance produces a maximum field current one-third of its 14V value. Thus, the number of ampere-turns remains the same, since field current is reduced by one-third and the number of field turns is increased by one-third. Since the rotor and stator current densities, the rotor-generated magnetomotive force, and the flux reluctance path all remain unchanged, the new 42V alternator retains its former power output capability when the alternator is powering a 42V load.

Recall the alternator output power versus rectifier output voltage characteristics presented for the 14V alternator in Figure 6.1. According to [25], rewinding the 14V alternator to achieve a 42V alternator as described above serves to stretch the horizontal axis of Figure 6.1 such that the curves peak with the same output power levels at three times the rectifier output voltage. Thus, the newly rewound 42V alternator is capable of generating the 1680 W power output level of the original 14V alternator, but only for a 42V output voltage. This power output versus output voltage characteristic for the rewound 42V alternator is provided in Figure 6.7. As the figure shows, output voltage levels below the optimized power delivery voltage serve to deliver substantially lower amounts of output power. This is physically explained by considering the averaged equivalent circuit model presented in Section 6.2. In order to source rated current to the 42V load, the 42V internal voltage must rise to a level significantly greater than the load voltage because of the large armature leakage inductances present in the Lundell machine. According to the averaged equivalent circuit model, this current level is equal to the difference between the armature's internal voltage and the bus voltage plus diode drop, divided by the armature impedance.

$$\langle i_o \rangle = \frac{V_e - (2V_d + V_o)}{Z_e} \quad (6.4)$$

Since internal voltage is large relative to $2V_d + V_o$, reductions in the output voltage V_o serve to increase output current $\langle i_o \rangle$ very little. Thus, reductions in output voltage below the optimized output voltage level significantly decrease the maximum power output capability, since the reductions in voltage produce very small increases in output current.

Based on this analysis, using the rewound 42V alternator to power a 14V load reduces the power output capability of the machine to approximately one-third its full capability, since the output voltage is reduced by a factor of three while the maximum output current increases very little. This maximum power output analysis as a function of output voltage is significant to the dual-rectifier architecture, because the dual-rectifier alternator uses this 42V single voltage machine to power both 42V and 14V loads. Given the manner in which the dual-rectifier's two rectifier sets modulate between a strictly 42V load and a strictly 14V load three times per electrical cycle, the alternator phase terminals see an average voltage somewhere between 42V and 14V. This average voltage depends on the distribution of loads between the two buses and upon the value of the phase angle α , which determines the length of time the 42V rectifier diodes are active before being deactivated by the 14V rectifier thyristors. If the total load is primarily concentrated on the 42V bus, then the alternator terminals see an average voltage close to the 42V bus voltage. This enables the most of the machine's full output power capability to be delivered to the loads. However, if the load is primarily concentrated on the 14V bus, then α is small and the alternator terminals see an average voltage close to the 14V bus voltage. This enables a substantially reduced level of output power (approximately one-third of the full output power capability) to be delivered to the loads.

Recalling that the power output capability of the present 14V alternator is approximately 840 W (60 A) at idle speed and 1680 W (120 A) at high speed, the above analysis brings to light two observations about the output power capability of the dual-rectifier alternator:

- A dual-rectifier alternator based on a 42V rewind version of the present 14V alternator is capable of delivering a maximum of approximately 280 W at idle speed and 560 W at high speed, under the worst case condition of an entirely 14V load. Under the best case condition of an entirely 42V load, the alternator is capable of delivering 840 W at idle speed and 1680 W at high speed.
- To construct a dual-rectifier alternator that is capable of generating at least as much output power under all combinations of 14V and 42V loads as the present 14V alternator, the 42V machine must be sized approximately three times larger than the simple 42V rewind version of the 14V machine.

According to economic analyses performed within the MIT Consortium regarding the manufacturing costs of dual voltage automotive electrical systems, the manufacturing cost of a 1.5 kW 42V alternator in annual production volumes of 500,000 is \$54.04. Similarly, the manufacturing cost of a 2 kW 42V alternator is \$61.84. [29] These alternator designs correspond to rewinding the stator and rotor of a machine similar in size to the present 14V alternator in order to achieve 42V operation, per bullet #1 above. The weight of this machine is to first order equal to the weight of the present 14V machine, since the volume of steel and copper change little in the rewinding process. Such a machine typically weighs from 5 kg to 6 kg.

Building a dual-rectifier alternator that is able to supply a full 840 W to the 14V bus at 2000 rpm and 1680 W to the 14V bus at 10000 rpm requires the construction of a machine with three times the power output capability of the simple 42V rewind machine. This becomes highly impractical, given the added size and weight of a machine rated three times greater than the 42V baseline case. Total cost is also greater, since power rating of such a machine increases by a factor of three while the generation cost per kilowatt decreases by roughly a factor of two. The final conclusion of this analysis is that the dual-rectifier alternator's 42V machine must be significantly oversized in order to ensure the same level of 14V power generation capability as exists in the present 14V machine. Thus, the dual-rectifier alternator is only practical if the total automotive load exists primarily on the 42V bus, such that the required oversizing of the 42V machine is minimized. This results from the alternator power generation characteristic in Figure 6.7, which illustrates that powering an automotive load whose voltage is significantly below the machine's design voltage (i.e., 42V) greatly reduces the maximum power output capability of the machine.

7.1.2 Dual-Stator Machine Structure

An analysis of dual-stator machine design is slightly more subjective than 42V single-stator machine design because the dual-stator machine has not been mass-produced and is not as easily extracted from the present 14V alternator. Thus, this discussion seeks to describe dual-stator machine design in terms of geometrical and winding modifications relative to a typical 14V alternator that are necessitated by the secondary stator. This thesis has assumed for simplicity that the two three-phase stator sets are wound using the same stator slots and are offset by 0° , implying that the two stator sets are linked concurrently by flux produced by the rotor. This analysis is also simplified by assuming the rotor is wound with three times the number of 14V rotor turns, each having one-third the cross-sectional area of the 14V rotor winding. When wound in this manner, the rotor retains the same size and flux generation capability as the 14V alternator rotor.

Given this set of assumptions, modifications to the machine's size and geometry are driven purely by design decisions concerning the machine's two stators. A simple first-pass design of this machine uses two wye-connected stators wound with a 3:1 turns ratio, with the 14V stator having the same number of turns as the a typical present-day 14V alternator and the 42V stator having three times the number of turns of the present 14V alternator. Chapter 6 demonstrated, although not rigorously, that this winding strategy becomes problematic when the 42V bus is lightly loaded and the 14V bus is heavily loaded. It also demonstrated that this problem is mitigated by reducing the number of 42V stator turns, thereby decreasing the stator – stator turns ratio. However, Chapter 6 also pointed out that a decrease in the number of 42V stator turns may tend to reduce the 42V winding's power output capability at idle speed by reducing the 42V winding's optimal power generation output voltage to a level below the 42V bus voltage. These issues are both significant to the ultimate design of the dual-stator alternator, but a rigorous quantification of these effects has not been performed. Thus, since these issues effect the machine design only by slightly modifying the number of 42V turns from the simple 3:1 case, reasonable analyses of the dual-stator machine's construction can still be performed under the assumption of a 3:1 stator – stator turns ratio.

Figure 7.1 illustrates the stator cross section of a typical 14V Lundell alternator. This particular machine has 36 slots filled with three sets of turns for the three-phase stator. Per the analysis in the previous section, this machine is easily rewound for 42V operation by using three times the number of 14V turns. The decreased current requirement for a constant level of generated power enables the cross-sectional area of the wire to be reduced by a factor of three, allowing both the stator and rotor to be rewound without changing the mechanical dimensions of the machine. Given the design assumptions stated above, the addition of the 14V stator winding to form the dual-stator machine effectively doubles the required slot area. This is because the 14V winding is assumed to have both the same number of turns and the same wire size as the present 14V alternator. Under this simplified analysis the new 14V winding occupies the same cross-sectional slot area as the 42V winding, since the 14V winding has one-third the number of turns of the 42V winding using wire having three times the cross-sectional area. Thus, the new

winding can be accommodated by increasing the stator's slot depth and outer diameter until the slot area is doubled.

To first order, the flux production and distribution characteristics of the machine remain relatively unchanged with the addition of a second winding. However, one effect that is neglected in this analysis is the increase in cross-slot leakage inductance caused by increasing the slot depth and outer slot width.¹ As slot depth is increased, larger levels of cross-slot leakage flux are produced flowing across the width of the slot perpendicular to the direction of rotor-generated flux. With the exception of this effect, machine changes brought about by the addition of a second stator change the magnetic properties of the stator magnetic circuit by very little.

This analysis also assumes that the rotor size of the original 14V machine can be retained with similar power output characteristics. It is assumed for this analysis that the slight lengthening of the stator teeth and slots has a small effect on the total path reluctance of rotor-generated flux, given the presence of a reluctance-dominating air gap between the rotor and stator. Thus, the dual-stator machine needs the same number of ampere-turns in its rotor as exist within the 14V and 42V single-stator machines in order to generate the same level of flux. The rotor can be rewound such that the number of turns increases by a factor of three, while the field current capability decreases by a factor of three. This generates the same number of ampere-turns as the 14V alternator case, while allowing the rotor to maintain its original size. Therefore, this analysis assumes the rotor can remain the same size as the single-stator case, and can produce enough flux to achieve the same levels of power output as the 14V and 42V single-stator machines.

Figure 7.2 illustrates a cross section of the previous 42V alternator, resized for dual-stator operation. Note that the primary modification present in this machine is the doubling of stator slot area in order to accommodate the second winding. This change in slot size causes the stator slot depth to increase from 11 mm in the Figure 7.1 example case to 20 mm and the outer radius of the machine to change from 131 mm to 149 mm. This change in the stator steel geometry adds 221 grams of steel to the stator back iron and teeth, at a cost of \$0.22. The addition of a second winding adds 687 grams of copper to the stator, at a cost of \$3.44.² Relevant dimensions for both machines are provided in Table 7.1, while the cost and weight effects of resizing the single-stator alternator for dual-stator operation are summarized in Table 7.2. Note that the costs presented in Table 7.2 only reflect cost increases mandated by increases in stack volume and copper volume, based on estimates of the cost of steel and copper per pound. Other factors influencing cost, such as changes in material costs for the alternator housing and increased manufacturing costs due to the additional windings, are not included in this analysis.

¹ This analysis assumes that the stator teeth have parallel walls, implying that an increase in slot depth increases the length of the slot's outer arc which forms its upper wall.

² A steel cost of \$0.45 per pound and a copper cost of \$2.27 are assumed, based on costs reported in an investigation of homopolar induction alternators in [30].

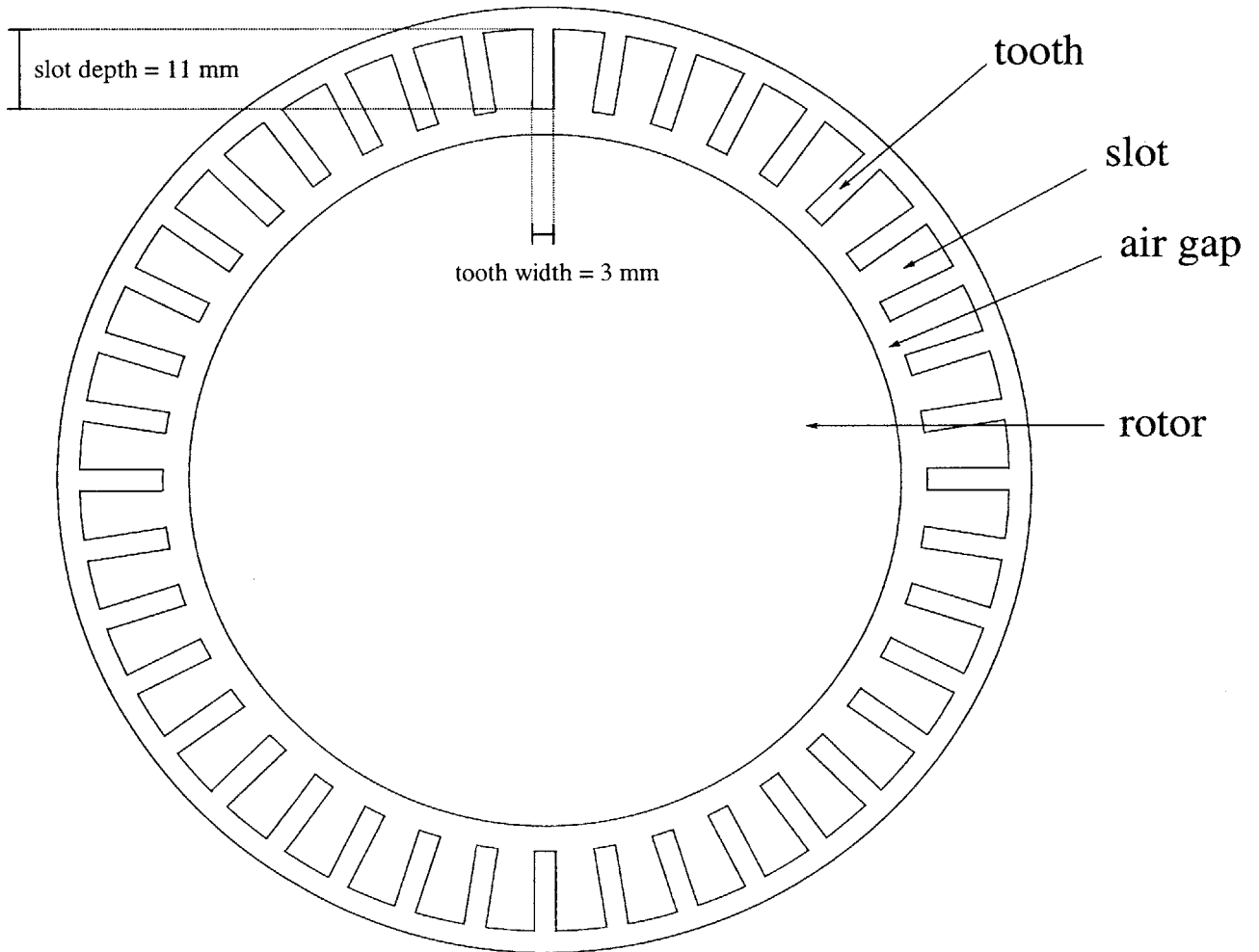


Figure 7.1: Cross-sectional diagram of the stator teeth and slots in a typical 14V single-stator alternator. As discussed, this machine can be rewound for 42V single-stator operation without changing the machine dimensions. (Note: illustration drawn actual size.)

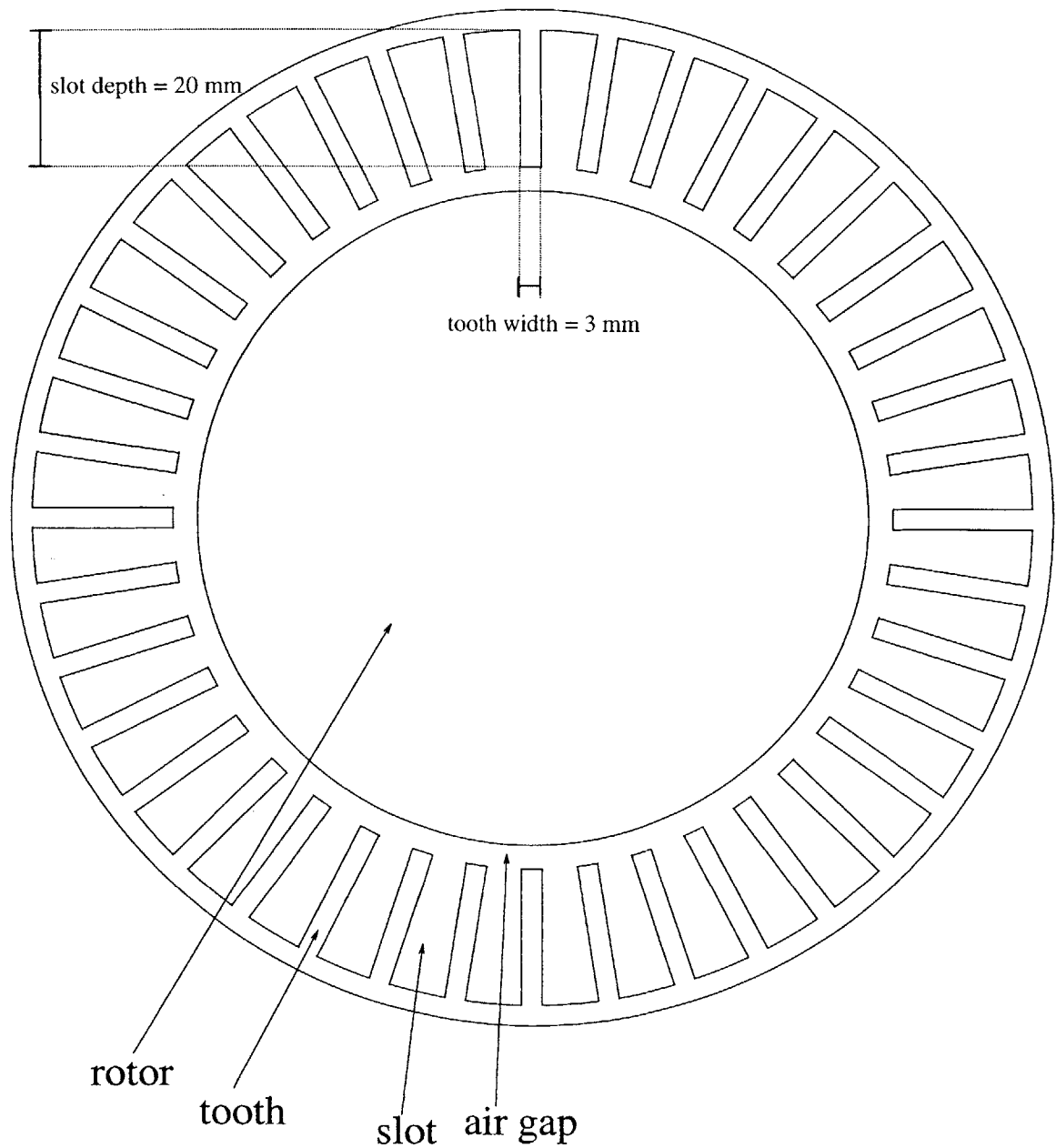


Figure 7.2: Cross-sectional diagram illustrating estimated changes in slot depth and machine diameter for a 42V / 14V dual-stator alternator. (Note: illustration drawn actual size.)

	Single-Stator Machine	Dual-Stator Machine
Inner Stator Radius (center to bottom of slots)	51.5 mm	51.5 mm
Outer Stator Radius (center to top of slots)	62.5 mm	71.5 mm
Outer Machine Radius	65.5 mm	74.5 mm
Tooth Width	3 mm	3 mm
Stack Length	26 mm	26 mm

Table 7.1: Measured dimensions of a single-stator machine and extrapolated dimensions of a dual-stator machine.

	Single-Stator Machine	Dual-Stator Machine
Stator Stack Weight	465 grams	686 grams
Stator Stack Cost	\$0.46	\$0.68
Stator Copper Winding Weight	595 grams	1282 grams
Stator Copper Winding Cost	\$2.98	\$6.42

Table 7.2: Weight and cost of the single-stator and dual-stator steel stacks and copper windings. Measurements were performed on a typical 14V single-stator alternator and extrapolated for the case of a dual-stator alternator.

7.2 Power Electronics Cost

The dual-rectifier architecture is implemented by adding a phase-controlled half-bridge rectifier and phase angle regulator to the standard single voltage machine and full-bridge diode rectifier configuration. Thus, the only extra power electronics required for this architecture are three thyristors and control circuitry to send firing pulses to the thyristors based on the desired phase delay. By contrast, the dual-stator alternator is implemented with the addition of a full-bridge controlled rectifier connected to the second set of stator windings. This architecture requires six extra thyristors³ to implement the rectifier and phase angle control circuitry used to regulate the 14V bus. Components used for power delivery typically dominate control and signal component

³ As mentioned in Chapter 2, the dual-stator's controlled rectifier could also be implemented with three thyristors in the top half and three diodes in the bottom half of the rectifier bridge.

costs, so this analysis focuses on the cost of the thyristors in evaluating the total power electronics cost.

The thyristors used in the dual-rectifier application normally experience a forward voltage equal to the difference between the 42V and 14V bus voltages. This occurs whenever the thyristor's corresponding diode in the upper half of the 42V full-bridge rectifier turns on and pulls the shared anode up to the 42V bus voltage, while the thyristor's cathode is connected to the 14V bus voltage. They also experience a negative voltage equal to the 14V bus voltage, which occurs whenever the thyristor's anode is pulled low by an activated diode in the lower half of the 42V bridge rectifier. In the dual-stator application, device voltages vary according to whether the device in the opposite half of the bridge is conducting. When a thyristor in the upper (lower) half of the bridge is conducting, the corresponding thyristor in the lower (upper) half of the bridge experiences a negative voltage equal to the difference between the 14V bus voltage and ground. When the lower thyristor is not conducting, the upper thyristor experiences the difference between the unloaded alternator terminal voltage (equal to the per-phase internal voltage minus voltages induced by mutual coupling) and the 14V bus voltage. Similarly, when the upper thyristor is not conducting, the lower thyristors experience the difference between ground and the unloaded alternator terminal voltage. Thus, under normal operating conditions with maximum unloaded stator terminal voltages not greater than approximately 80 V, devices rated at 100 V are appropriate. For the 1.6 kW alternator analyzed here, the maximum current drawn by the 14V bus is 120 A. Thus, the required thyristors should also be capable of carrying an average current of $I_{T(AV)} = 40$ A (or $I_{T(RMS)} \approx 60$ A from simulation data). Thyristors rated at such low voltage and current levels are difficult to find commercially since most present thyristor applications require devices rated for voltage levels of several hundred volts and RMS current levels of 25 A or less. Thus, the cost of these components in automotive quantities is not readily available, since they typically are not in production at present.

One currently produced component that provides a reference point for thyristor pricing is ON Semiconductor's MCR265-4 thyristor. [31] The MCR265-4, rated for $V_{DRM} / V_{RRM} = 100$ V and $I_{T(AV)} = 35$ A ($I_{T(RMS)} = 55$ A), provides a close approximation for the electrical characteristics required for this application. This component is manufactured in a plastic TO-220AB package, and prices at around \$1.42 in small consumer quantities and at \$0.70 in high volume automotive quantities. Another commercially available component with similar electrical ratings is International Rectifier's 50RIA10 thyristor, rated for $V_{DRM} / V_{RRM} = 100$ V and $I_{T(AV)} = 50$ A ($I_{T(RMS)} = 80$ A). [32] By contrast, this component is available in a metal stud TO-208AC package, and prices at \$10.34 in retail quantities and at \$6.00 in high volumes. These electrical and price characteristics are summarized in Table 7.3.

	ON Semiconductor MCR265-4	International Rectifier 50RIA10
Packaging	TO-220AB plastic	TO-208AC metal stud
V_{DRM} / V_{RRM}	100 V	100 V
$I_{T(AV)}$	35 A	50 A
Retail Price ⁴	\$1.42	\$10.34
Volume Price ⁵	\$0.70	\$6.00

Table 7.3: Electrical characteristics and pricing data for the ON Semiconductor MCR265-4 and International Rectifier 50RIA10 SCR thyristors. These two thyristors have voltage and current ratings similar to those needed for dual-voltage automotive alternator applications.

The significant difference in price between these two components can be attributed largely to the difference in packaging. The 55 A_{RMS} MCR265-4 thyristor has the largest current rating offered by ON Semiconductor in a thyristor, but is only marginally acceptable for use at the current levels needed for this application. The move to a thyristor with larger current-carrying capabilities would require a move to a large plastic or metal stud package, such as the IR 50RIA10 device. This package change would serve to at least double the cost, as is evidenced by the price difference between the MCR265-4 and the 50RIA10. [33]

Thyristors manufactured specifically for this application would likely be constructed using a JEDEC disk button (DB) or press fit (PF) package, both of which are commonly used for alternator diodes. [34, 35] In the case of alternator diodes, these devices are typically assembled into three-device subassemblies. Subassemblies intended for the lower half of the rectifier bridge have the devices' anodes connected together, while those intended for the upper half of the rectifier bridge have the cathodes connected together. Thyristors in DB or PF packages do not exist at present, making the pricing of these components in automotive quantities difficult. However, such components would be similar in shape and electrical rating to the metal stud package (JEDEC PM) already available, so the available pricing information for the 50RIA10 metal stud device is assumed to provide a ceiling for the prices of thyristors in the more suited DB or PF packages.

Based on this analysis, Table 7.4 provides price boundaries for the power devices used to implement the additional half-bridge and full-bridge rectifiers for the dual-rectifier and dual-stator alternators respectively. These prices assume the ceiling set by the 50RIA10 device, whose electrical characteristics and packaging are similar to those required by thyristors specifically constructed for this application. Actual prices for the thyristors of interest are likely to be lower, given that the 50RIA10 is manufactured in a metal, threaded stud package with more complexity than would be required by a device designed for automotive alternator use.

⁴ Represents minimum quantity pricing. Prices obtained from Avnet Marshall Industries on 6/20/00.

⁵ Represents high volume pricing appropriate for automotive applications, as provided by the manufacturer.

	Additional Components	Power Electronics Cost Ceiling
Dual-Rectifier Alternator	three thyristors used to implement 14V half-bridge rectifier	\$18.00
Dual-Stator Alternator	six thyristors used to implement 14V full-bridge rectifier	\$36.00

Table 7.4: Price boundaries for the additional power electronics components required to implement the dual-rectifier and dual-stator alternators, based on high-volume price quotes for the IR 50RIA10 thyristor.

A method for bounding thyristor price which is not explored in this thesis involves extrapolating price based on the silicon cost and packaging cost of devices presently in production. Silicon costs incurred by converting a diode to a thyristor can be estimated by pricing similarly rated diodes and thyristors in similar plastic packaging, and then estimating the cost delta incurred by implementing the additional thyristor functionality. Packaging costs can also be bounded by pricing alternator diodes currently produced in the appropriate DB or PF packages. Using this information, pricing data for diodes currently in production can be supplemented with the estimated cost delta incurred by the additional functionality of the silicon in order to produce a price bound more in line with the realistic volume prices of automotive alternator thyristors. This price bound is likely to be much smaller than \$6 per part, which was obtained for a thyristor in a more costly threaded metal stud package.

It should be mentioned that the diode rectifiers undergo little change during the conversion from 14V to 42V. For a constant power level, the current carrying requirements of each diode decrease by a factor of three between 14V and 42V. Diodes also typically have voltage ratings well above the bus voltage in order to protect the device in the event of high-voltage load dump transients. Thus, to first order, the change in rectifier cost is small as the full-bridge diode rectifier is converted for 42V operation.

7.3 Passive Filter Cost and Weight

One central theme of this research has been the evaluation of passive filtering solutions for dual-voltage alternators. This evaluation was performed under the supposition that passive filter stages provide the most economical filtering solution if they can be designed with reasonable costs and weights. This filtering results presented in Chapter 5 reveal that, in order to produce the desired levels of attenuation while passing rated current to each bus, passive filtering stages appear to be quite unreasonable for the dual-rectifier alternator but very appropriate for the dual-stator alternator. This is illustrated by the bills of materials for the two dual-rectifier and dual-stator filters as provided in Tables 7.5 and 7.6, and by the volume, weight, and cost summaries provided for each filter in Table 7.7. Illustrations of the required filtering stages for each architecture are also provided in Figures 7.3 and 7.4.

Dual-Rectifier Component Description	Quantity	Total Weight	Cost
14V L ₂ silicon steel C core inductor	1	9047 grams	\$118.06
14V L ₁ silicon steel C core inductor	1	358 grams	\$14.80
8200 μ F aluminum electrolytic capacitor for 14V filter	7	287 grams (41 grams each)	\$15.89 (\$2.27 each)
42V L ₂ silicon steel C core inductor	1	102 grams	\$2.60
42V L ₁ MPP toroidal inductor	1	39 grams	\$1.47
3900 μ F aluminum electrolytic capacitor for 42V filter	7	336 grams (48 grams each)	\$17.57 (\$2.51 each)

Table 7.5: Estimated weight and cost of passive filtering components required to implement the dual-rectifier 14V and 42V ripple filters. (Note: Damping resistances are not included, since their contribution to total weight and cost is negligible.)

Dual-Stator Component Description	Quantity	Total Weight	Cost
680 μ F aluminum electrolytic capacitor for 14V filter	2	20 grams (10 grams each)	\$1.18 (\$0.59 each)
180 μ F aluminum electrolytic capacitor for 42V filter	1	4 grams	\$0.43

Table 7.6: Weight and cost of passive filtering components required to implement the dual-stator 14V and 42V ripple filters. (Note: Damping resistances are not included, since their contribution to total weight and cost is negligible.)

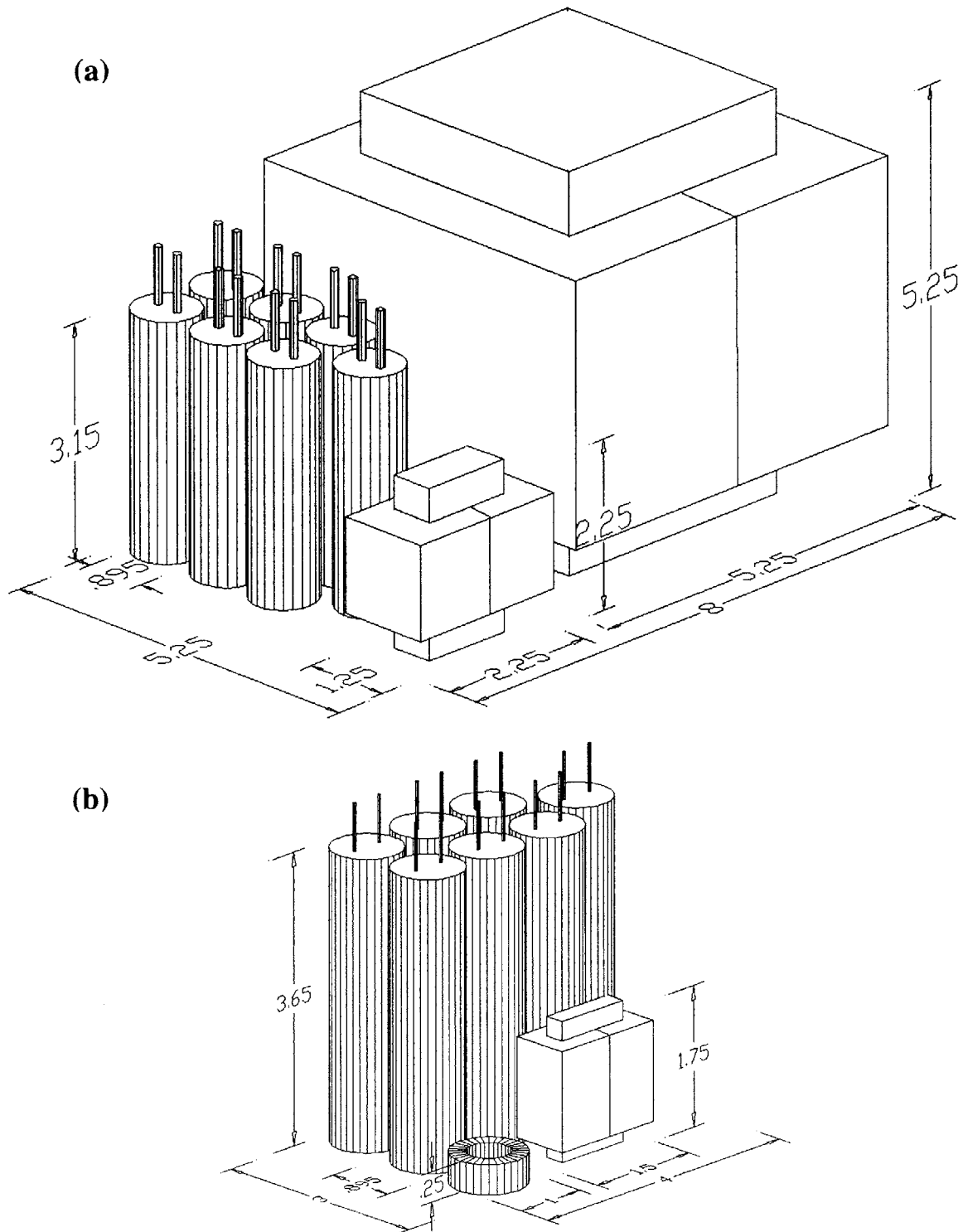


Figure 7.3: Scale drawing of the dual-rectifier voltage ripple filter: (a) 14V filter; (b) 42V filter. All dimensions are shown in inches. (Courtesy M. Astley)

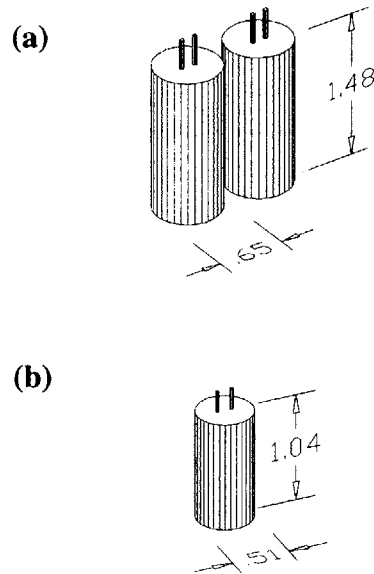


Figure 7.4: Scale drawing of the dual-stator voltage ripple filtering capacitors: (a) 14V filtering capacitors, (b) 42V filtering capacitors. All dimensions are shown in inches. Drawing scale is same as Figure 7.3. (Courtesy M. Astley)

Filter	Total Volume	Total Weight	Total Cost
14V Dual-Rectifier Filter	2236 cm ³	9692 grams	\$148.75
42V Dual-Rectifier Filter	298 cm ³	477 grams	\$21.64
14V Dual-Stator Filter	16 cm ³	20 grams	\$1.18
42V Dual-Stator Filter	4 cm ³	4 grams	\$0.43

Table 7.7: Total volume, weight, and cost per filter for the 14V and 42V dual-rectifier and dual-stator voltage ripple filters.

Note that the 14V dual-rectifier filter is by far the larger and more impractical of the dual-rectifier filters, due in part to the more restrictive ripple specification imposed on the 14V rectifier output at 2000 rpm alternator shaft speed. Recall that this filter is sized for a maximum of 1680 W power delivery to the 14V bus, which is only achievable with a dual-rectifier alternator rated for three times the power capacity of the simple rewind 42V machine. Thus, the actual dual-rectifier filter used with the simple rewind 42V machine will be significantly smaller due to the reduction of power output capability that occurs when the rewind 42V machine is providing power to a 14V load. By contrast, the dual-stator filters add very little cost and weight to the electrical system, since only capacitors are required to attenuate ripple

produced by the dual-stator's two independent full-bridge rectifiers. Thus, these results clearly illustrate that passive filters provide a less-than-optimal solution for ripple filtering with the dual-rectifier alternator. However, filtering capacitors are appropriate for voltage ripple attenuation with the dual-stator alternator, and hinder the overall viability of the dual-stator alternator very little.

7.4 Summary

This chapter has served to enumerate the relevant costs and weights involved with the implementation of dual-rectifier and dual-stator alternators. While the goal of this chapter was not to estimate the all-inclusive manufacturing cost of each architecture, this chapter did identify cost and weight trends that exist with the alternator machine, thyristors in each architecture's controlled rectifier, and passive filtering stages required to attenuate voltage ripple down to acceptable limits. With regard to machine implementation, it was shown that the dual-rectifier's 42V single-stator machine can be constructed by simply rewinding the present 14V alternator's stator and rotor with three times the number of turns having one-third the cross-sectional area. However, this machine maintains the power output capability of the present 14V alternator only when the alternator is exclusively powering a 42V load, and the machine's power output capability decreases by nearly two-thirds when the machine is exclusively powering a 14V load. Neglecting the controllability issues discussed in Chapter 6, reasonable estimates of the dual-stator machine's stator cost and weight were obtained by assuming the machine's 14V stator is wound with one-third the number of 42V turns using wire having three times the cross-sectional area. This winding scenario effectively doubles the required stator slot area and increases the stator's cost and weight by almost 50%. The addition of a second stator under this scenario also increases the cost and weight of copper windings by slightly more than 100%, due to increases in the second winding's mean path length and total copper volume. This chapter also examined the potential cost of thyristors designed for dual-voltage alternator controlled rectifier applications. Thyristors of the appropriate voltage and current rating are not widely produced at present due to the lack of low-voltage, high-current thyristor applications. Thus, truly satisfactory indications of thyristors have proven difficult to ascertain. For the application envisioned here, estimates all the way from \$1.00 to \$6.00 per part can be defended. This important cost parameter strongly influences the viability of the dual-stator architecture and thus deserves further investigation. For the dual-rectifier configuration, accurate estimates of thyristor cost are less important, both because fewer parts are required and because the costs of other components dominate the overall cost of the architecture. Finally, the costs and weights required to implement passive ripple-filtering stages for each architecture were analyzed. This analysis quantified the degree to which filtering cost and weight severely limit the practicality of the dual-rectifier alternator. By contrast, the analysis also illustrated that filtering capacitors affect the total cost and weight of the dual-stator alternator by very little. Ultimately, this chapter was able to quantify significant limitations to the practicality of the dual-rectifier alternator, while providing evidence to support the viability of the dual-stator alternator for automotive dual-voltage power supply applications.

Conclusions and Further Research

Previous work on dual-voltage automotive power generation systems has focused almost exclusively upon a dc / dc converter-based architecture. This is because the dc / dc converter provides a well studied power conversion solution that has been widely and successfully implemented in other power conversion applications. However, the dc / dc converter presents a significant size, weight, and cost burden to the automobile, motivating the search for less taxing dual-voltage power generation options. Two such options, the dual-rectifier alternator and dual-stator alternator, have been explored in this thesis. This study involved determining each architecture's baseline electrical performance characteristics and evaluating the potential that each holds for becoming a cost-effective dual-voltage power generation option. This chapter reviews the specific objectives with which this evaluation was approached, and summarizes conclusions reached regarding the filterability of voltage ripple, power output constraints, inherent weight and cost, and special implementation issues for each architecture. It then discusses issues relating to the viability of dual-voltage alternator architectures which are deserving of further research.

8.1 Thesis Conclusions

The goal of this thesis has been to analyze the efficacy of the dual-rectifier and dual-stator alternators as potential solutions for dual-voltage power generation within 42V / 14V automotive electrical systems. In accomplishing this goal, this thesis sought to fulfill five primary objectives:

- Analyze and quantify unfiltered voltage ripple produced by dual-voltage alternators.
- Design filtering solutions to attenuate this ripple down to predetermined limits of acceptability.
- Discuss implementation issues that effect the viability of dual-voltage alternators, such as the application of switched-mode rectification (SMR) techniques, dual-stator controllability as a function of turns ratio, and the appropriateness of aluminum electrolytic capacitors for automotive applications.
- Explore how machine design and winding strategy affect the power output characteristics of the dual-rectifier and dual-stator alternators.

- Analyze relevant cost and weight issues for dual-rectifier and dual-stator alternators meeting minimum performance voltage ripple specifications.

The conclusions reached with regard to each objective are enumerated below.

8.1.1 Unfiltered Voltage Ripple Characteristics

Voltage ripple is a significant issue with the dual-rectifier alternator, due to the manner in which the 42V full-bridge rectifier and 14V half-bridge rectifier switch full load current back and forth between the two buses. This switched current creates large fundamental voltage ripple harmonics that occur at very low frequencies on the order of the electrical frequency of the machine. Peak-to-peak voltage ripple is dominated in most cases by reverse-recovery transients that occur as these large phase currents are switched between diodes in the 42V rectifier and their corresponding thyristors in the 14V rectifier. Peak-to-peak ripple is significant both when the battery is connected (>20 Vpp on both buses) and when it is disconnected (>25 Vpp on 14V bus, >100 Vpp on 42V bus).

By comparison, voltage ripple is much less of an issue with the dual-stator alternator. This is because the two rectifiers are connected to two distinct sets of stator windings, and no current is shared between the two rectifiers as in the dual-rectifier case. The voltage ripple seen at the 42V rectifier outputs is indicative of typical six-pulse voltage ripple, while the ripple seen at the 14V rectifier outputs results from phase-angle control of a full-bridge thyristor rectifier. Voltage ripple for each bus is below the specified limits when the batteries are connected, and becomes significant only when the battery is removed from either bus.

8.1.2 Filtering Solutions Producing Acceptable Attenuation

Single stage LC filters were designed to attenuate dual-rectifier voltage ripple down to acceptable limits, based upon the peak current carrying requirement for inductors L_1 and L_2 and the ripple current carrying requirement for the shunt capacitors. The large amount of dc current (120 A at 10000 rpm) delivered to the 14V bus mandates large silicon steel C cores with high energy storage capabilities for use in each dual-rectifier filter. In addition, the substantial amount of ripple current and large capacitance required to produce the desired attenuation mandates the use of multiple aluminum electrolytic capacitors (seven in the designs presented in Chapter 5) for each bus.

However, the dual-stator alternator's voltage ripple is successfully attenuated with only the addition of relatively small amounts of capacitance to each bus. According to the dual-stator alternator model used in this research, ripple needs no attenuation while the battery remains connected, and only small amounts of attenuation when either battery becomes disconnected. This attenuation is realized with the addition of two parallel electrolytic capacitors to the 14V rectifier output and a single capacitor to the 42V rectifier output.

8.1.3 Implementation Issues Affecting Dual-Voltage Alternator Viability

The use of new switched-mode rectification was previewed in terms of the benefits these techniques provide to dual-voltage alternators. Load matching SMR techniques significantly increase the amount of power that can be obtained from the alternator. Additionally, they allow the frequency of voltage ripple to be increased by several orders of magnitude to frequencies on the order of the switching frequency of the FETs. This potentially decreases the size of passive filtering components needed to attenuate voltage ripple at the rectifier outputs, and thus increases the viability of the dual-rectifier alternator.

Examined next was the ability of the dual-stator alternator to simultaneously regulate its two outputs over a wide range of loading scenarios. Simultaneous controllability of the dual-stator alternator's two outputs was found to be an issue when the 42V bus is very lightly loaded and the 14V bus is very heavily loaded. This issue is generally mitigated by decreasing the number of turns in the 42V stator winding relative to the case in which the 42V stator is wound with three times the number of 14V turns. This effectively decreases the stator – stator turns ratio and increases the field current level for a given amount of loading on the 42V bus. The 14V internal voltage increases in concert with the field current level and enables more current to be delivered to the 14V bus for a given amount of loading on the 42V bus. However, a possible disadvantage of decreasing the number of 42V stator turns occurs as the current-output capability of the 42V stator is potentially reduced for a heavily loaded 42V bus at low alternator shaft speeds. Yet for the case considered here, a relatively modest change in the stator – stator turns ratio from 3:1 to 2.5:1 provided adequate control ability with modest reduction in the power capacity of the machine at idle speed.

Also examined was the suitability of aluminum electrolytic capacitor lifetimes for automotive applications. The lifetime of aluminum electrolytic capacitors bears a strong relationship to the capacitor's ambient operating temperature and to the capacitor's operating voltage relative to its rated voltage. When appropriately selected, aluminum electrolytic capacitors exhibit expected operating lifetimes on the order of the operating lifetime of the vehicle. Thus, aluminum electrolytic capacitors cannot be summarily eliminated from consideration for underhood automotive applications strictly on the basis of lifetime.

8.1.4 Power Output Capacity Issues Arising with Dual-Voltage Alternators

The dual-rectifier alternator is based upon a 42V single-stator machine whose output power characteristics vary significantly with output voltage. Specifically, the 42V single-stator machine loses nearly two-thirds of its power output capacity as the alternator's output voltage is reduced from 42V to 14V. This has significant ramifications for the dual-rectifier alternator, which modulates the machine's output voltage between 42V and 14V depending on the degree of loading attached to each bus. When the automobile's total load exists mostly on the 14V bus, the average voltage seen by the single-stator machine is closer to 14V and the output power obtainable from the machine is greatly reduced. However, when the 42V bus's load is predominant, the average voltage seen by the machine is closer to 42V and the output power

obtainable from the machine is closer to the machine's maximum rating. Thus, the dual-rectifier alternator provides a practical dual-voltage power supply solution only when the total automotive load exists primarily on the 42V bus.

The dual-stator alternator, by contrast, relies on two distinct sets of stator windings to individually power the 42V and 14V buses. As explained above, simultaneous controllability issues arising for a lightly loaded 42V bus and a heavily loaded 14V bus are resolved by decreasing the number of turns in the 42V stator winding. However, decreasing the number of 42V stator turns also reduces the power output capacity of the 42V stator by decreasing the maximum 42V internal voltage level producible with full field current. Thus, a design tradeoff is brought about between the maximum output power capacity of the 42V bus and the desire to successfully maintain the desired 14V bus voltage for a lightly loaded 42V bus. An optimal dual-stator machine design must therefore account for the maximum level of loading expected from each bus of the architecture in order to wind the two stators to satisfy the output power and control demands placed on the machine.

8.1.5 Cost and Weight Issues Involved with Dual-Voltage Alternator Implementation

The 42V single-stator machine upon which the dual-rectifier is based can be implemented by rewinding the present 14V machine. However, only approximately one-third of the 14V alternator's level of power production is available from the rewound 42V machine when the alternator exclusively powers a 14V load. This implies that the alternator must be sized three times greater than the 14V machine in order to supply the same level of power to the 14V load with the dual-rectifier implementation. The dual-stator machine is implemented by winding the machine with a 42V stator winding and a 14V stator winding with some established turns ratio. Assuming a 3:1 ratio, the machine can be constructed by doubling the slot area of the 14V machine, which serves to increase the stack cost and weight by almost 50% and the copper winding cost and weight by slightly over 100%.

Thyristors with voltage and current ratings appropriate for dual-voltage alternator controlled rectifier applications are generally not widely produced at present, due to a lack of applications where such devices are economically optimal. One thyristor with electrical characteristics similar to those desired for this application is available in high-volume quantities of \$6 per device. However, this device is available in a threaded metal-stud package as opposed to a more appropriate plastic DB or PF package, suggesting that thyristors specifically manufactured for dual-voltage alternator applications should be producible for well below this margin. Also, the diode rectifier undergoes only small price changes. This is because the current carrying requirements for a constant load level are smaller with the 42V rectifier, and such devices are already significantly overrated for voltage due to the threat of load dump transients.

The analysis of passive filter price and weight characteristics further emphasizes the impracticality of the dual-rectifier alternator in the configuration considered for this research. Conversely, the capacitors required to filter voltage ripple produced by the dual-stator alternator

add little to the total cost and weight of the alternator and thereby impinge on the viability of the architecture very little.

8.2 Further Research

Future work in the area of dual-voltage alternator development should focus on strategies for attenuating voltage ripple while minimizing the cost and weight that filtering components add to the architecture. Clearly, passive filtering strategies provide an impractical solution for dual-rectifier alternator ripple filtering, due to the low frequency of ripple and the large amounts of dc current that filtering inductors are required to carry. One strategy for dealing with the low ripple frequency involves the implementation of switched-mode rectifier (SMR) techniques, which both increase the output power capability of the machine and increase the fundamental frequency of voltage ripple. The increase in ripple frequency allows for an increase in the required filter's corner frequency, which allows for a reduction in the size of filtering components. An investigation into the applicability of active filtering techniques is also warranted to determine the degree to which active filtering components can reduce the cost and weight of the necessary filtering stages (see [36]).

One other topic worthy of investigation involves the choice of active switching components used to implement each architecture's controlled rectifier. This research was approached under the premise that thyristors would provide the most economical solution for controlled rectifier implementations if they are designed and produced for high volume automotive applications. However, one semiconductor manufacturer suggests that thyristors redesigned and produced in automotive quantities would provide no economic advantage relative to FETs, which provide greater functionality and are much more widely produced than thyristors. Furthermore, the use of FETs enables the designer to integrate SMR techniques and load dump control techniques into the controlled rectifier design. Thus, further dual-voltage alternator research should investigate the economic efficacy of FETs as well as thyristors for implementation of the controlled rectifiers.

Finally, issues related to the independent controllability of the dual-stator alternator under its expected range of loading conditions are worthy of more rigorous study. This thesis illustrated that regulation of a heavily loaded 14V bus in light of a lightly loaded 42V bus becomes an issue when the two stators are wound with a 3:1 stator – stator turns ratio. A solution to this issue was discussed in terms of the internal voltage required to source the desired amount of current from each stator. However, this issue is complicated by the load-dependent mutual coupling that occurs between the two stators. Thus, a specific design strategy is needed to size the two stator windings in terms of the simultaneous loading requirements of the dual-stator alternator's two output buses.

The ultimate viability test for dual-voltage alternators occurs as the cost and performance of the dual-rectifier and dual-stator alternators are evaluated relative to the dc / dc converter.

Consequently, further analyses of dual-voltage alternator machine design, power electronics components, and filtering techniques must focus on minimizing cost and maximizing performance. While further research may develop dual-rectifier and dual-stator designs that are judged electrically feasible for dual-voltage automotive applications, both must also be proven economically feasible in order to be employed in future automotive electrical systems. Thus, further research concerning the dual-rectifier and dual-stator alternators is valuable only to the degree that it facilitates electrically acceptable power generation solutions with the least amount of added weight and cost.

Saber Automotive Electrical Models

A.1 Saber MAST Code for Single-Stator Alternator

```
#####
#### Three Phase Alternator Model #####
#### Reference: Fitzgerald, Kingsley and Umans #####
#### "Electric Machinery", Chapter 7 #####
#### Vahe Caliskan, MIT #####
#### Email: vahe@mit.edu #####
#### WWW: http://web.mit.edu/vahe/www/home.html #####
#### Filename: ~/Circuits/NewAlternator/alt_3phase.sin #####
#### Created: November 2, 1997 #####
#####

template alt_3phase shaft a b c n fp fm = rs, lls, lms, rr, llr, lmr, p, theta0

rotational_vel shaft # rotor mechanical angular velocity connection

electrical a, # phase "a" voltage of the stator
           b, # phase "b" voltage of the stator
           c, # phase "c" voltage of the stator
           n, # Neutral terminal of alternator
           fp, # field "positive" terminal
           # Usually connected to the bp terminal (of rectifier)
           fm # field "minus" or "negative" terminal
           # Usually connected to the bm terminal (of rectifier)

number rs= 33m, # Stator winding resistance
       lls= 18u, # Stator leakage inductance
       lms= 180u, # Stator magnetizing inductance
       rr= 3.44, # Rotor winding resistance
       llr= 200m, # Rotor leakage inductance
       lmr= 300m, # Rotor magnetizing inductance
       p= 12, # Number of poles
       theta0= 0, # Initial rotor angle.

{

<consts.sin

number p2, # Number of pole pairs
       phase, # phase angle between stator windings (= 2*pi/3 = 120deg)
       ls, # Stator winding self inductance (= lls + lms)
       lr, # Rotor winding self inductance (= llr + lmr)
       lss, # Stator-Stator mutual inductance (= lms * cos(phase))
       m # Peak stator-rotor mutual inductance (= sqrt(lms*lmr))
```

```

val f      lambda_a,    # Flux linkage of "a" winding of stator.
           lambda_b,    # Flux linkage of "b" winding of stator.
           lambda_c,    # Flux linkage of "c" winding of stator.
           lambda_r     # Flux linkage of of rotor.

val l      lar,        # angle dependent mutual inductance between stator "a" and rotor
           lbr,        # angle dependent mutual inductance between stator "b" and rotor
           lcr,        # angle dependent mutual inductance between stator "c" and rotor
           lra,        # angle dependent mutual inductance between rotor and stator "a"
                   # (= lar)
           lrb,        # angle dependent mutual inductance between rotor and stator "b"
                   # (= lbr)
           lrc         # angle dependent mutual inductance between rotor and stator "c"
                   # (= lcr)

val w_radps omega_r    # rotor angular velocity
var ang_rad  theta_r   # rotor angular position (variable)
val ang_rad  theta_e   # rotor electrical angle (calculated)
val ang_rad  theta_el

# Branch current, voltage relationships for stator phases and rotor
branch ia=i(a->n),    va=v(a,n)
branch ib=i(b->n),    vb=v(b,n)
branch ic=i(c->n),    vc=v(c,n)
branch ir=i(fp->fm), vr=v(fp, fm)

# Define parameters
parameters {
    p2 = p/2          # Number of pole pairs
    phase = 2*math_pi/3 # phase angle between stator windings
    ls = lls + lms    # Self inductance of the stator
    lr = llr + lmr    # Self inductance of the rotor
    lss = -0.5*lms    # Stator-stator mutual inductance
    m = sqrt(lmr*lms) # Peak mutual inductance between stator and
                    # rotor
}

values {
    # Evaluate rotor angular velocity and electrical angle
    omega_r = w_radps(shaft) # rotor angular velocity
    theta_e = theta_r*p2     # rotor electrical angle

    if (theta_e > 500*2*math_pi) {
        theta_e = theta_e - 500*2*math_pi
    }
    else theta_e = theta_e

    # Evaluate angle-dependent mutual inductances
    lar = m*cos(theta_e)
    lbr = m*cos(theta_e - phase)
    lcr = m*cos(theta_e + phase)
    lra = lar
    lrb = lbr
    lrc = lcr

    # Evaluate flux linkages in the stator and rotor
    lambda_a = ls*ia + lss*ib + lss*ic + lar*ir

```

```
lambda_b = lss*ia + ls*ib + lss*ic + lbr*ir
lambda_c = lss*ia + lss*ib + ls*ic + lcr*ir
lambda_r = lra*ia + lrb*ib + lrc*ic + lr*ir

}

control_section{
    initial_condition(theta_r,theta0)
}

equations {
    va = rs*ia + d_by_dt(lambda_a)
    vb = rs*ib + d_by_dt(lambda_b)
    vc = rs*ic + d_by_dt(lambda_c)
    vr = rr*ir + d_by_dt(lambda_r)

    theta_r : d_by_dt(theta_r) = omega_r
}

}
```

A.2 Saber MAST Code for Dual-Stator Alternator

```
#####
### Three Phase Dual Wound Alternator Model #####
### Three phase sets offset by 0 degrees #####
### #####
### Vahe Caliskan, MIT #####
### Email: vahe@mit.edu #####
### WWW: http://web.mit.edu/vahe/www/home.html #####
### Created: November 11, 1998 #####
### Last Modified: December 2, 1998 #####
### #####
#####

template alt_dual_wound shaft a1 b1 c1 a2 b2 c2 fp fm n1 n2 =
rs1, rs2, lls1, lls2, lms1, lms2, lg1, lg2, rf, llf, lmf, p, theta0

rotational_vel      shaft # rotor mechanical angular velocity connection

electrical  a1,      # phase "a" voltage of the stator 1
            b1,      # phase "b" voltage of the stator 1
            c1,      # phase "c" voltage of the stator 1
            a2,      # phase "a" voltage of the stator 2
            b2,      # phase "b" voltage of the stator 2
            c2,      # phase "c" voltage of the stator 2
            fp,      # field "positive" terminal
            fm,      # field "minus" or "negative" terminal
            n1,      # neutral terminal of stator 1
            n2       # neutral terminal of stator 2

number       rs1 =    33m,      # Stator 1 winding resistance
            rs2 =   9*33m,      # Stator 2 winding resistance
            lls1 =   15u,      # Stator 1 leakage inductance
            lls2 =  9*15u,      # Stator 2 leakage inductance
            lms1 =  105u,      # Stator 1 magnetizing inductance
            lms2 = 9*105u,      # Stator 2 magnetizing inductance
            lg1  =   10u,      # Stator 1 saliency inductance magnitude
            lg2  =  9*10u,      # Stator 2 saliency inductance magnitude
            rf   =  9*3.44,     # Field (rotor) winding resistance
            llf  =  9*200m,     # Field (rotor) leakage inductance
            lmf  =  9*150m,     # field (rotor) magnetizing inductance
            p    =    12,      # Number of poles
            theta0 =  0,      # Initial rotor angle

{

<consts.sin

number      p2,      # Number of pole pairs
            phase,   # phase angle between stator windings (= 2*pi/3 = 120deg)
            ls1,     # Stator 1 winding self inductance, ignoring saliency
                  # (= lls1 + lms1)
            ls2,     # Stator 2 winding self inductance, ignoring saliency
                  # (= lls2 + lms2)
            lf,      # Rotor winding self inductance (= llf + lmf)
            lms11,   # peak stator 1 - stator 1 mutual inductance, neglecting
                  # saliency (= lms1*cos(phase))
```

```

lms22,      # peak stator 2 - stator 2 mutual inductance, neglecting
             # saliency (= lms2*cos(phase))
lms12,      # peak stator 1 - stator 2 mutual inductance, neglecting
             # saliency (= sqrt(lms1*lms2))
lms12p,     # peak stator 1 - stator 2 mutual inductance, neglecting
             # saliency (= lms12*cos(phase))
lg12,      # peak stator 1 - stator 2 saliency inductance magnitude
             # (= sqrt(lg1*lg2))
m1,        # Peak stator 1-rotor mutual inductance
             # (= sqrt(lms1*lmf))
m2         # Peak stator 2-rotor mutual inductance
             # (= sqrt(lms2*lmf))

val f      lambda_a1, # Flux linkage of "a" winding of stator 1.
            lambda_b1, # Flux linkage of "b" winding of stator 1.
            lambda_c1, # Flux linkage of "c" winding of stator 1.
            lambda_a2, # Flux linkage of "a" winding of stator 2.
            lambda_b2, # Flux linkage of "b" winding of stator 2.
            lambda_c2, # Flux linkage of "c" winding of stator 2.
            lambda_f   # Flux linkage of of rotor.

val l      la1a1,     # stator a1-a1 self inductance
            la2a2,     # stator a2-a2 self inductance
            lb1b1,     # stator a1-a1 self inductance
            lb2b2,     # stator b2-b2 self inductance
            lc1c1,     # stator c1-c1 self inductance
            lc2c2,     # stator c2-c2 self inductance
            lff,       # rotor self inductance
            la1b1,     # stator a1-b1 mutual inductance (same winding)
            la2b2,     # stator a2-b2 mutual inductance (same winding)
            la1c1,     # stator a1-c1 mutual inductance (same winding)
            la2c2,     # stator a2-c2 mutual inductance (same winding)
            lb1c1,     # stator b1-c1 mutual inductance (same winding)
            lb2c2,     # stator b2-c2 mutual inductance (same winding)
            la1a2,     # stator a1-a2 mutual inductance
            lb1b2,     # stator b1-b2 mutual inductance
            lc1c2,     # stator c1-c2 mutual inductance
            la1b2,     # stator a1-b2 mutual inductance
            la2b1,     # stator a2-b1 mutual inductance
            lc2a1,     # stator c2-a1 mutual inductance
            lc1a2,     # stator c1-a2 mutual inductance
            lb1c2,     # stator b1-c2 mutual inductance
            lb2c1,     # stator b2-c1 mutual inductance
            lb1a1,     # lb1a1 = la1b1
            lb2a2,     # lb2a2 = la2b2
            lc1a1,     # lc1a1 = la1c1
            lc2a2,     # lc2a2 = la2c2
            lc1b1,     # lc1b1 = lb1c1
            lc2b2,     # lc2b2 = lb2c2
            la2a1,     # la2a1 = la1a2
            lb2b1,     # lb2b1 = lb1b2
            lc2c1,     # lc2c1 = lc1c2
            lb2a1,     # lb2a1 = la1b2
            lb1a2,     # lb1a2 = la2b1
            la1c2,     # la1c2 = lc2a1
            la2c1,     # la2c1 = lc1a2
            lc2b1,     # lc2b1 = lb1c2
            lc1b2,     # lc1b2 = lb2c1

```

```

    lfa1,      # rotor-stator winding a1 mutual inductance
    lfb1,      # rotor-stator winding b1 mutual inductance
    lfc1,      # rotor-stator winding c1 mutual inductance
    lfa2,      # rotor-stator winding a2 mutual inductance
    lfb2,      # rotor-stator winding b2 mutual inductance
    lfc2,      # rotor-stator winding c2 mutual inductance
    la1f,      # la1f = lfa1
    lb1f,      # lb1f = lfb1
    lc1f,      # lc1f = lfc1
    la2f,      # la2f = lfa2
    lb2f,      # lb2f = lfb2
    lc2f,      # lc2f = lfc2

val w_radps  omega_r      # rotor angular velocity

var ang_rad  theta_r      # rotor angular position (variable)
val ang_rad  theta_e      # rotor electrical angle (calculated)

# Branch current, voltage relationships for stator phases and rotor
branch ial=i(a1->n1),     val=v(a1,n1)
branch ibl=i(b1->n1),     vb1=v(b1,n1)
branch icl=i(c1->n1),     vc1=v(c1,n1)
branch ia2=i(a2->n2),     va2=v(a2,n2)
branch ib2=i(b2->n2),     vb2=v(b2,n2)
branch ic2=i(c2->n2),     vc2=v(c2,n2)
branch ifield=i(fp->fm), vf=v(fp,fm)

# Define parameters
parameters {
    p2      = p/2          # Number of pole pairs
    phase   = 2*math_pi/3 # phase angle between stator windings
    ls1     = lls1 + lms1  # Self inductance of stator 1, neglecting
                          # saliency
    ls2     = lls2 + lms2  # Self inductance of stator 2, neglecting
                          # saliency
    lf      = llf + lmf    # Self inductance of the rotor
    lms11   = lms1*cos(phase) # peak stator 1 - stator 1 mutual inductance,
                          # neglecting saliency
    lms22   = lms2*cos(phase) # peak stator 2 - stator 2 mutual inductance,
                          # neglecting saliency
    lms12   = sqrt(lms1*lms2) # peak stator 1 - stator 2 mutual inductance,
                          # neglecting saliency
    lms12p  = lms12*cos(phase) # peak stator 1 - stator 2 mutual inductance,
                          # neglecting saliency
    lg12    = sqrt(lg1*lg2) # peak stator 1 - stator 2 saliency inductance
                          # magnitude
    m1      = sqrt(lmf*lms1) # Peak stator 1-rotor mutual inductance
    m2      = sqrt(lmf*lms2) # Peak stator 2-rotor mutual inductance
}

values {
    # Evaluate rotor angular velocity and electrical angle
    omega_r = w_radps(shaft) # rotor angular velocity
    theta_e = theta_r*p2     # rotor electrical angle

    # Evaluate angle-dependent stator and rotor self inductances
    la1a1 = ls1 + lg1*cos(2*theta_e)
    la2a2 = ls2 + lg2*cos(2*theta_e)
    lb1b1 = ls1 + lg1*cos(2*theta_e + phase)

```

```

lb2b2 = ls2 + lg2*cos(2*theta_e + phase)
lc1c1 = ls1 + lg1*cos(2*theta_e - phase)
lc2c2 = ls2 + lg2*cos(2*theta_e - phase)
lff   = lf

# Evaluate angle dependent stator-stator mutual inductances
la1b1 = lms11 + lg1*cos(2*theta_e - phase)
la2b2 = lms22 + lg2*cos(2*theta_e - phase)
la1c1 = lms11 + lg1*cos(2*theta_e + phase)
la2c2 = lms22 + lg2*cos(2*theta_e + phase)
lb1c1 = lms11 + lg1*cos(2*theta_e)
lb2c2 = lms22 + lg2*cos(2*theta_e)
la1a2 = lms12 + lg12*cos(2*theta_e)
lb1b2 = lms12 + lg12*cos(2*theta_e + phase)
lc1c2 = lms12 + lg12*cos(2*theta_e - phase)
la1b2 = lms12p + lg12*cos(2*theta_e - phase)
la2b1 = lms12p + lg12*cos(2*theta_e - phase)
lc2a1 = lms12p + lg12*cos(2*theta_e + phase)
lc1a2 = lms12p + lg12*cos(2*theta_e + phase)
lb1c2 = lms12p + lg12*cos(2*theta_e)
lb2c1 = lms12p + lg12*cos(2*theta_e)

lb1a1 = la1b1
lb2a2 = la2b2
lc1a1 = la1c1
lc2a2 = la2c2
lc1b1 = lb1c1
lc2b2 = lb2c2
la2a1 = la1a2
lb2b1 = lb1b2
lc2c1 = lc1c2
lb2a1 = la1b2
lb1a2 = la2b1
la1c2 = lc2a1
la2c1 = lc1a2
lc2b1 = lb1c2
lc1b2 = lb2c1

# Evaluate angle dependent rotor-stator mutual inductances
lfa1 = m1*cos(theta_e)
lfb1 = m1*cos(theta_e - phase)
lfc1 = m1*cos(theta_e + phase)
lfa2 = m2*cos(theta_e)
lfb2 = m2*cos(theta_e - phase)
lfc2 = m2*cos(theta_e + phase)
la1f = lfa1
lb1f = lfb1
lc1f = lfc1
la2f = lfa2
lb2f = lfb2
lc2f = lfc2

# Evaluate flux linkages in the stator and rotor
lambda_a1 = la1a1*ia1 + la1b1*ib1 + la1c1*ic1 + la1a2*ia2 + la1b2*ib2 +
            la1c2*ic2 + la1f*ifield
lambda_b1 = lb1a1*ia1 + lb1b1*ib1 + lb1c1*ic1 + lb1a2*ia2 + lb1b2*ib2 +
            lb1c2*ic2 + lb1f*ifield
lambda_c1 = lc1a1*ia1 + lc1b1*ib1 + lc1c1*ic1 + lc1a2*ia2 + lc1b2*ib2 +
            lc1c2*ic2 + lc1f*ifield

```

```

lambda_a2 = la2a1*ia1 + la2b1*ib1 + la2c1*ic1 + la2a2*ia2 + la2b2*ib2 +
            la2c2*ic2 + la2f*ifield
lambda_b2 = lb2a1*ia1 + lb2b1*ib1 + lb2c1*ic1 + lb2a2*ia2 + lb2b2*ib2 +
            lb2c2*ic2 + lb2f*ifield
lambda_c2 = lc2a1*ia1 + lc2b1*ib1 + lc2c1*ic1 + lc2a2*ia2 + lc2b2*ib2 +
            lc2c2*ic2 + lc2f*ifield
lambda_f  = lfa1*ia1 + lfb1*ib1 + lfc1*ic1 + lfa2*ia2 + lfb2*ib2 +
            lfc2*ic2 + lff*ifield
}

control_section{
    initial_condition(theta_r,theta0)
}

equations {
    va1 = rs1*ia1    + d_by_dt(lambda_a1)
    vb1 = rs1*ib1    + d_by_dt(lambda_b1)
    vc1 = rs1*ic1    + d_by_dt(lambda_c1)
    va2 = rs2*ia2    + d_by_dt(lambda_a2)
    vb2 = rs2*ib2    + d_by_dt(lambda_b2)
    vc2 = rs2*ic2    + d_by_dt(lambda_c2)
    vf  = rf*ifield + d_by_dt(lambda_f)

    theta_r : d_by_dt(theta_r) = omega_r
}
}

```


A.3 Saber MAST Code for Voltage Regulator

```
#####
#### Alternator Regulator Model #####
#### Using parameters found in CS-3341/51, CS-386-387, CS-3361 #####
#### Cherry Semiconductor http://www.cherrysemiconductor.com #####
#### Reference: Automotive Applications Using the Saber Simulator #####
#### Demo: Automotive Charging System #####
#### Vahe Caliskan, MIT #####
#### Email: vahe@mit.edu #####
#### WWW: http://web.mit.edu/vahe/www/home.html #####
#### Created: September 9, 1997 #####
#####

template alt_reg bp bm df = vreg, k, w

electrical bp,          # alternator "plus" connection
           bm,          # alternator "minus" or ground connection
           df           # alternator field connection

number    vreg= 14.5,   # Regulator set-point.
           k   = 10,    # Regulator low frequency gain
           w   = 100   # Regulator pole frequency (rad/sec).

{

#####
# limiting function with upper and lower limits as constant inputs
element template xlimit in out = plim, mlim

ref nu    in           # Input (must refer to a "nu" var in another template).
var nu    out          # Output.

number    plim=3,      # positive saturation limit
           mlim=1      # negative saturation limit

{
val nu    output       # Value of the output.

values {

    if (in >= mlim & in <= plim) output = in
    else if (in > plim) output = plim
    else if (in < mlim) output = mlim

}

}

equations {
    out : out = output
}
}

#####
# comparator (modulator) model used by alt_reg
#####

element template modulator control ramp out
```

```

ref nu  control          # (-) terminal control signal
ref nu  ramp             # (+) terminal periodic ramp signal
var nu  out              # Output

{
val nu  output          # Value of the output.

values {
    if (control >= ramp) output = 0
    else output = 1
}

equations {
    out : out = output
}
}

#####
# Some of the netlist based on a Saber demo: Automotive Charging System #
# #####

elec2var.p bp 0 px
elec2var.m bm 0 mx

constant.vreg vregx = vreg          # due to the r.r1, r.r2 v. divider
sum.ref vregx mx ref
sum.error px ref error1 = k1 = 1, k2 = -1
xlimit.error error1 error = mlim=-10, plim=10
lag.field error control1 = k = k, w = w          # H(s) = k/(1+s/w)
xlimit.control control1 control = mlim=0, plim=5

# 140 Hz ramp, rise/fall time ratio 17:1
src.ramp ramp = tran =(ppwl= [0,1m, 6.74m,5, 7.14m,1m])
modulator.field control ramp out

# generate binary electrical control signal v(out1,bm)
var2elec.out out out1 bm

# voltage controlled switch between field (df) and gnd (bm)
# controlling signal is from out1 to bm
sw_vc.field df bm out1 bm = model=(vt=0.5, ron=1m, roff=10meg), ic=on

# freewheeling diode (circulates field current when switch is off)
pwld.f df bp

}
#####

```

A.4 Saber MAST Code for Firing Angle Regulator

```
#####
#### Firing Angle Regulator Model #####
####
#### Vahe Caliskan, MIT #####
#### Email: vahe@mit.edu #####
#### WWW: http://web.mit.edu/vahe/www/home.html #####
#### Created: September 9, 1997 #####
#####

template fire2 omega alpha a b c pos neg t1 t2 t3 t4 t5 t6

rotational_vel omega # rotor angular velocity
rotational_ang alpha # rotor angular position
electrical a,b,c,pos,neg
state logic_4 t1,t2,t3,t4,t5,t6

{
<consts.sin

number k1,k2,k3,k4,k5
val nu s0,s1,s2,s3,s4,s5,period,td
val rad alpha1,wt

state nu s0_b,s0_a
state nu s1_b,s1_a
state nu s2_b,s2_a
state nu s3_b,s3_a
state nu s4_b,s4_a
state nu s5_b,s5_a
state nu t1fire,t2fire,t3fire,t4fire,t5fire,t6fire

parameters {
    k1=math_pi/3
    k2=2*k1
    k3=3*k1
    k4=4*k1
    k5=5*k1
}

values {
    alpha1=ang_rad(alpha)
    wt=w_radps(omega)*time
    period=(2*math_pi)/(w_radps(omega)+1n)
    td=(alpha1/(2*math_pi))*period
    s0=v(a,pos) # ref signal for t1 # s0=sin(wt)
    s1=v(neg,c) # ref signal for t2 # s1=sin(wt-k1)
    s2=v(b,pos) # ref signal for t3 # s2=sin(wt-k2)
    s3=v(neg,a) # ref signal for t4 # s3=sin(wt-k3)
    s4=v(c,pos) # ref signal for t5 # s4=sin(wt-k4)
    s5=v(neg,b) # ref signal for t6 # s5=sin(wt-k5)
}
}
```

```
#initialize all firing pulses to zero
when(dc_init) {
    schedule_event(time,t1,l4_0)
    schedule_event(time,t2,l4_0)
    schedule_event(time,t3,l4_0)
    schedule_event(time,t4,l4_0)
    schedule_event(time,t5,l4_0)
    schedule_event(time,t6,l4_0)
    schedule_event(time,t1fire,0)
    schedule_event(time,t2fire,0)
    schedule_event(time,t3fire,0)
    schedule_event(time,t4fire,0)
    schedule_event(time,t5fire,0)
    schedule_event(time,t6fire,0)
}

# thyristor #0 firing event
when(threshold(s0,0,s0_b,s0_a)) {
    if (s0_b<0 & s0_a>0) {
        schedule_event(time+td,t1,l4_1)
        schedule_event(time+td+(period*0.05),t1,l4_0)
        schedule_event(time+td,t1fire,1)
        schedule_event(time+td+5n,t1fire,0)
    }
}

# thyristor #1 firing event
when(threshold(s1,0,s1_b,s1_a)) {
    if (s1_b<0 & s1_a>0) {
        schedule_event(time+td,t2,l4_1)
        schedule_event(time+td+(period*0.05),t2,l4_0)
        schedule_event(time+td,t2fire,1)
        schedule_event(time+td+5n,t2fire,0)
    }
}

# thyristor #2 firing event
when(threshold(s2,0,s2_b,s2_a)) {
    if (s2_b<0 & s2_a>0) {
        schedule_event(time+td,t3,l4_1)
        schedule_event(time+td+(period*0.05),t3,l4_0)
        schedule_event(time+td,t3fire,1)
        schedule_event(time+td+5n,t3fire,0)
    }
}
```

```
# thyristor #3 firing event
when(threshold(s3,0,s3_b,s3_a)) {
    if (s3_b<0 & s3_a>0) {
        schedule_event(time+td,t4,l4_1)
        schedule_event(time+td+(period*0.05),t4,l4_0)
        schedule_event(time+td,t4fire,1)
        schedule_event(time+td+5n,t4fire,0)
    }
}

# thyristor #4 firing event
when(threshold(s4,0,s4_b,s4_a)) {
    if (s4_b<0 & s4_a>0) {
        schedule_event(time+td,t5,l4_1)
        schedule_event(time+td+(period*0.05),t5,l4_0)
        schedule_event(time+td,t5fire,1)
        schedule_event(time+td+5n,t5fire,0)
    }
}

# thyristor #5 firing event
when(threshold(s5,0,s5_b,s5_a)) {
    if (s5_b<0 & s5_a>0) {
        schedule_event(time+td,t6,l4_1)
        schedule_event(time+td+(period*0.05),t6,l4_0)
        schedule_event(time+td,t6fire,1)
        schedule_event(time+td+5n,t6fire,0)
    }
}
}
```


Appendix B

MATLAB Filter Component Estimation Algorithm

```
function [poles,filtdata,filtcomp,systems,data]=filter_finder(ripplespec,data)
% function [poles,filtdata,filtcomp,systems,data]=filter_finder(ripplespec,data)
%
% Description:  MATLAB script to compute poles and component value
% estimates based on desired level of ripple attenuation for a
% Saber numerical input sample of voltage ripple.  Assumes filter
% topology #5 from Phelps and Tate, "Optimizing Passive Input
% Filter Design," in Proceedings of the 6th National Solid-State
% Power Conversion Conference (POWERCON 6), May 1979, pp. G1-1 --
% G1-10.  Input ripple sample is provided either via the matrix
% "data" (X by 2 matrix containing time value in column 1 and
% corresponding voltage value in column 2)
%
% NOTE:  this estimation algorithm assumes that the input ripple
% seen by the filter does not change based on the filter
% design
%
% Arguments:
% poles - matrix used to store pairs of poles judged to produce
% the desired level of ripple attenuation on the ripple
% input data
%
% filtdata - matrix storing filtered version of numerical ripple
% sample for each acceptable pole pair
%
% filtcomp - matrix storing capacitor, inductor, and resistor
% component values that implement the acceptable
% pole pairs in the matrix "poles"
%
% systems - matrix storing filter transfer functions that correspond
% to the acceptable pole pairs in the matrix "poles"
%
% data - matrix used to input and/or store the numerical ripple
% input sample -- ripple sample can be input to the script
% via the matrix "data", or it can be read directly from
% the Saber output text file
%
% ripplespec - peak-to-peak ripple specification to be met by filtered
% ripple data
%
% Author:  Jamie C. Byrum
% Date:   9/15/99

% Process input file from Saber, if ripple sample not provided via "data"
% matrix.  Input file is generated by Saber Plotfile Report command
```

```

if nargin ~= 2,

    filename=input('Filename: ', 's');
    disp(['Reading File...'])
    [s1,s2]=textread(filename,'%s %s','whitespace','\b\r\n\t| ', 'headerlines',3);
    disp(['Processing File...'])
    entries = size(s1);
    entries = entries(1);

    % Convert text strings from input file to data
    for (ctr=1:entries),
        str1 = char(s1(ctr));
        str2 = char(s2(ctr));
        lenstr1=length(str1);
        lenstr2=length(str2);

        if str1(lenstr1) >= 'a' & str1(lenstr1) <= 'z'

            if str1(lenstr1) == 'm'
                str1(lenstr1) = 'e';
                str1 = cat(2,str1,'-3');

            elseif str1(lenstr1) == 'k'
                str1(lenstr1) = 'e';
                str1 = cat(2,str1,'3');

            elseif str1(lenstr1) == 'u'
                str1(lenstr1) = 'e';
                str1 = cat(2,str1,'-6');

            elseif str1(lenstr1) == 'p'
                str1(lenstr1) = 'e';
                str1 = cat(2,str1,'-12');

            elseif str1(lenstr1) == 'n'
                str1(lenstr1) = 'e';
                str1 = cat(2,str1,'-9');
            end

        end

        if str2(lenstr2) >= 'a' & str2(lenstr2) <= 'z'

            if str2(lenstr2) == 'm'
                str2(lenstr2) = 'e';
                str2 = cat(2,str2,'-3');

            elseif str2(lenstr2) == 'k'
                str2(lenstr2) = 'e';
                str2 = cat(2,str2,'3');

            elseif str2(lenstr2) == 'u'
                str2(lenstr2) = 'e';
                str2 = cat(2,str2,'-6');

            elseif str2(lenstr2) == 'p'
                str2(lenstr2) = 'e';
                str2 = cat(2,str2,'-12');

        end

    end
end

```



```

        elseif str2(lenstr2) == 'n'
            str2(lenstr2) = 'e';
            str2 = cat(2,str2,'-9');
        end
    end
end

num1 = str2double(str1);
num2 = str2double(str2);

% Write numbers from text file into "data" matrix
if ctr == 1
    data = [num1,num2];
else
    data = [data;num1,num2];
end
end

else
    entries=size(data);
    entries=entries(1);
end
% end of input file processing

% Select pole values and choose filter component values
maxpole = input ('Maximum Pole (in Hz): ');
polectr = 0;
compctr = 0;

% Step down pole values in fixed decrements and test each pair
decrement = -50;
for pole1h = maxpole: decrement: 0,
    for pole2h = pole1h: decrement: 0,

        pole1 = -2*pi*pole1h;          % radians
        pole2 = -2*pi*pole2h;          % radians
        den = poly([pole1 pole2]);
        num = prod([pole1 pole2]);
        sys = tf(num,den);              % create filter's transfer function
        % Filter the ripple sample with the generated filter and determine
        %   if output ripple results are acceptable

        filtered_data = filter_input_data(sys,data);
        good = acceptable_filter(entries,data,filtered_data,ripplespec);

        % Derive individual component values assuming poles are real.
        %   Component value derivations for form #5 filter are derived in
        %   Chapter 5.

        if good == 1,

            poleavg = (pole1 + pole2)/2; % a negative quantity
            polepart2 = min([pole1 pole2]) - poleavg; % a negative quantity

            % Use .1 ohm, 1 ohm, and 10 ohm damping resistor values
            for k = -1:1,

```

```

R = 10^k;
L = -R / 2 / poleavg;
C = 1 / L / (poleavg^2 - polepart2^2);

% Above values assume L2 is sized large enough to approximate
% two pole behaviour. Now, choose an L2 value sufficient for
% this approximation by iteratively finding an L2 value that
% produces the desired attenuation.

L2 = L/2;
good = 0;

while good == 0,

    L2 = L2 * 2;
    num = [(L+L2)/R 1];
    den = [L*L2*C/R L2*C (L+L2)/R 1];
    sys = tf(num,den);
    filtered_data = filter_input_data(sys,data);
    good = acceptable_filter(entries,data,filtered_data,ripplespec);

end

% write calculated pole values, filter transfer functions,
% component values, and filtered ripple data to output
% matrices

if compctr == 0,
    poles = [pole1h,pole2h];
    systems = [sys];
    filtcomp = [pole1h,pole2h,R,L,L2,C];
    filtdata = filtered_data;
    polectr = polectr + 1;
    compctr = compctr + 1;
else
    poles = [poles; pole1h,pole2h];
    systems = [systems;sys];
    filtdata = [filtdata,filtered_data];
    filtcomp = [filtcomp;pole1h,pole2h,R,L,L2,C];
end

disp([int2str(pole1h),' ',int2str(pole2h),' yes']);
end
break;
else

    disp([int2str(pole1h),' ',int2str(pole2h),' no']);

end
end
end
end

```

```
function filtered_data = filter_input_data(sys,data)
% function filtered_data = filter_input_data(sys,data)
%
% Description:  MATLAB script that receives unfiltered voltage ripple
% data and a filter transfer function from the pole_finder()
% script, applies the filter transfer function to the ripple data,
% and returns the filtered ripple data results.
%
% Arguments:
% filtered_data - matrix used to store filtered ripple data results
%                derived from applying the specified filter transfer
%                function to the provided ripple data
%
% sys - filter transfer function to be applied to the unfiltered ripple
%       data
%
% data - unfiltered ripple data
%
samppd = data(2,1)-data(1,1);
sysd = c2d(sys,samppd);
[b,a] = tfdata(sysd,'v');
filtered_data = filter(b,a,data(:,2));
```

```

function good = acceptable_filter(entries,data,filtered_data,ripplespec)
% function good = acceptable_filter(entries,data,filtered_data,ripplespec)
%
% Description:  MATLAB script that receives filtered voltage ripple
% data and determines whether the ripple peak-to-peak ripple in
% the filtered data is below acceptable limits.  The script
% returns a boolean value representing whether the filtered data
% is acceptable or unacceptable
%
% Arguments:
%   good - integer used to store boolean true (1) or false (0),
%         representing whether the filtered data does or does
%         not have the desired level of peak-to-peak ripple
%         attenuation
%
%   entries - number of data points in filtered ripple data
%
%   data - original unfiltered ripple data, used to determine the
%         average voltage value that should occur in the filtered data
%
%   filtered_data - matrix used to store filtered ripple data results
%                 derived from applying the specified filter transfer
%                 function to the provided ripple data
%
%   ripplespec - peak-to-peak ripple specification to be met by filtered
%               ripple data

% Beginning of filtered data set ignored since signal is ramping up to
% steady state.  Thus, analyze last 50% of filtered signal.

lowbound = round(entries*0.49);
highbound = round(entries*0.99);
low = min(filtered_data(lowbound:highbound));
high = max(filtered_data(lowbound:highbound));

peaktpeak = high - low;           % determine peak-to-peak ripple
meanfilt = mean(filtered_data(lowbound:highbound));
meanorig = mean(data(:,2));

% if peak to peak ripple is within the desired limit, and the mean
% of the last 50% of the filtered voltage ripple data is with
% a reasonable margin of the unfiltered voltage ripple mean,
% then filtered data meets ripple specification.

if peaktpeak < ripplespec & abs(meanfilt - meanorig) < 0.5,
    good = 1;
else
    good = 0;
end

```

Bibliography

- [1] J. G. Kassakian, "Automotive Electrical Systems -- The Power Electronics Market of the Future," *Proceedings of the IEEE Applied Power Electronics Conference and Exposition (APEC 2000)*, vol. 1, pp. 3 - 9, New Orleans, LA, February 2000.
- [2] J. G. Kassakian, H. -C. Wolf, J. M. Miller, C. J. Hurton, "Automotive Electrical Systems circa 2005," *IEEE Spectrum*, August 1996, pp. 22 - 27.
- [3] J. M. Miller, D. Goel, D. Kaminski, H. -P. Schöner and T. M. Jahns, "Making the Case for a Next Generation Automotive Electrical System," *International Congress on Transportation Electronics (Convergence '98)*, pp. 41-51, Dearborn, MI, October 1998.
- [4] J. M. Miller, P. R. Nicastrì and S. Zarei, "Automotive Power: Future Power System Architectures Face Formidable Hurdles," *Power Conversion and Intelligent Motion (PCIM)*, February 1999, pp. 44 - 45.
- [5] J. M. Miller, "Multiple Voltage Electrical Power Distribution System for Automotive Applications," *Proceedings of the 31st Intersociety Energy Conversion Engineering Conference (IECEC 96)*, vol. 3, pp. 1930 - 1937, Washington, DC, August 1996.
- [6] W. S. Chang, T. A. Keim, and J. G. Kassakian, *Fully Flexible Valve Drive*. Presented at Program Review Meeting of the MIT / Industry Consortium on Advanced Automotive Electrical / Electronic Components and Systems, Greenville - Spartanburg Airport Marriott, Greenville, South Carolina, January 2000.
- [7] K. K. Afridi, *A Methodology for the Design and Evaluation of Advanced Automotive Electrical Power Systems*, Ph.D. Thesis, Massachusetts Institute of Technology, Department of Electrical Engineering and Computer Science, February 1998.
- [8] T. C. Neugebauer, *Computer-Aided Design and Optimization of dc/dc Power Converters*, S.M. Thesis, Massachusetts Institute of Technology, Department of Electrical Engineering and Computer Science, September 1999.
- [9] C. J. Patterson, *Dual Voltage Alternator for Automotive Applications*, M.Eng. Thesis, University College Dublin, Department of Electrical and Electronic Engineering, January 1997.
- [10] Stephen J. Chapman, *Electric Machinery Fundamentals*, 3rd ed. New York: McGraw-Hill, Inc., 1991, pp. 255-256.

Bibliography

- [11] John G. Kassakian, Martin F. Schlecht, and George C. Verghese, *Principles of Power Electronics*. Reading, MA: Addison-Wesley Publishing Company, 1991.
- [12] V. Caliskan, D. J. Perreault, T. M. Jahns, and J. G. Kassakian, "Analysis of Three-Phase Rectifiers with Constant-Voltage Loads," in *IEEE Power Electronics Specialists Conference*, Charleston, SC, June 1999, pp. 715-720.
- [13] Society of Automotive Engineers, "Electromagnetic Compatibility Measurement Procedures and Limits for Vehicle Components (except Aircraft) (60 Hz to 18 GHz)," *SAE Standard J1113 / 1*, July 1995.
- [14] Society of Automotive Engineers, "Electromagnetic Compatibility Measurement Procedures and Limits for Vehicle Components (except Aircraft) – Conducted Immunity, 30 Hz to 250 kHz – All Leads," *SAE Standard J1113-2*, September 1996.
- [15] Hans-Dieter Hartmann, "Standardisation of the 42V PowerNet - History, Current Status, Future Action," *1st International Congress, 42V PowerNet: The First Solutions*, Villach, Austria, September 1999.
- [16] Standardisation Work Group (WGS) of the Vehicle Electrical Systems Architecture Forum, "Road Vehicles - Environmental Conditions for Electrical and Electronic Equipment for a 42V PowerNet -- Part 2: Electrical Loads," *WGS Working Draft WGS / WD 01/2000-2*, January 2000.
- [17] V. Caliskan, *Design and Analysis of Dual / High Voltage Automotive Electrical Power System Architectures*, Sc.D. Thesis, Massachusetts Institute of Technology, Department of Electrical Engineering and Computer Science, September 2000.
- [18] H. L. N. Wiegman and R. D. Lorenz, *Porous Electrode, Aqueous Solution Cell Modeling and State Estimation*. Lecture presented at the MIT Laboratory for Electromagnetic and Electronic Systems, Massachusetts Institute of Technology, Cambridge, Massachusetts, November 1999.
- [19] W. G. Hurley, S. Guttowski, F. Zhang, R. J. Thomas, and I. Rigney, *Progress Report on EMI / EMC in Dual-Voltage Electrical Systems*. Presented at Program Review Meeting of the MIT / Industry Consortium on Advanced Automotive Electrical / Electronic Components and Systems, Indianapolis Marriott North, Indianapolis, Indiana, June 1999.
- [20] T. Phelps and W. Tate, "Optimizing Passive Input Filter Design," in *Proceedings of the 6th National Solid-State Power Conversion Conference (POWERCON 6)*, May 1979, pp. G1-1 -- G1-10.
- [21] *Capacitors*, Cornell Dubilier Electronics, Inc., Liberty, SC, February 2000.

- [22] W. T. McLyman, *Transformer and Inductor Design Handbook*, 2nd ed. New York: Marcel Dekker, Inc., 1988.
- [23] W. T. McLyman, *Magnetic Core Selection for Transformers and Inductors*, 2nd ed. New York: Marcel Dekker, Inc., 1997.
- [24] *Tape Wound Cores*, National-Arnold Magnetics, Adelanto, CA, 1995.
- [25] D. J. Perreault and V. Caliskan, *Automotive Power Generation and Control*, LEES Technical Report TR-00-003, Laboratory for Electromagnetic and Electronic Systems, Massachusetts Institute of Technology, Cambridge, MA, May 2000.
- [26] A. Cobb, *Private Communication*, Cornell Dubilier Electronics, Inc., Liberty, SC, June 2000.
- [27] *Aluminum Electrolytic Capacitors*, ELNA America, Inc., Cypress, CA, 2000.
- [28] *Automotive Handbook*, 4th ed., Robert Bosch GmbH, Stuttgart, Germany, 1996.
- [29] K. S. Ofori-Atta, *Economic Analysis of Dual Voltage Automotive Electrical Systems*, LEES Technical Report TR-99-003, Laboratory for Electromagnetic and Electronic Systems, Massachusetts Institute of Technology, Cambridge, MA, July 1999.
- [30] L. M. Lorilla, *Investigation of the Homopolar Inductor Alternator for Automotive Applications*, M. Eng. Thesis, Massachusetts Institute of Technology, Department of Electrical Engineering and Computer Science, June 2000.
- [31] *MCR265-4 thru MCR 265-10 Thyristors* (product datasheet), Document MCR265/D Semiconductor Components Industries, L.L.C. (ON Semiconductor), 1999.
- [32] *50RIA Series Medium Power Thyristors* (product datasheet), Bulletin I2401, rev. A, International Rectifier, July 2000.
- [33] R. Frank, *Private Communication*, ON Semiconductor, Inc., Phoenix, AZ, July 2000.
- [34] L. Mays, *Private Communication*, ON Semiconductor, Inc., Phoenix, AZ, July 2000.
- [35] *Descriptive Designation System for Semiconductor-Device Packages*, JEDEC Standard JESD30-B, Engineering Department, Electronic Industries Association, Arlington, VA, April 1995.

Bibliography

- [36] M. Zhu, *Design of Feedforward Active Ripple Filters for Power Converters*, M. Eng. Thesis, Massachusetts Institute of Technology, Department of Electrical Engineering and Computer Science, May 1999.

76-3-99